A Carlos Óscar, Roberto, Robert y Samuel

Contents

Motivation and Objectives

Group background

This thesis has been conceived within a research group with large experience in the application of computational and experimental methodologies to the solution of key problems in biology (The Biocomputing Unit (BCU) of the National Center for Biotechnology (CNB): http://biocomp.cnb.csic.es/). For a group with these characteristics, the potential of positron emission tomography (PET) in modern biology (Cherry and Gambhir (2001)) and the need of tools for the management of PET data (Cherry and Chatziioannou (2004)) did not go unnoticed. For those reasons, PET was one of the sources of data considered in the proposal of the project "From information to knowledge: The management and analysis of large data set of complex objects in structural biology and functional genomics". Three research different groups with a common core in the topic of the development of new methods for the management and analysis of large data sets of complex biological objects, participated in the project. The Universidad Autónoma group (http://www.ii.uam.es/esp/investigacion/index.php?siglas=GTSB, attached to the BCU) was in charge of the subproject entitled "Toward Visual Proteomics: tools for 3D-Map Calculation and Management(BIO2007-67150-C03-03)". The aim of this subproject was the development of new data models and graphics environments that take into account PET

functional image data on small animals together with genomics and proteomics data, in order to place the knowledge on molecular mechanism in a physiological context. The group had never worked with PET and the important challenge of familiarization with a fairly complex technique had to be addressed before starting with the project. In exchange for the inexperience in the PET field, an important background in reconstruction of data from other image techniques existed (Marabini et al. (1997), Marabini et al. (1998), Sorzano et al. (2001), Marabini et al. (2004), Sorzano et al. (2008)) that was able to be transferred to the PET environment. For these reasons, the UAM group coordinated a Network-related project of six laboratories on PET reconstruction for small animals (FIS PI040683). This project proposed to adapt several reconstruction algorithms to the singularities of small animal scanners and to perform an objective quantitative comparison of their performance under realistic conditions. The project had, for the UAM group, a double purpose. First, from the point of view of contribution to the field, the application of the knowledge owned on image reconstruction to the development of PET reconstruction algorithms. The reconstruction algorithms are known to have an important role in the success of the small animal PET (Lewitt and Matej (2003)), and any chance of improvement in the reconstruction field is well justified. Second, from the point of view of learning, the project provided an excellent first contact with the PET data and environment, before focusing on the biological applications of the technique. The present work has been developed in the framework of the second mentioned project. This is thus a thesis on PET image reconstruction that has the underlying function of familiarize a group with PET; a tool that fits in perfectly with its line of research in techniques applied to the extraction of biological knowledge.

State of the art and objectives

Once focused on PET reconstruction, a clear trend towards the algorithms known as "iterative" was found in the literature (Qi and Leahy (2006)) and this work has been consequently devoted to this type of reconstruction. It is well know that what makes iterative algorithms to obtain images with better resolution and noise properties than other approaches is the accurate statistical model of the data formation and acquisition process they are based in. Concerning the data model, the Poisson distribution is a widespread accepted model for the positron emission process, which is the source of data in PET. The most popular family of iterative reconstruction algorithms (based on the Maximum Likelihood Expectation Maximization MLEM (Vardi et al. (1985)) algorithm) is indeed based on a Poisson model of the positron emissions. For that reason the MLEM has been chosen as the iterative scheme in which the reconstructions of this thesis are based in. Regarding the acquisition process model, in the MLEM algorithms family, it is composed of a collection of statistical terms, arranged in a matrix structure known as the "system matrix" or the "system response matrix". The system matrix terms result from the combination of a great variety of complex factors, many of which can be dependent on the particular scanner features and/or on the experiment conditions. Apart from being a complicated mathematical problem, the system matrix calculation requires high computational resources both in terms of time and storage (Herraiz et al. (2006)).

The computation of the system matrix terms is thus a challenging task that at the same time constitutes a crucial step in the achievement of high quality reconstructions. This assertion is in agreement with the large number of works that are continuously published on the topic (Veklerov et al. (1988), Mumcuoglu et al. (1996), Qi et al. (1998), Kudrolli et al. (2002), Rafecas et al. (2004), Alessio et al. (2006), Herraiz et al. (2006), Panin et al. (2006a),Panin et al. (2006b), Scheins et al. (2006), Moehrs et al. (2008), Tohme and Qi

(2009), Ortuño et al. (2010), Aguiar et al. (2010), Pratx and Levin (2011), Herraiz et al. (2011)), all of them focused on the computation of the system matrix in an accurate and efficient way. However, among all these works, no one has been found that gathers and takes into account all the peculiarities of the so-called "continuous detectors" technology (Karp et al. (1990)). Being the system modeling a key issue in statistical reconstructions, the lack of specific models implies that the reconstructions obtained so far from continuous detector data do not take fully advantage of the benefits of working with this technology. This is an important issue, in particular for the development of the FIS project, since one of the groups collaborating owned data from one of these scanners (Balcerzyk et al. (2009), Sánchez et al. (2012)), and in general for the PET community, where a renewed interest for this type of scanners has emerged in the last years (Hun et al. (2002), Tavernier et al. (2005))

The main problem that arises when the existing system matrix implementations want to be used with continuous detectors technology is that they are not able to retain the whole precision of the data this type of detectors provides. The analytical implementations of the system matrix that would be able to retain such precision (Vardi et al. (1985)), have been traditionally discarded in pursuit of other experimental (scanner measurements, Monte Carlo simulations) methodologies (Rafecas et al. (2004), Panin et al. (2006a), Alessio et al. (2006), Ortuño et al. (2010)). Apart from being specially suited for reconstruction of continuous detectors data, the analytical approaches to the system matrix computation have other benefits (noise free, precision, flexibility) for the PET reconstruction in general. The reason these benefits have not been fully explored so far is that elaborated analytical methodologies give place to high time consuming implementations. Consequently, only those analytical approaches based in simplified models of the PET process are feasible. However, now that the recent technological advances (computer clustering, use of

Graphical Processing Units (GPUs)) provide computational resources that allow increasingly complex implementations of the system matrix (Pratx and Levin (2011), Herraiz et al. (2011)), a door is open to check to what extent a proper analytical implementation of the system matrix can lead to improved reconstructions.

The study of the state of the art has lead therefore to two open problems in the field of PET reconstruction: the lack of reconstruction methods adapted to the requirements of the continuous detector technology and, more generally, the lack of elaborated analytical methodologies for the system matrix calculation. These have been the two main topics this work has been focused in.

Structure of the document

According to the previous discussion, and after a general introduction to the PET technique provided in Chapter 1, this dissertation is built around Chapters 2 and 3, whose contents are briefly described bellow:

1. Chapter 2 deals with the application of analytical methodologies to the computation of the system matrix. As has been mentioned, such methodologies have not been fully exploded so far, due to their slow performance. Now that the technology is allowing increasingly faster implementations, is the moment to check the improvements these methodologies can achieve. But, even if the analytical approaches are expected to have a great number of advantages, it has to be taken into account that the system matrix is a statistical model of a very complex process, in which effects of very different nature are involved. Some of these effects will undoubtedly be well modeled by an analytical approach, but there may be other effects for which an analytical treatment may not be appropriate. The objective of the chapter is not, therefore, to develop a purely anatitical system matrix implementation, but to explore

how the advantages of these approaches, that haves been traditionally discarded due to its inefficiency, can be exploited. In Chapter 2, a thorough study of the PET data acquisition and of how the different methodologies are appropriate to model this process in the system matrix is performed. The result of this study is a new approach for the calculation of the system matrix based on the synergy between the analytical and other experimental approaches. The main advantages and limitations of each of the previous works on this topic are analyzed so that they justify the choices made in the design of the new system matrix. Moreover, the implication each of these choices has in the image domain has been studied in order to evaluate to what extent the new scheme improves the reconstructions.

2. Chapter 3 deals with the reconstruction for continuous detectors data. The underlying reason that has led to the development of the new methodology introduced in Chapter 2 is the absence of specific approaches that are able to retain the precision of the data provided by the continuous detectors devices. Reconstructions of data from this kind of scanners are currently performed with system matrices that do not take into account this or other particularities of this technology. Consequently, the reconstructions obtained so far do not take advantage of the benefits of working with continuous detectors. Once the new approach to the system matrix computation has been developed in Chapter 2, it will be proved in Chapter 3 how it can be adapted not just to retain the precision of the continuous detector data, but to account for other peculiarities of this type of devices. Apart from the new methodology to compute the system matrix, other issues of the reconstruction (data format, sensitivity calculation) have been adapted to the continuous detectors requirements, giving place to a reconstruction scheme totally suited to this type of detectors, whose advantages in the image domain have been proved.

Chapter 1

Introduction to Positron Emission Tomography (PET)

1.1 Functional imaging

Medical imaging has traditionally been thought of as a way of viewing the body's anatomy. Indeed, x-ray computed tomography and magnetic resonance imaging yield exquisitely detailed images of the anatomical structures. However, in some cases it is useful to acquire images of physiologic function instead of (or in addition to) images of anatomy. Such images can be acquired by the class of imaging techniques known as nuclear medicine imaging, whose two major subbranches are the single-photon emission computed tomography (SPECT), and the positron emission tomography (PET).

Both techniques involve the injection of a radiopharmaceutical into the subject under study to image properties of the body's physiology. A radiopharmaceutical consits of two parts: a tracer compound that interacts with the body and a radioactive label. The tracer principle (George de Hevesy, early 1900s) states that the radioactive labeled compounds are

incorporated to biochemical pathways in the same way as nonradiactive materials. Therefore, by way of the emission of gamma rays, the radioactive labels can be used to track the flow and distribution of important substances in the body. The tracer principle has two powerful benefits as a basis for imaging biological processes. First, it can be used to measure molecular concentrations with tremendous sensitivity, as one can readily detect even minute quantities of radioactive material. Second, tracer measurements are noninvasive, since the concentration of tracer is deduced from counts of gamma rays emitted from within the body as the result of radioactive decay of the administered tracer.

A wide range of biologically interesting compounds can and have been synthesized with radionuclide tags thus permitting the measurement of quantities of interest going from glucose metabolism to gene expression. Among other applications, the nuclear imaging techniques can be used to detect tumors, locate areas of the heart affected by coronary artery disease or identify brain regions influenced by drugs (Cherry and Chatziioannou (2004)).

1.2 Positron emission tomography

1.2.1 Electronic collimation

SPECT uses radiouclides that emit single gamma rays in the $80 - 350$ keV range. These gamma rays can be detected externally by position-sensitive detectors, also known as gamma cameras. A collimator is inserted between the patient and the detector that lets pass only photons that approach the detector with certain angles while discarding the other photons (see Figure 1.1). In order to image the patient from many points of view, the process is repeated by positioning the gamma camera at many orientations about the patient. Although the majority of SPECT scans at the present time are done for the diagnosis of

cardiac disease, there are many other clinical and research applications where SPECT is used.

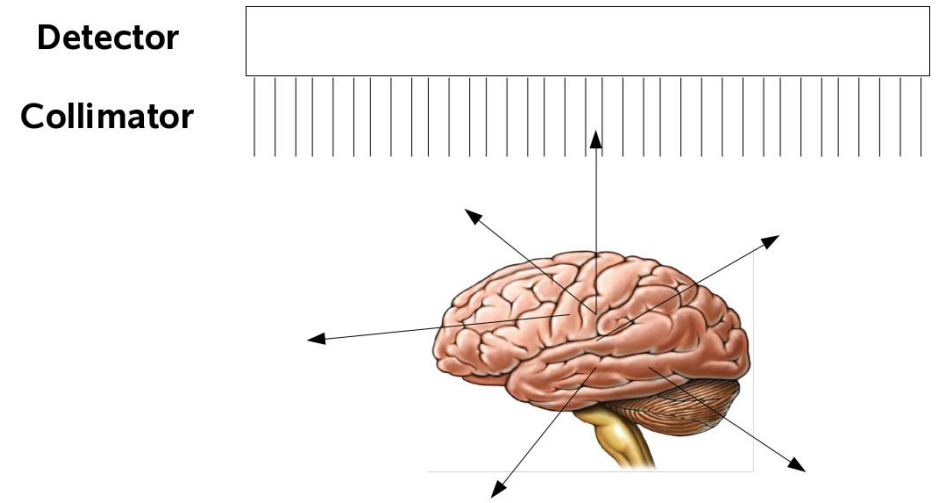

Figure 1.1: Parallel-hole collimator SPECT. Although photons are emitted isotropically at each point, only those emitted along lines parallel to the channels of the collimator reach the detector (drawings are not to scale).

SPECT collimation does an inefficient use of the emitted radiation, as the gamma rays not perpendicular to the camera face are absorbed by the lead walls between the holes. However, the collimator is necessary to define the direction from which the gamma rays are coming, thereby providing spatial information. PET studies do not require a physical collimator, but use a scheme of detection called "electronic collimation". Electronic collimation is based on the use of positron emitting radioisotopes as radioactive labels. Positrons are the antiparticles to the electrons, with the same mass but with opposite electric charge. When the positrons reach thermal energies, they interact with nearby electrons

by the formation of a hydrogen-like orbiting pair called positronium. Positronium is unstable and eventually decays, via annihilation, into a pair of 511 keV gamma photons emitted at 180 degrees relative to one another with completely random orientantion. A PET scanner consists basically of a collection of gamma-ray detectors connected to circuitry that senses the timing of the gamma-ray detections. When two gamma rays are detected roughly simultaneously (typically an acceptance time window of a few nanoseconds is imposed), the coordinates of each photon interception are recorded by the detector system. The segment line defined by the two detected points is usually referred to as line of response (LOR).

1.2.2 PET data

The data provided by a PET scanner are not directly in the form of a tomographic image, but consist of a collection of lines of response (LORs). Consequently, some computer reconstruction method must be applied in order to estimate the radiotracer distribution that gave place to the measurements.

The collection of LORs can be stored before the reconstruction in different formats. Data can be binned as a function of the LOR spatial orientations, through structures called sinograms. The sinogram is a representation of the detections measured at a given plane. For each plane, a sinogram is a two-dimensional matrix with the vertical columns representing projection angles and the horizontal rows representing spatial positions within the projections, as shown in Figure 1.3. An alternative option is the storage mode known as list-mode. List-mode acquisition is achieved by storing information regarding the acquired events as they are detected one-by-one in the form of a list.

There are some sources of error in the recorded data. The errors come from the assumption that an annihilation event occurred along each of the LORs that make up the PET data. Not all the coincidence events accepted by the tomograph meet this assumption.

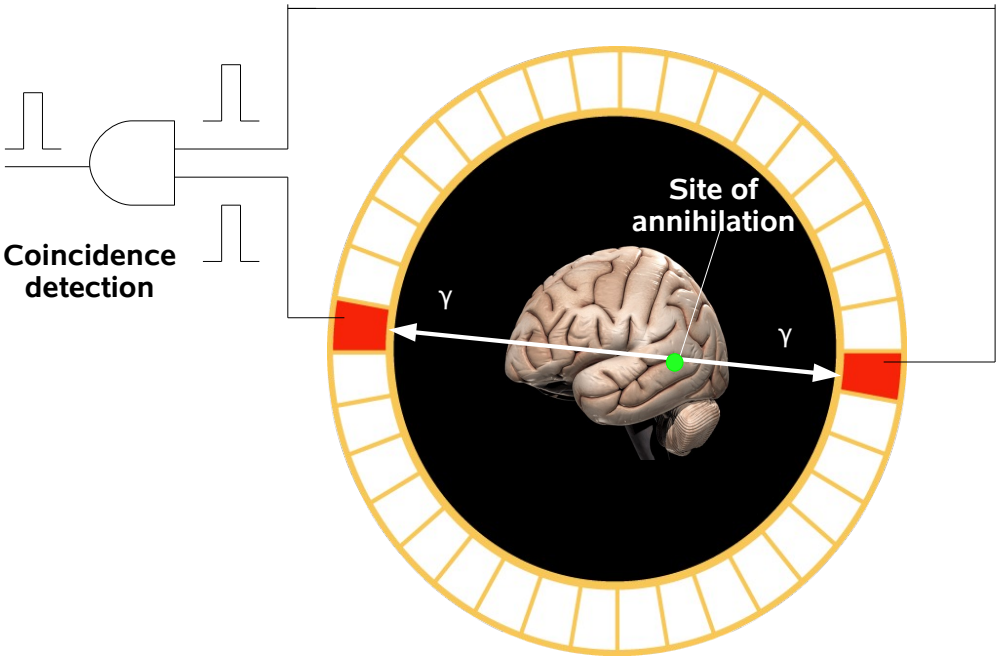

Figure 1.2: Schematic diagram of electronic collimation in PET. Two gamma rays emitted as a result of positron annihilation are sensed at two detectors at roughly the same instant. Thus, it can be inferred that a positron was generated along the line segment connecting the detectors involved.

It can happen that one or both annihilation photons interact in the object being scanned. Consequently, photons lose all (this effect is referred to as “attenuation”) or a part of their energy and can be scattered in a new direction. The interaction of the gamma rays with the object can give place to the existence of three different situations that cause coincidence events (see Figure 1.4):

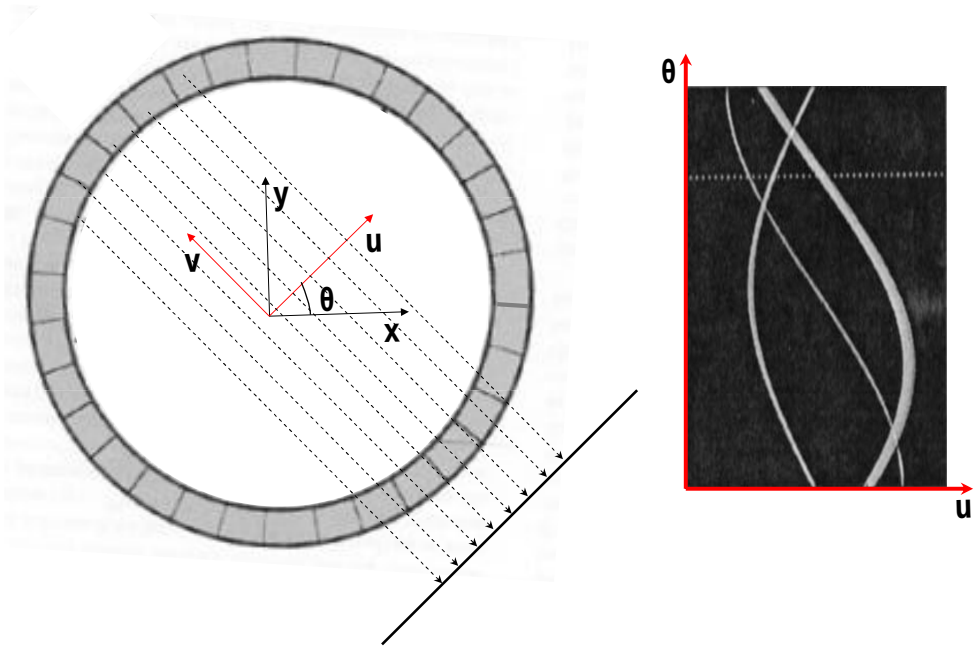

Figure 1.3: Sinogram formation. Coincidence events in PET scanner are categorized by plotting each LOR as function of its angular orientation versus its displacement from center of gantry

- A “True coincidence” occurs when a positron annihilates and both of the gamma rays are detected without either of them scattering in the object to be scanned.

- If one or both photons are scattered, but both photons are detected in coincidence, the result is a “Scattered coincidence” This is a source of error in the data, since the original annihilation is not on the line joining the coordinates of the detected photons and the resulting LOR will be misplaced.

- If one of the photons misses the detector (this can be due to an interaction or to the relatively small solid angle subtended by the detector ring), the time window will usually contain only one detected photon and the coordinates will be discarded, unless the same situation arises close enough in time with another annihilation. This case is called a "Random Coincidence" (or "Accidental coincidence") and is a source of error since the two detected photons come from different annihilations, neither of which is on the line in space joining the coordinates of the detected photons.

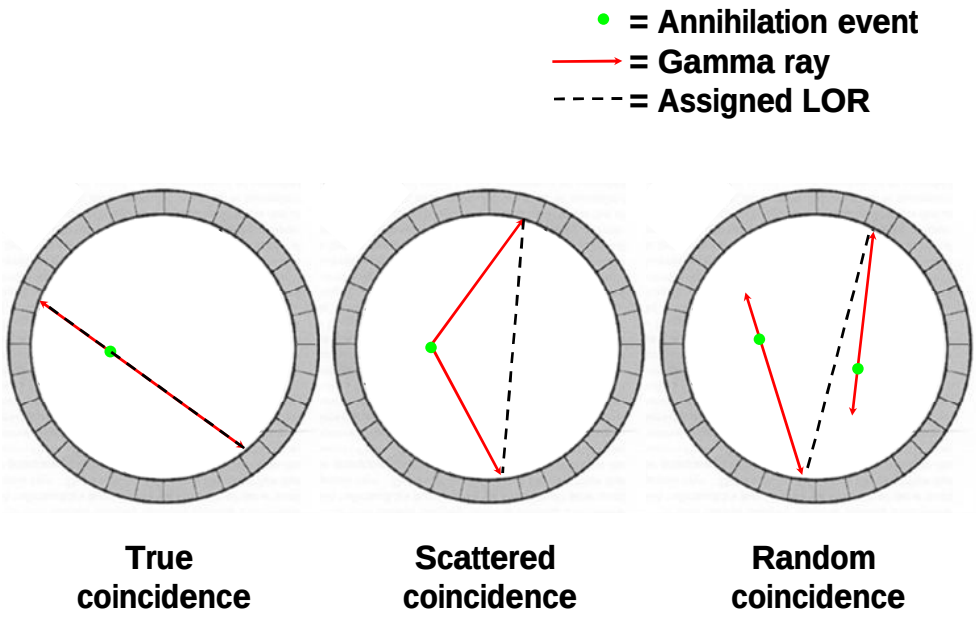

Figure 1.4: The three different situations that can give rise to a coincidence event measured in a PET scanner

During image reconstruction, corrections can be made for both randoms and scatter (Lewellen (2008)). There are two standard approaches for measuring the randoms. The delayed-window approach is based in applying a timing acceptance window that is delayed from the prompt window and only samples random events. The second approach calculates the randoms by measuring the single event rates in each detector. Scatter detection can be reduced by applying an energy acceptance criteria or estimated and corrected after data acquisition. Several analytical methods used with this purpose can be found in Lewellen and Karp (2004).

1.2.3 PET detectors

Although various alternatives continue to be considered (Lewellen (2008)), the most common PET detector block scheme is based on some form of scintillation detector coupled to photomultiplier (PMT) tubes. The overall function of the detection system is to convert the interaction of a 511 keV gamma ray in the scintillator into a robust current pulse that can be detected and processed by relatively standard electronics. Specifically, when a photon interacts in the scintillator, electrons are moved from the valence band to the conduction band. The electrons return to the valence band at impurities in the crystal, emitting many optical-wavelength photons in the process. The light obtained at the scintillator is collected by the PMTs, which convert the light photons into electrons and amplify the signal. This current is sensed by accompanying electronics, which compute the spatial coordinates of the gamma-ray event relative to the face of the camera and register the occurrence of an event.

In order to optimize the detection process, a scintillator should thus be fast (for accurate timing), dense (so that the probability level of the 511 keV gamma rays interacting in them is somewhat high), have high light output (for position accuracy) and be cheap to produce.

Currently, the high-end PET scanners being offered are mainly based on bismuth germinate (BGO), lutetium oxyorthosilicate (LSO) and gadolinium oxyorthosilicate (GSO).

Scintillator-based Detector designs

The first PET scanners used one PMT per scintillator crystal (Phelps et al. (1978)). As designs began to reduce the crystal cross section to obtain higher spatial resolution, several limitations to this approach were encountered. On the one hand, the existing PMTs were too large to pack them together with a full block of very small crystals. On the other hand, the large number of PMTs and electronic channels increased the cost of the system. As a result, two alternative scintillator detector designs (see Figure 1.5) emerged in the 1980s:

- The first scheme is based on large area continuous crystals viewed by an array of PMTs (Karp et al. (1990)). Traditionally, the position of an event in a continuous detector is determined by calculating the centroid of the emitted light by means of a modified resistor network amongst all PMT array pads. In a continuous crystal detector, the main characteristics of the detector (especially energy and spatial resolution) are expected to be strongly related to the crystal surface treatment. For this reason, the surface treatment of the crystal must be optimized before mounting the crystal on the final module.

- The second approach uses smaller discrete crystals that shape the light response function (LRF) to allow the decoding of crystal positions with a small number of PMTs (Casey and Nutt (1986)). The LRF can be controlled with different coupling compounds at the interface and surface finishing or by using different lengths of reflector between the crystals. Typically, four PMTs are placed over the crystals in a rectangular pattern and ratios are formed from the PMT signals to provide a transverse and axial position signal.

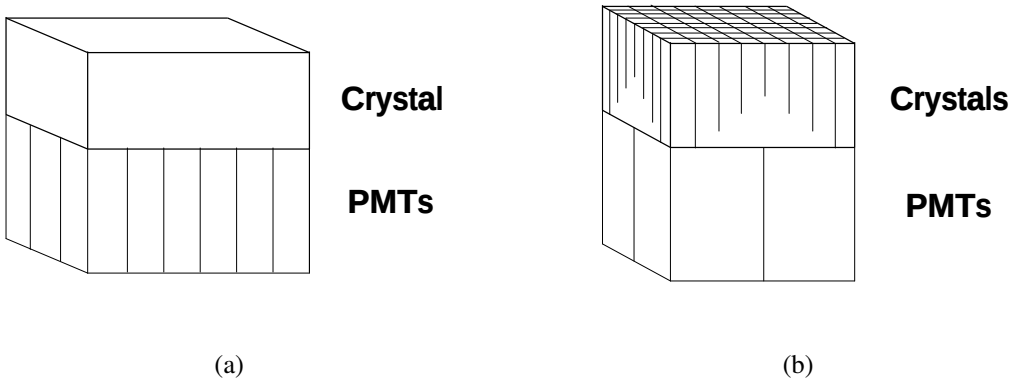

Figure 1.5: The major scintillator-PMT schemes options currently in use. (a) Continuous large crystal read by an array of PMTs. (b) Array of crystals with different treatments and/or reflectors viewed by a small number of PMTs.

The advent of new technical developments such as position sensitive photomultipliers PS-PMTs (Kume et al. (1986)) has led the PET scintillator-based detectors to evolve in a variety of design approaches, whose detailed description is out of the scope of this document. However, all these designs are based in the two above mentioned basic approaches, and their performance is still strongly associated to the continuous/pixelated nature of the scintillators:

- The use of continuous scintillators instead of pixellated blocks allows, in principle, to improve the spatial resolution (since the detected positions are not associated to the centers of pixelated components), while avoiding the problems of light collection efficiency that are related to fine pixellation of the crystals. Additionally, the cost and complexity of the detector are reduced. On the other hand, the large continuous crystal approach requires scintillators with higher stopping power, in order to prevent

the light from spreading too far in the crystal and achieve accurate spatial localization of the events. Unfortunately, the scintillators with higher stopping power can't currently be grown into large crystals. An exception is LSO, with high scintillation efficiency, high cross-section for 511keV gamma rays and fast decay time, which result in excellent count-rate performance (Siegel et al. (1995)). Other disadvantages currently associated to the use of this kind of scintillators are the non-uniformity and the nonlinearity in the camera response, but their effects can be minimized during the process of camera calibration (Sánchez et al. (2004)).

- The discrete crystal machines offer higher sensitivity due to the higher stopping power of the scintillators used (BGO, LSO or GSO) and much higher count-rate performance. On the other hand, as every scintillator pixel must be treated individually before being inserted in the detector block, the cost and complexity of the PET system increases. Moreover, in a pixelated detector, energy resolution is a function not only of the intrinsic scintillation efficiency of the crystals, but also of the crystal size (Giménez et al. (2004)). This is due to the fact that smaller cross section crystals exhibit greater light loss and, consequently, lower energy resolution (a high light yield from a scintillator normally improves the energy resolution because it reduces the Poisson noise of the PMT signal).

Detector geometry

A PET scanner is composed by several of the detector modules described in the previous section. The blocks can be configured as full static rings that completely surround the patient (Surti et al. (2005)) or as partial rings in a rotation device that allows the obtaining of the needed angular sampling (Del Guerra et al. (2006)).

In two-dimensional scanners, multiple planes of detectors surround the patient with

dense material, or “septa”, separating each plane, as shown in Figure 1.6 (left). The septa stop photons traveling between planes so that coincidence events are collected only between pairs of detectors in a single plane. Using this configuration, the data are separable and the image can be reconstructed as a series of two-dimensional sections. In contrast, the three-dimensional scanners (Figure 1.6 (right)) have no septa so that coincidence photons can be detected between planes. In this case, the reconstruction problem is not separable and must be treated directly in three dimensions. The septa removal in the three-dimensional mode increases the total number of detected photons and hence increases the signal to noise ratio. However, the number of scatter coincidences increases considerably when working in this mode (Townsend (1991)).

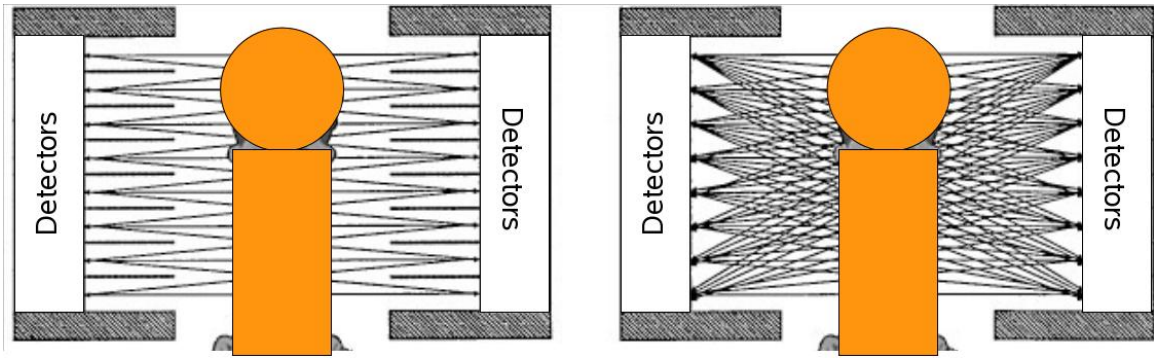

Figure 1.6: Schematic diagram of an axial cross section through (left) a 2D and (right) a 3D PET scanner. The septa in the 2D scanner stop out-of-plane photons while the 3D scanner detects these events as additional data

1.3 Small animal PET

PET scanners for human imaging have improved dramatically since their introduction in the mid-1970s. Clinical PET scanners typically produce reconstructed tomographic images with a spatial resolution in the 5 to 8 mm range. These clinical systems have also been used for animal research, predominantly in the larger laboratory animals such as non-human primates, dogs and pigs, where the spatial resolution is often adequate. There has been attempts to image smaller animals such as rats on these clinical scanners (Agon et al. (1988), Ingvar et al. (1991)) but the spatial resolution is sufficient for only a narrow range of applications. The first dedicated animal PET scanners were also designed for larger research animals, particularly for brain imaging in non-human primates (Cutler et al. (1992), Watanabe et al. (1997)). These systems were designed to obtain somewhat higher spatial resolution than clinical PET systems.

With the tremendous advances in mouse genomics and the wide range of animal models of human disease based on mice and rats, there has been significant motivation to extend the PET technique to imaging of small animals. The first dedicated small animal PET scanner (Bloomfield et al. (1995), Bloomfield et al. (1997)) took the standard detector technology being developed for clinical PET systems but placed these detector units in smaller diameter rings than common clinical PET scanners to form a compact PET system for rodent imaging. Although the spatial resolution was not superior to that found in clinical systems, it did elegantly demonstrate the concept of a dedicated small animal PET system and a tremendous amount of useful research was carried out with it. In the mid-1990s numerous groups began to develop small animal PET scanners with detector technology developed specifically for that application and with improved spatial resolution (Marriott et al. (1994), Lecomte et al. (1996), Bruyndonckx et al. (1996), Pichler et al. (1998), Chatziioannou et al. (1999)). It must be remarked that two Spanish research groups have been involved in the

design, development and manufacture of three of the commercially available small animal PET systems:

- The rPET (Vaquero et al. (2004)) and the ARGUS PET (Vaquero et al. (2005)) (commercialized under the name of eXplore VISTA by General Electric Health Care) are two pixelated small animal PET scanners developed by people of the Medical Imaging Laboratory at Gregorio Marañón Hospital (Madrid, Spain).

- The Albira PET (Balcerzyk et al. (2009)) is a small animall PET scanner with monolithic crystals developed in the Instituto de Física Corpuscular (IFIC) and manufactured by Oncovisión (Valencia, Spain)

1.3.1 Comparison of small animal imaging techniques

One of the main advantages of PET is its noninvasive character. It is clear that noninvasive techniques providing the same or similar information than other techniques in which it is needed to euthanize the animal (as autoradiography or tissue dissection do) have great value. It permits longitudinal, within-subjet study designs to follow disease models and interventions over periods of days, weeks and even months. Because the same animal is used at every time point, each animal serves as its own control and variability due to interanimal differences is effectively removed. Therefore, a single animal studied multiple times by PET may in some instances provide the same data that would have needed tens of animals using traditional invasive techniques requiring sacrifice of the animal. This means a great reduction in cost and speed results. It may also improve the quality of the data (because of the within-subject design), although this has yet to be unequivocally demonstrated.

There exist other non-invasive techniques such as magnetic resonance (MRI) and x-ray

computed tomography providing exquisite high resolution images that are largely reflective of anatomy. Although they have an important place in small animall imaging, these techniques do not provide functional data and they are in general more suited to address a different set of questions. Some limited functional information can be obtained with modern magnetic resonance imaging methods, although the sensitivity levels are much lower than those provided by PET.

There also exist optically based techniques for *in vivo* functional imaging. These are also non-invasive techniques, that provide functional image at high levels of sensitivity. The problem with these techniques is that the emitted light can penetrate just several millimeters of tissue. The depth limitation along with the lack of tomographic methods for accurately computing the 3D emission distribution limit optical imaging methods to the smaller laboratory animals (mice) or to superficial imaging in larger animal models.

Another important advantage of PET over the optical techniques is that it enables the distribution of the radionuclide (and therefore the molecule to which it is attached) to be measured in quantitative units, assuming that appropriate corrections are made for physical factors such as gamma ray attenuation and scatter in the tissue. In optical imaging, light scatter makes accurate quantification extremely challenging.

Finally, as has already been stated, compared with nuclear imaging techniques that use single gamma ray-emitting radionuclides (SPECT), PET has at least one order of magnitude advantage in sensitivity because the direction of an incident gamma ray is defined electronically by the detection of the opposing gamma ray. The physical collimation used by SPECT dramatically reduces the detected gamma ray event rate per unit of injected dose of radioactivity.

1.3.2 Applications

Dedicated small animal PET scanners are already being used for many different applications. These include measurements of the glucose metabolism in the rat brain and heart (Moore et al. (2000), Kornblum et al. (2000)) studies of the dopaminergic system in the rat (Hume et al. (1996)) and mouse (Chatziioannou et al. (1999)) brain, or investigation of the effect of photodynamic therapy in a mouse tumor model (Lapointe et al. (1999)).

Gene expression

In the environment of structural biology and functional genomics in which this dissertation has been conceived, an area of application that attracts great interest is the merger of PET with molecular biology to create methods to measure gene expression *in vivo* (Gambhir et al. (2000)). Genes direct the physical development and behavior of an organism. The long strand of nucleotides of which a gene consist of contains a coding sequence, which determines what a gene produces (such as a protein). This sequence is controlled by a promoter region, which regulates when, where, and to what extent the gene generates the product which it encodes. Gene expression is the process by which, under the promoter control, the coding sequence is made manifest as a physical and biologically functional gene product. Research into gene expression will enable scientists to decipher the functions of genes and their protein products, and to get a clearer picture of the complex regulatory networks that control fundamental biological processes. To understand these complex processes, there is a growing interest in studying the conditions under which each gene in the DNA sequence is expressed. The use of non-destructive imaging procedures like PET that allow to follow individual subjects of a same population over an extended period during which various procedures are performed, are especially valuable for the timely advancement of research in gene expression.

A PET reporter gene has been successfully used (Tjuvajev et al. (1998), Gambhir et al. (1999), Gambhir et al. (2000)) that is able to produce a protein that is capable of trapping a positron-labeled compound. The reporter gene is driven by the same promoter (the promoter can be thought of as a switch that controls the level of expression of the gene) as the gene of interest, such that when the gene of interest is expressed, the reporter gene is also expressed. The retention of the positron-labeled probe by the protein product of the PET reporter gene has been shown to be proportional to the level of reporter gene expression, which in turns reflects the level of expression of the gene of interest (Gambhir et al. (2000)). In this way, the location, magnitude of expression and time course of expression levels of any gene that is introduced in a mouse can be monitored *in vivo*. The same PET reporter gene approach can be used in transgenic mice where every cell in the mouse carries the PET reporter gene, but the signal is only detected when the promoter driving the PET reporter gene is switched on. This enables endogenous gene expression to be studied in mouse models. There are widespread applications for these PET reporter gene methods (Gambhir et al. (1999)). For example, genetic tagging of tumor cells that can then be followed over time after injection in an animal, studies of the efficiency of gene therapy vectors for delivering genes into experimental animals, interactions between cancer cells and the immune system, or studies of gene expression patterns during development to see when certain genes are switched on or off. This opens up many powerful research opportunities that take advantage of the ability of PET to longitudinally measure gene expression in an entire mouse.

1.3.3 Resolution and sensitivity in small animall PET

The previous sections have introduced the advantages and the benefits of the use of PET in the field of biomedical research. However, it must be taken into account that, due to

the differences in size between rodents and humans, small animal PET imaging imposes challenging performance requirements, particularly on system sensitivity and on image resolution (Vaquero and Desco (2005)).

Resolution

There are many examples in the small animal PET field where the ability to visualize and accurately measure radiopharmaceutical accumulation in structures that have dimensions of a millimeter or less in size is important (Stickel et al. (2007)). The typical image resolution of many of PET systems is in the 1-to 2.5-mm range (Cherry and Gambhir (2001)). Whether the submillimiter range is close to be reached for small animal PET is not all clear since there are several complex factors interacting to limit spatial resolution during data formation and collection:

- ***Positron physics***. The assumption that the annihilation that gave place to the true coincidences occurred somewhere along the line connecting the two involved detectors does not take into account the effect of two positron physics factors:
  - *Positron range*: Before reaching thermal energies, positrons travel through tissue giving up their kinetic energy principally by Coulomb interactions with electrons. The distance the positron travels before annihilating is termed positron range. The magnitude of this range depends on the positron energy, which varies widely among isotopes and with the fraction of air in the tissue. The only known way to reduce this effect is using a strong magnetic field, an attractive approach since the PET scanner can be potentially merged with a Magnetic Resonance Imaging (MRI) scanner (Blanco (2006)).
  - *Non-collinearity*: One would normally expect the annihilation gamma rays to be antiparallel. However, the residual kinetic energy and momentum of the

positron and electron at the time of annihilation results in an angular uncertainty in the direction of the 511 keV photons that can be modelled as a Gaussian distribution with a standard deviation of 0.212 degrees (DeBenedetti et al. (1950)). Scanner design can minimize non-collinearity by minimizing the separation between detectors.

- ***Crystal penetration***. Once the gamma rays reach the scintillator, they may travel some distance in the scintillator before being absorbed. As a result, if the gamma ray enters the crystal at an oblique angle, the location of the interaction will not be the same as the point of entry into the scintillator. Thus, an incorrect line of response will be assigned to the interaction because the LOR is normally assigned to a position at the front of the crystal interaction. This source of error worsens as the source position moves radially away from the center of the scanner because a larger fraction of the gamma rays enter the crystals at oblique angles. The consequence of this effect is a non uniform resolution response that degrades radially across the field of view.

  One solution that is a very active area of development is to add the ability to determine how deep in the crystal an event actually occurs (Lewellen et al. (2004), Inadama et al. (2006)). Moreover, crystals with high density help to reduce the crystal penetration effect, since their high stopping power reduces the variability of the depth of interaction (DOI) of incident gamma rays in the detectors.

- ***Detector scatter***. A 511 keV photon can undergo two main interactions in the scintillator: Compton scattering and photoelectric absorption. A Compton scattering interaction results in a scattered photon and a recoil electron. Photoelectric absorption results in a photoelectron and in a characteristic x-ray. The x-ray produced in photoelectric absorption and the Compton scattered photon may interact again at some distance from the original interaction site or alternatively they may escape from the

detector. As a result, each 511 keV gamma photon emitted can cause interactions at different points in the scintillator crystal. The position of the final event depends on the particular detector readout and signal processing of the system. The center of mass of the deposited energy is the positioning approach underlying most current PET detector technology, although other positioning approaches exist (Tavernier et al. (2005)). Independently of the positioning method, the increase in the number of interactions in the scintillator leads to an increase in the error of the location of the initial photon interaction (Stickel and Cherry (2005)).

The degradation of the spatial resolution due to the detector scatter can be fought using narrow detectors that reduce the room for secondary interactions and a good energy discriminator that rejects the low energy events coming from secondary interactions (Stickel and Cherry (2005)). However, both the detector thickness reduction and energy discrimination have the cost of a possible reduction in the overall scanner sensitivity. Rafecas et al. (2003) show how to overcome this problem by using individual crystal readout along with an appropriate identification scheme to select the primary crystal. Other techniques applied during calibrations (Surti et al. (2009)) have shown to reduce the effect of the detector scatter in the reconstructed spatial resolution.

- ***Light emission***. Unlike one to one scintillator-photomultiplier tube coupled detectors, detector blocks like those shown in Figure 1.5, have additional degradation of their spatial resolution, since the shared scintillation photons within the block create an uncertainty in positioning the events. In linear positioning algorithms, as the energy centroid computation, the result is a loss of resolution due to misidentification of the interaction point. An alternative, is to use positioning techniques based on statistical models of the light behavior within the scintillators (Joung et al. (2000))

rather than linear algorithms.

- ***Detector design***. Each of the detector designs described in Subsection 1.2.3 deals with particular issues that contribute to the resolution degradation:

  - For a detector composed of small discrete crystals, all interactions are assumed to occur at the center of individual crystals and consequently the spatial resolution of a pixelated scanner is limited to approximately half the width of an individual crystal (Lewellen (2008)).

  - In the case of continuous designs, where the light response function (LRF) is not shaped, the statistics of the light emission and collection as well as the distortions in the shape of the LRF due to reflections from the sides and back surfaces work to degrade the positioning of the event (Lewellen (2008)). The LRF can depend strongly on the DOI if the crystal is thick enough and the light reflections are not controlled. This DOI dependence can be either an hindrance or an added parameter to extract and utilize to address the parallax problem (Lerche et al. (2005)).

- ***Statistics of the light***. The resolution is affected as well by the statistical fluctuations of the phototube signals, which depend upon the light output of the crystal and the conversion efficiency of the photocathodes. High light output scintillators are chosen to minimise the statistical fluctuations.

Sensitivity

Sensitivity in the PET environment refers to the fraction of radioactive decays that result in a detected event. Being the amount of injected dose rather limited for small animals (in order to not perturb their biological systems), high levels of sensitivity are needed to

achieve acceptable numbers of detected events and consequently acceptable signal to noise ratios in the reconstructions (Cherry and Chatziioannou (2004)). However, the sensitivity of most current animal PET scanners is in the range of $0.5 - 2.5\%$ at the center of the scanner (Chatziioannou (2002)), indicating that a large number of decays do not lead to recorded events. There are three major ways in which events are lost (Stickel and Cherry (2005)). First, one or both of the 511 keV photons may not intersect the detector system. This is remedied by designing PET systems with good solid angle coverage. Second, if a photon intersects a detector it may not interact with it. This requires that detectors have reasonable efficiency. Typical efficiencies are in the range of $20 - 70\%$, and depend on the detector material and thickness. Finally, events are not detected if they fall outside the energy windows set in order to reject secondary interactions of the particles with the scintillator. Tight energy windows (e.g $350-650$ keV) can reject a very significant fraction of events. It is therefore important to set energy thresholds that can capture all possible events.

The path towards much higher sensitivity animal PET systems, without increasing cost, is to design high efficiency ($> 60\%$) detectors with adequate depth of interaction determination to compensate for the resolution degradation, as will be discussed in next section. They can be brought closer to the animal to reduce the detector area required per unit solid angle coverage. Using this approach, along with optimized energy selection, should yield system sensitivities in the range of $10 - 20\%$ (Stickel and Cherry (2005)).

1.4 Reconstruction

It has been mentioned that the small animal PET studies require higher sensitivity and resolution capabilities than the clinical applications. It is clear that, in spite of its advantages, these performance issues (along with the scanner cost, access to PET tracers, and user

friendliness) will ultimately dictate the level and extent of PET's participation in the future of the biology (Cherry and Chatziioannou (2004)). Initially, the effort to address these challenges had been focused largely on instrumentation (some outlines on this topic have been provided in Section 1.3.3). But as animal PET scanner technology started to mature, it encountered certain limitations to overcome these problems. For example, the requirements of high resolution and sensitivity can be satisfied using detector modules composed of narrow and long crystals, placed in a gantry with the smallest possible diameter. However, long pixelated crystals lead to significant detection uncertainties due to the crystal penetration. The use of short pixelated crystals reduces this effect but at the same time leads to a reduced detection efficiency. On the other hand, the increase of the gantry diameter can reduce the DOI effect but at the same time leads to a reduction of sensitivity and a degradation of the spatial resolution due to the non-collinearity of the pairs (Ortuño et al. (2010)). Under these paradoxical circumstances, other areas apart from the instrumentation have started to be given their due attention. A particularly important area is the reconstruction step, in which the acquired data are converted to tomographic images. There is actually strong evidence that the use of appropriate reconstruction algorithms will be required to achieve submillimeter reconstructed images at acceptable signal-to-noise values in small animal PET studies (Cherry and Chatziioannou (2004)).

1.4.1 Analytical reconstruction

The early techniques of image reconstruction from PET data were analytical approaches based on the method of Filtered Back Projection (FBP) (Shepp and Logan (1974)). FBP is a mathematical technique based on an idealized model of PET that ignores many significant features of real data. Specifically, FBP assumes that the number of detected gamma-ray events traveling a particular direction approximates the line-integral of the radio-isotope

distribution along that line, from which the image can be reconstructed using analytical inversion formulas. In spite of its approximate nature, FBP has enjoyed widespread use and great longevity largely because of its computational simplicity. Unfortunately, FBP amplifies the signal noise when applied to the low-count data of nuclear molecular imaging (it is still a good method for applications where the number of measured counts is high, as computed tomography), and there is a growing interest in the development of reconstruction alternatives that overcome this problem (Kinahan and Rogers (1989), Ollinger and Fessler (1997), Lewitt and Matej (2003)). These techniques represent an important contribution to the results obtained traditionally with FBP, providing better resolution and noise characteristics.

1.4.2 Iterative reconstruction

Analytical methods typically neglect noise and complicating physical factors in an effort to obtain frameworks that yield explicit inversion formulas for the reconstruction problem. The introduction of iterative methods allowed for the explicit inclusion of realistic factors in the reconstruction process. These algorithms achieve better spatial resolution and improved signal-to-noise ratio than the analytical methods, while maintaining the quantitative nature of the data (Johnson et al. (1997), Chatziioannou et al. (2000)). The price of this added refinement is that the resulting set of equations describing the problem becomes very large and non-linear, and solving for the tracer distribution by direct inversion of the forward problem becomes intractable. In this case, the equations must be solved using iterative methods (Lee et al. (2004)).

All the iterative reconstruction methods share a number of common traits. The general model behind statistical reconstruction involves repeating the process of projecting an image estimate, comparing the estimated projections to the measured data to compute some

form of error, backprojecting the error and using the error to update the image estimate.

Two wide classes of iterative algorithm exists, namely algebraic and statistical. Classical algebraic iterative algorithms, such as ART and MART (Gordon et al. (1970)) are based on the Kaczmarz method of solving systems of linear equations (Kaczmarz (1937)). Although not widely used in nuclear medicine, they form an important basis for understanding the statistical algorithms that were developed later and for which iterative methods are mainly used.

Statistical algorithms have two basic parts: a statistical criterion (the basis for determining which image among the many possible is to be the solution) and a numerical algorithm (the method for finding the solution prescribed by the criterion). The most successfull early statistical algorithm, MLEM (Vardi et al. (1985)) uses a Poisson model of the produced data, related to the maximum likelihood statistical criterion, along with the EM algorithm as numerical method.

A serious disadvantage of MLEM is its slow convergence, which can lead to prohibitive reconstruction times on standard computer platforms (Lewitt and Matej (2003)). Several acceleration techniques have been proposed for the MLEM algorithm. Lewitt and Muehllehner (1986) improved convergence speed by incorporating an over-relaxation parameter. Tanaka (1987) used a frequency amplification method to accelerate the estimation of the higher-frequency components in the image. The ordered subsets expectation maximization (OSEM) method (Hudson and Larkin (1994)) divides the data into subsets, giving a factor speed increase proportional to the number of subsets chosen. Browne and DePierro (1996) proposed the row-action maximum-likelihood algorithm (RAMLA), which uses as many subsets as there are projections. However, these block methods don't necessarily converge, as reported empirically by Byrne (1997). The space-alternating generalized EM (SAGE) (Fessler and Hero (1994)) improves the convergence rate by updating each pixel individually and using a matrix-based projection model. Rebinning methods such as single

slice rebinning (SSRB) (Daube-Witherspoon and Muehllehner (1987)) or Fourier rebinning (FORE) (Defrise et al. (1997)) can reduce the dimensionality of 3D acquisitions by performing a set of 2D reconstructions to obtain volumetric data, although there is a loss of image quality with respect to the more time consuming fully 3D implementation.

In addition to the slow convergence issue, there is another important drawback related to the MLEM derived methods: at high iteration numbers, images exhibit high-variance behavior (Leahy and Qi (2000)). This is usually attributed to either the fact that there is no stopping rule in this kind of iterative reconstruction or to the statistical (noisy) nature of the detection process and reconstruction method (Herraiz et al. (2006)). The usual approach to overcome this drawback is either to use stopping rules (Veklerov and Llacer (1987), Johnson (1994), Coakley (1991)) or to smooth the images with kernels (Snyder et al. (1987), Liow and Strother (1991)) filters (Slijpen and Beekman (1999)) or wavelet based methods (Mair et al. (1996)).

The Maximum a Posteriori (MAP) methods (Green (1990)) offer a more flexible and principled method of encouraging desirable properties in the reconstructed imagen by incorporating *a priori* information (priors) that models the distribution of activity and noise in the acquired data. The regularizing influence of the prior, controls the variance of the reconstruction, and hence the MAP methods do not exhibit the instabilities at higher iterations encountered using MLEM and OSEM (Qi et al. (1998))

There exist also statistical algorithms based on a Gaussian model of the produced data, related to the weighted least squares (WLS) criteria, which result in quadratic objective functions. These can efficiently use many established numerical algorithms, such as coordinate gradient (Tsui et al. (1991), Kaufman (1993)) or coordinate descent (Fessler (1994)), and result in faster reconstruction algorithms.

The algorithms mentioned above use binned data (projection sets) to reconstruct the image. Concerning the List-mode format, it is not amenable to analytic reconstruction

methods such as FBP without first histogramming the data into a standard sinogram or projection data format, which can be an inefficient procedure. However, there exist several versions of the MLEM and OSEM algorithms (Reader et al. (1998), Reader et al. (2002b), Rahmim et al. (2004)) for the list-mode data.

The MLEM algorithm

As mentioned in the previous section, the MLEM algorithm is a golden standard of the statistical reconstruction. Since its publication in 1985, most of the work in this field has been based on finding alternatives to the MLEM that offer faster convergence, improved resolution, contrast and/or signal-to-noise ratio. The MLEM reconstruction algorithm (Vardi et al. (1985)) is indeed a golden standard in the statistical reconstruction field. It seems worth to analyze in detail the work by Vardi et al. (1985) in order to have a clear idea about where the advantages of statistical reconstruction stem from.

The mathematical development of Vardi et al. (1985) starts from the well known statement that positron emissions from a large number of radioactive nuclei occur according to a Poisson distribution. The reconstruction problem consists of finding out the unknown intensity function $\lambda(\mathbf{r}) : \mathbf{r} \in \mathbb{R}^3$ of the emission spatial Poisson point process in a certain region H (the patient's body) of $\mathbb{R}^3$.

The measured data set $n^*(d)$, from which the Poisson intensity function must be estimated, are the total number of coincidences in each tube d formed by a pair of detectors. Since classifying the annihilations according to the discrete detectors pair that detected them amounts to a thinning of the Poisson point process, it can be shown that the data $n^*(d)$ (with $d = 1..D$, D being the the maximum number of detector bins), constitute a collection of independent Poisson random variables with mean:

$$\lambda^*(d) = \int_{\mathbb{R}^3} \lambda(\mathbf{r}) c(\mathbf{r}, d) \mathbf{dr} \quad d = 1, ..., D \tag{1.1}$$

where $c(\mathbf{r}, d)$ is the probability that a line originated at the spatial point $\mathbf{r}$ is detected at the discrete tube d.

The manipulation of images in digital form is an essential part of virtually all scientific disciplines. In applications in which the physical magnitude is not inherently discrete (as is the density function that PET reconstruction algorithms try to estimate), a digital image is used to represent the continuous image that, in turn, represents the physical magnitude. When implementing the reconstruction algorithm described in Vardi et al. (1985), it was assumed that the radiotracer volume can be approximated by a fine grid of B basis functions. If $v(\mathbf{r} - \mathbf{r}_b)$ stands for the general mathematical expression of the basis function centered at point $\mathbf{r}_b$, then:

$$\lambda(\mathbf{r}) \approx \sum_{b=1}^{B} \lambda(b) v(\mathbf{r} - \mathbf{r}_b) \tag{1.2}$$

where the weight $\lambda(b)$ will be the image value at the b-th basis function, which is proportional to the total number of positron-emitting nuclei contained in the volume spanned by the basis function. Substituting (1.2) into (1.1), the following expression is obtained for the mean of the measured data in each tube d:

$$\lambda^*(d) \approx \sum_{b=1}^{B} \lambda(b) p(b, d) \tag{1.3}$$

where

$$p(b, d) = \int_{\mathbb{R}^3} v(\mathbf{r} - \mathbf{r}_b) c(\mathbf{r}, d) d\mathbf{r} \tag{1.4}$$

is the probability that an event generated in the region defined by the b-th function is detected in the tube d. Coefficients $p(b,d)$ can be arranged in a matrix called the system response matrix or simply, the system matrix.

At this point, the activity distribution $\lambda(\mathbf{r})$ that maximizes the probability of obtaining the measured data $n^*(d)$ must be found. Since the collected data follow a Poisson model, this corresponds to the maximization of the probability function:

$$P(n^*) = \prod_{d=1}^{D} e^{-\lambda^*(d)} \frac{\lambda^*(d)^{n^*(d)}}{n^*(d)!} \tag{1.5}$$

The expression in (1.5) can be rewritten in terms of the set of basis functions by means of substituting $\lambda^*(d)$ by the expression given by (1.3). As the resulting expression is concave, hence it follows that sufficient conditions for λ to be a maximizer of the likelihood are the Karush-Kuhn-Tucker (KKT) conditions (Karush (1939)), which can be satisfied with many iterative schemes. Particularly appealing is the one given by the expectation maximization algorithm. The final expression given in Vardi et al. (1985) is an instance of this algorithm and constitutes the basis for much of the work in statistically based algorithms in medical image reconstruction over the last years:

$$\lambda^{new}(b) = \frac{\lambda^{old}(b)}{p(b,.)} \sum_{d=1}^{D} \frac{n^*(d)p(b,d)}{\sum_{b=1}^{B} \lambda^{old}(b)\, p(b,d)} \tag{1.6}$$

where

$$0 < p(b,.) = \sum_{d=1}^{D} p(b,d) \tag{1.7}$$

The term $p(b,.)$ is a normalization factor representing the probability of detecting (considering all possible detectors) a pair of photons arbitrarily emitted from within function b.

It is usually referred to as sensitivity matrix.

Nowadays, there is a growing trend to store PET measurements in the so-called list-mode data. This mode has the advantage of a higher accuracy since the detections need not be discretized into projections or sinograms. Reader et al. (1998) developed an expression equivalent to Eq (1.6) for the case of data sorted in list-mode:

$$\lambda^{new}(b) = \frac{\lambda^{old}(b)}{p(b,.)} \sum_{n=1}^{N} \frac{p(b,d)}{\sum_{b=1}^{B} \lambda^{old}(b)\, p(b,d)} \tag{1.8}$$

N is the total number of measured events. As can be observed, each line is treated individually instead of being grouped into tubes of response, and thus the measurement term $n^*(d)$ is now equal to one in the numerator of the summation. This adaptation requires also to change slightly the meaning of the terms of the system matrix $p(b,d)$, which now stand for the probability that an emission from the basis function b is detected along the LOR d defined by the n-th event. The list-mode reconstruction equation is especially suited for PET systems that make use of continuous detectors, since in these systems events are not binned into discrete detectors. In this case, the list-mode version of the algorithm can be used in order to avoid rebinning and preserve all the information obtained during the acquisition.

Chapter 2

Use of Integral Schemes for the System Matrix Calculation

2.1 Introduction

As stated in Chapter 1, there is strong evidence that statistical algorithms achieve better image quality than the analytical approximations. Two key features distinguish statistical algorithms from conventional analytical reconstruction techniques. First, their ability to optimize the performance in low-count situations by modeling the statistical variability inherent in photon limited coincidence detection. Second, their ability to maximize the resolution recovery by accurately modeling the geometry and the physics of the scanner (Qi et al. (1998)). In Chapter 1 it has been pointed out that the MLEM approach (Vardi et al. (1985)) constitutes a reference in the field of statistical reconstruction. This algorithm assumes that the emissions follow Poisson statistics and incorporates the data acquisition model through the so-called system matrix. The terms $p(b, d)$ that form the system matrix describe the relationship between sources and data. Specifically, each $p(b, d)$ stands for the

probability that an event generated in the region defined by a basis function b is detected in a LOR d. The operations in which the knowledge of the system matrix is required during the reconstruction are known as the forward and backward projection operations. The forward projection is the operation that predicts the data which would result from a source activity estimation λ^{old} (given by the mathematical relationship $\sum_{b=1}^{B} \lambda^{old}(b)\, p(b,d)$ in Eq (1.6)). The backprojection projects data onto a source volume distribution and is used to update the source estimation from the comparison between the predicted and the real data. In Eq (1.6), the backward projection is given by the updating of the volume elements $\lambda^{old}(b)$ in each iteration.

2.2 State of the art

It is well known that the quality of the images obtained through statistical reconstruction depends strongly on how faithfully the theoretical model incorporated through the system matrix depicts the real PET process (Tohme and Qi (2009)). The computation of the system matrix should take into account the geometry of the scanner, the positron physics (non-collinearity and positron range), the attenuation and scatter in the source volume, and the detector response associated effects, both in terms of sensitivity and resolution (crystal penetration, detector scatter, light detection/collection, electronics and readout design,...).

The price of the enhancements achieved by the accurate statistical schemes is that the reconstructions require substantially greater computation time and/or storage requirements than the analytical reconstructions. Iterative algorithms perform repeatedly the forward and backward projection. These operations are the most time consuming parts of the iterative reconstruction programs and require the knowledge of the whole system matrix (Herraiz et al. (2006)), whose size is large in high resolution 3D PET systems (Ortuño et al. (2010)). Reaching a good compromise between image quality and efficiency is thus a key challenge

in statistical reconstruction. This is the reason that an important effort has been devoted to find alternative implementations of the system matrix that provide high quality reconstructions at feasible reconstruction time and storage conditions. It should be also noted that this thesis is primarily aimed at contributing in this direction.

2.2.1 Basic methodologies

In descending order of accuracy, the approaches to the computation of the system matrix can be classified in three main categories:

1. **Empirical methodologies**: The most accurate description of the PET process would be obtained through direct measurement of the system matrix from the scanner for which data are going to be reconstructed. The system matrix could be obtained by scanning a source at every basis function position, and recording the response. Unfortunately, the large number of scans required makes this approach presently unpractical. (Panin et al. (2006b) makes a temporal estimation of 2.6 years to complete the system matrix acquisition of the clinical Hi-Rez scanner (Bercier et al. (2004)) assuming scanner azimuthal symmetries). Moreover, the experimental setup can be challenging due to the need to precisely locate the point source (Alessio et al. (2006))

2. **Monte Carlo methodologies**: Monte Carlo (MC) simulators offer the possibility of modeling the physics of a PET scanner very precisely. An alternative to the direct measurement of the system matrix is thus the MC simulation of the above mentioned source scanning process. The feasibility of this approach has been shown in Veklerov et al. (1988), Boning et al. (2001), Rafecas et al. (2004), Vandenberghe et al. (2006) or Ortuño et al. (2010). Nevertheless, the simulated acquisition of the system matrix encounters some difficulties:

- Although current Monte Carlo simulators provide very accurate modeling of the data scanning, there are still effects in the photon detection process that are difficult or impossible to model in a simulation (Tohme and Qi (2009)) an hence a Monte Carlo approach will be always less precise than an empirical approach.

- Monte Carlo simulators are fairly slow and, as stated in Moehrs et al. (2008), a substantial number of simulations are required to reduce the statistical noise of the estimated matrix elements. Several investigators have dealt with the compromise between time and statistical accuracy in the MC computation of the system matrix: Rafecas et al. (2002) studies the effect of the number of simulated events in the noise propagation from the matrix into the image and considers the role of system symmetries to improve the statistical quality of the matrix. Giménez et al. (2005) determines which simplifications can be done to accelerate the MC simulation without jeopardizing the accuracy of the system model. In despite of these proposals, the Monte Carlo based computation of the system matrix might be impractical if the number of LORs is too big or not enough computational power is available (Moehrs et al. (2008)).

- The computational time demand that imposes the statistical accuracy to the simulation of the system matrix often forces MC approaches to precompute the system matrix and store it to be used during reconstruction. The fact that the size of the system matrix for high-resolution 3D PET scanners is in the order of several billions of elements (Ortuño et al. (2010)) makes the precomputation of the whole system matrix a challenging task in terms of storage requirements. Certain implementations exploit the sparsity (Ortuño et al. (2010)) and the symmetries (Johnson et al. (1994), Rafecas et al. (2004)) of the system matrix in

order to save space. But in addition to the pure storage problem, the precomputation once and for all of the system matrix entails other complications:

- It limits the flexibility of the algorithm implementation to a fixed setup of the scanner and to a fixed type and size of the basis function used to approximate the continuous tracer distribution.
- Even if the size of the system matrix can be reduced enough to keep it in memory, the access to disk for every forward and backward projection operation can considerably slow down the reconstruction (Herraiz et al. (2006)).
- The sorting of the simulated data into the matrix is a computation-expensive procedure hindered by the huge size of the matrix. Rafecas et al. (2004) employs a database management system to overcome this problem.
- In the case of continuous scintillators, the positions d assigned to the detected photons do not correspond to a discrete group of crystal center pairs, but to continuous locations within the blocks. The resulting $p(b, d)$ terms are thus continuous functions of d. An artificial discretization of the detection locations has thus to be done in order to precompute and store the continuous $p(b, d)$ terms. The data under reconstruction would have to be rebinned to fit to the discretized system matrix terms. Since the main advantage of the continuous scintillators technology is indeed the precision with which the photons are positioned within the block, the rebinning of the acquired data involves a clear waste of resources.

3. **Analytical methodologies**: Finally, there exist analytical implementations of the system matrix. Unlike the Monte Carlo approaches, the analytical approaches are noise-free and usually very fast (Strul et al. (2003)). This allows the computation

of the elements of the system matrix on the fly at reconstruction time, thus avoiding the storage problems above mentioned. However, on its quest to speed up the reconstruction process, these methods typically overlook important physical effects of the PET acquisition process and use simple geometric system models based on the intersection of the lines (Siddon (1985)) or the tubes of response (Ollinger and Goggin (1996), Scheins et al. (2006), Schretter (2006)) with the basis functions, other improved ray-tracers (Aguiar et al. (2010)) or the solid angles subtended at the detectors by each basis function (Chen et al. (1991), Terstegge et al. (1996), Johnson et al. (1997), de la Prieta et al. (2006)).

2.2.2 Hybrid approaches

Johnson et al. (1994) and Selivanov et al. (2000) show how the enhancement of a simple analytical geometrical model with a spatially variant detector response may improve the quality of the results without significantly jeopardizing the efficiency of the system matrix computation. These works can be thought as the basis for a great amount of hybrid approaches that combine the analytical methods with empirical and MC results in order to obtain high precision models at affordable storage and/or time requirements.

Analytical-empirical approaches

Certain approaches combine analytical calculations with empirical measurements. Panin et al. (2006a) and Panin et al. (2006b) construct the forward projector for the Hi-Rez scanner (Bercier et al. (2004)) using parameterized responses estimated from point sources data measured at different positions in a portion in the field of view. In Frese et al. (2003) the parameterized responses are determined for the IndyPET scanner by processing scans of

line source phantoms positioned near the center of the field of view. While both methods result in significant improvements in image quality, their main weakness is their lack of flexibility, since they are aimed to specific devices. Based on the *a priori* geometrical knowledge of the scanners for which the system model is going to be computed, several assumptions and simplifications in the model are done that allow to reduce the number of empirical measurements needed to compute the analytical responses. Even after these simplifications, the methods require extensive and very accurate empirical measurements using a positioning robot.

Analytical-MC approaches

The combination of MC and analytical strategies results on less complex calculations of the system matrix that allow for a higher flexibility on its estimation. Kudrolli et al. (2002) implements the forward and backprojection operations using stochastic sampling techniques based on Monte Carlo tools. In this work the forward and backward projections are calculated on the fly relying on parallel processors to give fast reconstructions. The approach thus eliminates the need to explicitely calculate the system matrix while keeping the accuracy provided by the Monte Carlo methods. The accuracy and the speed of the work by Kudrolli et al. (2002) is proved, but just on ideal data, that ignores the effects of attenuation, scatter and response systematic errors. Herraiz et al. (2006) uses a MC simulator to precompute the elements of the system matrix considering sparseness along with all possible axial and in-plane symmetries as well as certain quasi-symmetries. The elements of the system matrix are stored as cubic spline profiles and matched to the voxel size during reconstruction. In this way, the advantages of on-the-fly calculation (matching the profiles to voxel size) and of fully stored system matrix are combined. While it is shown to be an accurate and efficient implementation of the system matrix, the precomputation of the source dependent effects (attenuation, scatter and positron range) relies on assumptions about the

properties of the imaged object.

Separated-effects approaches

Both the analytical-empirical and the analytical-MC approaches to the computation of the system matrix have still certain associated limitations. On the one hand, the analytical-empirical approaches (Panin et al. (2006a), Panin et al. (2006b), Frese et al. (2003)) lead to too *ad-hoc* system matrix implementations in order to reduce and simplify the measurements. On the other hand, the analytical-MC methods (Kudrolli et al. (2002), Herraiz et al. (2006)) may rely on assumptions about the data formation model, due to the limitations of the MC techniques and to the need of precomputation. This suggests that an optimal hybrid approach should make use of the three methodologies (empirical, MC and analytical) available for the system matrix computation. Such combination of strategies is achieved by the noteworthy family of hybrid approaches that model each effect that occurs in the data stream of a PET scanner separately (in the following, referred to as the "separated-effects" approaches). A great variety of works (Qi et al. (1998), Mumcuoglu et al. (1996), Reader et al. (2002a), Rahmim et al. (2003), Strul et al. (2003), Lee et al. (2004), Staelens et al. (2004), Alessio et al. (2005), Alessio et al. (2006), Bao et al. (2008), Sureau et al. (2008), Rahmim et al. (2008), Moehrs et al. (2008), Iriarte et al. (2009), Tohme and Qi (2009)) have proved the benefits of this approach, which rely on explicitely considering the diversity of the effects occurring during the PET acquisition process, for which an homogeneous treatment may result in non optimal calculations. By modeling each effect using the methodology that better fits to its requirements, these approaches achieve a synergy between the three basic methodologies. It is not worth to perform complex and costly empirical or Monte Carlo experiments to model the response of effects for which accepted analytical fast noise-free models are available. This is clearly the case of the geometrical factors, but also of other physical effects, such as the photon non-collinearity deviation

angle, which is known to have a Gaussian distribution (DeBenedetti et al. (1950)). In the cases where the analytical approach becomes either too complex to allow on-the-fly computation or too general to accurately reflect certain specific features, an experimental estimation can be used instead. This can be the case of effects such as the photon interaction physics within the scintillator. While in these cases an empirical model should provide more accurate results, the complexity of the measurement process can lead to the preference for a Monte Carlo estimation. In any case, since the model used to describe each effect may change from one reconstruction to another without altering the rest of models, the separated-effects approaches enjoy a great flexibility in terms of scanner setups (geometry, material...), experimental conditions (isotope, subject under study) or reconstruction features (type and size of the basis function).

Independently of the methodology used to model each part of the process, a different problem arises when the separately modeled effects have to be combined to form the whole system matrix. Different approaches exist to address this issue:

- **Factored approaches**: The most popular way of combination is to express the system matrix as a product of independent matrices, each one standing for one or a collection of effects. This approach achieves substantial savings both in storage (since each matrix component is highly structured and sparse) and computational requirements (since the forward and backward projection can be performed efficiently with the stored matrix). Although several approaches exist (Reader et al. (2002a), Rahmim et al. (2003), Sureau et al. (2008)), the scheme proposed by Mumcuoglu et al. (1996) for the two-dimensional case and extended by Qi et al. (1998) to the three-dimensional case is considered a golden standard that has given place to many successful system matrix implementations (Lee et al. (2004), Alessio et al. (2005), Alessio et al. (2006), Bao et al. (2008), Tohme and Qi (2009)) for PET iterative

reconstruction. The successful implementations of the system matrix based on the factored approach have shown to be efficient and to achieve good quality results. Probably this is the reason that the accuracy of the approach has never been much questioned, even if it completely ignores the interdependence between the different effects. Certain authors (Kudrolli et al. (2002), Herraiz et al. (2006), Ortuño et al. (2010)) have pointed out whether expressing the system matrix as a product of independent factors is a reliable approach, but the shortcomings of the factored schemes have never been further specified. Moreover, the effect that these limitations may have in the quality of the reconstructions has never been observed, since there is not an alternative that is able to compete with the factorization for the combination of effects.

- **Integral approaches**: Several schemes have been proposed (Strul et al. (2003), Staelens et al. (2004), Moehrs et al. (2008), Iriarte et al. (2009)) that model the effects separately through probability density functions and combine them by means of integration. These approaches have shown a good agreement with fully Monte Carlo based calculations using less computation. However, in these schemes the system matrix loses the sparsity of their factored counterparts, which makes its storage an impractical task. Furthermore, the resulting integral expressions are too complex to be analytically solved, which makes the on-the-fly calculation a computational challenge. For this reason, these schemes are forced either to ignore effects that are present in the factored models (Strul et al. (2003), Staelens et al. (2004), Iriarte et al. (2009)) or to consider these effects by means of corrections (Moehrs et al. (2008)). Furthermore, even after these simplifications, the incorporation of these response models in a reconstruction algorithm without assuming important simplifications beyond the unavoidable numerical integration (Moehrs et al. (2008)) has still to be

checked. Under these circumstances a suitable comparison between the integral and factored schemes is not possible. Consequently, although due to their higher degree of accuracy, the integral schemes can be expected to achieve better reconstructions than the efficient factorization, it has not been yet been proved to what extent this statement is true.

2.3 Objectives of the Chapter

The review of the literature on the system matrix computation suggests that the approaches that model separately the different parts of the PET data acquisition process have a great number of advantages, since they are able to simultaneously profit the benefits of the analytical, Monte Carlo and empirical methodologies.

While the benefits of the separation of the effects seem to be clear, the importance of the scheme used for their combination is a subject that has not yet been explored. As stated in the previous section, there are technically two possibilities for the combination of the effects: the factored and the integral schemes. In principle, the integral schemes are more accurate but the great computational challenge they pose has traditionally made them infeasible. As a result, factorization has become the only choice. As well as being the only option, the efficient factored schemes have led to high quality efficient reconstructions, and consequently, their limitations have never been much questioned.

Nowadays, several technological advances are making possible the use of increasingly complex system models at feasible reconstruction times. In Herraiz et al. (2006) the reconstruction algorithm runs on several CPUs using the message passing interface (MPI) protocol, whereas Herraiz et al. (2011) and Pratx and Levin (2011) perform graphics processing unit (GPU)-based implementation of the reconstruction iterative algorithms. In terms of reconstruction time, these advances allow for the implementation of the so-far

impractical integral schemes and for their comparison with the traditionally unquestioned factored approaches. Based on these statements, the objectives of this chaper are:

1. In Section 2.4, a new scheme for the system matrix computation is introduced. The new scheme benefits of the advantages of separating the effects, since each step of the PET acquisition process is able to be modeled with a different methodology, but uses a scheme of integration for the combination of the effects, in which their interdependence is explicitly considered. Since the same effects as in the most complete factored schemes are considered in its development, the new scheme can be considered as the first fair reference with which to compare the factorization.

2. A qualitative analysis of the schemes of combination of the separately modeled effects is performed along Section 2.5. Specifically, it will be shown in Subsection 2.5.1 how the factored scheme can be deduced from the integral scheme introduced in Section 2.4, after certain assumptions about the data formation process have been done. Moreover, in 2.5.1, other common assumptions done by the factored schemes in order to reduce their computational requirements will be pointed out. Next, in Subsection 2.5.2, the importance of each of these assumptions is analyzed, based on well-known properties of the effects each of them concerns. In this way, the simplifications in which the widespread factored scheme is based in, are, by first time, specified and analyzed.

3. The new integral scheme introduced in Section 2.4 plays a key role in the theoretical analysis of the schemes of combination of effects performed in Section 2.5. However, as it has been mentioned, its implementation is expected to be a great challenge, since it is based on a complex multidimensional integral. Moreover, although several techniques have been mentioned that can accelerate substantially the reconstructions (MPI, GPUs implementation), the increasing complexity of scanners implies a large

number of data and reconstructed basis functions, as well as more sophisticated acquisition protocols, such as dynamic studies, which always require the reconstruction approaches to be as efficient as possible (Herraiz et al. (2011)).

On the other hand, although several important weakpoints have been found in the factored schemes of combination, other parts of the factorization have been found to have a good agreement with the real acquisition process. Based on these statements, a new mixed scheme for the combination of the separately modeled effects is introduced in Section 2.6. The new scheme keeps the factorization of effects in those cases in which the assumptions involved have been found to be acceptable. In those cases in which the factorization has proved to be inaccurate, the combination of effects has been done by means of integration. In this way, the benefits of the (efficient and simple) factored schemes and the (accurate but impractical) integral schemes have been joined, in a justified and explicit way for the first time.

4. The new mixed scheme introduced in Section 2.6 is aimed to obtain higher quality results by maximizing the accuracy of the response model while simplifying its implementation and minimizing the computational resources employed. The achievement of these objectives is well backed up from a theoretical point of view, since the new scheme is the result of a thorough analysis performed along Sections 2.4, 2.5 and 2.6. In order to complete the study, it has been checked to what extent the objectives are accomplished in the reconstruction domain. With this purpose, the mixed scheme has been implemented and incorporated to a reconstruction algorithm in Section 2.7 and then has been evaluated in terms of quality and efficiency in Section 2.8.

2.4 An integral scheme

The system matrix terms, which have been referred to as $p(b, d)$, stand for the probability that a positron emission from the basis function b is detected at certain scanner position d. In this section a new scheme for the computation of these terms is introduced. With this purpose, a thorough tracking of the events that take place since a positron is emitted from b until a gamma pair is registered and positioned by the detection system will be performed in the following subsections. Each of these subsections deals with the description of a step in this process, which can embrace one or several of the effects ocurring during the PET acquisition data. Widespread noise-free analytical models are used to represent those effects for which such models exist. Otherwise, a brief review of the literature of existing models is done. In any case, the methodology is open for the modification, improvement or neglection of the models behind each effect, without altering the rest of the system matrix.

As it can be checked, the steps in which the acquisition process has been divided have been chosen to match the matrices in which the most popular factored schemes decouple the system matrix. These factors stand for the positron range, geometry, attenuation in the object, detection efficiency and detection positioning. The inclusion of all these effects in the new methodology ensures its loyalty to the PET acquisition process in the small animal field, based on the high quality results achieved by the factored approaches.

However, the combination of the different parts of the process to form the whole system matrix is not done following the widespread scheme of factorization. As it can be checked, each of the subsection builds on the previous one, taking into account the interdependence between the successive effects with a scheme of integrals and probability density functions. Consequently, an expected added value provided by the thoroughness of the new scheme of combination with respect to the factorization is expected to be provided.

The development is valid for both the static ring and to the rotating geometry although

for simplicity just the two detection blocks involved in the determination of d will be considered (as shown in Figure 2.1). Moreover, the two detectors shown in the following figures have been chosen to be parallel, but the results apply to any relative position of the blocks.

2.4.1 Basis function approximation

The aim of this section is to develop a mathematical representation of the physical data acquisition process beginning at a positron emission within a basis function b. Since the data acquisition process strictly starts with an emission from a certain point $\mathbf{r_0}$ of the continuous radiotracer, it would be more faithfully represented with continuous $p(\mathbf{r_0}, d)$ terms (with analogous definitions than the $p(b, d)$ terms). However, the need to manipulate data in a digital form imposes the construction of the continuous radiotracer as a sum of basis functions b that leads to a model based on discrete $p(b, d)$ terms. The relationship between $p(\mathbf{r_0}, d)$ and $p(b, d)$ can be easily computed if the basis function centered at position $\mathbf{r}_b$ is interpreted as the probability density function of the emitting points within a certain region of space $v(\mathbf{r}_0)$ (for this it is needed that the basis function is non negative and that it integrates to 1):

$$p(b, d) = \int_{\mathbf{r}_0 \in b} p(\mathbf{r}_0, d) v_b(\mathbf{r}_0) d\mathbf{r_0} \tag{2.1}$$

From this point the present section will focus on the computation of the continuous $p(\mathbf{r}_0, d)$ terms, through which the characterization of the data acquisition process will be done. Once these terms have been obtained, Eq (2.1) can be used to generalize the result to any type and size of basis function used to approximate the continuous radiotracer.

2.4.2 Positron range

In the computation of the probability that an emission from a point $\mathbf{r}_0$ gives place to a coincidence at d, it must first be observed that, since a positron travels certain distance before annihilating, the gamma pair can be emitted from a position $\mathbf{r}$ different from the emission point $\mathbf{r_0}$, as shown in Figure 2.1.

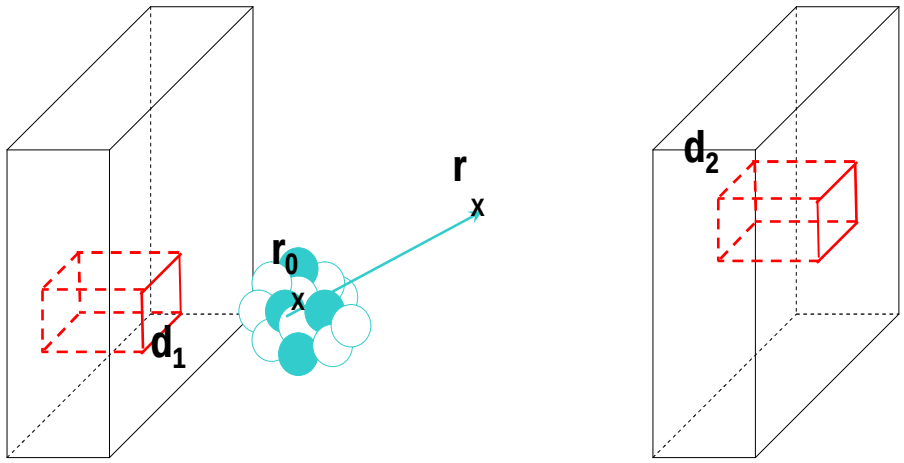

Figure 2.1: Positron range. A positron emitted from $\mathbf{r_0}$ may travel certain distance before annihilating at $\mathbf{r}$

The inclusion of the positron range effect in the computation of $p(\mathbf{r_0}, d)$ is given by the following expression:

$$p(\mathbf{r_0}, d) = \int_{\mathbf{r}} p(\mathbf{r}, d) f_{\mathbf{r_0}}(\mathbf{r}) d\mathbf{r} \tag{2.2}$$

$f_{\mathbf{r_0}}(\mathbf{r})$ represents the 3-D probability density function of the annihilation point for a positron emission occurred at $\mathbf{r_0}$. Since the positron range is an object and radioisotope dependent effect this distribution should be re-estimated for each experiment. Different approaches can be found in the literature to estimate the positron range via experimental measurements (Cho et al. (1975), Phelps et al. (1975)) MC simulations (Levin and Hoffman (1999), Champion and Loirec (2007), Alessio and MacDonald (2008)) and analytical expressions (Palmer and Brownell (1992)) and it has to be remarked that a considerable variation has been found among all of them (Cal-González et al. (2009)). The reason for this uncertainty is that the tortuous path that positron follows in tissue is probably the most poorly understood of the resolution degradation factors in PET.

$p(\mathbf{r}, d)$ stands for the probability that a positron-electron annihilation occurred at a generic location $\mathbf{r}$ gives place to a coincidence detected at position d. From this point the development will be focused on the computation of $p(\mathbf{r}, d)$.

2.4.3 Geometry

The pair of photons following an annihilation from $\mathbf{r}$ are emitted at 180 degrees (the non-collinearity effect will be considered later) relative to one another. If the line along which each gamma pair propagates is defined by two angles, azimuthal γ and polar φ (see Figure 2.2), the probability that a pair emission from $\mathbf{r}$ is detected at d can be expressed as:

$$p(\mathbf{r}, d) = \int_{\gamma} \left[\int_{\varphi} p(\mathbf{r}, \gamma, \varphi, d) f(\varphi, \gamma) d\varphi \right] d\gamma \tag{2.3}$$

where $f(\varphi, \gamma)$ is the likelihood that a gamma pair with orientation defined by φ and γ is emitted. Since it is known that the spatial orientation of the emitted pairs is random, this likelihood can be set to $f(\varphi, \gamma) = cos\varphi/2\pi$, which corresponds to an uniform distribution of the emissions in the space. In principle, the angular integration limits of Eq. (2.3) should be such that all the possible gamma pairs emitted from $\mathbf{r}$ are included in the integral. In practice, these limits can be restricted to account just for those emitted pairs that are likely to give place to a detection at d. The integration range should therefore exclude those pair emissions in which one or both of the gamma photons do not intersect the scanner and those pair emissions that, although intersecting the scanner, are not likely to give rise to a coincidence at d. The former restriction will be imposed by the scanner geometry and the later by the effects that will be modeled in the following sections through $p(\mathbf{r}, \gamma, \varphi, d)$, which will reduce the range of pairs detectable at d to those intercepting the detectors in a neighborhood of d. Appendix A shows how to compute the integration range for φ and γ that limits the emissions to such neighborhood.

2.4.4 Non-collinearity

The $p(\mathbf{r}, \gamma, \varphi, d)$ term stands for the probability that the gamma pair originated in $\mathbf{r}$ and with spatial orientation defined by φ and γ is positioned at d by the detection system. The following subsections deal with the computation of this term. The first phenomena that will be included in its computation is the photon non-collinearity. So far, it has been assumed that the two gamma photons emitted from $\mathbf{r}$ are antiparallel, and share, therefore, their spatial orientation, defined by the angles γ and φ. However, the variation in momentum of the positron results in an angular deviation from the antiparallel orientation. The inclusion of this effect in the computation of $p(\mathbf{r}, \gamma, \varphi, d)$ is as follows:

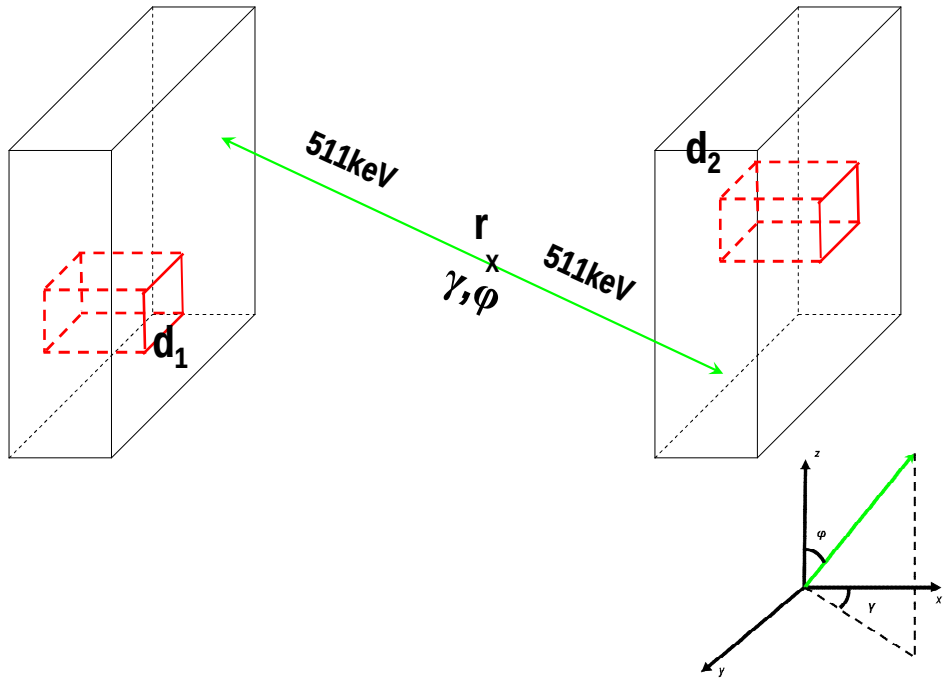

Figure 2.2: Geometry. The gamma pair spatial orientation is defined by the angles φ and γ in the coordinate system shown in the right bottom corner of the figure

$$p(\mathbf{r},\gamma,\varphi,d) = \int_{\theta_1} f(\theta_1)\left[\int_{\theta_2} p_{acc}(\mathbf{r},\gamma,\varphi,\theta_1,\theta_2,d)f(\theta_2)d\theta_2\right]d\theta_1 \tag{2.4}$$

where θ_1 is the deviation from the theoretical 180 degrees orientation given by the original (φ,γ) and θ_2 defines, among all the planes containing the original collinear pair, in which of them the deviation occurs (Figure 2.3 shows the case in which this plane is parallel to the z axis). $f(\theta_1)$ is the probability density of θ_1, which is well established as a

Gaussian-distributed variation from the 180 degrees with $\sigma = 25$ milliradians (DeBenedetti et al. (1950)). On the other hand, θ_2 can be assumed to be uniformly distributed between 0 and π radians, and therefore $f(\theta_2) = 1/\pi$. Appendix B shows how to compute the spatial orientation of the gamma photons from φ, γ, θ_1 and θ_2.

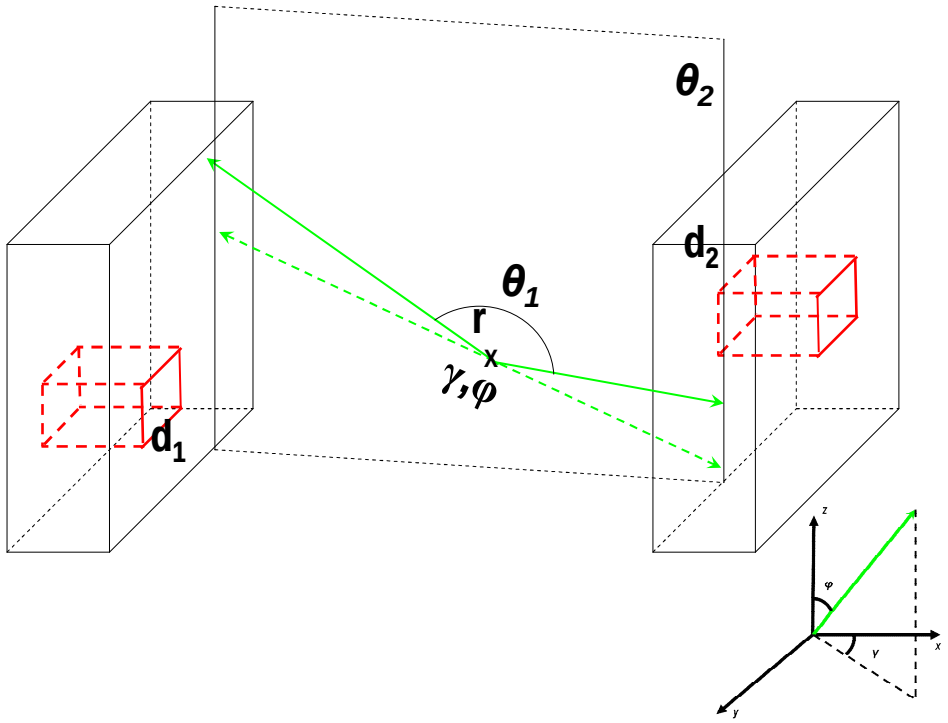

Figure 2.3: Non-collinearity. The deviation from the collinear situation is defined by the angles θ_1 (degree of non-collinearity) and θ_2 (plane where the non-collinearity takes place).

$p_{acc}(\mathbf{r}, \gamma, \varphi, \theta_1, \theta_2, d)$ is the probability that the gamma pair with orientation defined by $\varphi, \gamma, \theta_1$ and θ_2, gives place to a detection at d. The following sections study the computation of this term in depth.

2.4.5 Attenuation

The photons emitted by the radiopharmaceutical may interact with tissue and other materials as they pass through the subject to be imaged. The loss of detection of true coincidence events that are completely absorbed is referred to as attenuation. In order to account for this effect, $p_{acc}(\mathbf{r}, \gamma, \varphi, \theta_1, \theta_2, d)$ can be expressed as:

$$p_{acc}(\mathbf{r}, \gamma, \varphi, \theta_1, \theta_2, d) = p_{det}(\mathbf{r}, \gamma, \varphi, \theta_1, \theta_2, d) p_{att}(\mathbf{r}, \gamma, \varphi, \theta_1, \theta_2) \tag{2.5}$$

where $p_{att}(\mathbf{r}, \gamma, \varphi, \theta_1, \theta_2)$ is the probability that a gamma pair emitted from $\mathbf{r}$ and propagating along the direction defined by φ, γ and the deviation given by θ_1 and θ_2 is not absorbed by the object and reaches the detectors. This probability can be expressed as the product of the individual survival probabilities of each of the photons, which are known to follow an exponential distribution (Ollinger and Fessler (1997)):

$$p_{att}(\mathbf{r}, \gamma, \varphi, \theta_1, \theta_2) = e^{\int_0^{L_{att_1}} \mu(l) dl} e^{\int_0^{L_{att_2}} \mu(l) dl} \tag{2.6}$$

L_{att_1} $i = 1, 2$ are the distances traveled by the annihilation photons within the attenuating medium (before reaching the scintillator) in the direction given by γ, φ, θ_1 and θ_2 and the integration variables l cover these distances. The attenuation coefficient $\mu(l)$ is a function of the attenuating medium's physical properties (atomic number and density) and the energy of the photon. In most instances, a discretized version of the terms $p_{att}(\mathbf{r}, \gamma, \varphi, \theta_1, \theta_2)$ is experimentally estimated and stored. A source surrounding the patient is used with this purpose. Then, the probability of survival for each LOR of the scanner is computed as the ratio of the number of photons pairs detected with the patient present (the transmission scan) to the number detected in the absence of the patient or attenuation medium (blank scan) (Lewellen and Karp (2004)). Alternatively, the transmission scan

can be used to reconstruct an image of the linear attenuation values via statistical methods (Lange et al. (1987), Fessler et al. (1997), Mumcuoglu et al. (1994))

$p_{det}(\mathbf{r}, \gamma, \varphi, \theta_1, \theta_2, d)$ stands for the probability that a pair of photons that reach the detectors after propagating from the point $\mathbf{r}$ with orientations defined by γ, φ, θ_1 and θ_2, gives place to a coincidence at d, and its computation is discussed in the following subsections.

2.4.6 Detection efficiency

In the computation of $p_{det}(\mathbf{r}, \gamma, \varphi, \theta_1, \theta_2, d)$, it has to be taken first into account that the pair that reaches the detector faces may not be detected because no detector is 100% efficient. In order to include this effect in the system matrix model, the term $p_{det}(\mathbf{r}, \gamma, \varphi, \theta_1, \theta_2, d)$ can be splitted in two as follows:

$$p_{det}(\mathbf{r}, \gamma, \varphi, \theta_1, \theta_2, d) = p_{det\_sens}(\mathbf{r}, \gamma, \varphi, \theta_1, \theta_2) p_{pos}(\mathbf{r}, \gamma, \varphi, \theta_1, \theta_2, d) \tag{2.7}$$

where $p_{det\_sens}(\mathbf{r}, \gamma, \varphi, \theta_1, \theta_2, d)$ stands for the probability that the photon pair defined by $\mathbf{r}$, γ, φ, θ_1 and θ_2 finally leads to a coincidence event and $p_{pos}(\mathbf{r}, \gamma, \varphi, \theta_1, \theta_2, d)$ stands for the probability that the coincidence is assigned to LOR d. The next subsection will deal with the effects involved in the event positioning while this subsection deals with the calculation of $p_{det\_sens}(\mathbf{r}, \gamma, \varphi, \theta_1, \theta_2, d)$.

The first condition that a gamma pair that reaches the detectors must meet to generate a coincidence, is that both photons interact with the scintillators. As has been mentioned in the previous section, the probability of interaction of the photons with matter can be approximated by an exponential distribution. It can be easily inferred from this statement, that the probability that both photons interact with the scintillator is:

$$p_{int}(\mathbf{r}, \gamma, \varphi, \theta_1, \theta_2) = (1 - e^{\mu L_{sci_1}})(1 - e^{\mu L_{sci_2}}) \tag{2.8}$$

Where L_{sci_i} $i = 1, 2$ are the lengths the photons emitted from $\mathbf{r}$ intersect the scintillators in the direction given by φ, γ, θ_1, θ_2 and μ is the linear attenuation coefficient of the scintillator.

The interaction of both photons is a necessary but insufficient condition for the generation of a coincidence. Other effects may complicate the detection of both photons once they have interacted with the scintillators. For example, photons can't be detected during the so-called "dead time" because the counting system is busy processing previously detected events. Moreover, the differences in timing synchronization may cause misalignments in the timing windows between detectors pairs, reducing the detection efficiency. The detection efficiency drops as well due to other effects such as crystal imperfections, physical variations in the light guides, the PMTs or the electronics and variations in the PMT gains. Due to its *ad-hoc* nature, these effects are usually measured through calibration procedures in which the detectors are irradiated with a source of known activity and then applied in the form of normalization factors. Obviously, the procedures to obtain the normalization factors do not account just for the effects related to the detector sensitivity, but include all the effects involved in the measurement process. However, the normalization factors should account only for the effects that have not already been considered in other parts of the system matrix. The so-called component-based methods that include separated factors for the different effects (Hoffman et al. (1989), Casey et al. (1996), Badawi and Marsden (1999), Bai et al. (2002)), allow to match the normalization to the whole model. These methods are thus specially suitable to compute the normalization correction in the statistical framework.

Based on the previous discussion, the term $p_{det\_sens}(\mathbf{r}, \gamma, \varphi, \theta_1, \theta_2, d)$ will be expressed as follows:

$$p_{det\_sens}(\mathbf{r}, \gamma, \varphi, \theta_1, \theta_2, d) = p_{int}(\mathbf{r}, \gamma, \varphi, \theta_1, \theta_2) p_{cal}(\mathbf{r}, \gamma, \varphi, \theta_1, \theta_2) \tag{2.9}$$

In order to account for the fact that the detection of a gamma pair passes first through the interaction of the photons with the scintillators (whose probability, $p_{int}(\mathbf{r}, \gamma, \varphi, \theta_1, \theta_2)$, is given by Eq (2.8)) and then through a bunch of heterogeneous effects, represented by the term $p_{cal}(\mathbf{r}, \gamma, \varphi, \theta_1, \theta_2)$, for which no analytical accepted models exist but that can be incorporated to the model by means of calibration procedures.

2.4.7 Event positioning

The remaining term $p_{pos}(\mathbf{r}, \gamma, \varphi, \theta_1, \theta_2, d)$ stands for the probability that the coincidence generated by the gamma pair defined by $\mathbf{r}$,γ, φ, θ_1 and θ_2, is positioned at d. In principle, this term should be a binary function equaling one for those gamma pairs reaching the detectors within the limits imposed by d and zero otherwise. However, the effect of two important resolution degrading factors makes this probability to be a rather more complex function. First, it has to be taken into account that the photons may travel a certain distance within the scintillator before their first interaction. As a result, the interaction may be shifted to locations different from the entry crystals of the photons. This effect has already been referred to as crystal penetration. Second, it has to be taken into account that the product of the first interaction with the scintillator (the x-ray produced in photoelectric absorption or the Compton scattered photon) is available for additional interactions that, in turn, can give rise to further particles and interactions with the scintillator. This phenomena has been already referred to as detector scatter and, as stated in Mumcuoglu et al. (1996), may result in mispositioning.

Many works have shown how the incorporation of the crystal penetration and the detector scatter factors to the system matrix is highly advantageous in the reconstruction of high-resolution small animal PET data (Lee et al. (2004)). Nevertheless, these effects are known to be also a major cause of the non-sparsity of the system matrix (since they made

broader the volume of space that can produce coincidence counts in each pair of detectors (Selivanov et al. (2000))), and of the non redundancy of its components (since they show a highly spatially variant behavior (Alessio et al. (2006))). The crystal penetration and detector scatter factors are therefore a source of both accuracy and complexity for the system matrix. This makes their computation a challenging task, as is reflected by the extensive modeling that this part of the system matrix has been object of.

Certain approaches collectively model both effects by means of Monte Carlo simulations (Qi et al. (1998), Alessio et al. (2006), Bao et al. (2008)) or scanner measurements (Lee et al. (2004), Alessio et al. (2005), Tohme and Qi (2009)) and store the discretized results to be used during reconstruction. In other cases separated models for the two factors (Strul et al. (2003), Staelens et al. (2004), Rahmim et al. (2008), Moehrs et al. (2008), Iriarte et al. (2009)) are obtained and later combined in a single scheme. In the second case, for the crystal penetration, an analytical exponential model is typically used in all the cases, provided that the probability of interaction is known to drop exponentially with the distance the photon travels. For the detector scatter, the Klein-Nishina distribution (Klein and Nishina (1929)) along with the National Institute of Standard and Technology (NIST) photon cross section tables (/http://physics.nist.gov/PhysRefData/Xcom/Text/XCOM.html) cover the statistical information needed to accurately model the multiple interactions. However, dealing analytically with the infinite multiple interactions patterns that every single photon can give rise to is an impracticable problem, and the idea of developing analytical expressions to model the detector scatter has been traditionally discarded. These tools are much more well suited to be sampled by Monte Carlo simulators, as has already been done to estimate the effect of the detector scatter in Moehrs et al. (2008) and Rahmim et al. (2008). Other works have tried models based on Gaussian distributions (Staelens et al. (2004), Iriarte et al. (2009)). However, it can't be guaranteed that the mispositioning due to the detector scatter is going to behave as a Gaussian in all cases, since important differences may exist

among the event positioning in the different devices.

2.4.8 The whole system matrix

The phenomena involved in the positioning of the photons that have been described in Subsection 2.4.7 constitute the last step in the PET data acquisition process. Therefore, with their inclusion in the new integral scheme, the aim of this Section has been achieved. The final expression for the system matrix terms of the new integral scheme can be obtained by rearranging the terms that have been introduced along the previous subsections into a single expression:

$$p(b,d) = \int_{\mathbf{r_o}} v_b(\mathbf{r}_0) \left[\int_r f_{\mathbf{r_0}}(\mathbf{r}) \left[\int_\gamma \left[\int_\varphi f(\varphi,\gamma) \left[\int_{\theta_1} f(\theta_1) \left[\int_{\theta_2} f(\theta_2) p_{att}(\mathbf{r},\gamma,\varphi,\theta_1,\theta_2) \right.\right.\right.\right.\right.$$
$$\left.\left.\left.\left.\left. p_{det\_sens}(\mathbf{r},\gamma,\varphi,\theta_1,\theta_2) p_{pos}(\mathbf{r},\gamma,\varphi,\theta_1,\theta_2,d) d\theta_2 \right] d\theta_1 \right] d\varphi \right] d\gamma \right] d\mathbf{r} \left. \right] d\mathbf{r_0} \quad (2.10)$$

Where:

$v_b(\mathbf{r}_0)$ is the spatial distribution of the basis function b,

$f_{\mathbf{r_0}}(\mathbf{r})$ is the probability density function of the annihilation point for a positron emission occurred at $\mathbf{r_0}$,

$f(\varphi,\gamma)$ is the probability density function of the spatial orientation of the gamma pair emissions,

$f(\theta_1)$ is the probability density function of the non-collinearity angle,

$f(\theta_2)$ is the probability density function of the plane where the non-collinearity of the photons takes place,

$p_{att}(\mathbf{r},\gamma,\varphi,\theta_1,\theta_2)$ is the probability that a gamma pair emitted from $\mathbf{r}$ and propagating

along the direction defined by φ and γ and the deviation angles θ_1 and θ_2 is not absorbed and reaches the detectors,

$p_{det\_sens}(\mathbf{r}, \gamma, \varphi, \theta_1, \theta_2, d)$ stands for the probability that the photon pair that is not absorbed and reaches the detectors leads to a coincidence event,

$p_{pos}(\mathbf{r}, \gamma, \varphi, \theta_1, \theta_2, d)$ stands for the probability that the coincidence is assigned to LOR d.

One or several options to compute these expressions and their associated integration limits have been provided in the sections that have dealt with the effects each of them accounts for.

2.5 Analysis of the schemes of combination

In the previous section, a new methodology for the computation of the system matrix has been developed. As it has been pointed out, the new methodology shares advantages with the most popular factored models (Qi et al. (1998)), in terms both of accuracy (since the effects considered are the same) and of the flexibility with which each part of the acquisition process is able to be modeled (since each part of the model is individually considered). However, unlike the factored approaches, the methodology introduced combines the models of the different effects with a higher degree of mathematical precision, using integrals of probability density functions instead of products of independent discrete matrices. In this section, the importance of the differences between the integral and factored schemes of combination will be studied. This analysis will be performed in two steps:

1. In Subsection 2.5.1, the factored schemes will be questioned. Specifically, it will be first shown how the factored approach can be deduced from the new approach given by Eq (2.10), after certain assumptions about the data acquisition process are made. Then, it will be shown how the efficiency of the factorization relies also in certain

assumptions of the model. These are interesting results from the theoretical point of view, as the simplifications made by the factored models had never been formally stated before.

2. Once the assumptions made by the factored approaches have been specified, it will be discerned and justified in Subsection 2.5.2 which of them make sense, and which ignore important aspects of the data acquisition process. This analysis is expected to give an important clue of the influence of these assumptions in the reconstructions domain, since the accuracy of the model is directly related to the quality of the reconstructions achieved by iterative algorithms.

2.5.1 Analysis of the factored schemes

The most popular factored schemes (based on Mumcuoglu et al. (1996) and Qi et al. (1998)) express the system matrix as follows:

$$P = p_{det.sens} p_{blur} p_{att} p_{geo} p_{pos} \tag{2.11}$$

In a reconstruction in which the continuous radiotracer distribution is approximated as a sum of b_j ($j = 1, 2...N$) discrete basis functions and in which the scanner contains d_i ($i = 1, 2...M$) possible detector pairs, $p_{det.sens}$ and p_{att} are the $M \times M$ diagonal Normalization and Attenuation matrices. The diagonal elements ((i, i)) on these matrices contain, respectively, the correction factors for the detection efficiency of each LOR d_i and the survival probabilities of the photon pairs contained in each LOR d_i. p_{geo} is the $N \times M$ Geometric Projection matrix with each element (i, j) equal to the probability that a a photon pair produced in a basis function b_j reaches the front faces of the detector pair d_i in the absence of attenuation and assuming perfect photon-pair collinearity. p_{blur} is the $M \times M$

matrix known as the Blurring matrix. It is used to model the mispositioning of events produced by the photon-pair non-collinearity, detector scatter and penetration. Each element (i, i') in this matrix equals to the probability that a pair originally reaching the detector at pair d_i gives place to a detection in d'_i due to the mentioned effects. p_{pos} is the $N \times N$ Positron range matrix. Each (j, j') element in this matrix stands for the probability that a decay from within a basis function b_j gives place to an annihilation in another basis function b'_j due to the effect of positron range. It can be checked that all the effects behind the matrices $p_{det.sens}$, $p_{det.blur}$, p_{att}, p_{geo} and $p_{positron}$ have been included along Subsections 2.4.2 to 2.4.7 in the new integral model.

A term $p(b, d)$ of the factored system matrix, with b corresponding to one of the $j = 1, 2...N$ basis functions and d corresponding to one of the $i = 1, 2...M$ detector pairs can be demonstrated to be equal to:

$$p(b,d) = p_{det\_sens}(d) \sum_{i=1}^{M} \left\{ p_{blurr}(d_i, d) p_{att}(d_i) \sum_{j=1}^{N} \{ p_{geo}(b_j, d_i) p_{pos}(b, b_j) \} \right\} \qquad (2.12)$$

Scheme development

In the following, it will be shown how these terms can be obtained as a simplification of the terms of the new integral scheme, which, as shown in Subsection 2.4.8 are given by:

$$\begin{aligned} p(b,d) \;=\; & \int_{\mathbf{r_o}} v_b(\mathbf{r}_0) \left[\int_r f_{\mathbf{r_o}}(\mathbf{r}) \left[\int_\gamma \left[\int_\varphi f(\varphi,\gamma) \left[\int_{\theta_1} f(\theta_1) \left[\int_{\theta_2} f(\theta_2) p_{att}(\mathbf{r},\gamma,\varphi,\theta_1,\theta_2) \right.\right.\right.\right. \\ & \left.\left.\left.\left. p_{det\_sens}(\mathbf{r},\gamma,\varphi,\theta_1,\theta_2) p_{pos}(\mathbf{r},\gamma,\varphi,\theta_1,\theta_2,d) d\theta_2 \right] d\theta_1 \right] d\varphi \right] d\gamma \right] d\mathbf{r} \left. \right] d\mathbf{r_0} \qquad (2.13) \end{aligned}$$

The first modification needed to factorize Eq (2.13) is to extract from the integral

scheme the effects related to the detector efficiency and reconsider them in the form of correction factors for each LOR:

$$p(b,d) = p_{det\_sens}(d)\int_{\mathbf{r_o}} v_b(\mathbf{r}_0)\left[\int_r f_{\mathbf{r_0}}(\mathbf{r})\left[\int_\gamma\left[\int_\varphi f(\varphi,\gamma)\left[\int_{\theta_1} f(\theta_1)\left[\int_{\theta_2} f(\theta_2)\right.\right.\right.\right.\right.$$
$$\left.\left.\left.\left.\left. p_{att}(\mathbf{r},\gamma,\varphi,\theta_1,\theta_2)p_{pos}(\mathbf{r},\gamma,\varphi,\theta_1,\theta_2,d)d\theta_2\right]d\theta_1\right]d\varphi\right]d\gamma\right]d\mathbf{r}\right]d\mathbf{r_0} \quad (2.14)$$

The importance of this step will be discussed in detail in Subsection 2.5.2.

In order to continue the factorization of Eq (2.14), the gamma pairs emitted from the annihilating point $\mathbf{r}$ can be grouped according to their spatial orientations (γ,φ) as follows:

$$p(b,d) = p_{det\_sens}(d)\int_{\mathbf{r_o}} v_b(\mathbf{r}_0)\left[\int_r f_{\mathbf{r_0}}(\mathbf{r})\left[\sum_{i=1}^{M}\left\{\int_{\gamma_i}\left[\int_{\varphi_i} f(\varphi,\gamma)\left[\int_{\theta_1} f(\theta_1)\left[\int_{\theta_2} f(\theta_2)\right.\right.\right.\right.\right.\right. .$$
$$\left.\left.\left.\left.\left.\left. p_{att}(\mathbf{r},\gamma,\varphi,\theta_1,\theta_2)p_{pos}(\mathbf{r},\gamma,\varphi,\theta_1,\theta_2,d)d\theta_2\right]d\theta_1\right]d\varphi\right]d\gamma\right\}\right]d\mathbf{r}\right]d\mathbf{r_0} \quad (2.15)$$

The pairs with orientations defined by azimuthal and polar angles in the intervals γ_i and φ_i are those whose photons reach the scintillator at the front faces of the detector pair i (in the absence of attenuation and assuming perfect photon-pair collinearity). In the case of continuous detector technology, the grouping of gamma pairs should be done according to certain artificial discretization of the detectors. In any case, the expression in Eq (2.15) is still equivalent to the one in Eq(2.14) and this step does not constitute a modification of the integral model. Reordering terms in Eq (2.15), it becomes:

$$p(b,d) = p_{det\_sens}(d)\sum_{i=1}^{M}\left\{\int_{\mathbf{r_o}} v_b(\mathbf{r}_0)\left[\int_r f_{\mathbf{r_0}}(\mathbf{r})\left[\int_{\gamma_i}\left[\int_{\varphi_i} f(\varphi,\gamma)\left[\int_{\theta_1} f(\theta_1)\left[\int_{\theta_2} f(\theta_2)\right.\right.\right.\right.\right.\right.$$

$$\left.\left.\left.\left.\left.\left. p_{att}(\mathbf{r},\gamma,\varphi,\theta_1,\theta_2)p_{pos}(\mathbf{r},\gamma,\varphi,\theta_1,\theta_2,d)d\theta_2\right]d\theta_1\right]d\varphi\right]d\gamma\right]d\mathbf{r}\right]d\mathbf{r_0}\right\} \quad (2.16)$$

The second assumption that leads to the factored model is made at this point in order to discretize the attenuation effect. Within each subset of gamma pairs reaching the detector i the probability that neither of the photons of the pair is absorbed as they propagate towards the detectors, is considered as independent of the point from which the gamma pair has been emitted ($\mathbf{r}$) and of the spatial orientation of the gamma pair (given by γ, φ, θ_1 and θ_2). As a result, from now on, $p_{att}(\mathbf{r},\gamma,\varphi)$ will be referred to as $p_{att}(d_i)$ and pulled outside the integrals in $\mathbf{r}$, γ_i, φ_i, θ_1 and θ_2:

$$p(b,d) = p_{det\_sens}(d)\sum_{i=1}^{M}\left\{p_{att}(d_i)\int_{\mathbf{r_o}} v_b(\mathbf{r}_0)\left[\int_r f_{\mathbf{r_0}}(\mathbf{r})\left[\int_{\gamma_i}\left[\int_{\varphi_i} f(\varphi,\gamma)\left[\int_{\theta_1} f(\theta_1)\left[\int_{\theta_2} f(\theta_2)\right.\right.\right.\right.\right.\right.$$

$$\left.\left.\left.\left.\left.\left. p_{pos}(\mathbf{r},\gamma,\varphi,\theta_1,\theta_2,d)d\theta_2\right]d\theta_1\right]d\varphi\right]d\gamma\right]d\mathbf{r}\right]d\mathbf{r_0}\right\} \quad (2.17)$$

The importance of this assumption will be further analyzed in Subsection 2.5.2.

Now, in order to match to the factored model, where the non-collinearity, crystal penetration and detector scatter are gathered in the p_{blurr} term, the following notation will be adopted:

$$p_{blurr}(\mathbf{r},\gamma,\varphi,d) = \int_{\theta_1} f(\theta_1)\left[\int_{\theta_2} p_{pos}(\mathbf{r},\gamma,\varphi,\theta_1,\theta_2,d)f(\theta_2)d\theta_2\right]d\theta_1 \quad (2.18)$$

The system matrix expression can now be written as:

$$p(b,d) = p_{det\_sens}(d)\sum_{i=1}^{M}\left\{p_{att}(d_i)\int_{\mathbf{r_o}} v_b(\mathbf{r}_0)\left[\int_r f_{\mathbf{r_0}}(\mathbf{r})\left[\int_{\gamma_i}\left[\int_{\varphi_i} f(\varphi,\gamma)p_{blurr}(\mathbf{r},\gamma,\varphi,d)\right.\right.\right.\right.$$
$$\left.\left.\left.\left.d\varphi\right]d\gamma\right]d\mathbf{r}\right]d\mathbf{r_0}\right\} \tag{2.19}$$

Another simplification in the integral scheme has to be made at this point in order to reach the factored model. Similarly to what has been done for the attenuation term $p_{att}(\mathbf{r},\gamma,\varphi)$, the blurring term $p_{blurr}(\mathbf{r},\gamma,\varphi,d)$ will be pulled outside the integrals and renamed $p_{blurr}(d_i,d)$ in order to remove its dependence from $\mathbf{r}$,γ_i,φ_i within each tube i, which constitutes the basis of this assumption:

$$p(b,d) = p_{det\_sens}(d)\sum_{i=1}^{M}\left\{p_{blurr}(d_i,d)p_{att}(d_i)\int_{\mathbf{r_o}} v_b(\mathbf{r}_0)\left[\int_r f_{\mathbf{r_0}}(\mathbf{r})\left[\int_{\gamma_i}\left[\int_{\varphi_i} f(\varphi,\gamma)\right.\right.\right.\right.$$
$$\left.\left.\left.\left.d\varphi\right]d\gamma\right]d\mathbf{r}\right]d\mathbf{r_0}\right\} \tag{2.20}$$

The significance of this simplification in the model will be studied in Section 2.5.2. Now, the following notation will be adopted:

$$p_{geo}(r,d_i) = \int_{\gamma_i}\left[\int_{\varphi_i} f(\varphi,\gamma)d\varphi\right]d\gamma \tag{2.21}$$

Since this integral computes the solid angle spanned from the point $\mathbf{r}$ to the faces of the detector pair d_i, and therefore matches the geometrical factors of the system matrix. With the new notation, the expression for the system matrix terms becomes:

$$p(b,d) = p_{det\_sens}(d)\sum_{i=1}^{M}\left\{p_{blurr}(d_i,d)p_{att}(d_i)\int_{\mathbf{r_o}} v_b(\mathbf{r}_0)\left[\int_r f_{\mathbf{r_0}}(\mathbf{r})p_{geo}(r,d_i)\right.\right.$$

$$\left.\left. d\mathbf{r}\right] d\mathbf{r_0}\right\} \tag{2.22}$$

Two further assumptions have been done at this point in order to express Eq (2.22) in the factored form of Eq (2.12) . First, it will be assumed that the annihilation points r can be grouped according to the basis function b_j they belong to:

$$p(b,d) = p_{det\_sens}(d)\sum_{i=1}^{M}\left\{p_{blurr}(d_i,d)p_{att}(d_i)\int_{\mathbf{r_o}} v_b(\mathbf{r}_0)\left[\sum_{j=1}^{N}\left\{\int_{r_j} f_{\mathbf{r_0}}(\mathbf{r})p_{geo}(r,d_i)\right.\right.\right.$$

$$\left.\left.\left. d\mathbf{r}\right\}\right] d\mathbf{r_0}\right\} \tag{2.23}$$

The integration limits r_j cover now the annihilation limits that conform the basis function b_j. Next, it will be assumed that, for all the annihilation points r_j belonging to the basis function b_j, the solid angle subtended into the detector pair i is the same. Consequently, the term $p_{geo}(r,d_i)$ is renamed $p_{geo}(b_j,d_i)$ and can be pulled outside he integral in r:

$$p(b,d) = p_{det\_sens}(d)\sum_{i=1}^{M}\left\{p_{blurr}(d_i,d)p_{att}(d_i)\int_{\mathbf{r_o}} v_b(\mathbf{r}_0)\left[\sum_{j=1}^{N}\left\{p_{geo}(b_j,d_i)\int_{r_j} f_{\mathbf{r_0}}(\mathbf{r})\right.\right.\right.$$

$$\left.\left.\left. d\mathbf{r}\right\}\right] d\mathbf{r_0}\right\} \tag{2.24}$$

The relevance of these two assumptions will be analyzed in Subsection 2.5.1. Reordering terms in Eq (2.24) gives:

$$p(b,d) = p_{det\_sens}(d)\sum_{i=1}^{M}\left\{p_{blurr}(d_i,d)p_{att}(d_i)\sum_{j=1}^{N}\left\{p_{geo}(b_j,d_i)\int_{\mathbf{r_o}} v_b(\mathbf{r}_0)\left[\int_{r_j} f_{\mathbf{r_0}}(\mathbf{r}) d\mathbf{r}\right] d\mathbf{r_0}\right\}\right\} \tag{2.25}$$

And the last group of integrals of this expression can be renamed as $p_{pos}(b,b_j)$:

$$p_{pos}(b,b_j) = \int_{\mathbf{r_o}} v_b(\mathbf{r}_0)\left[\int_{r_j} f_{\mathbf{r_0}}(\mathbf{r})d\mathbf{r}\right] d\mathbf{r_0} \tag{2.26}$$

Since it can be easily demonstrated that it computes the probability that a decay from b_0 gives place to an annihilation within b_j, due to the effect of the positron range. With the new notation, the expression for the system matrix terms becomes:

$$p(b,d) = p_{det\_sens}(d)\sum_{i=1}^{M}\left\{p_{blurr}(d_i,d)p_{att}(d_i)\sum_{j=1}^{N}\{p_{geo}(b_j,d_i)p_{pos}(b,b_j)\}\right\} \tag{2.27}$$

which exactly matches the expression for the system matrix terms for the factored scheme shown in Eq (2.12).

Scheme storage

So far, it has been demonstrated how the traditional factored scheme for the system matrix computation can be obtained as a simplification of the new integral scheme proposed in Section 2.4, after certain assumptions about the data acquisition model have been made.

Once the system model has been expressed as a product of independent matrices, the factored schemes precalculate and store each of these matrices and then compute the system matrix terms at reconstruction time by applying Eq (2.12) on the fly. Even if the size saving from factoring the effects has been proved (Qi et al. (1998)), the computational challenge of the factored schemes still lies in the storage of each of the factors compounding Eq (2.11). Being both the number of basis functions (N) and the number of LORS (M) typically above the million in high resolution small animal PET scanners, these factors are expected to demand high memory resources. For that reason, the most popular factored approaches rely in other assumptions that, even though are not strictly inherent to the factorization process, are necessary in order to make the matrix storage feasible:

- The storage of the $M \times M$ normalizing and attenuation matrix does not represent such a challenge since, as it has been already mentioned, just the elements of the diagonal have to be saved.

- The $N \times M$ geometric matrix p_{geo} is very sparse, given the small fraction of basis functions that can produce coincidences at each detector pair, and a great saving in storage can be realized by storing only the non zero elements (Qi et al. (1998)). Moreover this matrix has in-plane, axial and parallel sinogram symmetries that can be exploited (Johnson et al. (1994), Chen et al. (1991)).

- Several measures are taken for the storage of the $p_{blurr}(d_i, d)$ terms of the $M \times M$ p_{blurr} matrix. First, the sparsity of the Blurring matrix is increased by considering that a LOR d_i "blurrs" just into a few neighboring elements d in the radial, azimuthal and axial direction (Mumcuoglu et al. (1996)). Moreover, in many cases the blurring effect is not just truncated, but completely ignored along the axial (Mumcuoglu et al. (1996), Qi et al. (1998), Lee et al. (2004), Tohme and Qi (2009)) and/or the azimuthal

directions (Alessio et al. (2005), Alessio et al. (2006), Bao et al. (2008)). The dimensionality of the Blurring matrix is reduced as well by assuming certain spatially invariances. Specifically, some approaches assume that the blurring remains the same for all azimuthal angles and only obtain the $p_{blurr}(d_i, d)$ terms for a single projection angle of d_i (Mumcuoglu et al. (1996), Qi et al. (1998), Lee et al. (2004), Alessio et al. (2005), Alessio et al. (2006)). Other approaches assume as well that the blurring terms are identical for all the ring differences (the axial difference between the two crystals that define the LOR d_i) and ring planes (i.e., the relative position of the plane containing two detectors). Such approaches apply the $p_{blurr}(d_i, d)$ terms obtained for the LORs d_i at the central transaxial plane (i.e., a plane perpendicular to the scanner axial axis placed at 0 mm from the axial center) to all other rings (Mumcuoglu et al. (1996), Qi et al. (1998), Alessio et al. (2005), Alessio et al. (2006)).

- Regarding the $N \times N$ positron range matrix, some works use analytical approximations. For example, in Rahmim et al. (2008) the contribution between basis functions is modeled as a 3D biexponential curve. However, in most cases the effect is just ignored by assuming ^{18}F studies with positron range in sub-millimetre, and the matrix p_{pos} is set equal to the identity matrix (Qi et al. (1998)).

The validity of the above mentioned assumptions, needed for the efficient storage of the matrix, will be studied in the following subsection.

2.5.2 Analysis of the simplifications

In the previous subsection, the simplifications involved in the factorization of the system matrix have been unraveled. Being the faithfulness to the data acquisition process the basis for the high quality of the images obtained by iterative algorithms, such simplifications can expected to have certain influence in the reconstructions. In order to get a clue of the extent

of this influence, an analysis of how much each of these simplifications disagree with the real PET process will be performed in the following.

Detector efficiency

First, in order to pass from Eq (2.13) to Eq (2.14), the effects related to the detector efficiency have been taken of the integral to turn them into correction factors $p_{det\_sens}(d)$ that can be measured for each LOR according to one of the component-based methods quoted in Subsection 2.4.6. It has to be noted that, as stated by Leahy and Qi (2000), multiplying the elements of the system matrix by measured efficiencies $p_{det\_sens}(d)p(b,d)$, is a common practice not restricted to the purely factored schemes based in the works of Mumcuoglu et al. (1996) and Qi et al. (1998). When the detector efficiency is considered in the form of correction factors the resulting expression for the reconstruction algorithm is:

$$\lambda^{new}(b) = \frac{\lambda^{old}(b)}{\sum_{d=1}^{D} p_{det\_sens}(d)p(b,d)} \sum_{d=1}^{D} \frac{n^*(d)p_{det\_sens}(d)p(b,d)}{\sum_{b=1}^{B} \lambda^{old}(b)\, p_{det\_sens}(d)p(b,d)} \tag{2.28}$$

And, as stated by Espallardo (2009), since the $p_{det\_sens}(d)$ factors can be canceled out in the second factor, the effect of modifying the system matrix by the efficiencies in the MLEM scheme is:

$$\lambda^{new}(b) = \frac{\lambda^{old}(b)}{\sum_{d=1}^{D} p_{det\_sens}(d)p(b,d)} \sum_{d=1}^{D} \frac{n^*(d)p(b,d)}{\sum_{b=1}^{B} \lambda^{old}(b)\, p(b,d)} \tag{2.29}$$

As scan be observed, the efficiencies $p_{det\_sens}(d)$ only modify the sensitivity matrix.

Since the success of iterative algorithms is mostly based in the accuracy with which the forward and backward projections are performed, removing the effects accounted in $p_{det\_sens}(d)$ from these operations is likely to jeopardize the quality of the reconstructions. Provided that the component-based methods allow to model in $p_{det\_sens}(d)$ just the phenomena that have not been considered in other parts of the system matrix, the collection of effects represented by $p_{det\_sens}(d)$ should be minimized. The factorization of the efficiency is justified in the case of the effects that have been included in the term $p_{cal}(\mathbf{r}, \gamma, \varphi, \theta_1, \theta_2)$ in Subsection 2.4.6, since its *ad-hoc* nature makes any other way of modeling these effects a rather complex task. On the other hand, the factorization does not seem to be necessary in the case of the probability of interaction of the photons with the scintillators, for which a wide accepted analytical model exists and has been provided in Eq (2.8). Based on this discussion, and being the probability interaction of photons with the scintillator a key factor of the detector efficiency, it can be concluded that the factorization of this effect should be avoided.

Attenuation

The second step in the factorization (pass from Eq (2.16) to Eq (2.17)) has been to discretize the attenuation term $p_{att}(\mathbf{r}, \gamma, \varphi)$ into attenuation factors for each LOR $p_{att}(d_i)$. This step entails the assumption that all the pairs whose photons reach the scintillators within the limits of the crystals that form d_i, have the same survival propability, independently of their annihilation point ($\mathbf{r}$), and orientation (given by the angles φ, γ, θ_1 and θ_2).

Being the tendency in the small animal environment to reduce the size of the pixelated crystals (Surti et al. (2009)), the gamma pairs restricted to a pair d_i will be concentrated in a narrow tube of response. The non-collinearity of the pairs may increase the size of this tube. However, being the Gaussian standard deviation from the collinear situation in the order of 25 milliradians, and given the reduced diameter of the small animal scanners, the

tube is not expected to get much wider by the effect of the non-collinearity. The gamma pairs confined to a tube of response are therefore expected to transverse a similar portion of the attenuation object which will have similar tissues properties. Consequently, within the limits imposed by d_i, the probability that neither of the photons are absorbed is not expected to vary significatively from one pair to another. This statement, along with the fact that the total thickness of the attenuation medium makes the attenuation a relatively minor effect for small animal (Yao et al. (2005)), make the factorization of the attenuation term reasonably acceptable.

Blurring

In the next step to the factorization (from (2.19) to (2.20)), the so-called blurring term $p_{blurr}(\mathbf{r}, \gamma, \varphi, d)$ has been pulled outside the integrals in $\mathbf{r}$, γ and φ. The new blurring term, that has been renamed as $p_{blurr}(d_i, d)$, stands for the probability that a gamma pair that reaches the scintillator within the limits of a detector pair d_i and is detected by the system, is positioned at d. This step involves thus the assumption that the gamma pairs reaching d_i share their probability of being positioned at LOR d, independently of its emitting point and orientation.

As has been stated, the pair mispositioning that the blurring term represents accounts for the effects of the non-collinearity, crystal penetration and detector scatter. In the factored approaches, just the depth dependence (i.e., distance of the positron annihilation point from the detectors) of these effects is discussed. Specifically, the work by Mumcuoglu et al. (1996) justifies the depth dependence for the inter-crystal detector scatter and for the crystal penetration. On the other hand, the non-collinearity is assumed as depth independent for the benefit of sparseness, even if the uncertainties in the angular separation of the pair are clearly dependent of the distance of the annihilation point from the detectors. The mispositioning due to the non-collinearity is not expected to be critical in the small animals

environment, where the detector spacing is reduced (Cherry and Gambhir (2001)). As a result, the depth independence or other assumptions regarding the non-collinearity are not expected to trade the quality of the reconstructions.

Unlike the non-collinearity, the penetration and the detector scatter effects are known to be highly resolution degrading effects in the small animal environment (Lee et al. (2004)). The factored approaches ignore the dependence of these effects with the radial position of the annihilation point within the detector tube and with the orientation of the gamma pair, but no justification is given for these assumptions. However, the properties of these effects suggest that this dependence might exist. In the case of the crystal penetration, the rays that enter the crystal at large incidence angles will be clearly more likely to cross the detectors and be detected at further positions from the entry point than those with normal incidence (as shown in Figure 2.4 (top)). Moreover, the crystals crossed by a photon on its trajectory depend on its entry point in the scintillator, which in turn depends on the radial position of the pair within the detector pair (as shown in Figure 2.4 (bottom)).

The radial and angular dependence of the detector scatter can't be predicted in such a direct manner, since the multiple interactions give place to a rather more complex effect than the penetration. However, certain clues of this dependence can be found based on general characteristics of the phenomena that give place to the multiple photon interactions. On the one hand, the location of the first interaction, in which the direction and radial position of the gamma photon are involved, can be expected to have an important role in the final position of the event. On the other hand, it might be expected that photons propagating along different angular trajectories will give place to different scatter processes that will give place to different mispositioning patterns, since the energy of the Compton scattered photons is known to be dependent upon the angle between the incident and the scattered photon.

The previous discussion suggests that certain radial and angular dependency of the

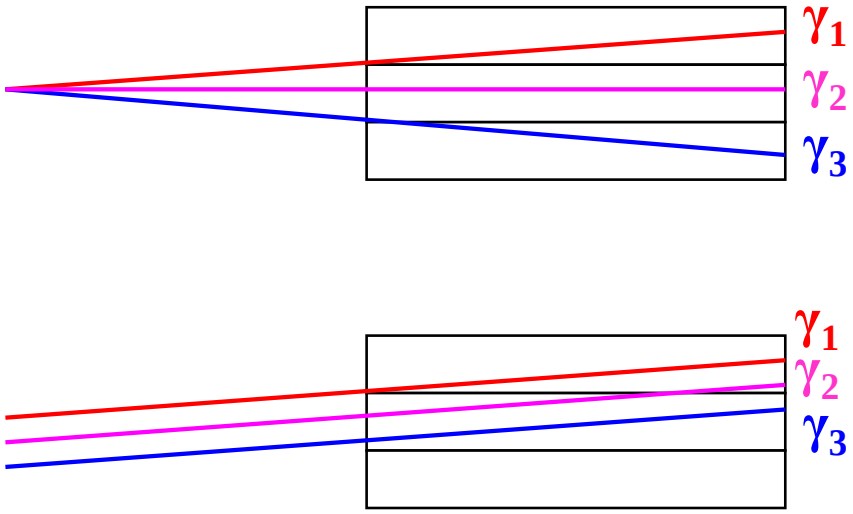

Figure 2.4: Influence of the angular (top) and radial (bottom) position of the gamma ray in the mispositioning due to the penetration effect. The photons labeled γ_1 and γ_3 on the top will be more likely to be positioned in the upper and lower crystals respectively whereas the photon labeled γ_2 wont give place to mispositioning due to the penetration. The photon labeled γ_1 at the bottom will be more likely to be positioned in the upper crystal than the photon labeled γ_2, which in turn will be more likely to be positioned in the upper crystal than the photon labeled γ_3.

penetration and the detector scatter can be expected, but it is not enough to justify whether the invariance assumptions about these effects made by the factored approaches should be

accepted or not. On the one hand, the great influence that these effects are known to have in the resolution achieved by the small animal devices makes them worthy of extremely accurate models, and any possible discrepancy of these models with the real acquisition process should be avoided. On the other hand, the fact that the invariability assumptions are limited to the photon pairs confined to the tube of response defined by a pair of narrow detectors, surely limits the range of variation of the effects along the radial and angular dimensions. Moreover, it is known that the resources saving from factoring out the detector blurring as compared to incorporating it in the geometric matrix is high (Qi et al. (1998)). Being the assumption or not of the blurring invariance a critical point in the algorithm performance, further experiments have been carried on in order to precise to what extent the variability of $p_{blurr}(\mathbf{r}, \gamma, \varphi, d)$ with r, γ and φ is worth to be considered in the model.

For fixed $\mathbf{r}$, γ and φ the terms $p_{blurr}(\mathbf{r}, \gamma, \varphi, d)$ can be interpreted as the statistical distribution of the LORs in which the pair defined by these parametres can be positioned (i.e., an histogram of assigned LORs d for a given gamma pair). The objective of the experiments has been to test if, as assumed by the factored schemes, all the pairs confined within a given tube of response d_i give place to the same distributions of d, independently of the radial component of r and of the orientation of the gamma pair γ, φ (i.e., if $p_{blurr}(\mathbf{r}, \gamma, \varphi, d) = p_{blurr}(d_i, d)$ for all the pairs within a detector pair d_i)

For the sake of simplicity, the experiments have been run just on detector pairs d_i placed on the central transaxial plane of the devices simulated. Moreover, just the blurring into other detector pairs d of this plane has been studied. This means that just the transanxial component of the blurring has been considered, but the results obtained can be directly extrapolated to the axial direction. Once limited to the central transaxial plane and in order to account for cases with different order of incidence angle, the invariance of the blurring has been analyzed in a center and an off-center detector pair. Figure 2.5 shows the resulting simulation setup, whose dimensions (scanner diameter and crystal size) have been matched

to the characteristics of three different commercially available devices: the A-PET (Surti et al. (2005)), the YAP-S(PET) II (Del Guerra et al. (2006), Moehrs et al. (2008)) and the microPET II (Tai et al. (2003)) scanners. As can be checked in Table 2.1, three cameras with rather different features have been chosen for the study, to ensure that the conclusions obtained won't be restricted to the peculiarities of a particular device.

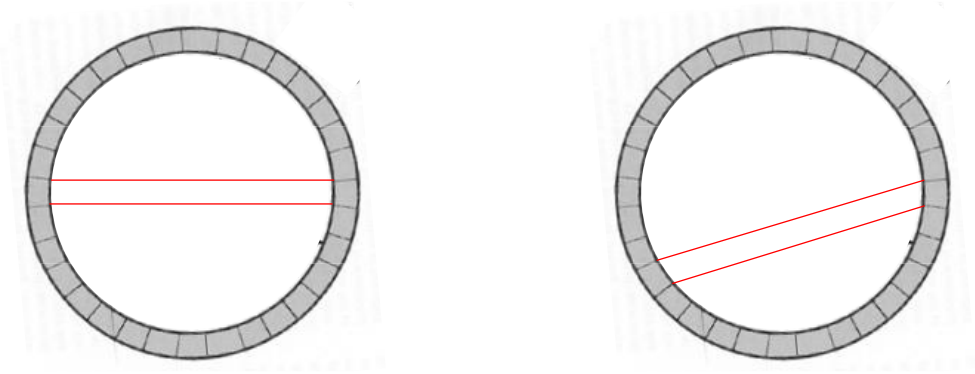

(a) (b)

Figure 2.5: Center (a) and off-center (b) detector pair of the central transaxial plane of the setups for which the blurring invariance will be studied

	A-PET	YAP-S(PET) II	microPET II
Crystal cross section (mm)	2	1.5	0.975
Crystal depth (mm)	10	20	12.5
Scanner Diameter (cm)	19.7	4	16
Scintillator Material	LYSO	YAP:Ce	LSO

Table 2.1: Main features of the scanners for which the blurring invariance will be studied

In order to check to what extent all the gamma pairs confined to the center and off-center detector pairs share their $p_{blurr}(\mathbf{r}, \gamma, \varphi, d)$ term, the distributions generated by different pairs emitted at the central depth of the tubes with different angular orientations and from different radial positions have been compared. Figure 2.6 shows an example of the experimental setup for the case of two pairs emitted at different radial positions within the center detector pair.

Assuming that the timing synchronization related effects are considered in the normalization procedure (through the term $p_{cal}(\mathbf{r}, \gamma, \varphi, \theta_1, \theta_2)$ defined in Subsection 2.4.6), the LOR distribution $p_{blurr}(\mathbf{r}, \gamma, \varphi, d)$ associated to a gamma pair can be considered as the composition of two independent crystal distributions (referred to as $p_1(r_k, \varphi, \gamma, c)$ and $p_2(r_k, \varphi, \gamma, c)$ in Figure 2.6), each of them associated to one of their forming photons. Without loss of generality, the comparison has been reduced to the crystal distributions produced by just one of the photons of each pair.

The crystal distributions have been obtained with the well-known simulator GATE, (the GEANT4 Application for Tomographic Emission) (Jan et al. (2004)), which encapsulates the GEANT4 libraries for the simulation of the passage of particles through matter (Agostinelli et al. (2003)). Several beam photon sources (see Figure 2.7 for further details) have been simulated within each detector pair to generate the distributions. A large number of photons have been generated from each of the beams to obtain high SNR estimations. The hits generated by the photons in the scintillators have been reduced to single events whose position is obtained with an energy-weighted centroid of the different hit positions and stored in an output file. The single positions have then been histogrammed in the crystal positions to give place to the searched distributions. The differences between these distributions have then been measured using the Kullback-Leibler (KL) divergence (Kullback and Leibler (1951)), which is often used to measure the distance between probability distributions.

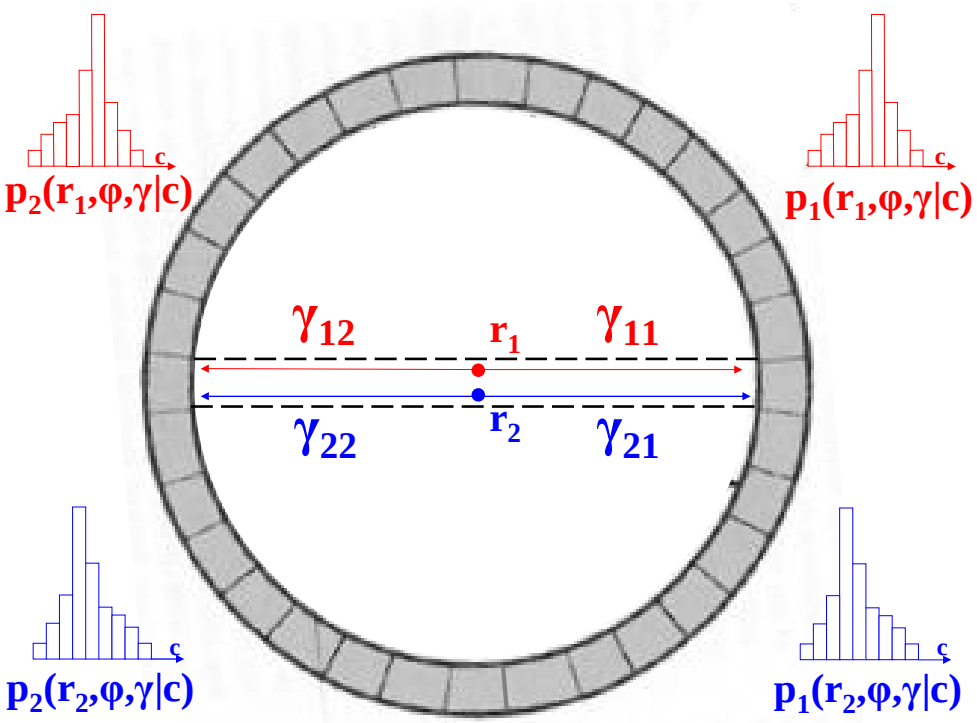

Figure 2.6: Example of experimental setup. The aim of this experiment is to check wether the two gamma pairs emitted from different radial positions r_1 and r_2 within the detector tube give place to the same LOR positioning distribution. Since such LOR distributions can be obtained as a composition of the individual crystal distributions each photon of the pair gives place to, the comparison will be performed over one of the crystal distributions (i.e., it will be checked whether $p_1(r_1, \varphi, \gamma, c) = p_1(r_2, \varphi, \gamma, c)$)

Table 2.2 shows, for the three simulated scanners, the KL values among the beams emitted with different angular orientations. Table 2.3 shows the KL values among the beams emitted from different radial positions. The left side contains the results for the

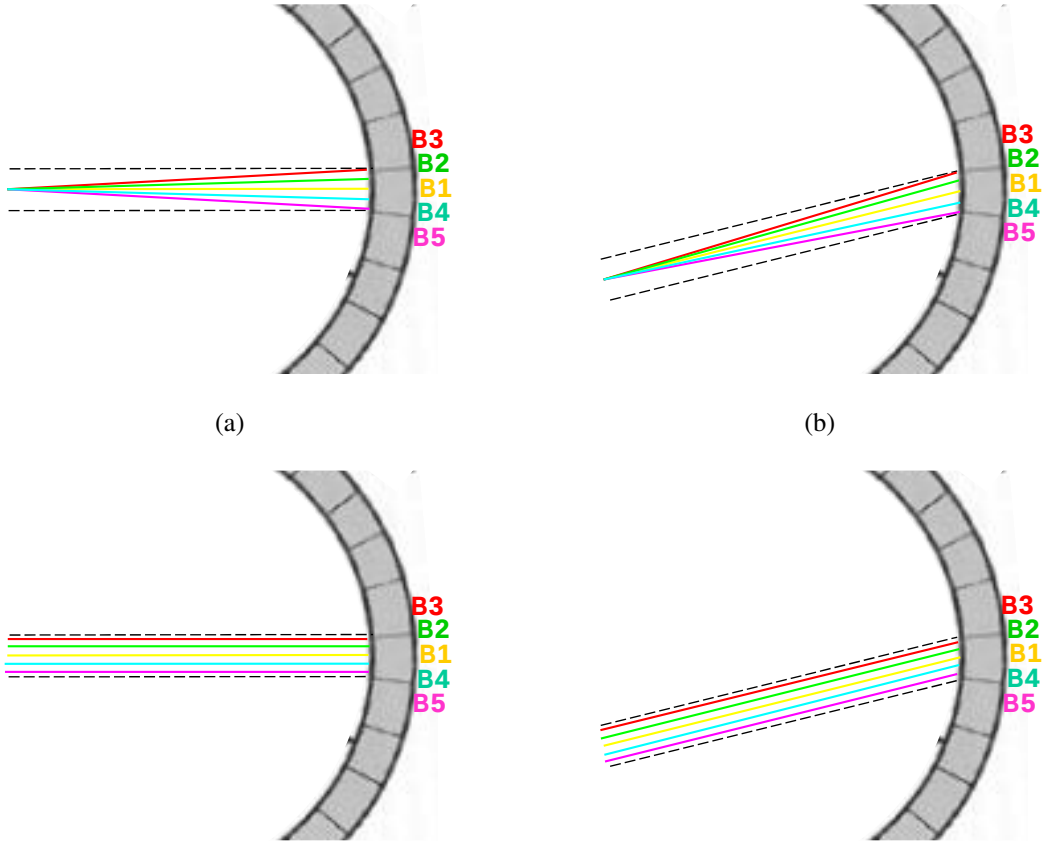

Figure 2.7: Beams simulated to study the influence of the angular orientation (top) and radial position (bottom) of the gamma pairs in the positioning. The yellow beams (B1) correspond to the pair connecting the centers of the two detectors that define the LOR. The red and pink beams (B3 and B5) correspond to the maximum angular/radial deviation from the centered pair that a gamma pair can have within the detector limits (i.e., the beams connecting the ends of the detector pairs).The green and blue beams (B2 and B4) correspond to intermediate angular/radial deviations.

center LOR shown in Figure 2.7(a) whereas the right side contains the results the off-center LOR shown in Figure 2.7(b). Since the KL divergence is not a symmetric measure (the KL from P to Q is not necessarily the same as the KL from Q to P), for each pair of beams it has been computed in both directions. However, it can be checked in Tables 2.2 and 2.3, that the two values obtained for a pair of beams are very similar in all cases. As expected, the KL divergence is null when comparing distributions of identical beams. In order have a reference value with which to interpret the non null values, the accepted depth independence of the blurring (Mumcuoglu et al. (1996)) has been used. This value has been obtained by comparing the distributions obtained from beams generated at different depths of the center and the off-center pairs (see Figure 2.8). For all the depths simulated, the KL values obtained are in the order of 10^{-5}, which is several orders below the values obtained for the KL divergences among the beams shown in Figure 2.7. This suggests that the angular and radial invariance of the blurring produced by the beams within a detector pair should not be as unquestionably accepted as the depth invariance.

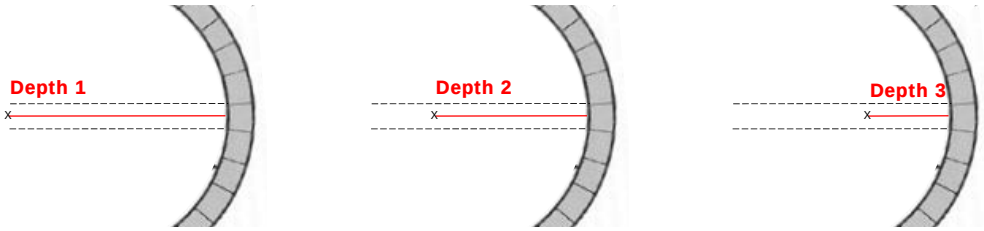

Figure 2.8: Setup used to check the depth invariance of the blurring

A-PET										
	Centre LOR					Off-Center LOR				
KL	b1	b2	b3	b4	b5	b1	b2	b3	b4	b5
b1	0.000	0.013	0.483	0.013	0.480	0.000	0.076	0.363	0.034	0.142
b2	0.014	0	0.386	0.053	0.563	0.086	0.000	0.104	0.197	0.366
b3	0.725	0.528	0.000	0.901	1.334	0.336	0.085	0.000	0.525	0.754
b4	0.017	0.053	0.563	0.000	0.386	0.035	0.191	0.615	0.000	0.037
b5	0.722	0.901	1.334	0.528	0.000	0.141	0.370	0.924	0.036	0.000

microPET										
	Centre LOR					Off-Centre LOR				
KL	b1	b2	b3	b4	b5	b1	b2	b3	b4	b5
b1	0.000	0.009	0.079	0.008	0.079	0.000	0.000	0.000	0.013	0.023
b2	0.009	0.000	0.040	0.034	0.126	0.000	0.000	0.000	0.016	0.028
b3	0.098	0.048	0.000	0.156	0.270	0.000	0.000	0.000	0.019	0.031
b4	0.009	0.034	0.126	0.000	0.040	0.013	0.017	0.020	0.000	0.001
b5	0.097	0.156	0.270	0.048	0.000	0.024	0.029	0.032	0.001	0.000

YAP										
	Centre LOR					Off-Centre LOR				
KL	b1	b2	b3	b4	b5	b1	b2	b3	b4	b5
b1	0.000	0.010	0.714	0.010	0.715	0.000	0.024	0.119	0.017	0.057
b2	0.010	0.000	0.621	0.042	0.779	0.025	0.000	0.034	0.084	0.146
b3	0.936	0.752	0.000	1.091	1.456	0.104	0.029	0.000	0.205	0.290
b4	0.011	0.042	0.779	0.000	0.621	0.016	0.080	0.228	0.000	0.014
b5	0.938	1.091	1.456	0.752	0.000	0.056	0.148	0.341	0.013	0.000

Table 2.2: KL divergences among the beams emitted with different angular orientations

A-PET										
	Centre LOR					Off-Centre LOR				
KL	b1	b2	b3	b4	b5	b1	b2	b3	b4	b5
b1	0.000	0.010	0.064	0.011	0.064	0.000	0.061	0.297	0.028	0.109
b2	0.011	0.000	0.026	0.042	0.118	0.067	0.000	0.087	0.160	0.289
b3	0.076	0.029	0.000	0.137	0.241	0.276	0.073	0.000	0.434	0.614
b4	0.011	0.042	0.118	0.000	0.026	0.029	0.158	0.507	0.000	0.027
b5	0.076	0.137	0.240	0.029	0.000	0.110	0.299	0.751	0.026	0.000

microPET										
	Centre LOR					Off-Centre LOR				
KL	b1	b2	b3	b4	b5	b1	b2	b3	b4	b5
b1	0.000	0.009	0.080	0.008	0.079	0.000	0.012	0.064	0.008	0.029
b2	0.009	0.000	0.041	0.035	0.127	0.012	0.000	0.019	0.036	0.072
b3	0.099	0.048	0.000	0.157	0.272	0.058	0.017	0.000	0.099	0.149
b4	0.009	0.035	0.127	0.000	0.041	0.008	0.039	0.117	0.000	0.007
b5	0.098	0.157	0.272	0.048	0.000	0.031	0.080	0.183	0.007	0.000

YAP										
	Centre LOR					Off-Centre LOR				
KL	b1	b2	b3	b4	b5	b1	b2	b3	b4	b5
b1	0.000	0.006	0.032	0.006	0.032	0.000	0.006	0.032	0.006	0.032
b2	0.006	0.000	0.010	0.025	0.064	0.006	0.000	0.010	0.025	0.064
b3	0.034	0.011	0.000	0.069	0.122	0.034	0.011	0.000	0.069	0.122
b4	0.006	0.025	0.064	0.000	0.010	0.006	0.025	0.064	0.000	0.010
b5	0.035	0.069	0.122	0.011	0.000	0.035	0.069	0.122	0.011	0.000

Table 2.3: KL divergences among the beams emitted from different radial positions

In order get an idea of where the causes for the high KL values lie in, some of the crystal distributions obtained in the above mentioned experiments are shown next. The graphs in Figures 2.8-2.13 plot these distributions for the A-PET, microPET and YAP scanners. Each column in these figures plots the distributions obtained for three different beams emitted from within one of the detector pairs (center or off-center) for which the experiments have been carried on. The left columns show distributions for beams with different radial positions whereas the right columns show distributions for beams with different angular orientations. The top figures at each column provide a graphical reference to identify each distribution with the beam from which it has been obtained: the yellow distributions correspond to the beams connecting the centers of the detectors (the beams labeled B1), whereas the red and pink distributions correspond to the maximum angular/radial deviation from this line that a gamma beam can have within the detector limits (the beams labeled B3 and B5). Since each of the Figures 2.8-2.13 shows the distributions for beams emitted from within a same detector pair, all the distributions in a figure should be identical if the radial and angular invariance assumptions of the blurring were correct. However, important differences can be observed among the shape of these distributions. The figures illustrate as well, how difficult is to find a single distribution that gathers the (in many cases conflicting) properties of all the distributions in a single detector tube. For example, in the case of the centred detector pairs (Figures 2.8, 2.10 and 2.12), it is not possible to find a distribution that keeps both the symmetric shape of the distribution of the beam B1 and the oppositely symmetric shapes of the distributions of the beams B3 and B5. Similar incongruencies can be found among the off-center pair distributions. The grey filled areas plotted in the graphs correspond to the crystal distributions proposed by Mumcuoglu et al. (1996) and Qi et al. (1998) to represent the blurring produced by any gamma pair within the detector pair, once the invariance is assumed. These reference distributions are generated by photons striking the pair from an in-plane line source oriented normal to, and at the center of the detector pair (the grey line shown in Figure 2.9 for the center line case). This seems to be a good approach, since the reference distribution contains contributions from beams emitted from all the radial positions and with all the angular orientations. However, the differences between this distribution and the distributions of the

pairs it is supposed to represent, become evident in the figures.

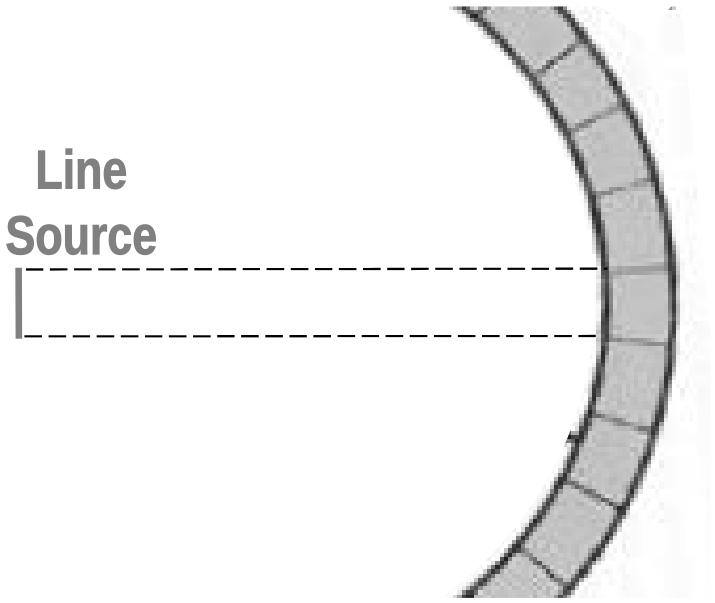

Figure 2.9: In-plane line source used to obtain the reference distributions for the center line.

The experimental results suggest that all the gamma pairs confined to a given detector pair do not share at all the statistical distribution of the LORs in which they can be eventually detected. This confirms that the radial and angular invariance of the penetration and the detector scatter should not to be accepted. It has to be noted, however, that among the three scanners that have been simulated, the microPET scanner shows the maximum blurring invariance levels. It can be checked that the KL-divergences values of Tables 2.2 and 2.3 are rather lower that the values obtained for the A-PET and YAP scanner and that the distributions in Figures 2.10 and 2.11 are more uniform than their counterparts for the other scanners. It could be expected therefore that the good results achieved by the factored schemes in the works of Qi et al. (1998) and Mumcuoglu et al. (1996) for the microPET scanner were not achieved for reconstructions from the A-PET and the YAP data.

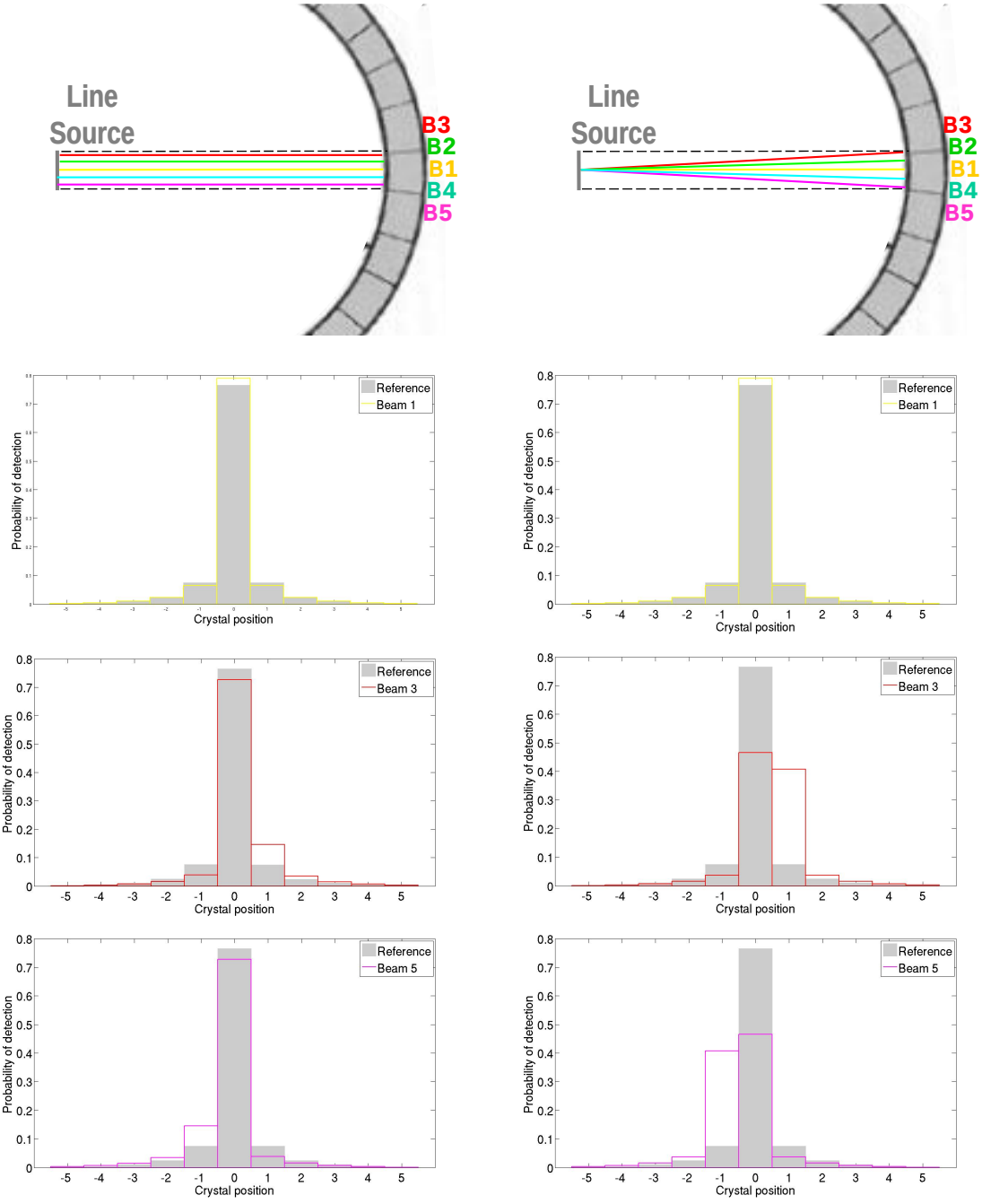

Figure 2.8: Crystal distributions obtained for the center LOR of the A-PET scanner.

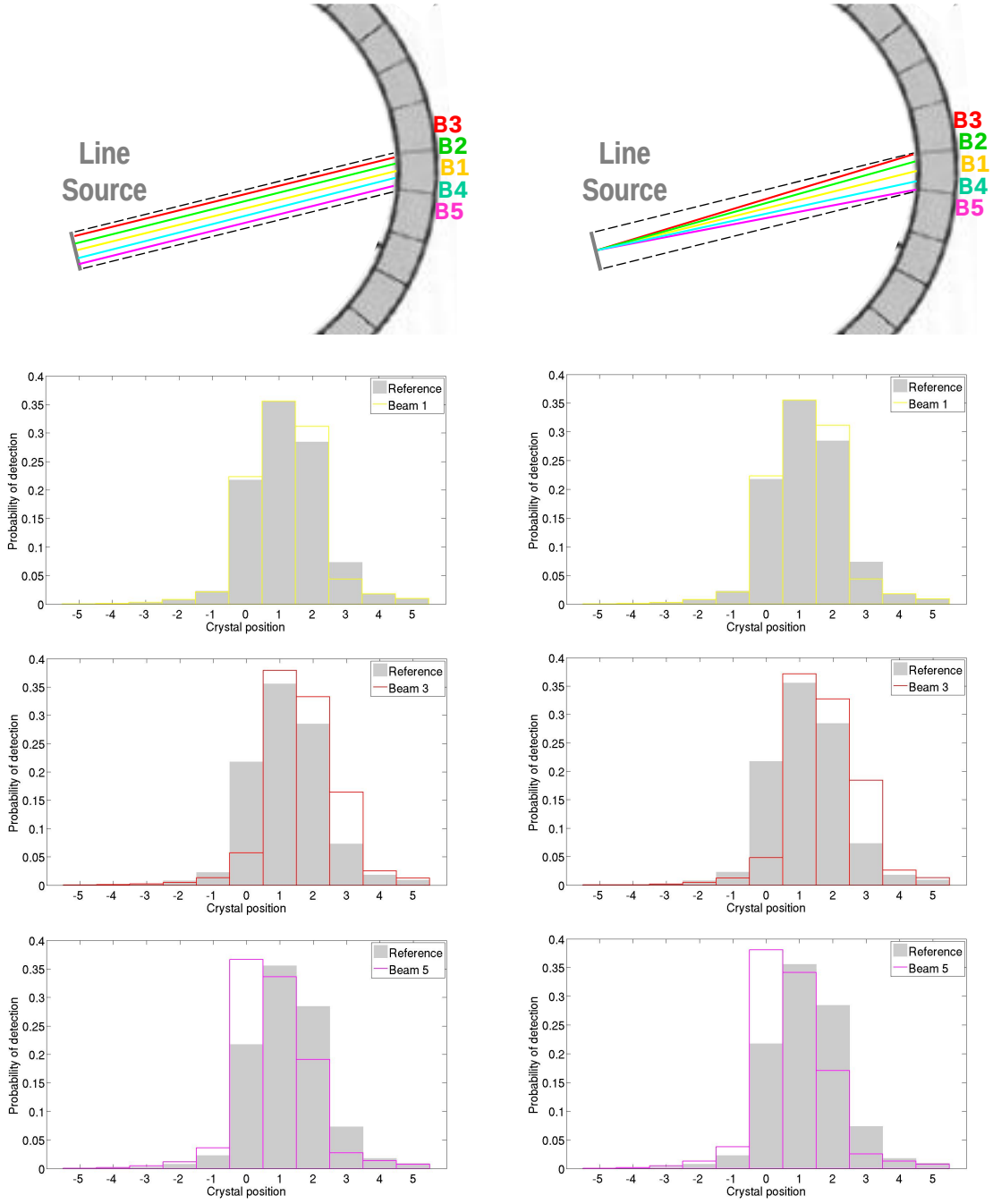

Figure 2.9: Crystal distributions obtained for the off-center LOR of the A-PET scanner.

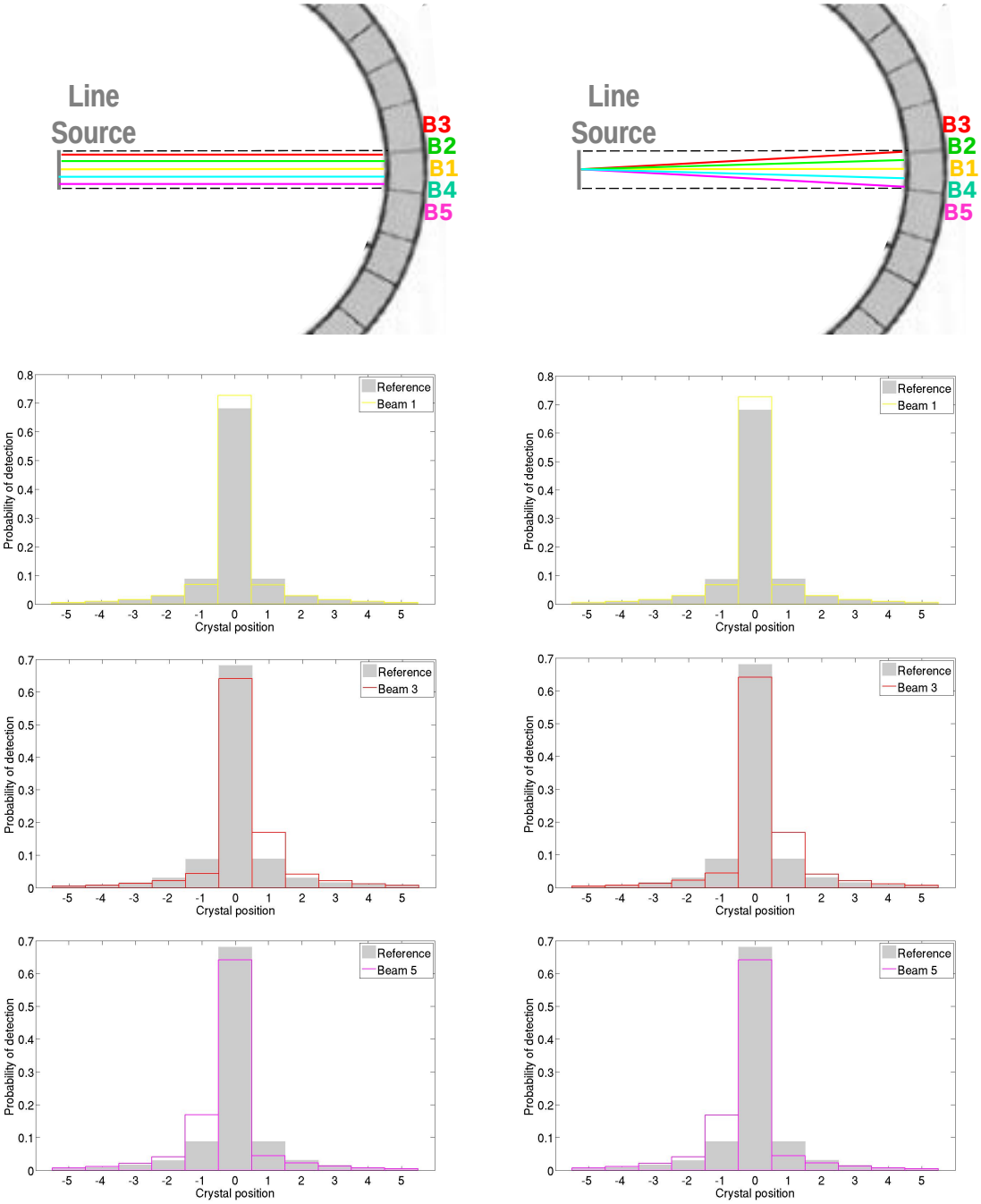

Figure 2.10: Crystal distributions obtained for the center LOR of the microPET scanner.

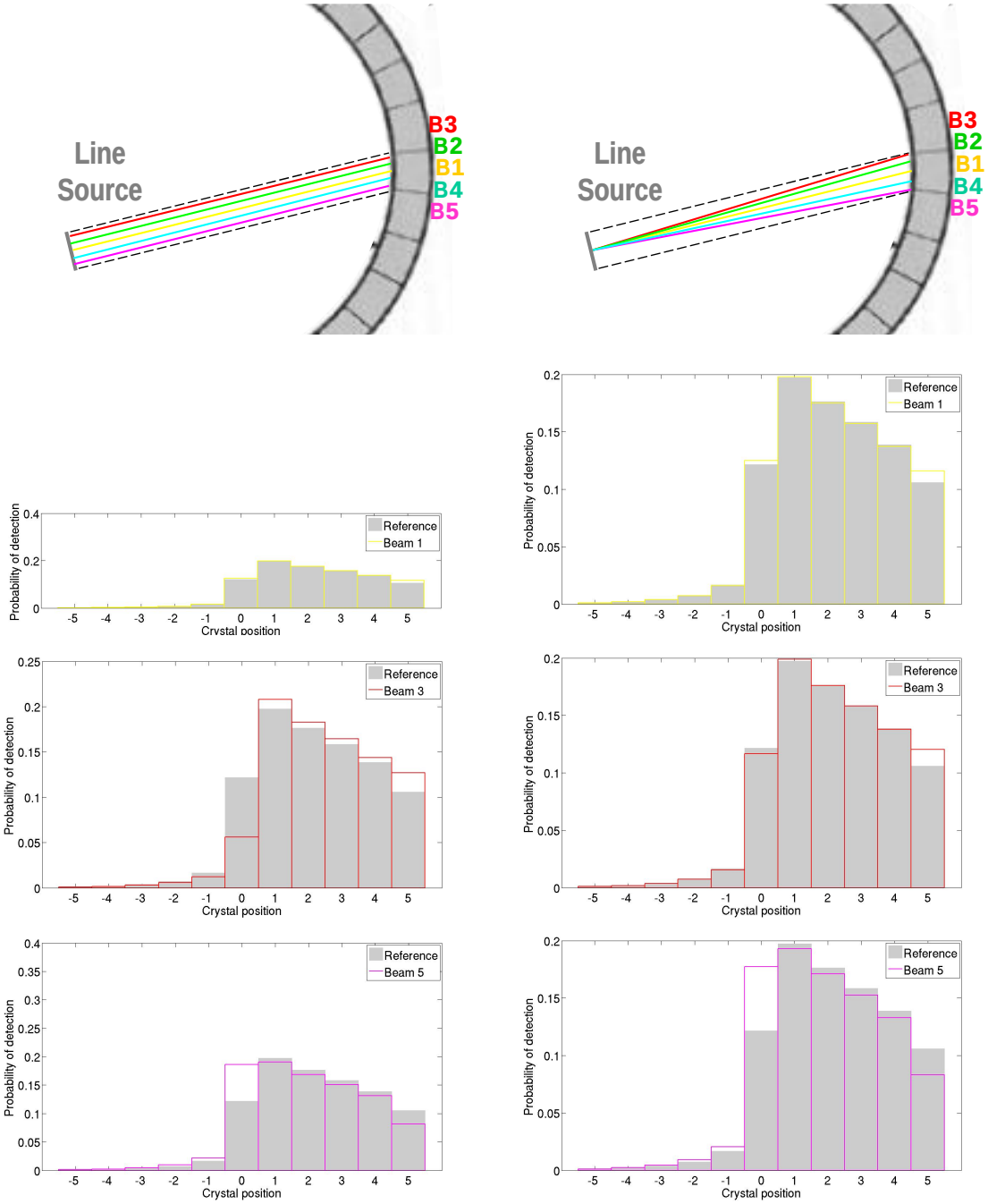

Figure 2.11: Crystal distributions obtained for the off-center LOR of the microPET scanner.

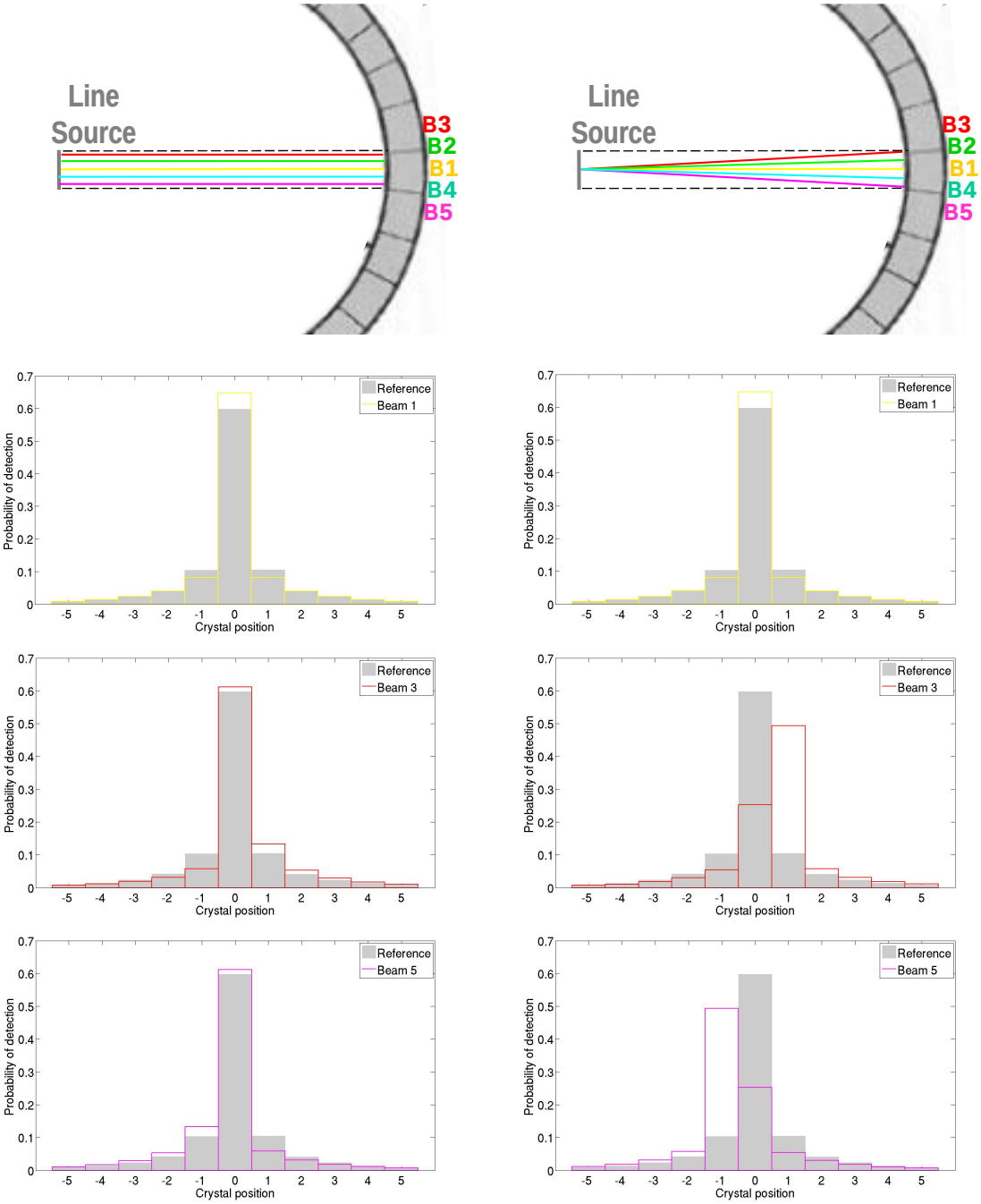

Figure 2.12: Crystal distributions obtained for the center LOR of the YAP-S scanner.

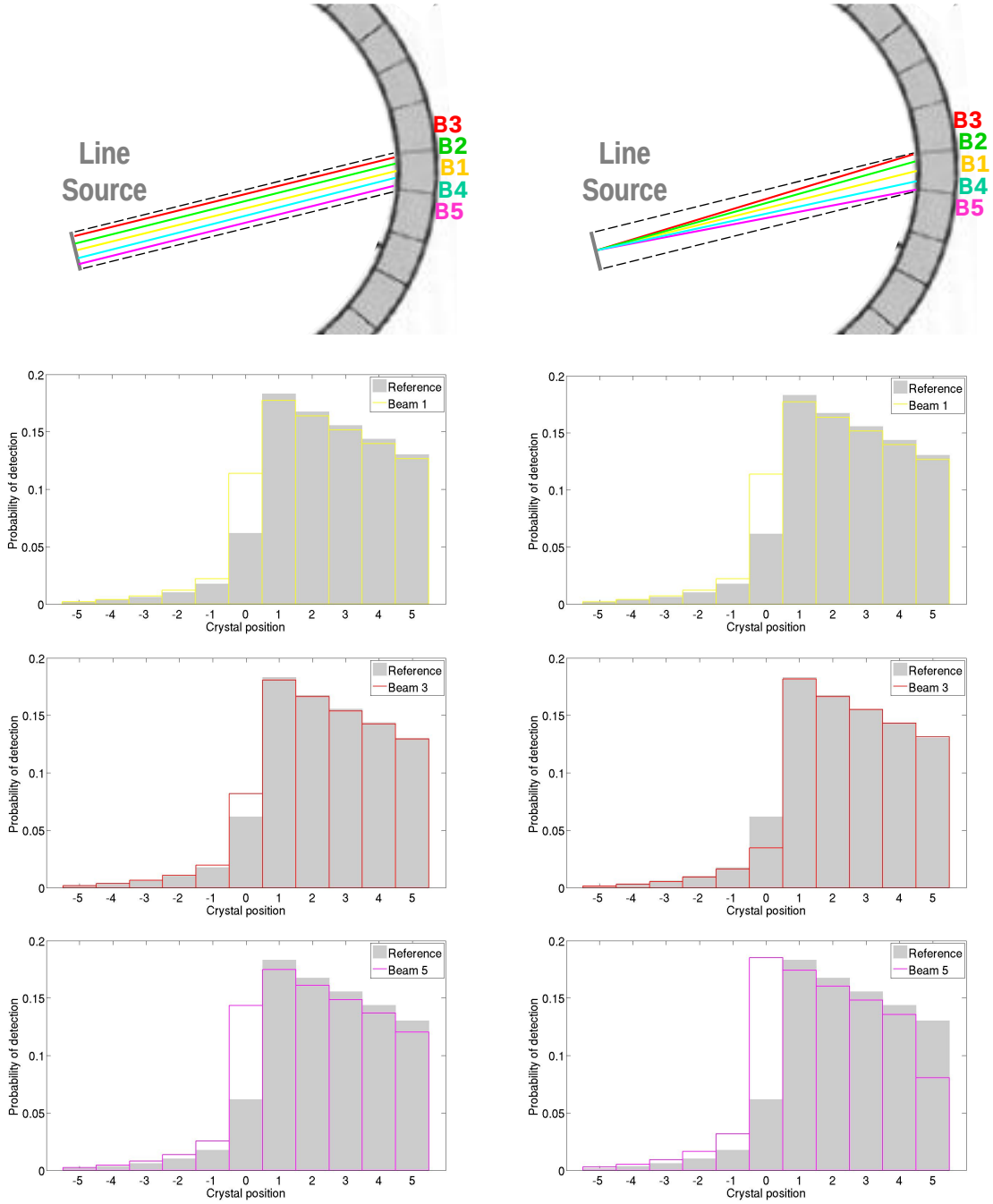

Figure 2.13: Crystal distributions obtained for the off-center LOR of the YAP-S scanner.

Basis functions

Two more assumptions have been done to definitely factorize the integral approach. These assumptions concern the properties of the basis functions used to represent the continuous radiotracer distribution. The first of them (pass from Eq (2.22) to Eq (2.23)), states that the annihilation points can be grouped according to the basis function they belong to. Clearly, such grouping can be done just when no overlapping between the basis functions that conform the radiotracer distribution exists. In principle, this is not such a restrictive condition, since the voxels, which constitute the most popular type of basis function used in PET reconstruction (Qi2006), meet this condition. However, it has to be noted that this assumption closes a door to other types of basis functions such as blobs or splines, that have shown to have certain advantages over the voxels in other reconstruction environments (Marabini et al. (1998)).

Once limited to the reconstruction with voxels, the second assumption (pass from Eq (2.23) to Eq (2.24)) states that the term $p_{geo}(r, d_i)$ is constant within the limits of the voxel b_j. In statistical terms, this means that the geometrical probability that an emission from r reaches the detector d_i is the same for all the points r that conform b_j. The validity of this assumption depends clearly on the voxel size, since the differences among the solid angles subtended by the points of the voxel into the detector d_i will be larger as the distances among these points increase. Nowadays there is a clear tendency in the small animal environment towards the reconstruction with decreasingly voxel sizes, based on the search for covering small imaging details (Shakirin et al. (2008)). Consequently, this assumption is not expected to have a great influence in the quality of the reconstructions.

Based on the current reconstruction tendencies, it can be said that the two assumptions concerning the basis functions are not expected to trade the accuracy of the model. However, they certainly limit the flexibility of the reconstructions as they restrict the type and size of basis functions that can be used.

Storage

Once the factored scheme has been obtained as a simplification of the integral scheme, it has been stated at the end of Subsection 2.5.1 that the works based in the factorization usually rely on some assumptions about the model in order to achieve a practical storage of the Geometrical, Blurring and Positron range matrices:

- Regarding the Geometrical matrix, the symmetries in which its size reduction is based are well backed up by the works of Chen et al. (1991) and Johnson et al. (1994).
- Concerning the Blurring matrix, several strategies have been followed, whose validity is justified in the following:
  - Concerning the truncation of the $p(d_i, d)$ terms to a few neighboring elements d of d_i, the number of affected elements is set according to a prefixed selected window size that eliminates just the $p(d_i, d)$ terms below a certain percentage of the maximum value. It is not therefore expected to have a great influence in the quality of the results.
  - However, the limit case in which the blurring is completely ignored along the axial or azimuthal direction is not such a reasonable assumption since, as shown by Alessio et al. (2006), each LOR d_i "blurrs"' in all three dimensions. Even if the work by Qi et al. (1998) provides justifications for these simplification in the projection domain, the effect of these simplifications in the reconstructions has never been checked.
  - The assumption of rotational symmetry would be true for perfect ring scanner geometries, but not in modern PET scanners that use block detectors and have a polygonal shape. As it has been proved by Tohme and Qi (2009), in these cases the symmetry is only true on the block level and the variations that may occur due to the block effects (e.g, photons scattered between a pair of adjacent detectors in two adjacent blocks do not behave the same way as those scattered between adjacent detectors in the same block) should be considered. The effect or the block structure is particularly significant for small animal pet scanners, which have a small ring diameter (Tohme and Qi

(2009)).

  - The use of the $p(d_i, d)$ terms obtained in the central transaxial plane for all other rings is acceptable for scanners with small axial field-of-view, like the microPET (4.9 cm), but it is not appropriate for scanners with larger axial length, like the A-PET scanner (12 cm). The effect of this assumption in the images should therefore be checked.

- As for the $N \times N$ positron range matrix, ignoring the effect is clearly not a suitable option in all cases. As stated by Cal-González et al. (2009), recent developments in detector technology have reduced crystal size and now there are small animal PET scanners with near $1mm$ spatial resolution, which is comparable to positron range of most commonly used isotopes. Being the positron range an object dependent effect, no sparsity, symmetries or invariance assumptions can be exploited in order to reduce the resources that the storage of a huge $N \times N$ matrix requires. The on-the-fly approach prevails, therefore, over an experimental precomputation. On the other hand, whether the analytical approach followed by Rahmim et al. (2008) is a good option of not, is a question out of the scope of this work, since, at it has been mentioned, the positron range is an effect that still needs to be further studied.

2.6 A mixed scheme

A new mixed scheme for the combination of the separately modeled effects of the PET data acquisition process is introduced in this section. The new scheme is a compromise between the accuracy of the (otherwise impractical) integral scheme introduced in Section 2.4 and the efficiency of the factored schemes, which, as shown in the previous subsections, are based on several simplifications of the data formation process. In order to reach such compromise, the new scheme will be obtained, as the factored approach, as a simplification of the integral model introduced in Section 2.4, but now based just on the assumptions that have found to be acceptable in Section 2.5. The development of the mixed scheme starts, therefore, on the expression for the integral scheme, given by:

$$p(b,d) = \int_{\mathbf{r_o}} v_b(\mathbf{r}_0) \left[\int_r f_{\mathbf{r_0}}(\mathbf{r}) \left[\int_\gamma \left[\int_\varphi f(\varphi,\gamma) \left[\int_{\theta_1} f(\theta_1) \left[\int_{\theta_2} f(\theta_2) p_{att}(\mathbf{r},\gamma,\varphi,\theta_1,\theta_2) \right.\right.\right.\right.\right.$$

$$\left.\left.\left.\left.\left. p_{det\_sens}(\mathbf{r},\gamma,\varphi,\theta_1,\theta_2) p_{pos}(\mathbf{r},\gamma,\varphi,\theta_1,\theta_2,d) d\theta_2 \right] d\theta_1 \right] d\varphi \right] d\gamma \right] d\mathbf{r} \right] d\mathbf{r_0} \quad (2.30)$$

The first modification that has been done to factorize this expression has been to extract the detector efficiency $p_{det\_sens}(\mathbf{r},\gamma,\varphi,\theta_1,\theta_2)$ and reconsider it in the form of a measured normalization factor for each LOR. However, in Subsection 2.5.2 it has been found convenient to let the probability of interaction of the photons with the scintillators inside the integral and to factorize the rest of effects related to the efficiency of the detection, grouped in a term called $p_{cal}(\mathbf{r},\gamma,\varphi,\theta_1,\theta_2)$. The resulting expression after these considerations is:

$$p(b,d) = p_{cal}(d) \int_{\mathbf{r_o}} v_b(\mathbf{r}_0) \left[\int_r f_{\mathbf{r_0}}(\mathbf{r}) \left[\int_\gamma \left[\int_\varphi f(\varphi,\gamma) \left[\int_{\theta_1} f(\theta_1) \left[\int_{\theta_2} f(\theta_2) p_{att}(\mathbf{r},\gamma,\varphi,\theta_1,\theta_2) \right.\right.\right.\right.\right.$$

$$\left.\left.\left.\left.\left. p_{int}(\mathbf{r},\gamma,\varphi,\theta_1,\theta_2) p_{pos}(\mathbf{r},\gamma,\varphi,\theta_1,\theta_2,d) d\theta_2 \right] d\theta_1 \right] d\varphi \right] d\gamma \right] d\mathbf{r} \right] d\mathbf{r_0} \quad (2.31)$$

where, as stated in Section 2.4.6:

$$p_{int}(\mathbf{r},\gamma,\varphi,\theta_1,\theta_2) = (1 - e^{\mu L_{sci_1}(\mathbf{r},\gamma,\varphi,\theta_1,\theta_2)})(1 - e^{\mu L_{sci_2}(\mathbf{r},\gamma,\varphi,\theta_1,\theta_2)}) \quad (2.32)$$

being L_{sci_i} $(i = 1, 2)$ the lengths that the photons emitted from $\mathbf{r}$ intersect at each scintillator in the direction given by $(\varphi,\gamma,\theta_1,\theta_2)$, and μ the linear attenuation coefficient of the scintillator.

Next, as has been done in Subsection 2.5.1, and provided that it does not constitute a modification of the integral model, the gamma pairs emitted from the annihilating point $\mathbf{r}$ can be grouped according to the LOR d_i their photons reach. Reordering the terms after this rearrangement leads to:

$$p(b,d) = p_{cal}(d)\sum_{i=1}^{M}\left\{\int_{\mathbf{r_o}} v_b(\mathbf{r}_0)\left[\int_r f_{\mathbf{r_0}}(\mathbf{r})\left[\int_{\gamma_i}\left[\int_{\varphi_i} f(\varphi,\gamma)\left[\int_{\theta_1} f(\theta_1)\left[\int_{\theta_2} f(\theta_2) p_{att}(\mathbf{r},\gamma,\varphi,\theta_1,\theta_2)\right.\right.\right.\right.\right.\right.$$

$$\left.\left.\left.\left.\left. p_{int}(\mathbf{r},\gamma,\varphi,\theta_1,\theta_2) p_{pos}(\mathbf{r},\gamma,\varphi,\theta_1,\theta_2,d) d\theta_2\right] d\theta_1\right] d\varphi\right] d\gamma\right] d\mathbf{r}\right] d\mathbf{r_0}\right\} \quad (2.33)$$

Then, according to the discussion in Subsection 2.5.2, the attenuation term can be factored for each LOR d_i without serious consequences on the model:

$$p(b,d) = p_{cal}(d)\sum_{i=1}^{M}\left\{p_{att}(d_i)\int_{\mathbf{r_o}} v_b(\mathbf{r}_0)\left[\int_r f_{\mathbf{r_0}}(\mathbf{r})\left[\int_{\gamma_i}\left[\int_{\varphi_i} f(\varphi,\gamma)\left[\int_{\theta_1} f(\theta_1)\left[\int_{\theta_2} f(\theta_2)\right.\right.\right.\right.\right.\right.$$

$$\left.\left.\left.\left.\left. p_{int}(\mathbf{r},\gamma,\varphi,\theta_1,\theta_2) p_{pos}(\mathbf{r},\gamma,\varphi,\theta_1,\theta_2,d) d\theta_2\right] d\theta_1\right] d\varphi\right] d\gamma\right] d\mathbf{r}\right] d\mathbf{r_0}\right\} \quad (2.34)$$

At this point, the factored models group the non-collinearity, crystal penetration and detector scatter effects in a single term, $p_{blurr}(\mathbf{r},\gamma,\varphi,d)$ (see Eq (2.35)) and pull it outside the integrals in $\mathbf{r}$,γ and φ, removing its variability with these parametres within each detector pair. Things have to be done differently in the new hybrid model. On the one hand, the grouping of effects necessarily entails the additional incorporation of the probability of interaction term $p_{int}(\mathbf{r},\gamma,\varphi,\theta_1,\theta_2)$. This term can't be pulled out the integrals in θ_1 and θ_2, and hence it can't be separated from the rest of effects. On the other hand, as has been concluded in Subsection 2.5.2, the penetration and detector scatter should be kept within the integrals, in order to account for their variability with $\mathbf{r}$,γ and φ. A particular model for the blurring effects is thus needed, that accounts for the probability of interaction of the photons and that considers the variability of the penetration and the detector scatter with $\mathbf{r}$, γ and φ within each tube of detection. The approach used by Moehrs et al. (2008), Rahmim et al. (2008) and Iriarte et al. (2009) to model the penetration and detector scatter meets these requirements. According to these works, the probability that a pair of photons that interact with the detectors gives place to a detection in d can be expressed as:

$$p_{int}(\mathbf{r},\gamma,\varphi,\theta_1,\theta_2)p_{pos}(\mathbf{r},\gamma,\varphi,\theta_1,\theta_2,d) = p(d_1)p(d_2) =$$

$$\left(\int_0^{L_1} p_{mult}(\mathbf{r},\gamma,\varphi,\theta_1,\theta_2,l,d_1)f(l)dl\right)\left(\int_0^{L_2} p_{mult}(\mathbf{r},\gamma,\varphi,\theta_1,\theta_2,l,d_2)f(l)dl\right) \quad (2.35)$$

In this expression, the probability of detection in d has first been decomposed as the individual probabilities of detection of the photons in d_1 and d_2, being these the two crystals that define d. Then, in each integral the variable l covers the length the photons enter into the scintillators in the direction given by φ, γ, θ_1 and θ_2, accounting for the crystal penetration. As shown in Figure 2.10, L_1 and L_2 stand for the maximum value of these lengths in the detectors containing d_1 and d_2 respectively. $f(l)$ stands for the likelihood that the first interaction of a $511keV$ photon occurs at each l, in account for the probability of interaction. This likelihood is modeled with an exponential distribution:

$$f(l) = \mu \mathrm{e}^{-\mu \mathrm{l}} \quad (2.36)$$

that integrated over the intersection length with the crystal gives place to the expression for the probability of interaction that has been given in Eq (2.8).

The terms $p_{mult}(\mathbf{r},\gamma,\varphi,\theta_1,\theta_2,l,d_k)$ $(k = 1,2)$ account for the detector scatter. Each of them stands for the probability that a gamma photon emitted from r in the direction defined by φ, γ, θ_1 and θ_2, that interacts after traveling a distance l within the scintillator, is finally positioned at d_k. The work by Iriarte et al. (2009) models this effect with a Gaussian distribution, whose standard deviation varies with l and is estimated with Monte Carlo simulations. The works by Moehrs et al. (2008) and Rahmim et al. (2008) estimate the distributions directly from Monte Carlo simulations.

Substituting Eq (2.35) in Eq (2.34) leads to:

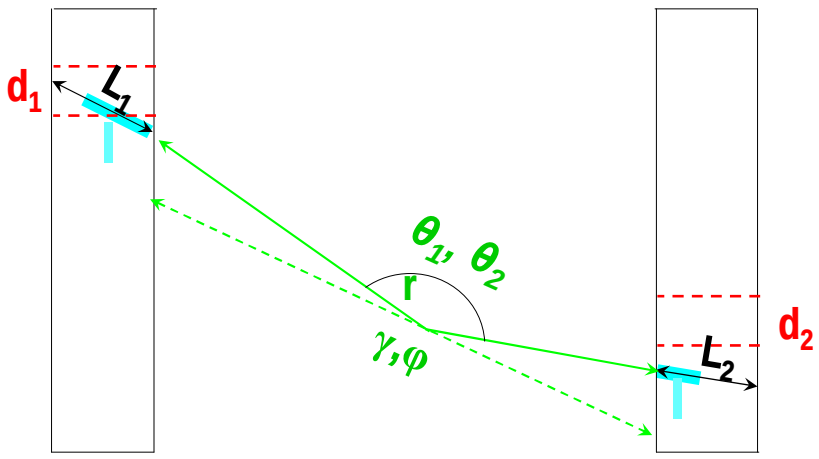

Figure 2.10: L_1 and L_2 stand for the intersections of the photons paths with the detectors containing d_1 and d_2 respectively. The integration variable l (cyan line) covers these lengths.

$$
\begin{aligned}
p(b,d) \;=\; & p_{cal}(d)\sum_{i=1}^{M}\Bigg\{p_{att}(d_i)\int_{\mathbf{r_o}} v_b(\mathbf{r}_0)\left[\int_r f_{\mathbf{r_0}}(\mathbf{r})\left[\int_{\gamma_i}\left[\int_{\varphi_i} f(\varphi,\gamma)\left[\int_{\theta_1} f(\theta_1)\left[\int_{\theta_2} f(\theta_2)\right.\right.\right.\right.\right. \\
& \left.\left.\left.\left.\left.\left(\int_0^{L_1} p_{mult}(\mathbf{r},\gamma,\varphi,\theta_1,\theta_2,l,d_1)f(l)dl\right)\left(\int_0^{L_2} p_{mult}(\mathbf{r},\gamma,\varphi,\theta_1,\theta_2,l,d_2)f(l)dl\right)\right.\right.\right.\right.\right. \\
& \left.\left.\left.\left.\left.d\theta_2\right]\,d\theta_1\right]\,d\varphi\right]\,d\gamma\right]\,d\mathbf{r}\right]\,d\mathbf{r_0}\Bigg\}
\end{aligned}
\tag{2.37}
$$

In order to highlight the fact that the new hybrid model explicitely considers the interdependence of the blurring effects (non-collinearity, crystal penetration and detector scatter) with the geometry, these effects will be expressed jointly through the following new term:

$$p_{geo\_blurr}(\mathbf{r}, d_i, d) = \int_{\gamma_i} \left[\int_{\varphi_i} f(\varphi, \gamma) \left[\int_{\theta_1} f(\theta_1) \left[\int_{\theta_2} f(\theta_2) \left(\int_0^{L_1} p_{mult}(\mathbf{r}, \gamma, \varphi, \theta_1, \theta_2, l, d_1) f(l) dl \right) \right. \right. \right.$$
$$\left. \left. \left. \left(\int_0^{L_2} p_{mult}(\mathbf{r}, \gamma, \varphi, \theta_1, \theta_2, l, d_2) f(l) dl \right) d\theta_2 \right] d\theta_1 \right] d\varphi \right] d\gamma \quad (2.38)$$

$p_{geo\_blurr}(\mathbf{r}, d_i, d)$ stands for the probability that an annihilation in r whose photons reach the detector pair d_i, leads to a coincidence event positioned at d, accounting for the non-collinearity, penetration and detector scatter effects. Actually, by modifying the limits of integration γ_i and φ_i, the right side of Eq (2.38) can be used to compute this probability for any range of gamma pairs emitted from r (i.e., not just those pairs reaching d_i). With the new notation, the expression for the system matrix becomes:

$$p(b, d) = p_{cal}(d) \sum_{i=1}^{M} \left\{ p_{att}(d_i) \int_{\mathbf{r_o}} v_b(\mathbf{r}_0) \left[\int_r f_{\mathbf{r_0}}(\mathbf{r}) p_{geo\_blurr}(\mathbf{r}, d_i, d) d\mathbf{r} \right] d\mathbf{r_0} \right\} \quad (2.39)$$

Finally, if the assumption of working with non-overlapping small basis functions is accepted, the same procedure that has been applied to Eq (2.22) can be carried out on Eq (2.39), leading to the definitive expression of the new mixed scheme:

$$p(b, d) = p_{cal}(d) \sum_{i=1}^{M} \left\{ p_{att}(d_i) \sum_{j=1}^{N} \{ p_{geo\_blurr}(b_j, d_i, d) p_{pos}(b, b_j) \} \right\} \quad (2.40)$$

In the new scheme, $p_{pos}(b, b_j)$ stands again for the probability that a decay from b gives place to an annihilation within b_j, due to the effect of the positron range. The term $p_{geo\_blurr}(\mathbf{r}, d_i, d)$ has been renamed $p_{geo\_blurr}(b_j, d_i, d)$ because under the mentioned assumptions about the basis

functions, its behavior has been stated to be the same for any point $\mathbf{r}$ within the basis function b_j. The generalization from point to basis function can be extrapolated to the $p_{mult}(\mathbf{r}, \gamma, \varphi, \theta_1, \theta_2, l, d_k)$ terms included in the $p_{geo\_blurr}(b_j, d_i, d)$ expression, and consequently these terms will be referred to as $p_{mult}(b_j, \gamma, \varphi, \theta_1, \theta_2, l, d_k)$ in the following.

Eq (2.40) computes the system matrix terms for the new mixed scheme. As has been mentioned, this scheme intends to be a tradeoff between the accuracy of the integral and the simplicity and efficiency of the traditional factored schemes. Based on the conclusions of Subsection 2.5.2 the fidelity to the data formation process has been ensured in each step between the integral model in Eq (2.30) and the new scheme in Eq (2.40), while keeping the factored structures in the cases where it does not compromise the accuracy of the model.

2.7 Implementation

The new hybrid scheme introduced in Section 2.6 has been applied to the system matrix calculation of a commercial PET camera. In the next section, the reconstructions obtained with the newly introduced model will be compared with those provided by previous existing models. Previously, this section deals with the characterization of the camera for which the system model has been obtained (Subsection 2.7.1) and the details on the system matrix implementation (Subsection 2.7.2).

2.7.1 PET camera

The equipment that has been simulated in this study is an A-PET scanner. This device is composed of 14.456 $2 \times 2 \times 10$ mm LYSO crystals individually coupled (i.e., without forming blocks) with a 2.3 mm pitch in a single annular lightguide. Further specifications can be found in Surti et al. (2005).

2.7.2 System matrix

The computation of each system matrix term using Eq (2.40) passes through the individual knowledge of $p_{cal}(d)$, $p_{att}(d_i)$, $p_{geo\_blurr}(b_j, d_i, d)$ and $p_{pos}(b, b_j)$ for any combination of b, b_j, d and d_i. The terms $p_{cal}(d)$, $p_{att}(d_i)$ and $p_{pos}(b, b_j)$ keep the meaning they had in the factored schemes and the sparse structures proposed by the factored approaches to store them can be thus kept. Either previous or new methodologies can be used to model each of these effects, since the scheme allows for the individual modification of the models without altering the rest of the components of the matrix.

The computational challenge of the new scheme is the computation of the $p_{geo\_blurr}(b_j, d_i, d)$ terms given by Eq (2.38), that explicitely consider the interdependence of the blurring with the geometry. The combination of both factors leads to a loss of the sparsity of the new term (as compared with the factorization of the effects) that increases considerably the memory requirements needed for its storage. Qi et al. (1998) calculate an increase by a factor of three, but it must be noted that it is an underestimation, based on several spatially invariance assumptions made to store the blurring component (mentioned at the end of Subsection 2.5.2).

Since the precomputation of $p_{geo\_blurr}(b_j, d_i, d)$ seems not to be a plausible option, its on-the-fly computation is imposed. The expression for $p_{geo\_blurr}(b_j, d_i, d)$ as given by Eq (2.38) is a four dimensional integral that cannot be analytically expressed in a closed form and has to be calculated by means of numerical integration. Since this integration has to be repeatedly solved at reconstruction time, several accelerating techniques have been used in order speed up the reconstructions:

1. First of all, the whole Eq (2.40) has been reexpressed to achieve a combination of the geometry and the blurring effects more convenient for its on-the-fly calculation. The first step to obtain the new expression is to substitute in Eq (2.40) the expression of $p_{geo\_blurr}(b_j, d_i, d)$ given by Eq (2.38):

$$
\begin{aligned}
p(b,d) \;=\; & p_{cal}(d)\sum_{i=1}^{M}\Bigg\{p_{att}(d_i)\sum_{j=1}^{N}\Bigg\{\Bigg[\int_{\gamma_i}\Bigg[\int_{\varphi_i} f(\varphi,\gamma)\Bigg[\int_{\theta_1} f(\theta_1)\Bigg[\int_{\theta_2} f(\theta_2) \\
& \left(\int_0^{L_1} p_{mult}(b_j,\gamma,\varphi,\theta_1,\theta_2,l,d_1)f(l)dl\right)\left(\int_0^{L_2} p_{mult}(b_j,\gamma,\varphi,\theta_1,\theta_2,l,d_2)f(l)dl\right) \\
& d\theta_2\Bigg]\, d\theta_1\Bigg]\, d\varphi\Bigg]\, d\gamma\Bigg]\, p_{pos}(b,b_j)\Bigg\}\Bigg\}
\end{aligned}
\tag{2.41}
$$

the summations and integrals can now be rearranged and the term $p_{att}(d_i)$ can be put inside the integrals in γ_i and φ_i:

$$
\begin{aligned}
p(b,d) \;=\; & p_{cal}(d)\sum_{j=1}^{N}\Bigg\{\sum_{i=1}^{M}\Bigg\{\Bigg[\int_{\gamma_i}\Bigg[\int_{\varphi_i} p_{att}(d_i)f(\varphi,\gamma)\Bigg[\int_{\theta_1} f(\theta_1)\Bigg[\int_{\theta_2} f(\theta_2) \\
& \left(\int_0^{L_1} p_{mult}(b_j,\gamma,\varphi,\theta_1,\theta_2,l,d_1)f(l)dl\right)\left(\int_0^{L_2} p_{mult}(b_j,\gamma,\varphi,\theta_1,\theta_2,l,d_2)f(l)dl\right) \\
& d\theta_2\Bigg]\, d\theta_1\Bigg]\, d\varphi\Bigg]\, d\gamma\Bigg]\, p_{pos}(b,b_j)\Bigg\}\Bigg\}
\end{aligned}
\tag{2.42}
$$

The combination of sums $\sum_{i=1}^{M}\int_{\gamma_i}\int_{\varphi_i}$ entails an artificial grouping of the gamma pairs emitted from b_j, as a function of the detector pair they reach. This grouping, which has been performed for demonstration purposes, can now be undone for a more efficient implementation of the system matrix:

$$
\begin{aligned}
p(b,d) \;=\; & p_{cal}(d)\sum_{j=1}^{N}\Bigg\{\Bigg[\int_{\gamma}\Bigg[\int_{\varphi} p_{att}(d_i(b_j,\gamma,\varphi)f(\varphi,\gamma)\Bigg[\int_{\theta_1} f(\theta_1)\Bigg[\int_{\theta_2} f(\theta_2) \\
& \left(\int_0^{L_1} p_{mult}(b_j,\gamma,\varphi,\theta_1,\theta_2,l,d_1)f(l)dl\right)\left(\int_0^{L_2} p_{mult}(b_j,\gamma,\varphi,\theta_1,\theta_2,l,d_2)f(l)dl\right) \\
& d\theta_2\Bigg]\, d\theta_1\Bigg]\, d\varphi\Bigg]\, d\gamma\Bigg]\, p_{pos}(b,b_j)\Bigg\}
\end{aligned}
\tag{2.43}
$$

The angular limits γ, φ now cover all the gamma pairs emitted from b_j (as it has been mentioned in Subsection 2.4.3, these limits can be reduced to account just for those pairs reaching the detector at a neighborhood of d). The attenuation term $p_{att}(d_i)$ has been renamed as $p_{att}(d_i(b_j,\gamma,\varphi))$, since it is still the same function of the discrete detectors the gamma pair reaches, which are fully defined by the variables b_j, γ and φ.

The original expression provided by Eq (2.40) is the result of a development in which it wanted to be shown how the new scheme is an improvement of the factored approach and has had, therefore an important role for demonstration purposes. Moreover, it would still be the appropriated expression in case that the $p_{geo\_blurr}(b_j,d_i,d)$ terms were needed to be precomputed and stored. However, the precomputation option has been discarded in this work. The new expression in Eq (2.43) is more appropriate for the on-the-fly computation of the conjoint geometrical and blurring effects since just one four-dimensional numerical integral has to be solved, instead of the M integrals that the implementation of Eq (2.40) involves.

2. As has been done for the $p_{att}(d_i(b_j,\gamma,\varphi))$ terms, the values for the distributions $f(\varphi,\gamma)$, $f(\theta_1)$, $f(\theta_2)$, $f(l)$ and $p_{mult}(\mathbf{r},\gamma,\varphi,\theta_1,\theta_2,l,d_k)$ that have to be calculated each time the numerical integration is computed, have been discretized and stored in look-up tables. An effort

has been done to fit these tables in RAM, avoiding thus costly disk access. This constraint does not pose a problem for $f(\varphi,\gamma)$, $f(\theta_1)$, $f(\theta_2)$ and $f(l)$, since they are unidimensional distributions on a bounded domain, for which a fine discretization does not require high storage needs.

The discretization of the seven dimensional detector scatter terms $p_{mult}(b_j,\gamma,\varphi,\theta_1,\theta_2,l,d_1)$ and $p_{mult}(b_j,\gamma,\varphi,\theta_1,\theta_2,l,d_2)$ is apparently a more challenging task. However, a more in-depth analysis of these terms can reduce the storage requirements to the extent that enables their allocation in the RAM. For a photon emitted from a point $\mathbf{r}$ of b_j (for small basis functions it has been assumed that all their conforming points are equivalent in the model) that propagates along the direction defined by γ, φ, θ_1 and θ_2 and interacts with the scintillator after traveling a distance l within it, the terms $p_{mult}(b_j,\gamma,\varphi,\theta_1,\theta_2,l,d_k)$ $k=1,2$ can be thought as the statistical distribution of the discrete positions d_k in which it can be positioned (i.e., an histogram of assigned crystals d_k for a given photon interaction). Since the positions d_k are already discrete variables in a pixelated device like the Phillips A-PET, the discretization has to be applied to $\mathbf{r}$, γ, φ, θ_1, θ_2 and l. If the depth-independence is accepted, what these four variables define is the position of the first interaction with the scintillator of a photon that enters the scintillator at an angle defined by γ, φ, θ_1 and θ_2. The $p_{mult}(b_j,\gamma,\varphi,\theta_1,\theta_2,l,d_k)$ can be thus reexpressed as a function of these two parametres, as $p_{mult}((x',y',z'),\gamma',\varphi',d_k)$, where (x',y',z') define the the position of the interaction in a crystal relative coordinate system and γ',φ' define the orientation of the photon (see Figure 2.11). If all the crystals are assumed to be identical, the $p_{mult}((x',y',z'),\gamma',\varphi'|d_k)$ distributions can be estimated just for one of the crystals of the arrangement and then applied to all the rest by performing the appropriate translation and/or rotation. In case of block systems, the distributions should be estimated for each crystal element inside a detector block and the results can be applied to the rest of blocks.

The A-PET is under the first assumption, and therefore the range of variation of (x',y',z') is bounded by the reduced crystal dimensions. Given the FOV and scanner dimensions for the

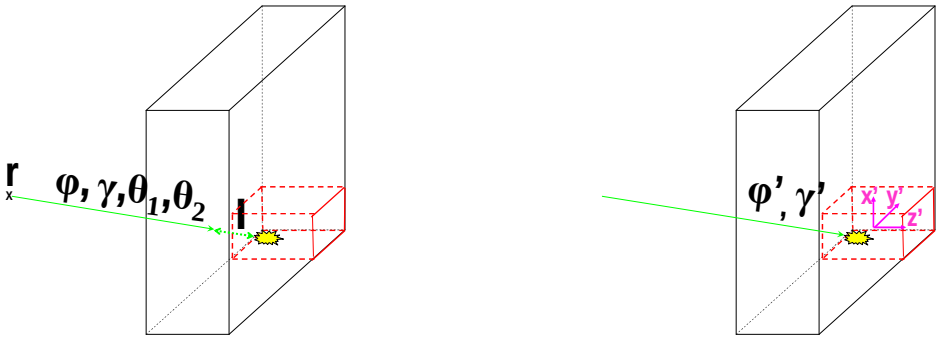

(a) (b)

Figure 2.11: Position of the first interaction as a function of **r**, γ, φ, θ_1, θ_2 and l (a) and as a function of (x', y', z') and ,γ', φ' (b)

A-PET, the maximum incidence angles γ' and φ can be estimated to be below 50°. Moreover, in a scanner with pixelated detectors that shape the light response, the spread in the positioning due to the detector scatter is expected to be rather limited, which allows to truncate the distributions to a few crystal positions d_k. In these conditions, the storage of the detector scatter distributions in RAM becomes apparently feasible.

Nevertheless, the previous works with a similar model of blurring (Moehrs et al. (2008), Rahmim et al. (2008)), achieve further reductions on the storage size of the detector scatter distributions by ignoring their dependency with the (x', y', z') coordinates of the first interaction with the crystal (i.e., considering just the dependency on the pair orientation (γ',φ')). Since no justification for this assumption is provided by these works, an analysis of its reliability has been done in order to determine whether it should be incorporated or not to the model. The GATE Monte Carlo simulator has been used with this purpose.

In order to study the dependency of the distributions with the x' coordinate of the first interaction, a collection of point sources in the central transaxial plane of the FOV, covering half

a pixelated crystal in the tangential direction have been simulated (see two of these sources in Figure 2.12). 511 keV gamma-ray beams normally incident to the detector have been generated from each of the sources. For each generated beam, one million of emissions were simulated and the events generated were positioned using a centroid approach. Since the GATE simulations allow to follow the track of events for each annihilated photon, each detection has been recorded along with the positions of the interactions that preceded it. In this way, the distributions (histograms of the crystal detections) can be obtained as a function of the position of the first interaction with the scintillator (x', y', z'). In order to study the variability along the tangential direction x', the position distributions for the events whose first interaction took place at a fixed DOI (the crystal center, at $z' = 5$, as shown in Figure 2.12) have been compared. Table 2.4 shows the KL divergences among the distributions for interactions at different x' positions. The results obtained for the variability of the distributions with the x' coordinate can be directly extrapolated to the variability with the y' coordinate.

In order to study the variablity along the DOI (radial direction z'), the distributions for the events whose first interaction took place at a fixed tangential position (the crystal center, at $x' = 0$, as shown in Figure 2.13) have been compared. Table 2.5 shows the KL divergences among the distributions obtained for different z' positions of the interaction with the crystal.

In order to measure the variablity of the detector scatter with the photon orientation, several beams have been generated with their gamma rays entering the crystals at different oblique angles γ' ((being $\gamma' = 0$ equal to perpendicular incidence)), but all of them transversing the center of the crystal (two of these beams are shown in Figure 2.14). The distributions for events with first interaction at this point (i.e., the position $x' = 0, z' = 5$ in the crystal system), have been obtained. Table 2.6 shows the KL divergences among these distributions.

Tables 2.4 and 2.5 suggest that remarkable differences exist among the detector scatter distributions obtained along the radial and tangential dimensions of a crystal. Moreover, these differences are comparable to (or even larger than) the differences due to the different photon orientations, given by Table 2.6. For that reason, and provided that it does not compromise

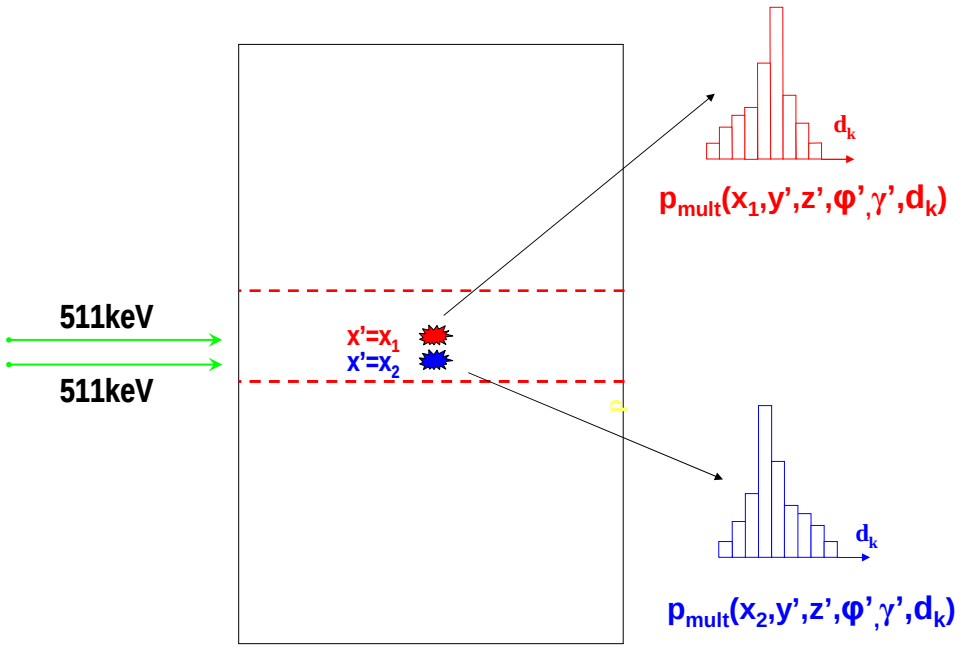

Figure 2.12: Experimental setup to compute the variability of the detector scatter distributions as a function of the x' position of the first interaction with the crystal

x'(mm)	-1.0	-0.5	0.0	0.5	1.0
-1.0	0.0000	0.1903	0.3432	0.5196	0.8526
-0.5	0.1507	0.0000	0.0260	0.0894	0.3674
0.0	0.2495	0.0242	0.0000	0.0242	0.2473
0.5	0.3674	0.0894	0.0250	0.0000	0.1507
1.0	0.8526	0.5196	0.3392	0.1903	0.0000

Table 2.4. KL divergences among distributions for interactions at different x'

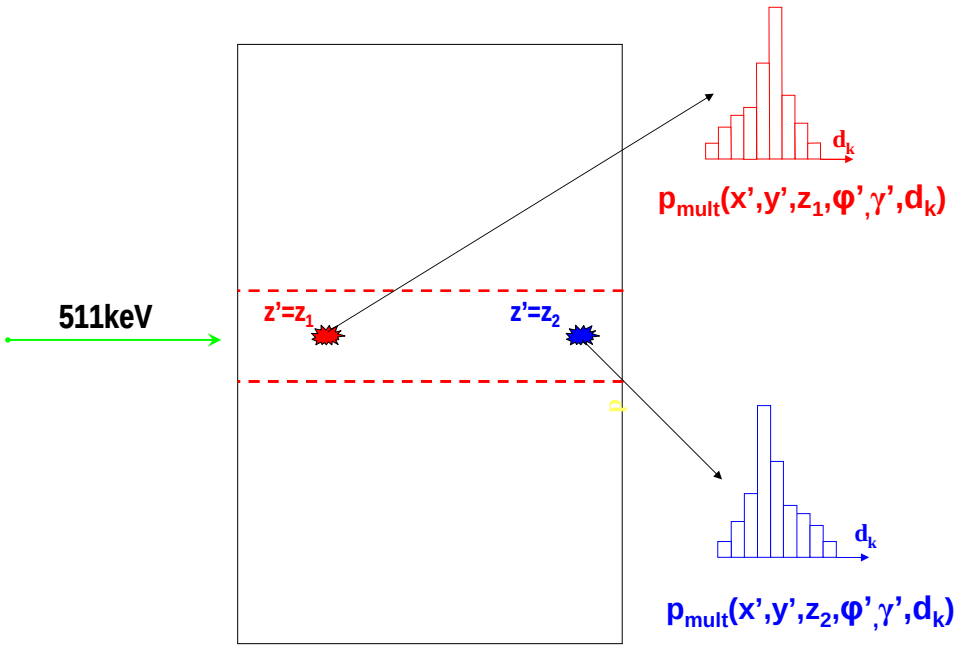

Figure 2.13: Experimental setup to compute the variability of the detector scatter distributions as a function of the z' position of the interaction in the crystal

z'(mm)	-4.0	-2.0	0.0	2.0	4.0
-4.0	0.0000	0.0060	0.0235	0.0875	0.2070
-2.0	0.0043	0.0000	0.00143	0.0650	0.1901
0.0	0.0194	0.0138	0.0000	0.0202	0.0969
2.0	0.0585	0.0494	0.0147	0.0000	0.0364
4.0	0.1443	0.1404	0.0790	0.0371	0.0000

Table 2.5. KL divergences among distributions for interactions at different z'

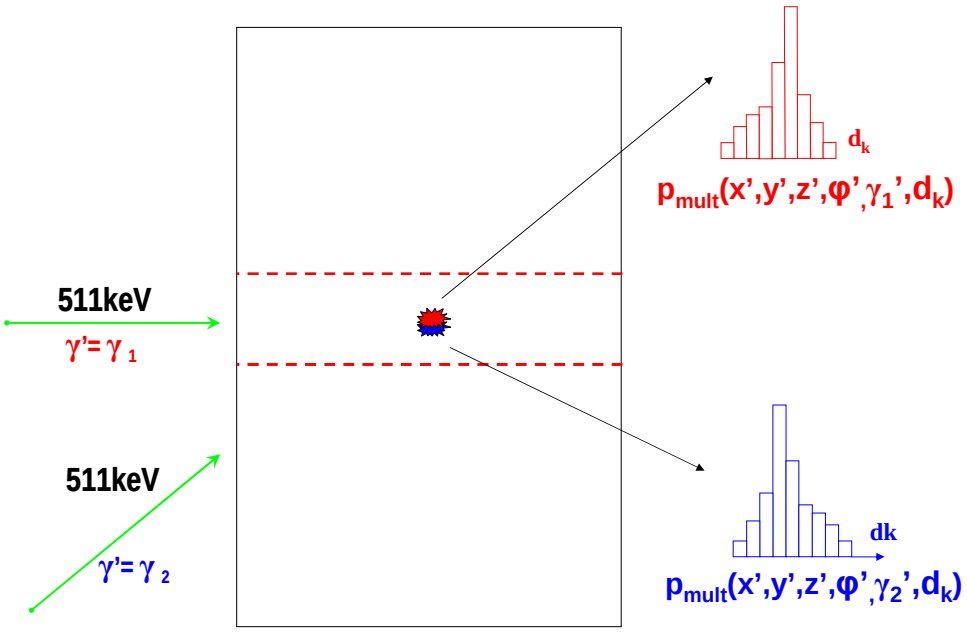

Figure 2.14: Experimental setup to compute the variability of the detector scatter distributions as a function of the angular orientation of the photon leading to the first interaction in the crystal

γ'(deg)	-40	-20	0.0	20	40
-40	0.0000	0.0314	0.2368	0.2504	0.5160
-20	0.0289	0.0000	0.0512	0.1059	0.2316
0.0	0.0963	0.0293	0.0000	0.0245	0.0869
20	0.2316	0.1059	0.0492	0.0000	0.0289
40	0.5160	0.2693	0.1969	0.0314	0.0000

Table 2.6. KL divergences among distributions for interactions with different γ

the efficiency of the approach in terms of storage, it has been decided to precompute and store distributions that take into account the variability of the detector scatter effect along all these dimensions, unlike previous approaches that just consider the angular orientation.

3. Finally, the number of integration points used to approximate each integral of Eq (2.43) has been minimized. The number of points between the integral limits is estimated *ad-hoc* for each integral performed by fixing the distance among integration points, which keeps the precision with which all the integrals are estimated. In order to minimize the number of points without trading the accuracy of the numerical approximation, several arbitrary system matrices have been obtained with a extremely small interpoint distance. These references have been compared with the same matrix obtained using descending degrees of precision (i.e., enlarged interpoint distances). The normalized root-mean-square error ($NRMSE = \frac{\sqrt{\langle\left(x_m - x_c\right)^2\rangle}}{\max(x_m) - \min(x_m)}$, with x_m and x_c being the vectors containing the values of the system matrices being compared) has been used as the comparison measure. The interpoint distance has been chosen to be the maximum distance that keeps the NRMSE value below 10^{-3}

2.8 Evaluation

In this section, the system model that has been developed, implemented and incorporated to an iterative algorithm has been tested with reconstructions from simulated data. Subsection 2.8.1 deals with the mechanisms of the iterative schemes in which the system matrix has been incorporated. The sets of data along with the figures of merit used to evaluate the reconstructions are described in Subsection 2.8.2. Subsections 2.8.3 and 2.8.4 deal with the evaluation of the reconstructions from two different points of view: the accuracy and the efficiency. These two viewpoints correspond with the two main pillars on which the new scheme has been built. On the one hand, the development of the new model has been based on finding out the weak points of previous approaches. The degree of incongruence with the real PET process of these shortcomings has been analyzed in order to decide whether to keep them in the new model or to overcome them. In Subsection 2.8.3 it will

be checked to what extent the decisions that have been taken at this regard have a positive effect in the reconstruction domain. On the other hand, as has been already pointed out, the measures taken in order to increase the accuracy of the system response, lead to an increase of the computational cost of the algorithm. As a result, and even if only the strictly necessary modifications have been done, the new model will give place to less efficient reconstructions than the previous approaches. Subsection 2.8.4 examines the efficiency of the new model as well as the efficiency of the previous approaches in which it is based, and whose limitations overcome.

2.8.1 Reconstruction algorithm

The system matrix computed as described in Section 2.7.2 has been incorporated to an iterative reconstruction scheme in order to evaluate the adequacy of the model through the quality of the reconstructed images. The basis of the reconstruction algorithm has been the MLEM algorithm (Vardi et al. (1985)). The list-mode version has been chosen (Reader et al. (1998)) to preserve all the information obtained during the data acquisition. The sensitivity matrix has been calculated for each voxel once at the beginning of the reconstruction, as the sum of the individual probabilities of detection over all possible system tubes, as Eq (1.7) states. As can be checked in the preceeding sections, both the accuracy improvement and the efficiency reduction that are going to be checked concern just the geometrical and blurring (which, in turn, concerns the non-collinearity, penetration and detector scatter factors) terms of the system matrix model. The aim of this work is to test the adequacy of the modifications to previous works that have lead to the new mixed model. Consequently, and provided the scalability of the scheme, just these effects have been considered in the reconstructions. Moreover, and as has been stated before, the assumptions concerning the non-collinearity are not expected to have a great influence in the quality of the reconstructions, since it is a relatively minor effect in the small animal PET. Consequently, and in order to speed up the reconstructions, it has been as well eliminated from the model. On the other hand, in order to mantain the Poison statistical nature of the data (Qi et al. (1998)), no pre-corrections have been done in account for the randoms and scatter effects. The results that will be shown in the following have been thus obtained

for a comparative purpose and should not be interpreted in absolute terms (i.e., for comparison with other algorithms or scanners).

Algorithm parallelization

The new mixed scheme for the system matrix computation has been developed in Section 2.6 to keep the efficient factorization as far as possible. Moreover, in Section 2.7.2 it has been shown how the implementation of the system matrix can be accelerated using several strategies. However, the expression in Eq (2.43) still involves costly multi-dimensional numerical integrations, that have to be evaluated in each iteration for every LOR of the data and for every voxel of the reconstructed volume. Consequently, any mean to improve the efficiency of the implementation will contribute to the feasibility of the method. For this reason, a parallelized version of the MLEM algorithm has been implemented. In this algorithm, each volume element is updated once at the end of each iteration. The updating term is the sum of the independent correction contributions of each LOR of the data set. Each of these contributions is obtained after the forward and backward projection operations that require the costly computation of the system matrix. Based on this property, a parallel version of the MLEM algorithm has been implemented to run in clusters of several processors. The whole data set is split in data slices. Each processor deals with the calculation of only one part of the updating term, corresponding to a slice of the data set. The parallel version has been implemented following a dynamic scheme using the message passing interface protocol (MPI). Whenever an idle processor is available in the cluster, it will be assigned a slice of the data to compute its correction contribution. In this way, the workload is balanced among the processors, as those processors that run faster will claim for their slice of data more often that those that run slower. Once each data slice has been processed, the whole iteration updating term is computed by summing up the correction terms estimated by each processor.

2.8.2 Data and figures of merit

The GATE Monte Carlo simulator has been used to generate different data sets of phantom activity distributions for the scanner described in Subsection 2.7.1:

Point sources: In order to observe how the resolution changes throughout the FOV, a subset of dimensionless point sources with a zero background at the central transaxial plane has been simulated. The sources were positioned 15 mm apart along the radial direction departing from the transaxial center so that face the crystal center. The data set contained approximately $800,000$ total coincidences. Profiles have been taken through the point reconstructed images in the axial, radial and tangential directions and the full width at half maximum (FWHM) has been measured to determine the resolution. As stated by Moehrs et al. (2008), using point sources with a zero background with MLEM might lead to an underestimation of the spatial resolution. However, as has been already mentioned, this work is aimed to compare different methodologies and not to obtain absolute measurements.

Cylindrical phantom: The resolution studies illustrate the potential gain that can be realized by accurately modeling the data. However, this gain is only useful if it can be achieved without large levels of noise amplification. A cylindrical phantom with a diameter of 30 mm and length 10 mm has been simulated in order to study the noise. The cylinder uniform activity has led to a data set of $5,000,000$ coincidences. The standard deviation has been measured in the reconstructed phantom and plotted as a function of the iteration number.

Since the positron range, non-collinearity, scatter and attenuation factors have been eventually eliminated in the validation process (as stated in Section 2.7), they have not been considered in the simulation of the already described phantoms.

2.8.3 Image quality

Three measures have definitely been taken in order to increase the accuracy of the new mixed model with respect to previous approaches. In the following, the effect that these measures have in the

image domain is shown:

- In Section 2.5.2 it has been concluded that the interaction of the gamma photons with the scintillator, which is usually considered through the normalization procedure, should be rather included in the system model. As shown in Section 2.5.2, when considered as a normalization, the interaction of the photons is just accounted in the sensitivity term and not in the forward and backward projection operations. In order to test the effect of this issue in the image domain, the phantoms have been reconstructed using two approaches. In the first approach, the hybrid model proposed has been used both to perform the forward and backward projections and to compute the sensitivity term. In the second approach, the system model has been modified so that the probability of interaction is not taken into account in the forward and backward projections. This has been achieved by normalizing the blurring term for each gamma photon by its analytical probability of interaction:

$$\int_0^{L_k} p_{mult}(b_j, \gamma, \varphi, \theta_1, \theta_2, l, d_k) f(l) dl \rightarrow \frac{\int_0^{L_k} p_{mult}(b_j, \gamma, \varphi, \theta_1, \theta_2, l, d_k) f(l) dl}{(1 - e^{-L1})} \quad (2.44)$$

  for $k = 1, 2$. The probability of interaction is however, accounted in the system model used for the computation of the sensitivity matrix. According to the discussion in Subsection 2.5.2, the inclusion of the probability of interaction in the sensitivity matrix should have been done thorough the normalization factors instead of analytically, but the aim of the study is to just test the influence of its placement in the algorithm and not the model used to represent it.

  Figures 2.15-2.17 illustrate the comparison performed between these two approaches. The results labeled as *Mixed* have been obtained using the new mixed scheme and the results labeled as *Norm* have been obtained using the approach that accounts for the efficiently just in the normalization factors. The radial, tangential, axial and average resolution (as measured by FWHM) of the reconstructed point phantoms after 20 MLEM iterations is shown at Figure 2.15. Figure 2.16 shows a region of the central transaxial slice of the reconstructions. The

noise results are shown in Figure 2.17, measured as the standard deviation (normalized to the mean) of the reconstructed cylindrical phantom with uniform activity.

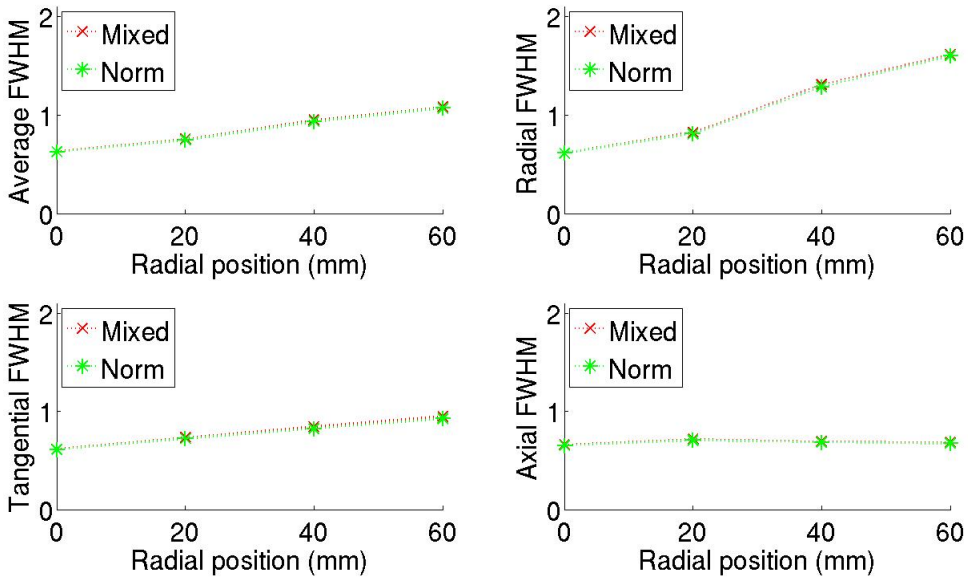

Figure 2.15: Average, radial, tangential and axial FWHM or the reconstructed point sources plotted against the radial position.

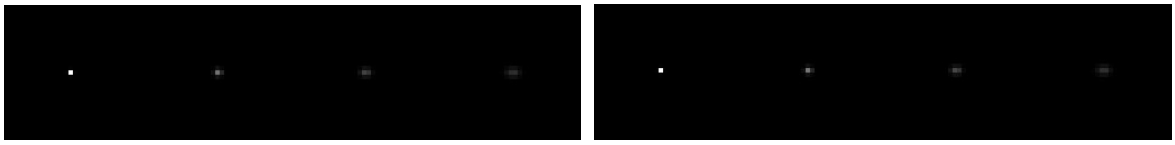

(a) Mixed (b) Norm

Figure 2.16: Region of the central slice of the point sources reconstructed after 20 MLEM iterations

- In Subsection 2.5.2 it has been demonstrated how the crystal penetration and the detector

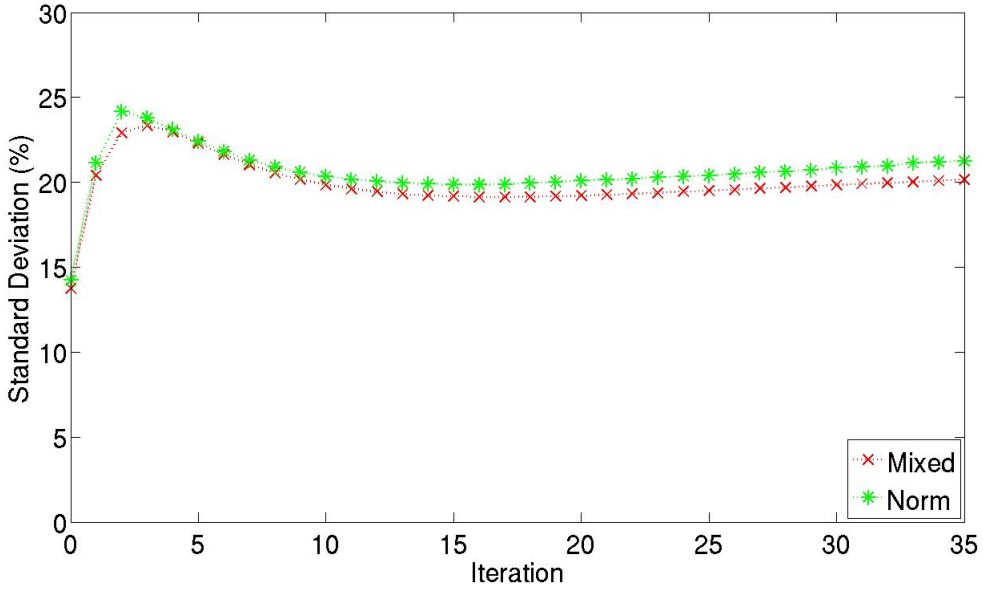

Figure 2.17: Normalized standard deviation of the reconstructed cylindrical phantom plotted against the iteration number.

scatter effects vary with the geometry of the pair (i.e., the emitting point and the pair orientation) within a detector tube. As a result, it has been concluded that these effects should not be separated from the geometric factors, as the factored schemes do. In this subsection the effect of factorizing the geometry and the blurring has been studied in the image domain. With this purpose, the phantoms described in Subsection 2.8.2 have been reconstructed using a factored and a non-factored scheme (both of them reduced just to include the geometrical and blurring factors, as has been previously mentioned). The non-factored scheme is the mixed model proposed in Section 2.6 in which the interdependence of the blurring and the geometry is explicitly considered. In the implementation of the factored scheme, the geometrical terms have been computed as the solid angle spanned from the voxel centers into the detector pairs. Concerning the blurring terms p_{blurr}, it has been already mentioned that they represent the probability that any pair reaching a detector pair d_i gives place to a detection at other LOR

d. Different approaches are followed by the factored approaches to compute these terms. In this work, it has been chosen to represent the blurring experimented by any pair confined to a detector tube d_i by the blurring of the pair that reaches the crystal centers thar define the LOR. The reason for this choice is that, it has been observed in the experiments performed in Subsection 2.5.2 that the KL distance between the distributions obtained for this pair and the distributions obtained for other simulated pairs is minimum in all cases. Once the central pair has been chosen as a reference, the same approach as in the mixed scheme has been followed in the computation of the blurring term for this pair (i.e., Eq (2.35) has been applied to the pair connecting the pair centers). In this way, the comparison reduces to the invariance assumption and not to the blurring model itself.

The effect that separating the blurring from the geometry has the image domain is illustrated in Figures 2.18-2.20. In the results labeled as *Mixed*, the scheme that considers the interdependence between geometry and blurring has been used in the reconstructions. In the results labeled as *Fact*, the scheme in which the geometrical and blurring terms are factorized has been used. The radial, tangential, axial and average resolution (as measured by FWHM) of the reconstructed point phantoms after 20 MLEM iterations is shown at Figure 2.18. Figure 2.19 shows a region of the central transaxial slice of the reconstructions. The noise results are shown in Figure 2.20, measured as the standard deviation (normalized to the mean) of the reconstructed cylindrical phantom with uniform activity.

- In Section 2.7.2 the variability of the detector scatter terms $p_{mult}(b_j, \gamma, \varphi, \theta_1, \theta_2, l, d_k)$ within the pixelated crystals, which is neglected by previous approaches, has been demonstrated. In this subsection the effect of accounting for such variability in the system model has been studied in the image domain, and is shown in Figures 2.21-2.23.

  In order to obtain these figures the simulated phantoms have been reconstructed using two system models. In the first of them (which corresponds to the results labeled as *Mult_Var*) , the dependency of the detector scatter effect on the position of interaction within the crystal is taken into account. Consequently, the detector scatter distributions $p_{mult}(b_j, \gamma, \varphi, \theta_1, \theta_2, l, d_k)$

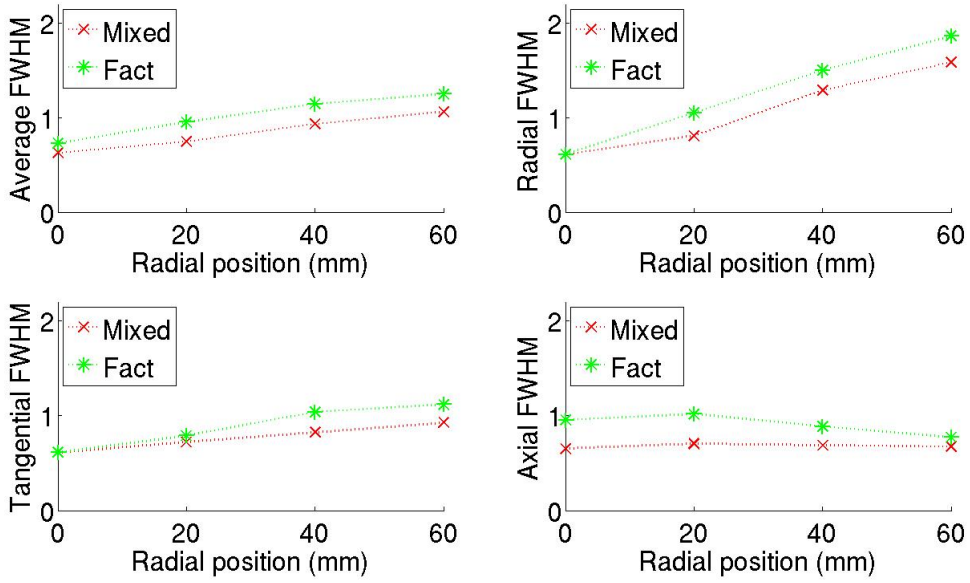

Figure 2.18: Average, radial, tangential and axial FWHM or the reconstructed point sources plotted against the radial position

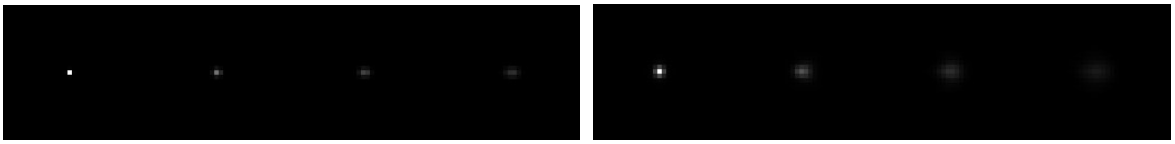

(a) Mixed (b) Fact

Figure 2.19: Region of the central slice of the point sources reconstructed after 20 MLEM iterations

have been estimated (following the procedures described in Subsection 2.7.2) from photon interactions at different positions within the pixelated crystal. Specifically, the interaction positions from which the distributions have been estimated were spaced 0.02 mm along the x' and y' dimensions and 0.5 mm along the z' dimensions of the crystal coordinate system

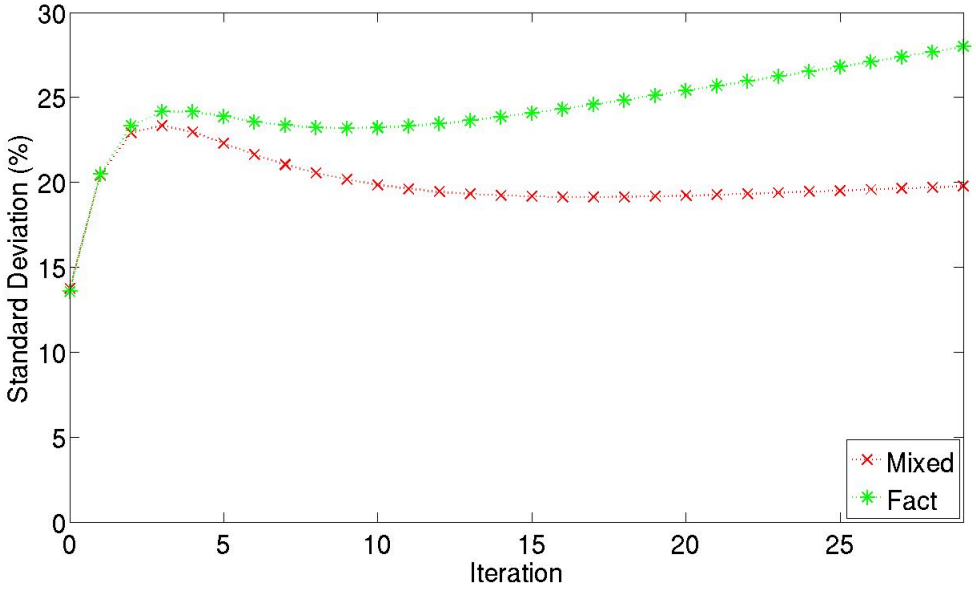

Figure 2.20: Normalized standard deviation of the reconstructed cylindrical phantom plotted against the iteration number.

shown in Figure 2.11, since it has been found that these distances are enough to account for the variability of the distributions. In the second approach (which corresponds to the results labeled as *Mult_Cent*), the detector scatter distributions have been estimated just from photons interacting at the center of the pixelated crystal, and used to model interactions occurring at any other crystal position.

As for the resolution results, the radial profiles of the sources after 20 MLEM iterations are provided in Figure 2.21, instead of the FWHM values. The profiles obtained with the invariant scatter model (*Mult_Cent*) show several local maxima for the source at 60 mm and this makes the FWHM an inappropriate measure for this comparison. A region of the central transaxial slice of the reconstructions is shown in Figure 2.22. Figure 2.23 shows the noise results, measured as the standard deviation (normalized to the mean) of the reconstructed cylindrical phantom with uniform activity.

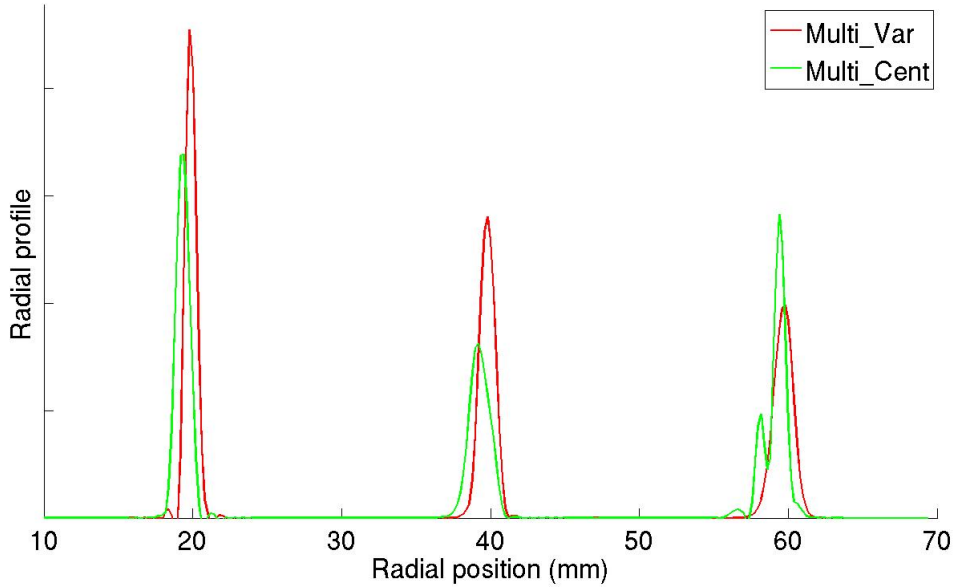

Figure 2.21: Radial profile of the reconstructed point sources.

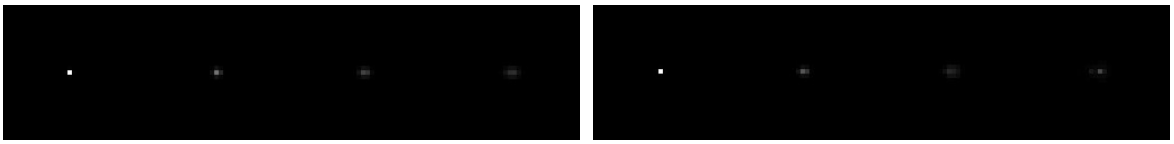

(a) *Mult_Var* (b) *Mult_Cent*

Figure 2.22: Region of the central slice of the point sources reconstructed after 20 MLEM iterations

2.8.4 Efficiency

In this section, an analysis of the computational resources needed by the new mixed model, and by the previous approaches whose limitations it overcomes, is performed.

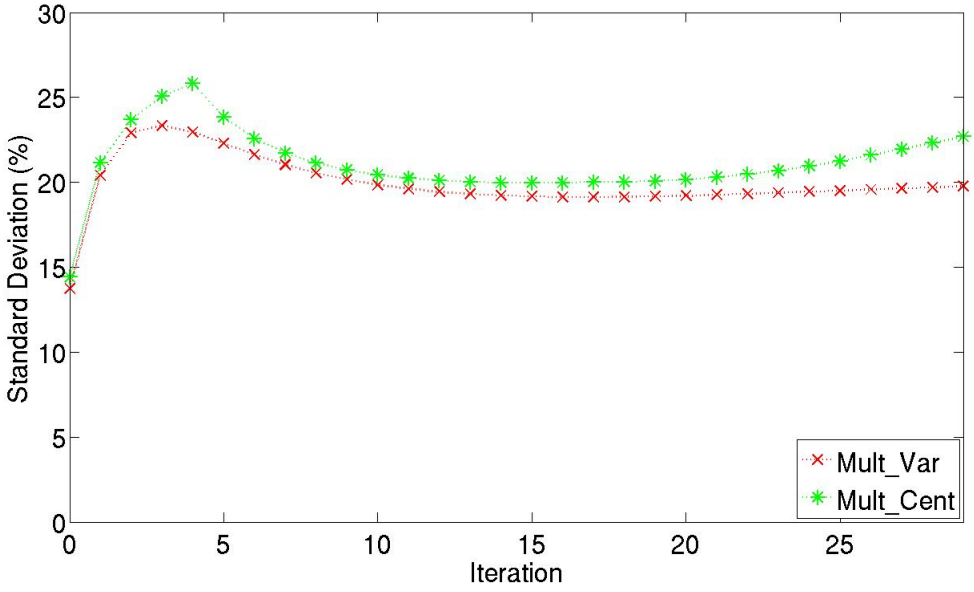

Figure 2.23: Normalized standard deviation of the reconstructed cylindrical phantom plotted against the iteration number.

Time

In the development of the new mixed scheme for the computation of the system matrix, the efficient factored structures have been preserved in those parts of the system matrix where they do not compromise the accuracy of the model. However, it has been demonstrated that such restriction imposes the joint calculation of the geometrical and blurring effects, at which the probability of interaction of the gamma photons has been incorporated (see Section 2.6). A costly on-the-fly computation of these terms is thus imposed. Several measures have been adopted in order to speed up the system matrix computation (Section 2.7) and to optimize the reconstruction algorithm (Section 2.8.1). But even after these measures, the reconstruction time is the computational challenge of the new mixed scheme and will be therefore the focus of the analysis of its efficiency.

The reconstructions of the phantoms described in Subsection 2.8.2 show indeed that even if the

new approach if feasible (as the images have been obtained and are shown in Subsection 2.8.3), it is rather impractical. For the point sources (reconstructed with $156x156x156$ voxels, with voxel sizes of $0.5x0.5x0.5$), the computational cost of the 20 iterations has been about 30 days on 64 Itanium Montvale cores of 1.66 GHz. In despite of such alarming numbers, it has to be pointed out that the implementation of the approach has been done focusing on theoretical purposes (corroborate the predictions stated along Section 2.5) rather than in functional applications. Several measures are proposed in chapter 4 that can significantly reduce the reconstruction times and allow the new system matrix to be put into practice.

Storage

The only extra storage requirement that the new mixed methodology introduces with respect to previous approaches, is the precomputation of the detector scatter terms with higher sampling precision (as discussed in in Subsection 2.7.2). However, this issue does not affect the computational efficiency, since it has been proved that the distributions obtained in this way still fit into RAM memory. On the other hand, the factored approaches, being based in the precomputation of the matrix, have to face a rather complex storage challenge. As has been mentioned in Section 2.5, some of the strategies followed to store the huge Geometric and Blurring matrix are well justified but others have never been tested in the image domain. This is the case of the neglection of the blurring along the azimuthal or axial dimensions and the use of the central transaxial plane to represent all other rings.

Figures 2.24-2.28 illustrate the effect that these simplifications have in the reconstruction of the phantoms described in Subsection 2.8.2. The results labeled as *Fact* serve as a reference and correspond to reconstructions obtained with a factored approach in which no simplifications about the blurring model have been made (i.e., the same approaches used to study the factorization of the blurring in Subsection 2.8.3). In the results labeled as *No_ax*, a factored approach has been used in which the blurring effects have been neglected in the axial dimension (i.e., it has been considered that the gamma pairs that reach a LOR will not give place to detections in the axial neighbours

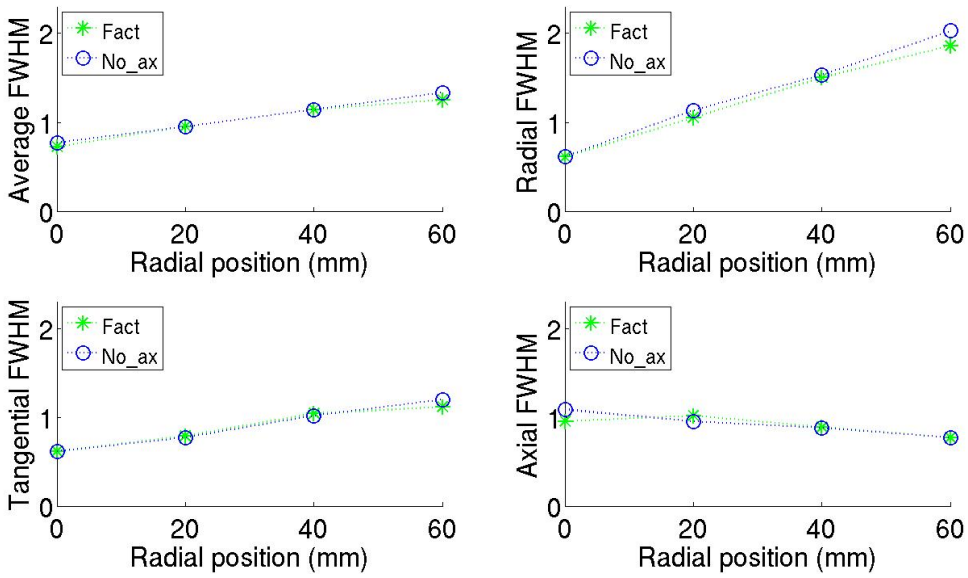

Figure 2.24: Average, radial, tangential and axial FWHM or the reconstructed point sources plotted against the radial position.

(a) Fact (b) No_ax

Figure 2.25: Region of the central slice of the point sources reconstructed after 20 MLEM iterations

of that LOR). In the results labeled as *No_az*, the azimuthal component has been ignored (i.e., it has been considered that the gamma pairs that reach a LOR d_i will not give place to detections in neighboring LORs with different azimuthal projection angle). In both cases, the terms of p_{blurr} have been obtained for the central transaxial plane and applied to any other plane of the scanner.

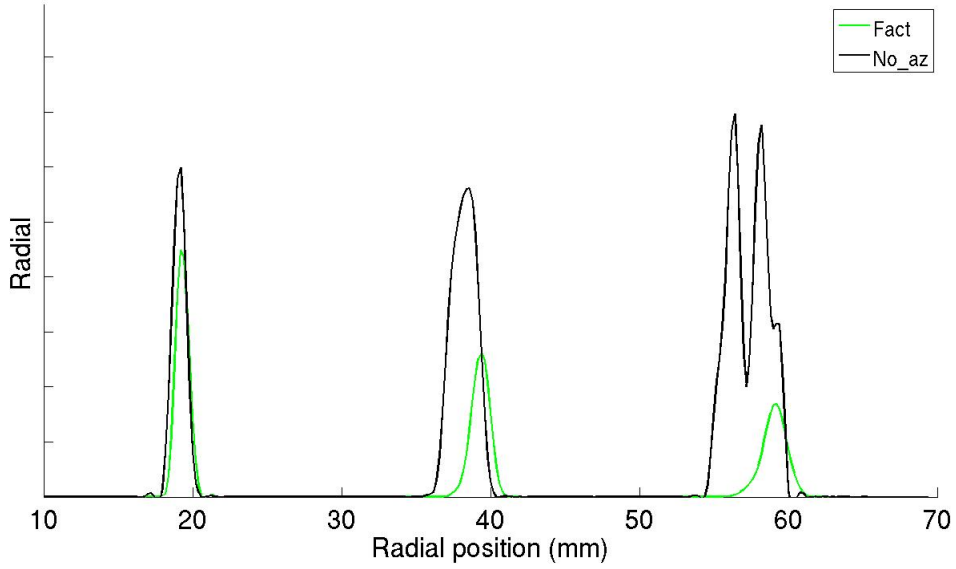

Figure 2.26: Radial profile or the reconstructed point sources.

(a) Fact (b) No_az

Figure 2.27: Region of the central slice of the point sources reconstructed after 20 MLEM iterations

Figures 2.24 and 2.25 show the comparison, in resolution terms, of the factored approach with no simplifications and the factored approach ignoring the axial component. These figures show the radial, tangential, axial and average resolution (as measured by FWHM) of the reconstructed point phantoms after 20 MLEM iterations using both methods and a region of the central transaxial slice of the reconstructions. In order to compare the factored approach with the scheme ignoring

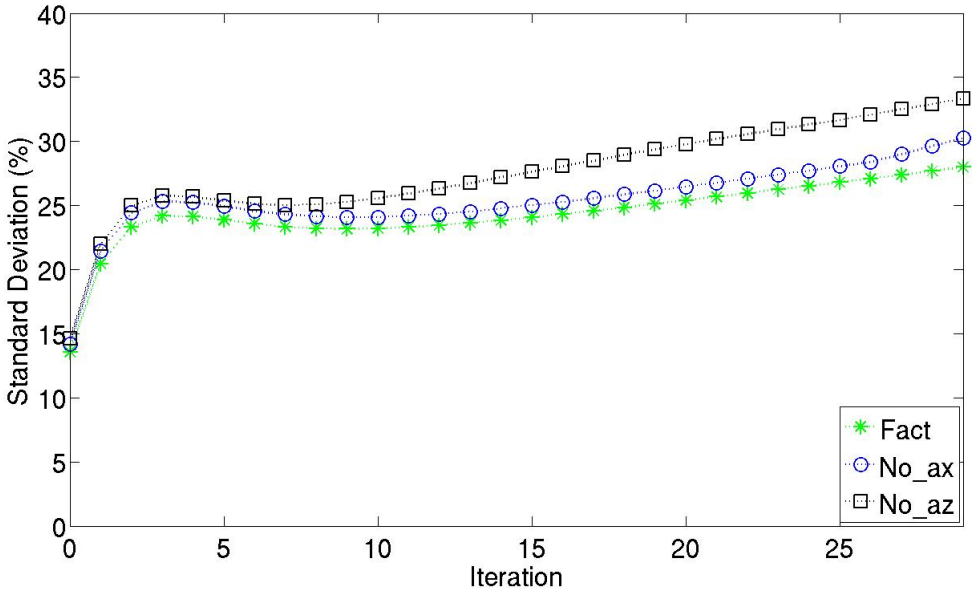

Figure 2.28: Normalized standard deviation of the reconstructed cylindrical phantom plotted against the iteration number.

the azimuthal component of the blurring, Figure 2.26 shows the radial profile (a more appropriate figure in this case, given the profiles obtained with the simplified scheme) of the reconstructed point sources after 20 MLEM iterations. Figure 2.27 shows a region of the reconstruction in the central transaxial plane. The noise results for the three methods are shown in Figure 2.28, measured as the standard deviation (normalized to the mean) of the reconstructed cylindrical phantom with uniform activity.

2.9 Discussion

Iterative methods for PET reconstruction have shown to offer remarkable improvements over the analytical approaches. The success of the iterative algorithms relies to a great extent in the accuracy with which the detection of the gamma pairs is modeled in the so-called system matrix. Unfortunately, an extensive modeling of the acquisition process is often against the computational cost of the algorithm, in terms both of reconstruction time and of memory requirements. This trade-off between quality and performance has made the computation of the system matrix a very active subject of research.

In this chapter, the different approaches to the system matrix computation have been classified according to the methodologies they use. Three basic existing methodologies (experimental, MC and analytical) exist, each of them exhibiting a different level of compromise between complexity, accuracy and computational cost. This is the reason why those approaches that combine methodologies have been found to achieve higher quality reconstructions at more affordable reconstruction times and storage requirements. Particularly appealing within this group are those approaches in which the diverse effects involved in a PET data acquisition are separately modeled, using the methodology more suited to the phenomena they account for. Then, the models are usually stored as a set of independent matrices. Even if it is clearly not the most rigorous way of combining the individual models, to date no approaches exist that can rival in quality with the factorization. Although there exist a few analytical alternatives to the combination of effects, all of them overlook important effects in order to achieve feasible reconstruction times.

In light of recent works that show how the last technological advances allow to use increasingly complex system matrix at acceptable reconstruction times, this chapter has tackled the task of developing proper analytical alternatives to the factorization of effects. This work has given place to several significant results, which are summarized in the following:

1. The **first result** obtained is Eq (2.10). This expression provides a new analytical scheme in which the separately modeled effects are combined in a mathematically rigorous way, since it has been obtained after a detailed tracking of the data acquisition process along

Subsections 2.4.1-2.4.7. Unlike previous analytical approaches, the scheme in Eq. (2.10) is commensurate with the most popular factored schemes, since it accounts for the same effects those do. Even if, from a practical point of view, the complex model in Eq (2.10) can be expected to slow down considerably the reconstructions, it has important theoretical implications, as shown in the following.

2. The **second result** is the analysis of the schemes performed in Section 2.5. Even if certain disagreement of the factorization with the real acquisition process had already been suggested, it had never been further specified, probably due to the absence of alternative schemes with which to be compared. The scheme in Eq (2.10) is such an alternative, and serves as a reference in the study of the weaknesses of the factorization, which has been approached in two ways:

   (a) From the point of view of the accuracy, it has been shown how the most popular factored schemes can be obtained from the analytical scheme in Eq (2.10), after certain simplifications in the model. Then, the validity of each assumption behind the factorization has been analyzed. This study has given place to the **third result** provided in this chapter: the development and implementation of a new scheme that gathers the efficiency of the factorization with the exactitude of an analytical combination of the effects. Such compromise has been achieved by rejecting the factorization of effects when it has been found to compromise the accuracy of the model while accepting it otherwise:

      i. The factorization of the attenuation and of the positron range has been found acceptable, under the usual circumstances of the small animal PET reconstruction (increasingly narrower tubes of response and smaller voxels).

      ii. The factorization of the detection efficiency through the normalizing matrix has been found to be inadequate, since, as shown in Eq (2.29) it excludes the effects it involves from the forward and backward operations. Although for certain of these

effects the calibration seems to be the only plausible modeling, the factorization of the scintillation efficiency (which in the end is the main factor contributing to the general detection efficiency) has been found to be avoidable, as it responds to a simple and widely accepted mathematical model. The reconstruction results provided in Subsection 2.8.3 show that the effects of pulling the scintillation efficiency out of the normalization matrix are not significant in terms of resolution (Figures 2.15 and 2.16 show similar results for the reconstructed sources regardless of where the efficiency is considered). On the other hand, the noise increases slightly faster when factorizing the efficiency, as shown in Figure 2.17.

iii. Finally, it has been found that the factorization of the blurring term ignores several geometrical dependences of the effects it encloses (noncollinearity, crystal penetration and the detector scatter). Bearing in mind that these effects (specially the crystal penetration and the multiscatter) are determinant resolution degrading factors in the small animal environment, the importance of these inconsistencies has been experimentally weighted through a set of MC simulations. The results in Tables 2.2 and 2.3 and Figures 2.9-2.13 show that the mispositioning of events due to the mentioned effects may vary considerably with the position and orientation of the gamma pairs within a tube of detection. The reconstructions confirm that the resolution is notably worsen (as shown in Figures 2.18 and 2.19) and the noise propagation is greatly enhanced (as shown in Figure 2.20) when ignoring this issue. However, the improvements in the image quality achieved by modeling the interdependence of the blurring and the geometry, entail a considerably increase in the reconstruction times. The times reported suggest indeed that the computational cost is the weakpoint of the new hybrid scheme. It must be noted, however, that the time quoted has not been measured from an optimal implementation of the algorithm, neither in terms of software code nor in terms of the execution platform.

(b) From the point of view of the efficiency, it has been observed that the precomputation once and for all of the individual matrices is very advantageous in terms of reconstruction time. But on the other hand, the factored approaches are forced to rely in several simplifications of the model in order reduce the storage resources. These simplifications have been found to be specially constraining in the modeling of the blurring (the more memory-demanding term, given the typical scanner designs and reconstruction FOVs) and include several assumptions about the invariance and anisotropy of the effects involved. The reconstructions of the phantoms with models under these assumptions show that the use of the central transaxial plane to represent all other rings and ignoring the axial component and of the blurring lead to a slight improvement in the resolution results (as can be observed in Figures 2.24 and 2.25). On the other hand, ignoring the azimuthal component greatly degrades the reconstruction of the point sources, as can be observed in the results for the reconstruction sources shown in Figures 2.26 and 2.27. Moreover, all the assumptions have a negative impact in the noise properties of the images, as shown in Figure 2.28. This means that, in pursuit of the efficiency, the most popular factored approaches provide images of suboptimal quality (i.e., lower than the quality that could be obtained without the mentioned assumptions, which in turn has been demonstrated to be lower than the quality provided by the non-factored schemes).

3. Once the new system matrix scheme has been introduced, the model of one the effects it accounts for has been studied in depth. The **fourth result** of this chapter is a new methodology for the estimation of the detector scatter effect using MC simulations, that allows to obtain more accurate models than previous similar approaches. Specifically, the new methodology accounts for the variability of the detector scatter not just as a function of the orientation of the gamma pair, but also of the position of interaction of the photons in the crystal. The methodology has been used to study the behavior of the detector scatter in the A-PET scanner in Subsection 2.7.2, but can be extrapolated to any other scanner, allowing to account

for the particular detection system properties of each device. The results obtained show how the variations in the detector scatter observed in the experiments can be added to the model without compromising the storage requirements and how this inclusion leads to significant improvements of the reconstructions. Ignoring this variations degrades the resolution of the images (as shown in Figures 2.21 and 2.22) and enhances the noise propagation (as shown in Figure 2.23).

Chapter 3

Reconstruction for Continuous Detectors

3.1 Introduction

The use of continuous scintillators instead of pixelated arrays provides higher spatial and energy resolution at a lower manufacturing cost and complexity (Mendes et al. (2007)). Additionally, the use of undivided scintillator blocks avoids the problems of light collection efficiency that are related to fine pixelation of the crystals, which significantly increases the sensitivity of high-resolution PET systems (Llosa et al. (2006)).

Large continuous scintillation crystals were originally introduced in PET cameras by the university of Pennsylvania (Karp et al. (1990)). This approach was developed for use with thallium-doped sodium iodide (Nai(TI)), since it requires a good light output. However, the low stopping power of Nai(TI) had some disadvantages. First, a thick detector was required to obtain sufficient sensitivity, which degraded the spatial resolution, mainly due to the large Compton scattering effect (Benlloch et al. (2006)). Moreover, it limited the maximum countrate capability of the scanners (Muehllehner and Karp (2006)). In addition to the limitations of the Nai(TI), the large size of the detection area of

the used photomultiplier tubes contributed to the degradation of the intrinsic resolution (Benlloch et al. (2006)). As a result, most of the groups ended up abandoning the use of continuous Nai(TI) detectors in favor of discrete crystal configurations.

Recent technical developments have led to a renewed interest in the use of continuous scintillators (Hun et al. (2002), Tavernier et al. (2005), Balcerzyk et al. (2009), Sánchez et al. (2012)). First, the invention of position-sensitive photomultipliers (PM-PMTs) solved the problem of the PMTs size (Benlloch et al. (2006)). Second, the advent of LSO and LYSO, whose high scintillation efficiency, high cross section for 511 keV gamma rays and fast decay time achieve good spatial localization and excellent count-rate performance (Siegel et al. (1995)).

It has been already pointed out the important role that the statistical reconstruction plays in the quality of the PET studies. It has been mentioned as well that the success of such reconstruction algorithms relies to a great extent on the faithfulness with which they model the PET scanning process. The literature on statistical reconstruction focuses mainly on pixelated devices, since it has been the prevailing technology for a long time. However, the continuous scintillator cameras have certain peculiarities with respect to their discretized counterparts that should be accounted in the reconstructions in order to fully exploit their advantages. In spite that many academic research groups have resumed the use of continuous sctintillation crystals in the last years, just certain works account for the specific features of the continuous scintillators in the reconstruction.

3.2 State of the art

There are several peculiarities of the continuous scintillators that have to be taken into account in the data acquisition and reconstruction process if the highest quality images want to achieved.

3.2.1 Definition of the LORs

The first difference the continuous cameras introduce with respect to the pixelated devices is the definition of the LORs. For a detector composed of small discrete crystals all interactions are

assumed to occur at the center of individual crystals whereas in a continuous detector such restriction does not apply. Therefore, if a pixelated design is being considered, a LOR d will be a tube defined by a pair of discrete detectors (c_1 and c_2, see Figure 3.1(a)) whereas if continuous scintillators are used, then the detector tube reduces to a single line defined by a pair of continuous positions at the detectors (p_1 and p_2, see Figure 3.1(b)).

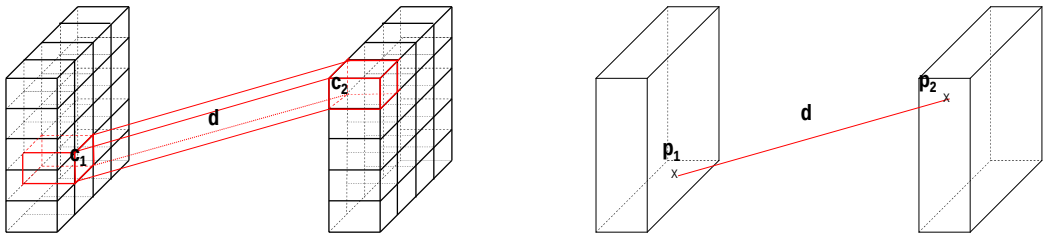

(a) (b)

Figure 3.1: Definition of a LOR d in a pixelated (a) and in a continuous (b) design.

Reconstruction Algorithm

The more accurate lines of response (LORs) that the continuous cameras provide can be naturally handled by list-mode versions of the MLEM reconstruction algorithm (Reader et al. (1998), Reader et al. (2002b), Rahmim et al. (2004)). As has been mentioned, list-mode reconstruction algorithms modify the MLEM equations so that each LOR is considered individually instead of being grouped in discrete detector bins:

$$\lambda^{new}(b) = \frac{\lambda^{old}(b)}{p(b,.)} \sum_{n=1}^{N} \frac{p(b,d)}{\sum_{b=1}^{B} \lambda^{old}(b)\, p(b,d)} \tag{3.1}$$

Since it allows to retain the full precision of the LORs, the list-mode MLEM algorithm represented by Eq (3.1) is an appropriate reconstruction scheme for PET systems that make use of continuous detectors.

System matrix

The continuous nature of the LORs still involves other important considerations. The terms $p(b,d)$ of the system matrix have been defined as the probability that an emission from a basis function b is detected at certain LOR d. A LOR d in a continuous scintillator can be considered as a limit case of a LOR in a pixelated scintillator with infinitesimal crystal size. Consequently, in the continuous case the discrete probabilities of detection in a LOR should be thought of as the likelihood values of a continuous statistical distribution.

The new statistical meaning of the system matrix makes many of the existing methodologies for the system matrix computation unsuitable for reconstruction of continuous detectors data. In principle, it rules out all previous approaches based on the experimental precomputation of the whole system matrix, since it would not be possible to store the theoretically infinite LOR values that make up each continuous $p(b,d)$ distribution. A very fine sampling of the continuous distributions of $p(b,d)$ can be done in order to retain the maximum precision of the LOR positioning. But this would just make more difficult the already complicated storage tasks the precomputation entails. The continuous nature of the LORs can be fully retained by using analytical approaches that allow the on-the-fly *ad-hoc* computation of the system matrix terms for each LOR registered. However, as has been mentioned, the analytical on-the-fly approaches ignore important effects involved in the data acquisition process, which make them an inaccurate option for either the pixelated or the continuous detector case.

Both the pure analytical and the pure experimental (precomputed) approaches have been discarded for the system matrix computation in the continuous detectors case, due, respectively, to its inaccuracy and to its inability to retain the continuous nature of the LORs. Under these conditions, the use of hybrid approaches that try to combine the accuracy of the empirical and MC methods with the efficiency of the analytical procedures (and have been throughfully studied in Section 2.2.2) seems to be an appropriate option. However, not all the hybrid approaches are suitable to be used for reconstruction with continuous detectors data. Just those in which the experimental part does not involve huge precomputed components based on the discretization of the LORs d will be appropriate. Such models will be able to preserve the accuracy of the LORs without imposing stringent storage requirements. Unfortunately, the factored methodology of Qi et al. (1998), which to date is the most successful of the hybrid approaches type, does not fulfill this condition. This approach is based on the precomputation of the geometrical and blurring matrix. The precomputation of these matrices already poses an storage problem in the pixelated detector case, and it would be still more challenging in its adaptation to continuous cameras. Although other hybrid approaches might fit the requirements needed to preserve the LOR positioning to a great extent, all of them have been found to have drawbacks in the general case (see Section 2.2), that would be inherited in their adaptation to continuous detectors. To sum up, to date there is not a system matrix implementation that is able to efficiently take into account the continuous nature of the LORs provided by continuous scintillators.

Sensitivity matrix

The reformulation of the system matrix terms to account for the continuous nature of the LORs affects as well to the computation of the sensitivity matrix. The sensitivity matrix $p(b, .)$, has been defined for a basis function b in the FOV of a PET scanner, as the probability that a pair of gamma photons emitted from that basis function is detected by the scanner. This probability has been traditionally computed as the summation over the probabilities of detection in each LOR, making use of the discrete nature of the pixelated detectors:

$$0 < p(b,.) = \sum_{d=1}^{D} p(b,d) \tag{3.2}$$

In the continuous detectors environment, where the terms $p(b,d)$ are distributed over a continuous distribution, the summation in Eq (3.2) should be correctly expressed as an integral. Some authors have proposed analytical calculations of the sensitivity term (Reader et al. (1998), Levkovtiz et al. (2001), Soares et al. (2003)) that solve this problem. However, the rotational symmetry assumption all these methods share is in disagreement with the polygonal shape of modern PET scanners that use block detectors.

3.2.2 Optical photons behavior

So far, the formal differences that the use of continuous scintillators make in the statistical reconstruction have been tackled. However, the use of continuous scintillators also makes some important differences in the physical detection process. These differences concern mainly the behavior of the scintillation photons. Unlike in pixelated designs, the optical photons resulting of each of the interactions with the scintillator are not confined to one optically isolated crystal but propagate all over the continuous block (Levin (2004)), as shown in Figure 3.2. As a result, additional light losses occur due to the multiple reflections on the inside surfaces of the crystal, degrading the energy resolution. Moreover, the light distribution subtended at the PMTs is broadened and distorted, which causes resolution degradation and compression in the image domain (Giménez et al. (2004), Benlloch et al. (2006)).

The use of reflectors, absorbers as well as special crystal surfaces finishes, difusses and shapes can enhance the light collection in order to minimize the losses associated with multiple reflections and to achieve higher spatial resolution and lower compression images (Karp and Muehllehner (1985), Giménez et al. (2004)). But even if these design features highly overcome the difficulties associated to the absence of discrete detectors, important differences between the light collection properties in pixelated and continuous designs still remain after the manufacturing process. In

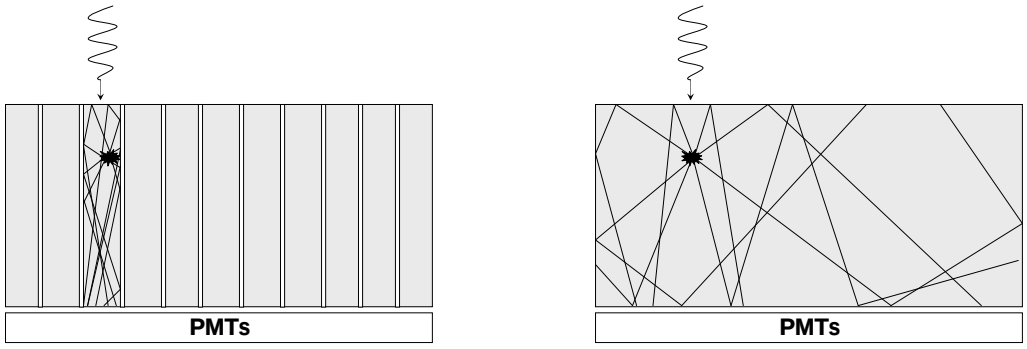

(a) Pixelated design

(b) Continuous design

Figure 3.2: Schematic drawings of the light ray propagation for typical pixelated and continuous camera designs. For the pixelated design, scintillation light is confined to one crystal and focused on one spot of the photodetecting array. For the continuous design, the light cone subtended at the photodetector is broaden by the reflections at the top and sides of the single crystal.

pixelated arrays, the light response properties are approximately identical regardless of the point within the segmented array from which the optical photons are emitted. However, in the continuous designs the position of the light source (the position of the interaction with the scintillator) gives place to very different reflection patterns from the sides and the back surfaces. As a result, the light response function (LRF) can vary in shape dramatically depending on the source position (Lewellen (2008), Miyaoka et al. (2008)). First, the LRF varies with the tangential 2D position on the crystal. For the light sources close to the crystal side edges the reflecting light from the side surfaces contributes to the width and tail of the LRF, as shown in Figure 3.3. The LRF changes as well with the DOI of light source due to reflections from the top and back surfaces. Specifically, as shown in Figure 3.3, the LRF is less spread out for positions close to the photosensor, compared to positions far from the photosensor.

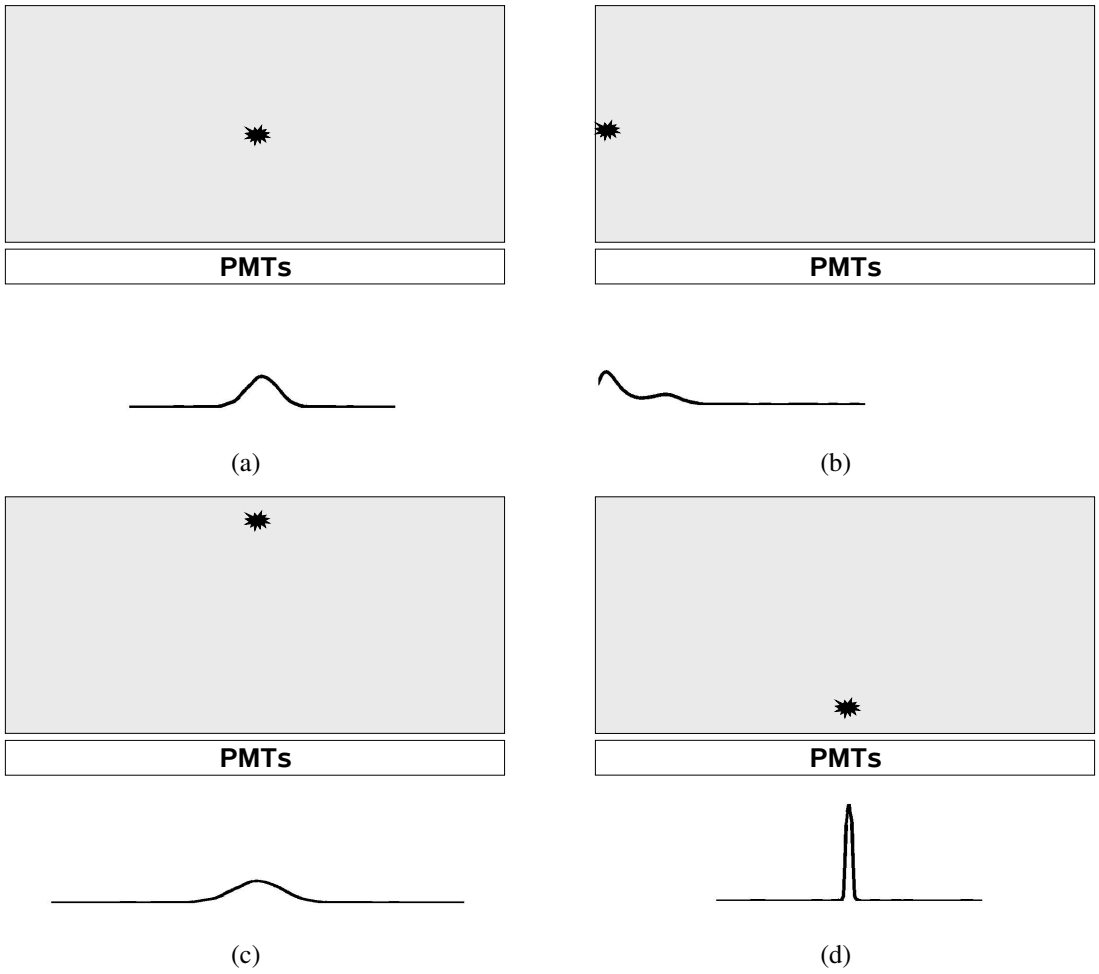

Figure 3.3: Approximated shape of the LRF in a continuous scintillator for a light source located at the center(a), the block side(b) the block bottom surface(c) and the block top surface(d) of the block.

The DOI dependence of the LRF can be an added parameter to extract and utilize to address the parallax problem (Lewellen (2008)). Nevertheless, in the general case, the distortions in the shape of the LRF work to degrade the positioning of the event, which has a strong effect on the intrinsic spatial resolution achievable with a continuous detector. In order to improve the spatial resolution,

the detector light characteristics can be compensated at either the detector level or as part of the image reconstruction process:

1. At the detector level, apart of the already mentioned surfate treatment procedures (Giménez et al. (2004), Karp and Muehllehner (1985)), non-linear preamplifiers (Karp and Muehllehner (1985)) can be used to sharpen the light distribution. The positioning bias can be reduced as well with the use of statistical estimation techniques to determine the point of interaction in the crystal array rather than linear algorithms (Milster et al. (1985), Pouliot et al. (1991), Tomitani et al. (1999), Miyaoka et al. (2008)). However, just a few of these models (Miyaoka et al. (2008) and Lerche et al. (2009)) address how to model the LRF near the edge of the detector, where mathematical modeling is very difficult. Certain works correct for the undesirable border effects using position calibration methods (Benlloch et al. (2006)) and could be used along with the incomplete statistical positioning methods.

2. As for the compensations of the light characteristics in the image reconstruction process, to date no work has been found in which the optical photons behavior is included in the system model in which the statistical reconstruction is based. This is likely due to the fact that, as has been already mentioned, the pixelated crystal configurations, where the LRF is not such an important issue, have been the most popular choice in the past decades. However, the renewed interest by the continuous configurations in the last years makes this possibility worth of an effort, either as an alternative or complementary to the already mentioned design, positioning and calibration techniques.

3.3 Objectives of the Chapter

As shown in the previous section, just a few works exist that are able to take into account the particular characteristics of the continuous scintillators in the reconstruction process and all of them still have certain limitations. Moreover, each of the mentioned works deals just with a part of the requirements the reconstruction for continuous scintillators imposes. However, to the best of our

knowledge, all the specific aspects of the reconstruction for continuous detectors have never been gathered in a single scheme. In the absence of such a reconstruction scheme, the advantages of the continuous detectors technology are not being fully exploited. The present chapter addresses this problem, through the achievement of the following goals along the following sections:

1. In Section 3.4, a method to compute the system matrix will be introduced that accounts for the specific features of the continuous detector devices (discussed in Section 3.2) while fulfilling the general accuracy and efficiency requirements every statistical reconstruction imposes. Specifically, it will be shown that, due to its analytical and flexible nature, the new system model introduced in Chapter 2 is specially well suited to be adapted for its use in continuous detector reconstructions. Furthermore, it will be specified how the adaptation of the scheme should be carried on.

2. In Section 3.5, a new method for the computation of the sensitivity matrix for the MLEM algorithm has been developed. The new method is independent of the continuous/pixelated nature of the scintillators, since it is not based in the sum of probabilities over the individual detectors. Moreover, unlike previous similar approaches, it is not based on a rotational symmetry assumption.

3. The new methods developed for the system and sensitivity matrix computation have been incorporated to an algorithm in order to test the benefits in the image domain of a reconstruction specially adapted for continuous scintillators. Section 3.6 deals with the details of the implementation of the new methodologies whereas Section 3.7 deals with their evaluation and validation.

3.4 System matrix for continuous scintillators

It has been concluded in Section 3.2 that, in order to reconstruct from continuous scintillators data, statistical algorithms should make use of a system matrix that is able to fit two requirements. First,

as has been pointed out in Subsection 3.2.1, it should be able to retain as much as possible the continuous positioning provided by this technique. Second, it should account for the particular behavior of the optical photons in the continuous blocks, whose consequences in the shape of the LRF have been described in Subsection 3.2.2.

Concerning the first objective, it has been already mentioned that an hybrid scheme that combines experimental and analytical methodologies giving priority to the analytical calculations while minimizing the precomputed components should be used. Such an scheme allows to retain as much as possible the continuous LOR nature without imposing stringent storage requirements. Unfortunately, the factored model proposed by Qi et al. (1998), which to date was the most complete, accurate and popular of the existing hybrid schemes, has been found not to be appropriate for reconstruction with continuous data, since it is based on the storage of huge precomputed factors.

Chapter 2 has dealt thoroughly with the type of hybrid system matrix schemes that combine methodologies and, as a result, an alternative mixed scheme that is able to compete with the factored approaches has been obtained in Section 2.6. The new scheme is based on the substitution of the separated factors by analytical expressions in those parts of the scheme where the factorization of effects has found to be an inaccurate approach. The accuracy principle in which the new scheme has been built has shown to lead to higher quality reconstructions than the purely factored approaches. Moreover, and according to the previous paragraph, the priority the new scheme gives to the analytical expressions over the precomputed components makes it to be very well suited to retain the LOR positioning provided by continuous detectors.

Concerning the second objective, the new hybrid scheme has been conceived as a flexible frame for the combination of the different effects that a system matrix should account for. This allows to select which effects are incorporated into the model and the methodology with which each of these effects is modeled. The incorporation of the optical photons related effects to the existing model can thus expected to be an achievable task.

The new scheme proposed in Section 2.6 can be therefore thought as an appropriate scheme

to fulfill the requirements imposed by the use of continuous scintillators in the system model estimation. In the following it will be shown how it can be adapted to achieve these requirements: Subsection 3.4.1 deals with the retaining of the data precision whereas Subsection 3.4.2 deals with the incorporation of the optical photons behavior to the model.

3.4.1 LOR positioning

In this section it will be checked to what extent the scheme proposed in Section 2.6 is able to retain the continuous nature of the LORs provided by continuous detectors. The priority the scheme gives to the analytical calculations that allow to retain the LOR definition, becomes specially apparent in the expression proposed in Section 2.7:

$$\begin{aligned} p(b,d) &= p_{cal}(d)\sum_{j=1}^{N}\int_{\gamma}\int_{\varphi} p_{att}(d_i(b_j,\gamma,\varphi))\int_{\theta_1}\int_{\theta_2}\int_{0}^{L_1} p_{mult}(b_j,\gamma,\varphi,\theta_1,\theta_2,d_1)f(l)dl \\ &\int_{0}^{L_2} p_{mult}(b_j,\gamma,\varphi,\theta_1,\theta_2,d_2)f(l)dl f(\theta_2)f(\theta_1)f(\varphi,\gamma)d\theta_2 d\theta_1 d\varphi d\gamma p_{pos}(b,b_j) \end{aligned} \quad (3.3)$$

However, the scheme still relies on the precomputation and storage of the models for some of the effects it accounts for. Specifically, and even if the methodology used to model each effect can be modified, it is expected that the normalizing $p_{cal}(d)$, attenuation $p_{att}(d_i(b_j,\gamma,\varphi))$ and detector scatter $p_{mult}(b_j,\gamma,\varphi,\theta_1,\theta_2,l,d_k)$ terms are experimentally computed and stored due, respectively, to its scanner dependent, object dependent and complex nature.

The terms $p_{att}(d_i(b_j,\gamma,\varphi))$ contain the attenuation values for the gamma pairs (defined by γ,φ) emitted from a voxel b_j. Since the attenuation properties do not depend on the continuous or pixelated nature of the scanner, the storage of the attenuation terms does not compromise the accuracy in the positioning of the LORs.

On the other hand, the normalizing ($p_{cal}(d)$) and detector scatter ($p_{mult}(b_j,\gamma,\varphi,\theta_1,\theta_2,l,d_k)$) terms depend explicitly on the LOR definition d (d_k $k=1,2$ stand for the two positions that define

d). In order to store the precomputed values of these terms, the continuous variable d will have therefore to be discretized. Consequently, the values of normalization and detector scatter won't be, in principle, available for every registered LOR d, but will have to be obtained by means of some kind of interpolation.

The computation and storage of $p_{cal}(d)$ is not expected to have severe consequences in the reconstructions. On the one hand, in the development of the new scheme it has been decided to transfer the main effects this term traditionally accounted for to the system model, which has shown to improve the quality of the results, in Section 2.8. On the other hand, being an unidimensional function of d, a fine discretization of $p_{cal}(d)$ can be achieved without compromising the storage requirements, as shown in Benlloch et al. (2006).

The discretization of d in the detector scatter terms $p_{mult}(b_j, \gamma, \varphi, \theta_1, \theta_2, l, d_k)$ is more challenging. On the one hand, the multiple interactions are known to be an important image degrading effect in the small animal field, and any issue involved on their estimation has to be carefully considered. On the other hand, the precomputation and storage of a five dimensional function poses a more complex storage problem. In the general pixelated case, these terms have been precomputed as a set of discrete probability distributions of d. Each of the distributions corresponds to a different combination of b_j, γ, φ, θ_1 and θ_2, and computes the probability that an event whose first interaction with the scintillator is defined by these four parametres is finally positioned at the discrete crystal d. Each distribution has been obtained by generating with a MC simulator a large number of photons interacting at the defined position and obtaining normalized histograms of the recorded detections. Since in the case of continuous scintillators, the positions d are continuous variables, the discrete probability distributions should be restated as continuous probability distributions. For that reason, instead of estimating them by histogramming the recordered positions, a more appropriate estimation based on a smoothing normal kernel (Bowman and Azzalini (1997)) is proposed. The number of points at which the estimated continuous distributions are evaluated to be stored will determine the level of discretization of d. The minimum level of discretization of d will be imposed by the sampling rate necessary to preserve the information of the distributions. The maximum level

of discretization will be imposed by the RAM memory available to store each distribution, which in turn, will depend on the memory resources and on the number of distributions that have to be stored. This number can be minimized, by studying the variability with b_j, γ, φ, θ_1 and θ_2 of the distributions, as has been done in the general pixelated case (see Subsection 2.7.2)

The previous paragraph summarizes the guidelines that are proposed to compute the detector scatter terms in the case of continuous scintillators. These guidelines constitute the only modification introduced in the system matrix computation with respect to the general pixelated case, which corroborates the adequacy of the chosen scheme for its adaptation to continuous scintillators reconstruction. In Section 3.6 it will be shown how these guidelines are applied to the discretization and storage of the detector scatter distributions for a specific continuous detectors scanner.

3.4.2 Optical photons

The first step to incorporate the light related effects to the scheme in Eq (3.3) is to locate the emission of optical photons in the data acquisition process this equation models. As depicted by Figure 3.4, each interaction associated with a gamma photon can be modeled as one of the sources with spherically symmetric distributions of sctintillation light whose behavior has been described in Subsection 3.2.2.

There exist several analytical models for the estimation of the light distribution each source gives place to (Aykac et al. (2003), Levin (2004)). An attempt could be made to use these models to describe the behavior of the optical photons generated in the crystal, but this approach would pose a complex challenge. According to the scheme of Figure 3.4, one different light distribution should be modeled for each possible interaction. Such an approach would require a prediction of every possible interaction with the crystal for each incident photon. The use of analytical optical models would just thus increase the complexity of the already unworkable problem of analytically modeling the multiple interactions (for which it has already been chosen a MC approach). Consequently, this option has been discarded.

On the other hand, the MC simulator (GATE) used to generate the detector scatter distributions,

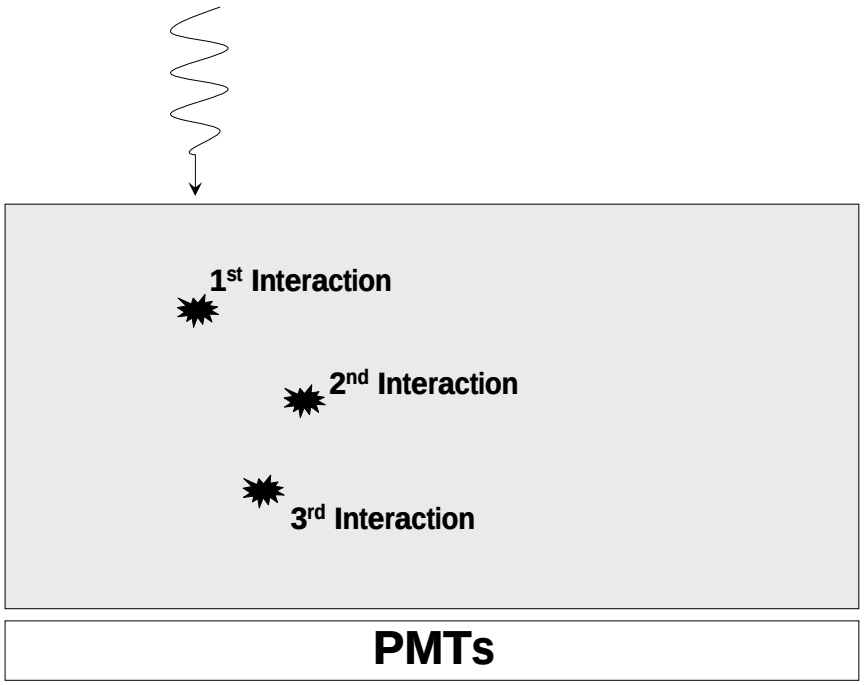

Figure 3.4: A gamma photon entering the detector gives place to a complex and unpredictable pattern of multiple interactions, each of which becomes a source of optical photons, whose behavior in the continuous scintillators has to be modeled.

can be used to accurately generate and track optical photons. The optical photon tracking capabilities of GATE have been switched off in the estimation of the detector scatter for pixelated detectors (in Section 2.7), since they increase dramatically the simulation time and the optical photons are known to be a minor issue for this kind of devices. However, in the case of continuous scintillators, where the light effects are known to play an important role, switching on the optical photons generation during the detector scatter estimation allows to include their effect in a very advantageous way. On the one hand, it does not involve an increase in the complexity of the system matrix computation.

The procedure for the computation and storage of the detector scatter distributions needs to be repeated anyway for each scanner, in order to account for its particular characteristics. The activation of the optical photons just involves an increase in the simulation times, but the simulations have to be run just once and for all before the beginning of the reconstruction process. On the other hand, being the optical photons model precomputed and stored along with the $p_{mult}(b_j, \gamma, \varphi, \theta_1, \theta_2, l, d_k)$ terms, its inclusion in the scheme may affect the memory requirements, but not the reconstruction time, which has been shown to be the weak point of this particular system matrix scheme. In Section 3.6, further details on how to include the optical photons in the simulations and its consequences on the estimation of the detector scatter terms will be given for a specific device.

3.5 Sensitivity matrix for continuous scintillators

As has been pointed out in Section 3.2, due to the continuous nature of the LORs in the undivided detector devices, the sensitivity matrix can't be computed as the sum of individual probabilities of detection over every LOR of the scanner. In the following, an analytical method is introduced to compute the sensitivity matrix of PET scanners, which is not based on the continuous or pixelated nature of the detectors and can be, therefore, used for both types of devices. Furthermore, unlike previous analytical developments of this type, the following development does not assume rotational symmetry. A detailed discussion of the experimental importance of this factor is given in Subsection 3.6.3.

The sensitivity term $p(b, .)$ stands for the probability that a pair of gamma photons emitted from a basis function b in the FOV of a PET scanner gives place to a coincidence event. In order to provide a methodology that is valid for any type and size of basis function, the calculation will be performed for a single emitting point $\mathbf{r}_0$, and referred to as $p(\mathbf{r}_0, .)$. As has been shown in Subsection 2.4.1, the results obtained for a single emitting point can be easily extended to the general case of any basis function by means of integration over its domain.

The development is valid for both static rings and rotating geometries, although it will start

considering the basic scanner consisting of just two parallel planar detector heads (which can be either continuous or pixelated) whose dimensions and coordinate axes are shown in Figure 3.5.

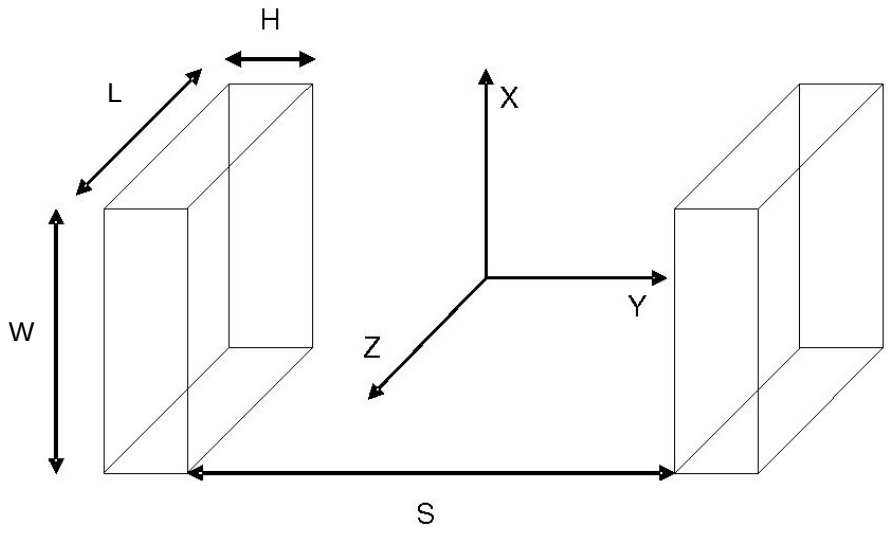

Figure 3.5: Dimensions and coordinate axes of the two parallel detector heads for which the methodology for the sensitivity matrix computation will be developed.

Let φ and γ be the polar and azimuthal angles, respectively, that define the orientation of a gamma pair emitted from a point $\mathbf{r}_0$. If we assume an uniform distribution of the emissions over the sphere (i.e., the joint probability density function of φ and γ is $f(\varphi, \gamma) = \frac{\cos\varphi}{2\pi}$), the probability that an emission from a point $\mathbf{r}_0$ of coordinates $(\mathbf{x}_0, \mathbf{y}_0, \mathbf{z}_0)$ in any plane Π_γ parallel to the z-axis (as shown in Figure 3.6) intersects both of the planar detector heads can be computed as:

$$p(\mathbf{r_0}, \Pi_\gamma) = \int_{\alpha_\varphi(\mathbf{r_0},\gamma)}^{\beta_\varphi(\mathbf{r_0},\gamma)} \frac{\cos\varphi}{2\pi} d\varphi \tag{3.4}$$

As can be observed in Figure 3.6, the integration limits $\alpha_\varphi(\mathbf{r_0}, \gamma)$ and $\beta_\varphi(\mathbf{r_0}, \gamma)$ are the maximum detectable angles from $\mathbf{r_0}$ within the plane Π_φ. Closed-form expressions for $\alpha_\varphi(\mathbf{r_0}, \gamma)$ and $\beta_\varphi(\mathbf{r_0}, \gamma)$ are given in Appendix C.

Even if a photon intersects a detector it may not interact with it. The detection efficiency of the scintillator material (the most important factor at this regard), quantified through its physical attenuation constant, μ_0, will be considered. The probability of detecting a pair of gamma photons that intersect the left and right detectors with lengths $L_1(\mathbf{r_0}, \varphi, \gamma)$ and $L_2(\mathbf{r_0}, \varphi, \gamma)$ respectively can be approximated by:

$$p(\mathbf{r_0}, \varphi, \gamma) = (1 - e^{\mu_0 L_1(\mathbf{r_0},\varphi,\gamma)})(1 - e^{\mu_0 L_2(\mathbf{r_0},\varphi,\gamma)}) \tag{3.5}$$

The probability of detecting an emission from a point $\mathbf{r_0}$ in any plane Π_γ is:

$$p(\mathbf{r_0}, \Pi_\gamma) = \int_{\alpha_\varphi(\mathbf{r_0},\gamma)}^{\beta_\varphi(\mathbf{r_0},\gamma)} \frac{\cos\varphi}{2\pi} p(\mathbf{r_0}, \varphi, \gamma) d\varphi \tag{3.6}$$

The expression for the probability of detection of any pair of photons emitted from $\mathbf{r_0}$ in the case of the basic two parallel detector heads can be obtained by integrating $p(\mathbf{r_0}, \Pi_\varphi)$ over all the planes Π_φ detectable by the detector heads:

$$p(\mathbf{r_0}) = \int_{\alpha_\gamma(\mathbf{r_0})}^{\beta_\gamma(\mathbf{r_0})} p(\mathbf{r_0}, \Pi_\varphi) d\gamma \tag{3.7}$$

The range of detectable planes is defined again by the angle seen by the point $\mathbf{r_0}$ into the detector

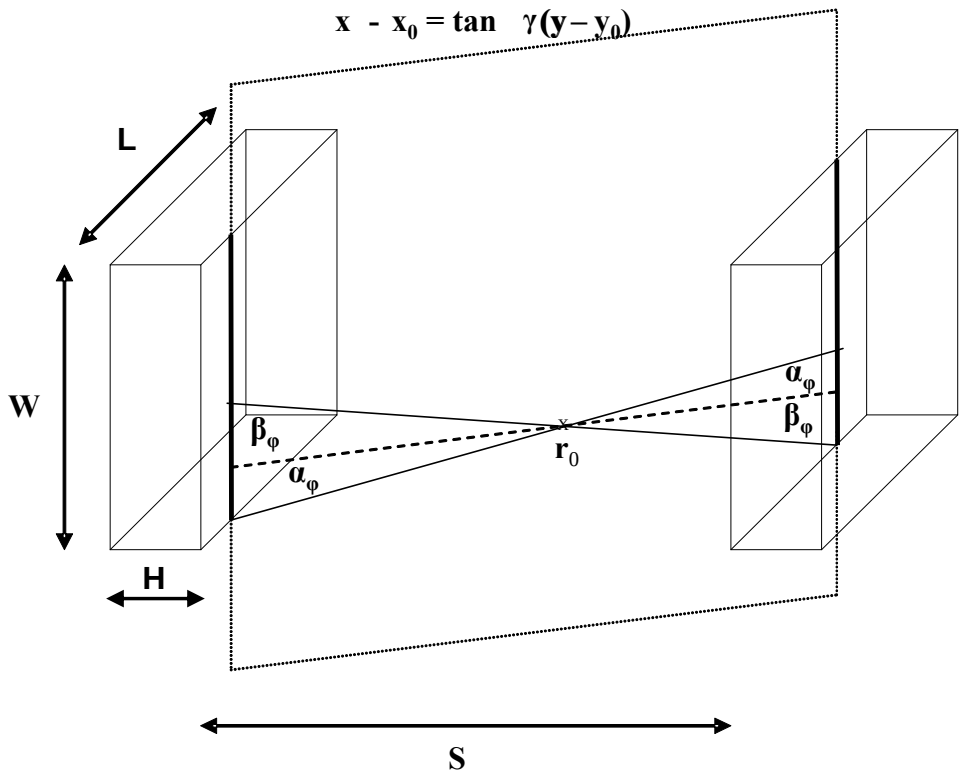

Figure 3.6: Geometrical characterization of the range of detectable emissions from the point $\mathbf{r_0}$ within the plane Π_φ. φ is the angle formed by the plane parallel to the z-axis Π_φ and the plane $x = x_0$. The angles $\alpha_\varphi(\mathbf{r_0}, \gamma)$ and $\beta_\varphi(\mathbf{r_0}, \gamma)$ define the maximum and minimum detectable LORs within the plane Π_φ. The dashed line is the intersection of $z = z_0$ and Π_φ planes. The reference axis used is supposed to be centered with respect to the planar detectors but for space reasons are shown at the right-down corner of the figure.

heads, now in the xy plane, as shown in Figure 3.7. Appendix C provides analytical expressions for the angular limits $\alpha_\gamma(\mathbf{r_0})$ and $\beta_\gamma(\mathbf{r_0})$.

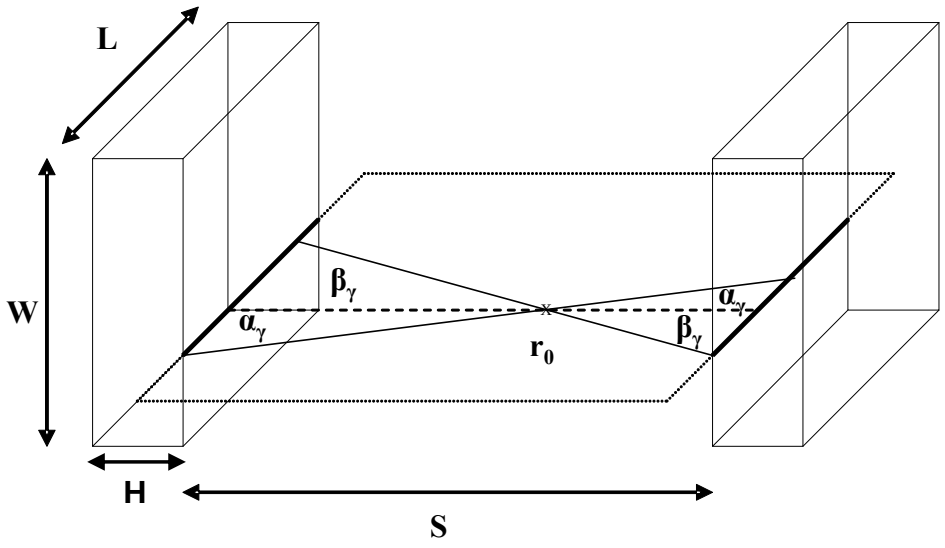

Figure 3.7: Geometrical characterization of the range of detectable emissions from the point $\mathbf{r_0}$ within the plane xy. The angles $\alpha_\gamma(\mathbf{r_0})$ and $\beta_\gamma(\mathbf{r_0})$ define the maximum and minimum detectable LORs within the plane xy.

The previous development can be applied, using simple rotation operations, to detector heads in angular positions different from the ones shown in Figure 3.5, either with both heads rotated by an angle around the z axis or with each of the heads rotated by a different angle around the z axis. In the following, $p(\mathbf{r_0}, \Phi_1, \Phi_2)$, will stand for the probability that a pair of photons emitted from $\mathbf{r_0}$ is detected by two detector heads in positions given by rotation angles of Φ_1 and Φ_2 around the z axis (as shown in Figure 3.8).

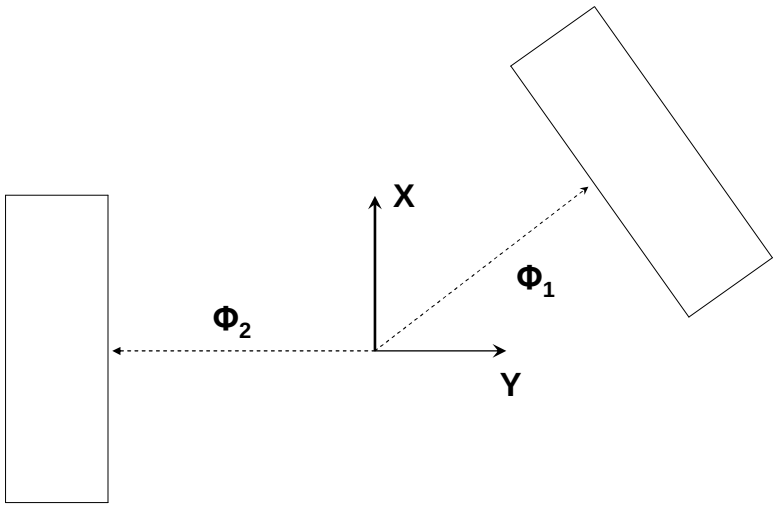

Figure 3.8: Geometrical characterization of the angular positions of the detector heads in a rotating device

The sensitivity matrix for the general case of scanners composed by partial or full rings of detector heads either static or in rotation can be obtained as a composition of $p(\mathbf{r_0}, \Phi_1, \Phi_2)$ terms. In a scanner in which the detector heads can be situated at N different angular positions $ang_1...ang_N$, the probability of detection of an emission from $\mathbf{r_0}$ would be:

$$p(\mathbf{r}_0, .) = \sum_{\Phi_1=ang_1}^{ang_N} \sum_{\Phi_2=ang_1}^{ang_N} p(\mathbf{r_0}, \Phi_1, \Phi_2) p_{pos}(\Phi_1, \Phi_2) p_{coinc}(\Phi_1, \Phi_2) \tag{3.8}$$

where $p_{pos}(\Phi_1, \Phi_2)$ is the probability that the dual heads are situated at the angular positions Φ_1, Φ_2. For static PET scanners, $p_{pos}(\Phi_1, \Phi_2) = 1$, whereas for rotating scanners, assuming that the detector

heads spend the same amount of time in each position $p_{pos}(\Phi_1, \Phi_2) = 1/N$. $p_{coinc}(\Phi_1, \Phi_2)$ equals 1 if coincidences are allowed for the pair of detectors situated at Φ_1, Φ_2 and 0 if such coincidences are not allowed.

3.6 Implementation

In the previous sections, it has been figured out how to adapt the computation of the system models used by the statistical algorithms to the requirements imposed by the use of continuous scintillators. This section deals with the details of the implementation of the system (Subsection 3.6.2) and sensitivity (Subsection 3.6.3) matrices for a commercially available continuous scintillator camera, whose basic features are detailed in Subsection 3.6.1.

3.6.1 PET camera

The continuous scintillators camera with which the new system and sensitivity models have been evaluated is the Albira small animal positron emission tomograph. As shown in Figure 3.9, this tomograph utilizes eight trapezoidal lutetium-yttrium orthosilicate (LYSO) crystals of 9.8 mm thickness with the face towards the center of the FOV measuring 40x40 mm and the face towards the readout system measuring 50x50 mm, (although in the simulations rectangular 40x40 mm heads have been considered). The separation between the opposite detectors is 110.78 mm. Further specifications can be found in Balcerzyk et al. (2009) and Sánchez et al. (2012).

3.6.2 Implementation of the system matrix

In Section 3.4, it has been discussed why the new scheme for the system matrix computation introduced in Chapter 2 is specially appropriate to be used for continuous scintillator data reconstruction. Then, it has been concluded that the adaptation of this scheme to the continuous scintillators constraints involves several changes, all of them concerning the calculation and storage of the detector scatter model (the $p_{mult}(b_j, \gamma, \varphi, \theta_1, \theta_2, l, d_k)$ terms in Eq (3.3)). In this section, it will be shown

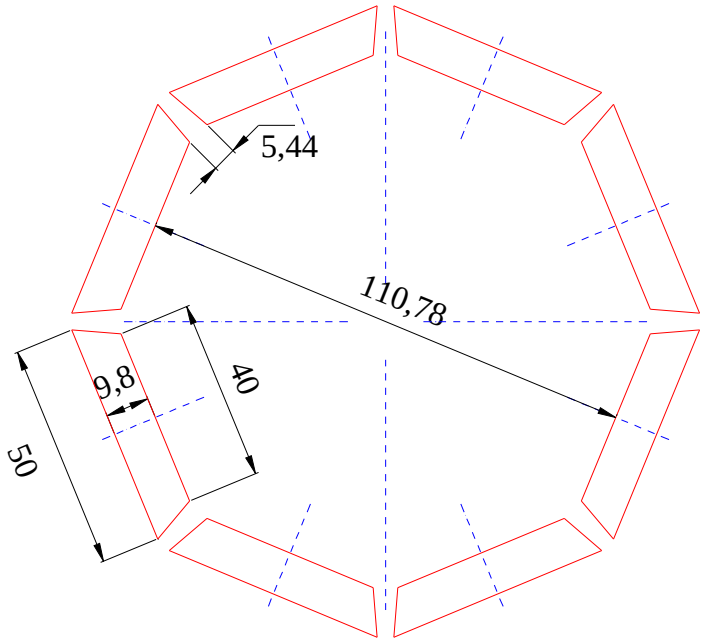

Figure 3.9: Schematic of the Albira PET scanner

how the $p_{mult}(b_j, \gamma, \varphi, \theta_1, \theta_2, l, d_k)$ terms have been calculated and stored for the Albira PET scanner, following the guidelines given in Section 3.4.

Simulation of optical photons

One of the novelties introduced in the precomputation of the detector scatter terms, is that the generation and tracking of optical photons has to be switched on in the MC simulator used to estimate them.

Being the treatment of the crystals a factor that strongly determines the behavior of the optical photons, many parameters are needed to correctly characterize the materials and surfaces of the

scintillators for the optical simulations. In many cases it is not trivial how to match the simulated parametres to the detector properties (Giménez et al. (2004)), which, in turn, are difficult to precise unless a deep knowledge of the manufacturing process is owned. The process of accurately modeling the surface properties in the MC simulations is actually a very complex problem out of the scope of this work. In order to remove possible mismatches between the system model and the real data acquisition process due to an unprecise characterization of the surfaces, the evaluation of the new approach will be carried on just with reconstructions from data simulated with the same parameters used to estimate the system models. A typical configuration (Giménez et al. (2004)) has been chosen in which the crystal has all the surfaces finely ground and the photon-incident surface and the sides are painted black with a reflection factor of 0 (i.e., they absorb the 100% of the light).

Storage of the detector scatter distributions

Once the MC optical parametres have been settled, the behavior of the simulated detector scatter functions $p_{mult}(b_j, \gamma, \varphi, \theta_1, \theta_2, l, d_k)$ has to be studied in order to optimize the storage resources. As has been pointed out in Section 2.7 for a pixelated scanner case, this kind of analysis may seem a complex task when carried out for a seven-dimensional function, but it can be simplified if the detector scatter terms are correctly interpreted. As has been repeatedly mentioned, $p_{mult}(b_j, \gamma, \varphi, \theta_1, \theta_2, l, d_k)$ stands for the probability that a photon emitted from a point $\mathbf{r}$ that belongs to b_j (as stated in Subsection 2.5.2, if the b_j are assumed to be a small voxels, the specific $\mathbf{r}$ considered doesn't make a difference) that propagates along the direction defined by γ, φ, θ_1 and θ_2 and interacts with the scintillator after traveling a distance l within it, gives place to a detection in a crystal d_k. This means that for each combination of b_j, γ, φ, θ_1 and θ_1, a statistical distribution of d_k has to be estimated (now as a continuous density function, instead of as a normalized histogram, as pointed out in Subsection 3.4.1). The variability among distributions obtained for different b_j, γ, φ, θ_1 and θ_1 can be measured using the KL divergence, and will determine the number of distributions that need to be stored. Then, the sampling rate needed to discretize the continuous variable d_k in each distribution will determine how many points have to be stored for each distribution. This step

constitutes another added requirement with respect to the pixelated detectors, where the number of values that make up each distribution is fixed by the discrete nature of the positions d.

According to these requirements, the procedure of computation and storage of the detector scatter terms will be performed as following. First, the detector scatter distributions will be obtained with a very fine sampling of d. The oversampled distributions will be used to study its variability with b_j, γ, φ, θ_1 and θ_1. Using a large number of points improves the reliability of the comparisons among distributions, and do not pose a problem of storage resources, since rapid RAM access to the data is not needed in this part of the process, and distributions can be stored in disk. Once it has been determined how many distributions have to be estimated and for which values of b_j, γ, φ, θ_1 and θ_1, the number of points with which each of them is finally stored will be set. This number will be obtained as a compromise between the minimum that guarantees a correct sampling of the distributions and the maximum allowed by the RAM memory resources. This effort to maximize the precision with which the variable d is sampled is in agreement with the objective of retaining as much as possible the continuous nature of the LORs.

In the following, it will be shown how this procedure has been carried out, using the GATE Monte Carlo simulator, on one of the detector blocks of the Albira PET scanner. The results can be extrapolated to the rest of the detectors. Concerning the variability of the distributions with $\mathbf{r}, \gamma, \varphi, \theta$, as stated in Section 2.7, if the depth-independence is accepted, what these five variables define is the position and orientation of the first interaction of a photon that enters the scintillator. The $p_{mult}(b_j, \gamma, \varphi, \theta_1, \theta_2, l, d_k)$ can thus be restated as a function of these two factors, as $p_{mult}((x', y', z'), \gamma', \varphi', d_k)$, where (x', y', z') are the coordinates of the position of the interaction in the continuous block coordinate system (see Figure 3.10) and γ', φ' are the azimuthal and polar angles that define the angle of incidence. Moreover, based on the way the positioning network works, the terms $p_{mult}((x', y', z'), \gamma', \varphi', d_k)$ can be decomposed in two orthogonal components $p_{mult}((x', y', z'), \gamma', \varphi', d_{kx})$ and $p_{mult}((x', y', z'), \gamma', \varphi', d_{ky})$, where d_{kx} and d_{ky} are respectively, the tangential and axial components of d_k in the block reference system. Next, it will be shown how the variability of the tangential component of the distributions, $p_{mult}((x', y', z'), \gamma', \varphi', d_{kx})$, with

the parametres $x', y', z', \gamma', \varphi'$ has been estimated. The results have been found to apply to the axial component $p_{mult}((x', y', z'), \gamma', \varphi', d_{ky})$ by simple orthogonal rotation of the distributions.

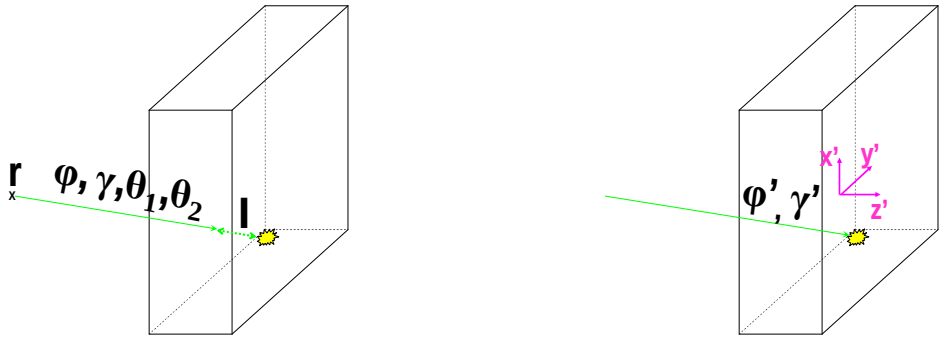

(a) (b)

Figure 3.10: Position of the first interaction as a function of $\mathbf{r}, \gamma, \varphi, \theta, l$ (subfigure a) and as a function of $x', y', z', \gamma', \varphi'$ (subfigure b)

Figure 3.11 shows the experimental setup used to measure the variability of the distributions $p_{mult}((x', y', z'), \gamma', \varphi', d_{kx})$ with the DOI (i.e., coordinate z' being $z' = 0$ the crystal center) of the first interaction in the crystal block. A 511 keV gamma-ray beam normally incident to the detector has been generated from a point source placed in the center of the FOV. One million of emissions were simulated and the events generated were positioned using a centroid approach, recording each event along with the positions (x', y', z') of all the interactions that went before it. Then, the detections have been classified according to the DOI (z' component) of the first interaction that gave place to them. The positions of the detections associated to each DOI constitute the sample used to estimate $p_{mult}((x', y', z'), \gamma', \varphi', d_{kx})$ for that DOI. A normal kernel smoother has been used to estimate the continuous distributions, that have been evaluated at $40,000$ points covering the $40mm$ of detector width (giving place to an interval sampling of 0.001). Table 3.1 shows the KL divergences

among distributions obtained for interactions separated $2mm$ in the z' direction.

The results show great differences among distributions corresponding to different DOIs. Specifically, the KL values are much higher that the values obtained for identical DOI differences in the case of pixelated crystals (see Table 2.11). This is due to the added effect of the optical photons in the continuous scintillators, which as stated in Subsection 3.2.2, give place to LRFs that get narrower as the interaction occurs close to the PMTs. This effect can be clearly observed in Figure 3.12, in which the distributions compared in Table 3.1 have been plotted.

In order to study the variability along the tangential direction x', a collection of point sources in the central transaxial plane located $3mm$ apart in the x' direction covering half of the block (block symmetry has been assumed) have been simulated (Figure 3.13 shows two of these sources). Again, one million of 511 keV gamma photons normally incident to the detector have been generated from each source. The position distributions for the events whose first interaction took place at a fixed DOI (the crystal center, at $z' = 0$, as shown in Figure 3.13) have been estimated using the same procedure as in the previous DOI study. The resulting distributions can be observed in Figure 3.14.

Since each distribution covers a different asymmetric range relative to the distribution center (the position of the first interaction), the KL divergence has not been found to be an appropriated measure in this case. However, by visual inspection, important distortions in the shape of the distributions can be appreciated as the first interaction occurs closer to the detector edge. This means that the distribution obtained for the interaction at the central tangential position ($x' = 0mm$) can be applied, by simple translation, to photons interacting close to the center, but specific distributions have to be calculated for interactions occurring close to the border. Specifically, after further checks, the point $x' = 8mm$ has been found to be the threshold beyond which the border effect is noticeable.

The variablity of the distributions with the photon orientation has been studied for the azimuthal angle γ', since it is the angular component involved in the tangential positioning, but the results can be applied to the axial orientation. Several beams have been generated in the central transaxial plane with their photons entering the crystals at different γ' (being $\gamma' = 0$ equal to perpendicular incidence) but all of them transversing the center of the crystal, as shown in Figure 3.15. The

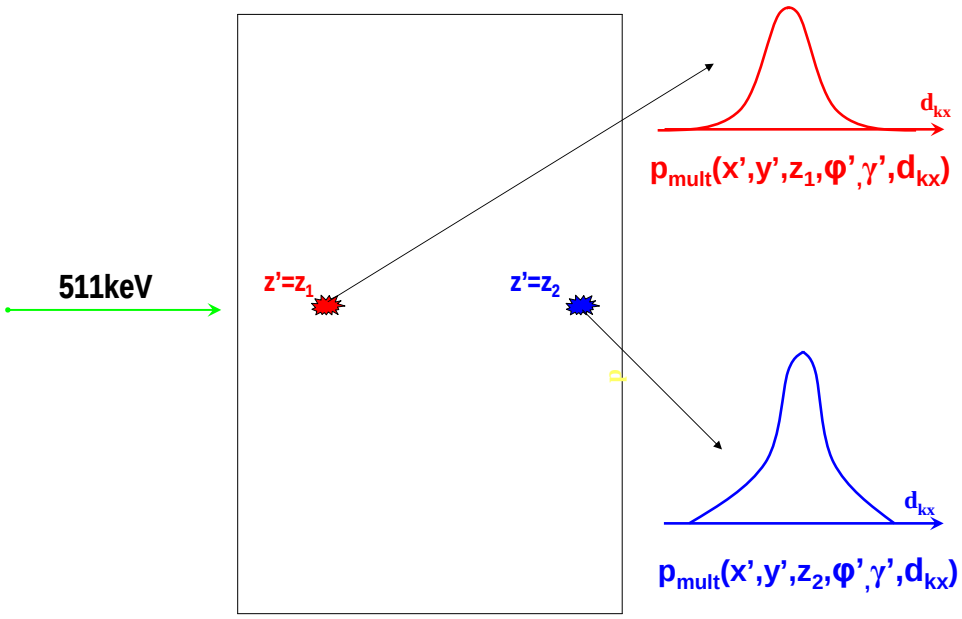

Figure 3.11: Experimental setup to compute the variability of the detector scatter distributions as a function of the doi (z' position, being $z' = 0$ the crystal center) of the interaction in the crystal

z'(mm)	-4.0	-2.0	0.0	2.0	4.0
-4.0	0.0000	0.0719	0.5560	1.9969	120.7
-2.0	0.0668	0.0000	0.2179	1.3549	104.6
0.0	0.4332	0.1837	0.0000	0.5305	74.29
2.0	1.2614	0.8822	0.3639	0.0000	33.81
4.0	3.2651	2.8456	2.1159	1.2006	0.0000

Table 3.1 Variability of the detector scatter distributions with the DOI

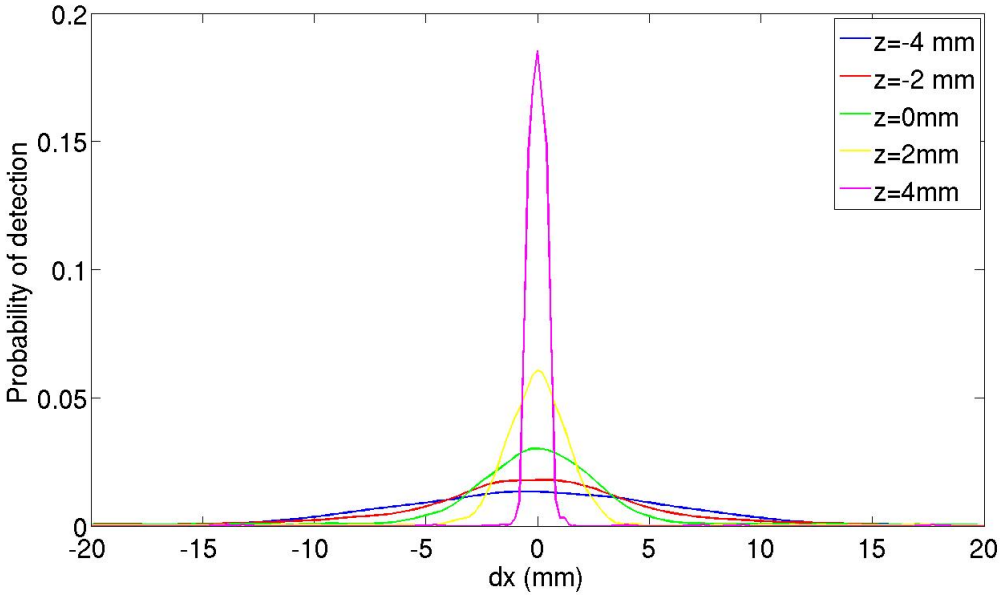

Figure 3.12: Detector scatter distributions for photons interacting at different DOIs

distributions for events with first interaction at this point (i.e., the position $x' = 0$ mm, $z' = 0$ mm in the crystal system), have been obtained following the same procedures as in the previous tests. Table 3.2 shows the KL divergences among these distributions. The differences due to the photon orientation are rather smaller than the differences due to the DOI of the first interaction shown in Table 3.1. It can be indeed observed in Figure 3.16 how the distributions obtained for the different beam orientations are almost identical.

On the basis of the previous experiments, it has been decided to account for the variability of the detector scatter distributions with the position of the interaction in the crystal, but not with the orientation of the photon leading to that interaction. Then, further tests have been performed to determine the final number of distributions that have to be stored. For each DOI z', a distribution has to be computed for the tangential center of the block ($x' = 0$) and its neighborhood (the red crosses in Figure 3.17), and from the threshold fixed at $x' = 8mm$ to the edge of the block at $x' = 20mm$,

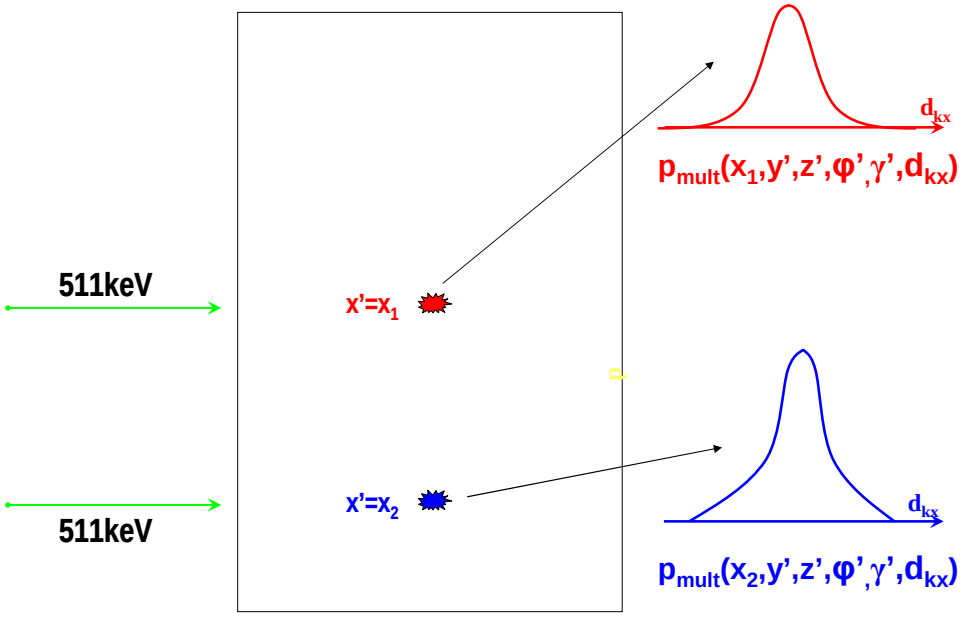

Figure 3.13: Experimental setup to compute the variability of the detector scatter distributions as a function of the x' position of the interaction in the crystal

the distributions affected by the border effect have to be individually estimated (the blue crosses in Figure 3.17). A separation of $1mm$ between the border distributions has been found to be enough to account for their differences. As a result, a total of 13 distributions have to be computed for each DOI. Then, it has been determined that, in the DOI (z) direction, the minimum separation between interactions that gives place to different distributions is $0.1mm$. Being the radial dimension of the scanner $9.8mm$, this means that 98 collections of 13 tangential distributions have to be computed, which makes a total of 1274 $p_{mult}((x', y', z'), \gamma', \varphi', d_{kx})$ distributions. Since, as previously stated, these distributions can be rotated to be used as axial distributions $p_{mult}((x', y', z'), \gamma', \varphi', d_{ky})$, 1274

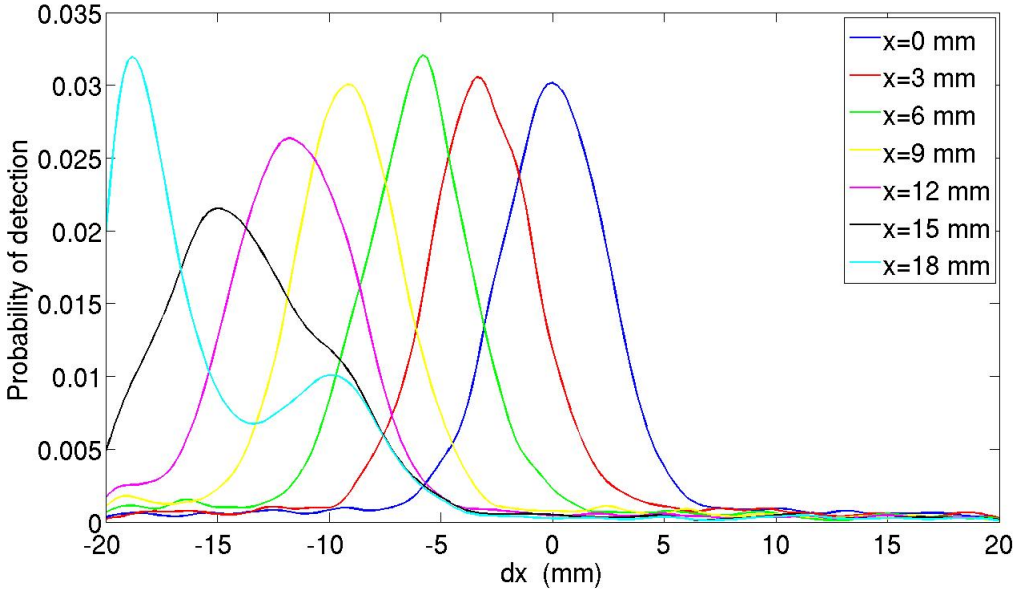

Figure 3.14: Detector scatter distributions for photons interacting at different tangential coordinates.

is the total number of distributions that have to be stored.

Once the total number of distributions has been calculated, it has to be determined the number of points at which each one will be finally evaluated and stored. In each of the distributions, the continuous variable d_{kx} that has to be sampled covers a range of $40mm$, defined by the detector dimensions. However, 98 of the distributions (those corresponding to those centred in the tangential center of the block) are symmetric, and just a half of the range has to be stored. Assuming that the same uniform interval $\delta x'$ will be used to discretize all the distributions, a total of $1176 * 40mm + 98 * 20mm = 49000mm$ of d_{kx} have to be sampled at intervals $\delta x'$. A thorough study of the distribution properties reveals that a sampling value of $\delta x' = 0.2mm$ is enough to represent all of them. The total number of points that have to be stored is therefore $\frac{49000}{0.2} = 245000$. Assuming that the points can be recorded as 4 bytes floating numbers, the storage requirements needed to allocate the detector scatter distributions are in the order of 1MB, which is much less than the current RAM

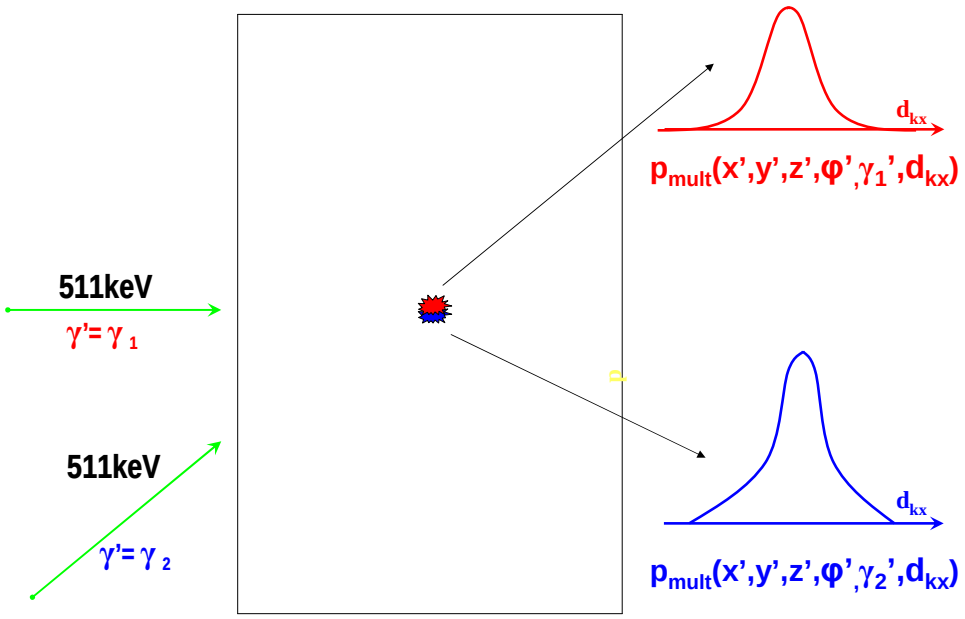

Figure 3.15: Experimental setup to compute the variability of the detector scatter distributions as a function of the angular orientation of the photon leading to the first interaction with the crystal

γ' (deg)	-40	-20	0.0	20	40
-40	0.0000	0.0069	0.0105	0.0142	0.0187
-20	0.0067	0.0000	0.0107	0.0161	0.0139
0.0	0.0088	0.0094	0.0000	0.0072	0.0066
20	0.0139	0.0161	0.0086	0.0000	0.0067
40	0.0187	0.0142	0.0083	0.0069	0.0000

Table 3.2 Variability of the distributions with the angular orientation

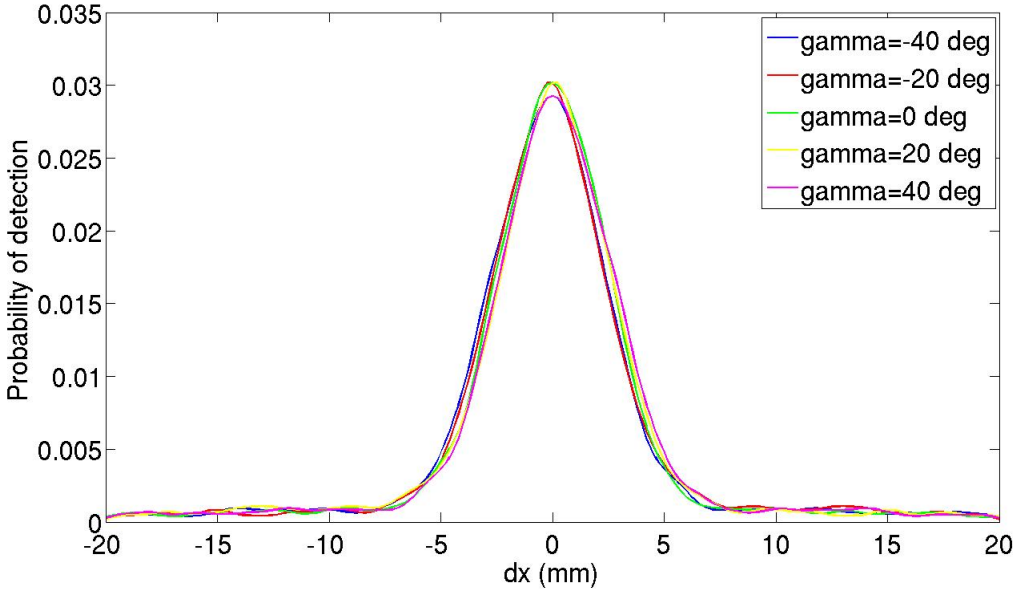

Figure 3.16: Detector scatter distributions for photons entering the detector with different angle of incidence

amount of ordinary industry-standard computers.

3.6.3 Implementation of the sensitivity matrix

The analytical scheme that has been developed in Section 3.5 to compute the sensitivity matrix has been adapted for the small animal Albira PET. The integrals in Eq (3.5) have been numerically estimated for several regions of the FOV of the scanner. Then, two important aspects of the new methodology have been evaluated. First, since the method developed is new (i.e., not based in previous approaches), its reliability and accuracy have to be checked. The Monte Carlo simulator GATE has been used to validate the mathematical model and its implementation. Second, being the main novelty of the new method that it does not assume cylindrical symmetry, it will be checked to what extent this issue is important.

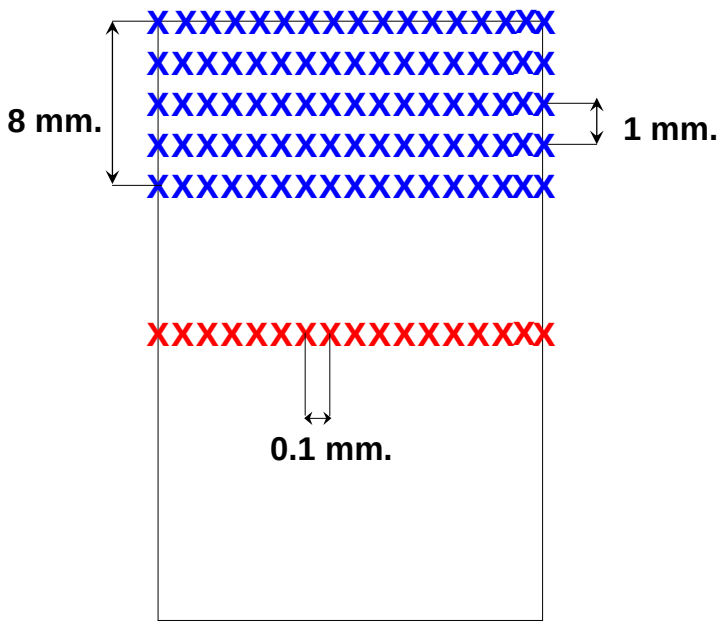

Figure 3.17: Layout of the detector scatter distributions for a generic continuous crystal. Each cross marks the interacting position for which a distribution should be computed. The final number of distributions resulting for the Albira PET scanner dimensions is provided in the text. (Drawings are not to scale).

Validation

The sensitivity terms $p(\mathbf{r}_0, .)$ have been computed using both the new methodology and GATE for two collections of points: the points along a circumference in the central transaxial plane (plane xy in Figure 3.6) placed in the center of the scanner and a grid of points in the yz plane. For both experiments, the normalized root-mean-square error (NRMSE) between both methods is in the

order of 10^{-3}. With regard to the computational time, for the yx plane simulations, one million of gamma-pair emissions from 120 different point sources have been simulated using the Monte Carlo method. The execution time for GATE was around 500 hours whereas the results achieved by means of the analytical method have been obtained in less than 40 seconds in the same computer.

It can be thus concluded that, within the limitations of the Monte Carlo simulations, the new analytical method provides the same results, but noise-free and at a small fraction of the computational cost. The computational time is not an issue in the calculation of the sensitivity term since it has to be computed just once and for all before the reconstruction process, but the speed in the calculations can be an advantage when the sensitivity has to be repeatedly computed due to changes in the camera configuration, the reconstructed FOV, the type and size of the basis functions, etc. In this regard, the method developed could be thought as an excellent tool for the design and evaluation of PET cameras and algorithms.

Rotational symmetry

In order to check the rotational symmetry assumption, Figure 3.18 plots the sensitivity terms computed by means of the proposed analytical method along 90 degrees (note that the normalizing term must be periodic with a periodicity no greater than 45 degrees, since this is the rotational step between consecutive detector blocks) of different radius circumferences in the central transaxial plane centered in the z-axis. A simple look at this plot shows that the sensitivity terms computed along a circumference centered in this axis is not a constant, and therefore it can be concluded that the cylindrical symmetry condition is not always fulfilled. To better illustrate this fact, the percentages of variation (computed as the ratio of the peak-to-peak difference to the mean value) of the normalizing term along some of these circumferences have been computed, and fluctuations over a 17% of variation have been found.

The periodical behavior in the sensitivity that can be observed in Figure 3.18 is caused by the block configuration of the scanner (the angular distance between two consecutive peaks corresponds to the angular step between two consecutive blocks). This means that the cylindrical symmetry

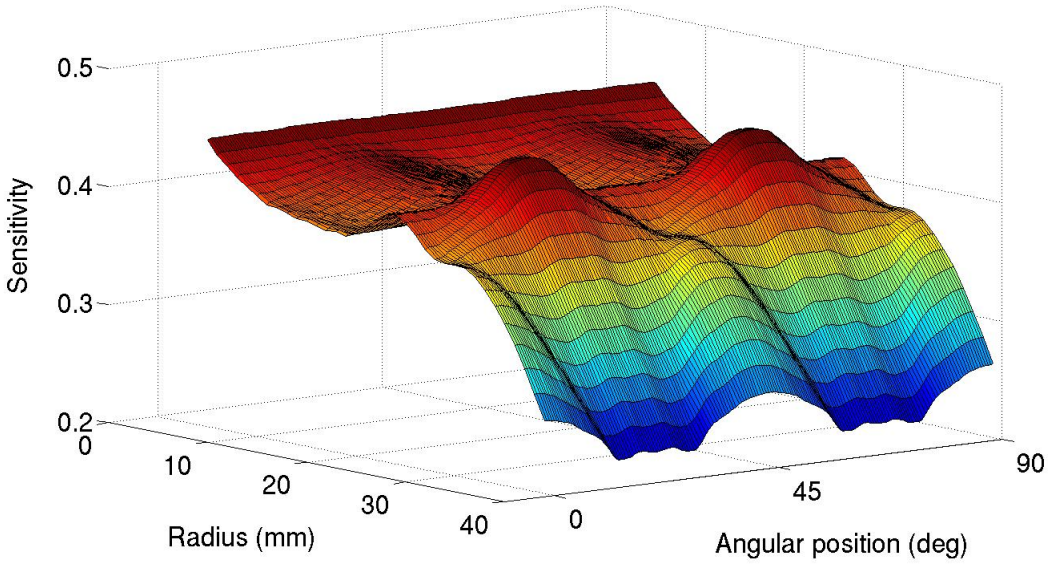

Figure 3.18: Sensitivity along sectors of 90 degrees of circumferences of different radius in the central transaxial plane (xy).

assumption can be appropriate for the case of scanners in which the detector heads rotate continuosly around the z-axis, and it can even be reasonable for the case of stepped rotation in very small angular steps. However, as the angular step between detector heads, either static or in rotation, gets larger, this assumption can give rise to important inaccuracies in the computation of the sensitivity term. This statement can be corroborated through a set simulations for one of the commercially available small animal PET systems, the YAP-PET (Del Guerra et al. (2006)). The YAP-PET is a rotating planar detector PET scanner whose computer controlled rotation allows to perform rotation angular steps of 0.7, 1.4, 2.8, 5.6, 11.2, 22.5, 45 and 90 degrees. Figure 3.19 shows, for the configurations with the highest rotation steps, the values of fluctuation of the sensitivity (computed by means of the analytical method proposed here) along a circumference in the central transaxial plane as a function of its radius. As has been pointed out before, the percentage of variation gets more and more important as the rotation angle increases, reaching values of more than 300% in the 90 degrees

case.

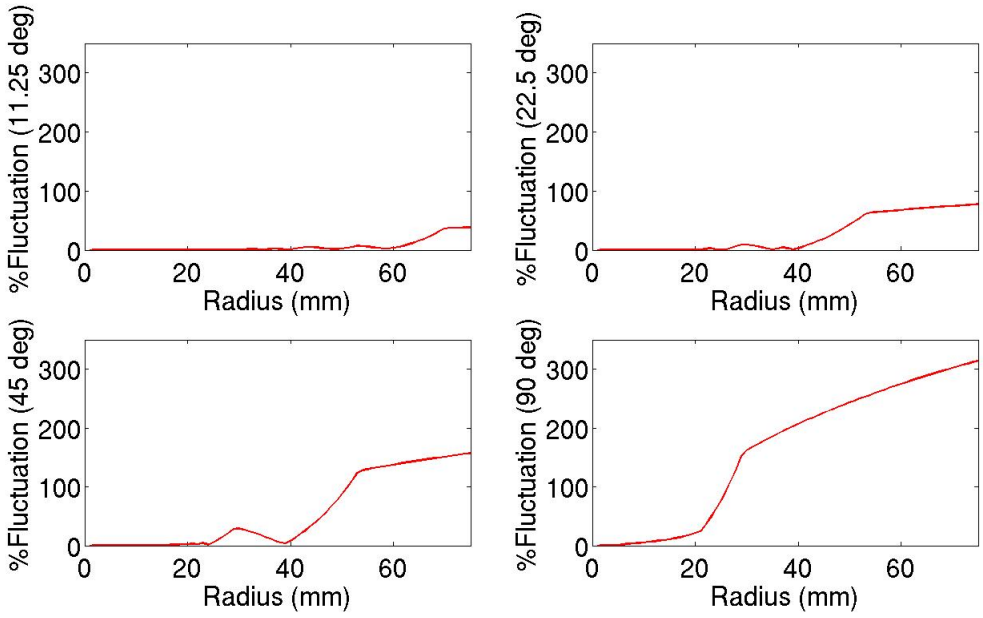

Figure 3.19: Fluctuation of the sensitivity along a circumference as a function of its radius for the different rotation configurations (rotation angular steps of 11.2, 22.5, 45 and 90 degrees) of the YAP-PET scanner. The variation reaches values of more than 300% for the 90 degrees rotation case

3.7 Evaluation

In this section, it will be studied to what extent the quality of the reconstructions from continuous scintillators data can be improved with the use of the new models that have been developed. Subsection 3.7.1 shows how the system and sensitivity matrix implemented for the Albira PET scanner in

Section 3.6 have been incorporated to a reconstruction algorithm in order to be evaluated from different points of view. Subsection 3.7.2 describes the sets of data along with the figures of merit that will be used to evaluate the reconstructions, that will be finally shown and analyzed in Subsection 3.7.3.

3.7.1 Reconstruction algorithm

The system and sensitivity matrix computed as described in Section 3.6 have been incorporated to the list-mode version of the MLEM reconstruction algorithm. As stated in Section 3.2, the list-mode version is specially suited to reconstruction for continuous scintillators data, since it allows to preserve the whole positioning precision of the LORs. Moreover, in order to preserver the Poison statistical nature of the data, no pre-corrections have been done. The parallelized version of the algorithm described in Section 2.8 has been used in order to accelerate the reconstruction process.

Concerning the incorporation of the system matrix to the reconstruction scheme, it has to be noted that the modifications performed to account for the specific features of the continuous scintillators, affect just the computation of the detector scatter terms. In order to speed up the evaluation of the novelties of the model, the whole system matrix scheme in Eq (3.1) has been simplified to account just for the detector scatter effect along with the geometrical and crystal penetration factors, from which, as has been demonstrated in the previous chapter, it should not be separated. Since important effects of the data acquisition process have been ignored in this mathematical model, the reconstructions obtained have a comparative purpose, and their quality should not to be judged in absolute terms.

Concerning the sensitivity matrix, the reliability of new methodology introduced in Section 3.5 for its computation has been tested by direct comparison with MC simulations in Subsection 3.6.3. The differences of the new analytical method with respect to previous similar approaches have been as well checked. Since the new methodology has been sufficiently evaluated, it has not been tested in the image domain but has been used to precompute the sensitivity matrix at the beginning of the reconstruction and then incorporated to the algorithm.

3.7.2 Data and figures of merit

As has been stated in Subsection 3.6.2, all the data used to test the new approaches for the system and sensitivity matrix computation will be simulated with the GATE Monte Carlo simulator. The following data sets of phantom activity distributions for the Albira scanner described in Subsection 3.6.1 have been generated:

1. **Point sources**: With the purpose of measuring the resolution throughout the FOV, a subset of dimensionless point sources has been simulated at the central transaxial plane in different radial positions facing the block center. The corresponding data set contained approximately $800,000$ total coincidences. Profiles have been taken through the point reconstructed images in the axial, radial and tangential directions and the FWHM has been measured to determine the resolution.

2. **Cylindrical phantom**: Once the resolution studies illustrate the potential gain that can be realized by accurately modeling the PET process, a cylindrical phantom with a diameter of 30 mm and length 10 mm has been simulated in order to study the levels of noise amplification achieved. The cylinder uniform activity has led to a data set of $5,000,000$ coincidences. The standard deviation has been measured in the reconstructed phantom and plotted as a function of the iteration number.

3.7.3 Reconstructions

Once the scheme has been simplified to focus on the evaluation of the detector scatter, as mentioned in 3.7.1, reconstructions of the simulated phantoms have been obtained with three different detector scatter models. First, the distributions $p_{mult}(b_j, \gamma, \varphi, \theta_1, \theta_2, l, d_k)$ as obtained in Subsection 3.6.2 have been used to calculate the system matrix during the reconstructions. In the following, these distributions will be referred to as $p_{mult\_ref}(b_j, \gamma, \varphi, \theta_1, \theta_2, l, d_k)$. Then, additional reconstructions have been obtained using two simplified models of detector

scatter. Each of these models ignores one of the guidelines that have been followed to account for the continuous scintillators features in the estimation of the $p_{mult\_ref}(b_j, \gamma, \varphi, \theta_1, \theta_2, l, d_k)$ distributions:

- In order to account for the continuous nature of the LORs, the detector scatter terms, $p_{mult\_ref}(b_j, \gamma, \varphi, \theta_1, \theta_2, l, d_k)$, have been estimated as continuous distributions of d_k using a kernel smoothing function and then discretized using the maximum precision allowed by the storage resources. In order to evaluate whether the methodology and precision used to estimate the detector scatter makes a difference with respect to those used in the general pixelated case, the distributions of the first simplified model have been estimated as discrete histograms of d, with 1 mm (the average size of discrete crystals) bins. In the following, these distributions will be referred to as $p_{mult\_LOR}(b_j, \gamma, \varphi, \theta_1, \theta_2, l, d_k)$,
- In order to account for the particular behavior of the scintillation light in continuous crystals, the generation and tracking of optical photons have been activated in the simulations used to estimate the $p_{mult\_ref}(b_j, \gamma, \varphi, \theta_1, \theta_2, l, d_k)$ terms. As has been observed in Figures 3.12 and 3.14, the added effect of the optical photons is that important differences are found in the shape of the detector scatter distributions as the position of the first interaction with the crystal (defined by the x', y', z' coordinates in Figure 3.10b) changes. In order to evaluate whether taking into account such differences makes a difference in the reconstructions, the second simplified model uses an invariant detector scatter distribution, independent of the point of interaction. Specifically, the distribution corresponding the center of the crystal (i.e., the interaction point $x = 0, y = 0, z = 0$) has been used. In the following, this distribution will be referred to as $p_{mult\_INV}(b_j, \gamma, \varphi, \theta_1, \theta_2, l, d_k)$.

Figures 3.20-3.22 illustrate the comparison performed between the three mentioned approaches. The results are labeled as *ref*, *LOR* and *INV*, according to the detector scatter model that has

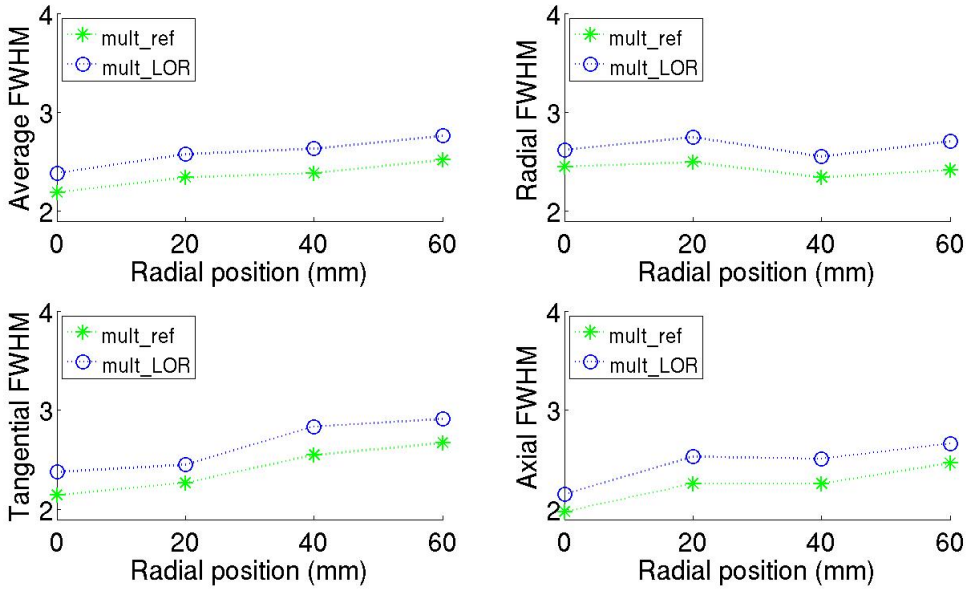

Figure 3.20: Average, radial, tangential and axial FWHM or the reconstructed point sources plotted against the radial position using the new scheme for reconstruction with continuous detectors (results labeled as *ref*) and an approach in which the LORs have to be binned to discrete positions (results labeled as *LOR*).

been used in the reconstructions. The radial, tangential, axial and average resolution (as measured by FWHM) of the reconstructed point phantoms after 20 MLEM iterations is shown in Figure 3.20 in order to compare the resolution properties of the reconstructions using the *ref* and *LOR* models. Figure 3.21 compares in the same way the resolution achieved using the *ref* and *INV* models. The noise tests are shown in Figure 3.22, measured as the standard deviation (normalized to the mean) of the reconstructed cylindrical phantom with uniform activity.

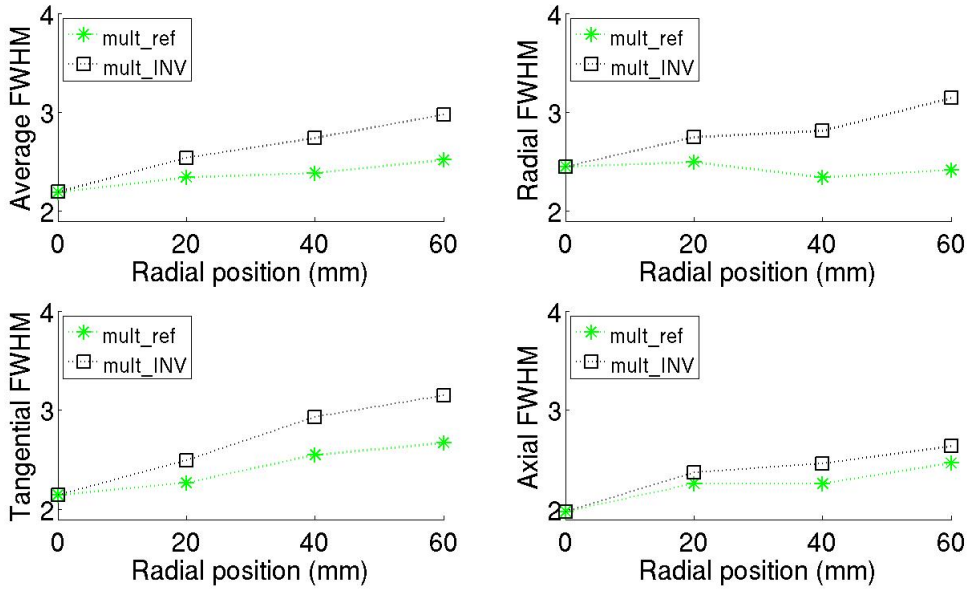

Figure 3.21: Average, radial, tangential and axial FWHM or the reconstructed point sources plotted against the radial position using the new scheme for reconstruction with continuous detectors (results labeled as *ref*) and an approach in which the LRF variations are not accounted for (results labeled as *INV*).

3.8 Discussion

Several technical developments have led to a comeback of the continuous scintillators in the last years. Some important differences exist, in terms both of equipment and of the data formation process, between the resurgent continuous detector scanners and the prevailing pixelated devices. On the one hand, these differences translate into certain advantages of the continuous detectors over their pixelated counterparts. On the other hand, if the peculiarities of the continuous detectors are not incorporated to the system model used in the statistical reconstructions, these advantages won't be fully exploited. In this chapter, it has been studied

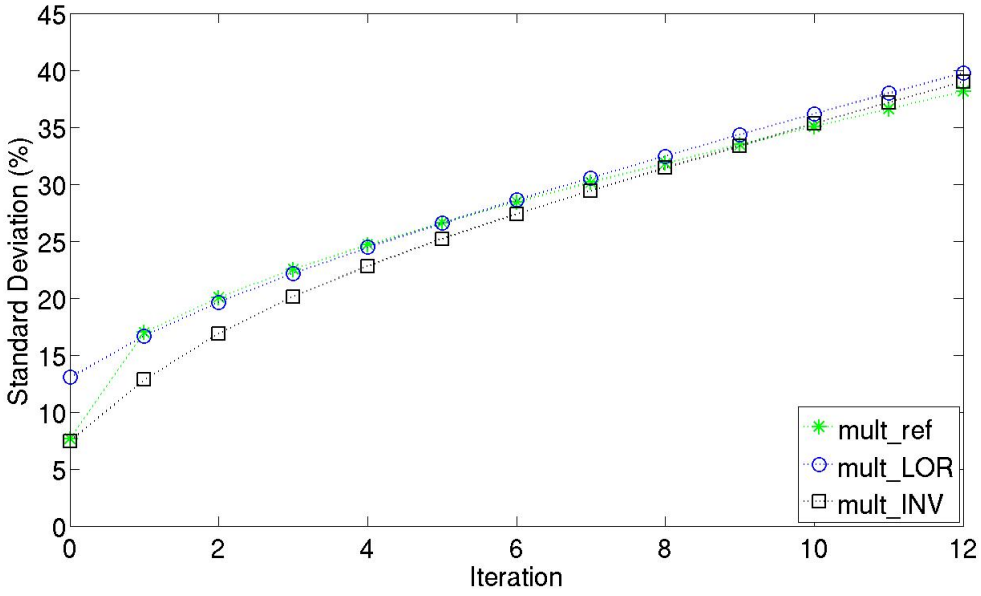

Figure 3.22: Normalized standard deviation of the reconstructed cylindrical phantom plotted against the iteration number.

how some of the specific features of the continuous scintillators can be accounted for in the statistical reconstructions and to what extent this can improve the quality of the images:

(a) One of the distinguishing features of the continuous detector devices is that the positions defining the LORs are not associated to the centers of individual crystals. Grouping the continuous LORs in discrete bins to suit to the existing reconstruction methods for pixelated cameras involves, therefore, a waste of accuracy. To avoid this issue, a list-mode version of the algorithm is needed along with an appropriate system matrix. As discussed in Section 3.2, such system model should maximize the analytical calculations in order to keep as much as possible the original LORs while minimizing the experimental estimations so that the data rebining they involve can be finely done without high storage requirements. The new system matrix scheme introduced in Chapter

2 (Eq (2.10)) meets these requirements (indeed the original motivation leading to the development of this scheme has been the search for an appropriate continuous detectors model, as discussed in Motivation and Objectives). The **first result** in this chapter has been to adapt the system matrix scheme in Eq (2.10) so that it keeps as much as possible the original positions of the LORs provided by the continuous detectors. It has been shown in Subsection 3.4.1 how this adaptation involves just modifications in the methodology used to estimate the detector scatter. The histogramming of events has been substituted by a kernel smoothing estimation, to account for the continuous nature of the LORs, followed by a careful discretization of the data, based on a compromise between precision and storage. In Section 3.6 it has been demonstrated how to carry out this procedure in the estimation of the detector scatter of the Albira PET scanner and then, in Section 3.7, it has been shown how its use increases the resolution (as shown in Figure 3.20) while reducing the noise propagation (as shown in Figure 3.22) of the reconstructions.

(b) Another differentiating feature of the continuous scintillators is that, in the absence of the isolation provided by the pixelated crystals, the light is not channeled and can propagate over the continuous block. This translates into LRFs that can vary remarkably depending on the position of the light source within the scintillator. The **second result** in this chapter is the incorporation of this effect to the system matrix by activating the optical photons in the MC simulations used to model the detector scatter. As has been discussed in Subsection 3.4.2, this is the best way to account for the scintillation light, since it is intrinsically related to the multiple interactions (each interaction with the scintillator behaves as a light source). Moreover, this measure just affects the existing system model in terms of the simulation time of the detector scatter distributions, which is performed just once and for all. The effect of incorporating the optical photons to the detector scatter model can be observed in the results shown in Section 3.6, for the simulations carried out for the Albira PET scanner. Strong variations in the detector

scatter behavior as the position of the first interaction in the crystal varies can be observed in Figures 3.12 and 3.14. Moreover, the KL divergences among detector scatter distributions obtained at different DOIs shown in Table 3.2 are remarkably different than their counterparts in a pixelated scanner (Table 2.5 in Chapter 2). A significant improvement in the resolution of the reconstructions is achieved with the incorporation of the optical phenomena (as shown in Figure 3.21) with lower noise levels (as shown in Figure 3.22).

(c) Finally, in the continuous detector case, the sensitivity term can't be computed according to Eq (3.2), as it is based on the discrete nature of the detectors. The **third result** in this chapter is the development of an analytical methodology for the sensitivity computation, which, unlike previous similar approaches, is not based on a cylindrical symmetry assumption. The results obtained with the new method show that, within the limitations of the Monte Carlo simulations, the new analytical method provides similar results at a small fraction of the computational cost. Moreover, the results obtained shown in Figures 3.18 and 3.19 confirm that in many cases the cameras do not present exact cylindrical symmetry.

Chapter 4

Conclusions and Future Work

Conclussions

Chapters 2 and 3 have dealt with the two aims set out at the beginning of this thesis. First, Chapter 2 has addressed the exploitation of analytical methodologies for the calculation of the system matrix, now that the technological advances in computing allow using increasingly higher complex models. Then, in Chapter 3 the results of Chapter 2 have been adapted and combined with new results to develop a system model that suits the specific requirements of the resurgent continuous detectors devices. The main results of this work can be summarized as follows:

- A new system matrix scheme has been developed that gathers the efficiency of the successful factored approaches with the (so far unexploited) precision of the analytical methodologies. The new approach has been obtained after a thorough study of the faithfulness with which both approaches depict the data formation process, using a criterion of maximum accuracy at lower computational cost.

- A new procedure for the detector scatter estimation using Monte Carlo simulations has been developed. Unlike previous approaches, the new method accounts for the variability of the detector scatter within the scintillators, whose importance has been experimentally demonstrated in this work. The new procedure is crucial in order to take fully advantage of the new system matrix scheme, and any other scheme based on modeling the individual effects with the most appropriate methodology and the maximum accuracy.

- For the first time, a statistical reconstruction has been fully adapted to continuous detectors, in order to optimize the performance of this type of devices. Two different issues of the list-mode statistical algorithms have been addressed with this purpose:

  - Concerning the **system matrix**, the new approach developed, described in the two previous points, has been shown to be highly appropriate for use with continuous detectors. The properties of accuracy and flexibility in which it is based allow to improve the quality of the reconstructions by incorporating two important features of the continuous detector devices to the statistical model:

    * The definition of the lines of response (LORs), that in the continuous blocks is not determined by the discrete positions of individual crystals. It has been demonstrated how, unlike previous approaches based on the precomputation of the matrix, the analytical nature of the new scheme allows to retain the original data without demanding high storage resources, just by slightly redefining the detector scatter estimation procedure.

    * The behavior of the optical photons in the continuous blocks, which causes the light response function (LRF) to change with the position of the source within the crystal. This effect has been incorporated just by activating the simulation of optical photons in the detector scatter simulations. This adds further refinement to the model and, therefore, quality to the reconstructions, at the only prize of increasing the time of the detector scatter precomputation.

- Concerning the **sensitivity matrix**, a new method for its computation has been introduced that is not based in the discrete nature of the detectors. Unlike previous similar approaches, the new method does not rely on the azimuthal symmetry of the scanners, an assumption whose inaccuracy for rotating planar devices has been experimentally demonstrated in this work.

Future work

There are several lines of research arising from this work which should be pursued:

- Concerning the new system matrix scheme, although its development has been based on both accuracy and efficiency principles, its implementation and use have focused on proving the improvements achieved in the images (which was the aim or this work) rather than on practical purposes. Once the benefits of the new model in the reconstructions have been demonstrated, the times reported have to be reduced in order to make it workable. Several measures are suggested that can decrease the reconstruction times to the level of the feasibility:
  - More efficient implementations of the system matrix can surely be achieved. Even if several strategies have already been applied to speed up its computation, there are still other advanced tactics for attacking code optimization (profiling, register allocation, disassembling, using CPU/platform specific features etc) that have not been explored yet.
  - More efficient numerical integration techniques can be used to calculate Eq (2.40). For example, Moehrs et al. (2008) show that the Gaussian integration gives better results compared to equally spaced integration points (trapezoidal integration, used in this work), allowing to reduce the number of points used in the numerical estimations.

- The research centers in which the PET experiments are performed own greater clusters with more powerful computers than the one used to measure the reconstruction times in this work. For example, it has been estimated that the reconstruction of the point sources phantom described in Subsection 2.8.2 could be reduced from the reported 30 days to 5 days, using the Crunchy cluster of the Spanish National Center for Biotechnology (CNB-CSIC)(28 nodes, each with 8 cores with 2.83GHz Intel(R) Xeon(R) processors)

- A block iterative method can be used to accelerate the reconstructions. These approaches are significantly faster than the MLEM algorithm (Vardi et al. (1985)), since they do not use all the data at each iteration. The MLEM has been the reconstruction scheme used in this work, in order to remove from the comparison among system models the convergence issues related to the block methods. But once the comparison has shown the advantages of the new method for the system matrix computation, it can be incorporated to a faster algorithm. For example, the ordered-subset version of the MLEM (OSEM) (Hudson and Larkin (1994)) produces images of similar quality than MLEM in a fraction of the time on the order of the number of subsets in which the data are splitted.

- Further reductions on reconstruction time can be achieved by resorting to multiresolution schemes (Ranganath et al. (1988), Raheja and Dhawan (2000)). Since the hybrid model in Eq (2.40) allows for the size of the basis function to be changed between iterations, the number of voxels of the FOV can be set to a low value during the first stages of reconstruction, when only the low frequencies (gross details) of the image are recovered and then it may be increased as the high frequency components begin to appear.

- Finally, the emergent field of the GPU implementations, that has demonstrated to accelerate significatively other reconstructions (Herraiz et al. (2011), Pratx and Levin (2011)) could be exploited in order to improve the current efficiency.

Once the reconstruction times have been reduced, reconstructions from complex measured data should be obtained, in which the noncollinearity, attenuation and normalization factors, that have not been considered in the reconstructions performed in this work, are accounted too. This would allow to measure the performance of the new method in absolute terms and not just with comparison purposes, as has been done in this work.

- Concerning the new detector scatter modeling, although the experiments performed to estimate the distributions have been based on real scanners features, there are several realistic aspects related to the detection and processing of the multiple interactions (photomultipliers layout and features, positioning algorithms, the already mentioned surface treatment in continuous scintillators...) that have not been matched in the simulations. Such a specific modeling requires expert knowledge both of the devices and of the simulation tools that is out of the scope of this work. Here it wanted to be shown how a proper detector scatter estimation, that has been traditionally discarded, can improve significantly the quality of the reconstructions. Once this issue has been tested with simulated phantoms (for which the experiments performed do match the data acquisition process) and the procedure to account for it has been established, its use with real measured data, would require expert simulations for each specific scanner.

Appendix A

Angular integration limits for the system matrix

In this Appendix, it will be shown how to compute the value of the integration limits for φ and γ in Eq (2.3). It has been pointed out in Subsection 2.4.3 that these variables define the orientation of the gamma pairs emitted from the point $\mathbf{r}$ and that the integration interval should include just those pairs that reach the detectors in a certain neighbourhood of the LOR d. Although the extent of the neighbourhood depends on the specific characteristics of the device (Stickel and Cherry (2005)) and has to be estimated for each camera (Iriarte et al. (2009) shows a procedure to undertake this task), it will be generically represented as shown in Figure A.1 by rectangles of dimensions z_{max}, x_{max} in the axial and tangential direction respectively, centred in the points $\mathbf{p_1}$ and $\mathbf{p_2}$ that define the LOR d in the detectors. The integration limits of Eq (2.3) will be computed as the angles spanned by $\mathbf{r}$ into the rectangles.

The range covered by the polar angle γ will be considered first. As shown in Figure A.2, the angle of view of the point $\mathbf{r}$ with coordinates x_p, y_p, z_p in the axial direction of the rectangle

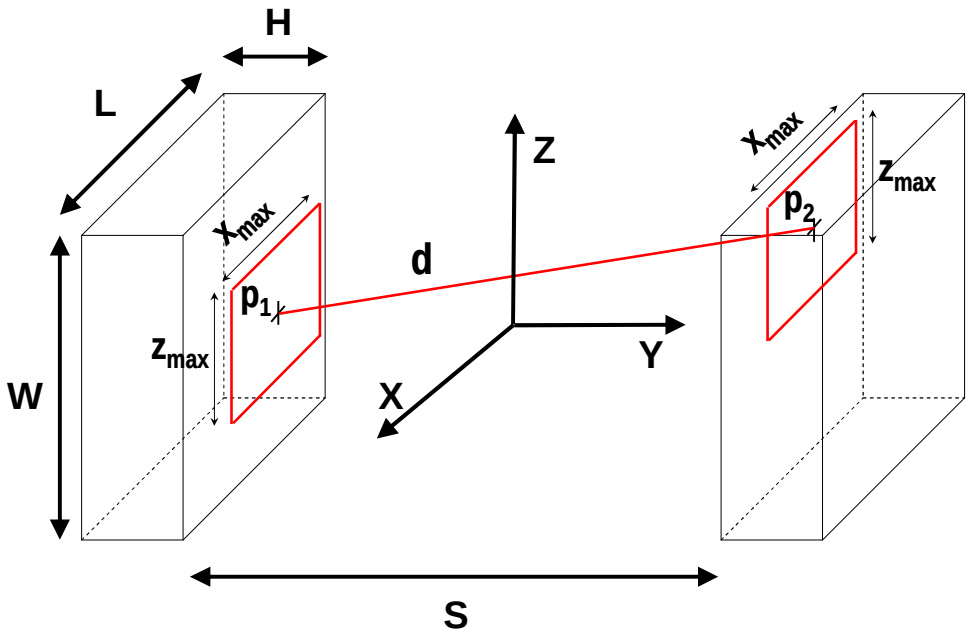

Figure A.1: Geometrical characterization of the neighbourhood of the LOR d. The angles defining the pairs that reach the detectors within the red rectangles are those that have to be considered in the integration

is defined by the points A, B, C, D, whose coordinates are:

$$A = (x_1 + (\frac{S}{2} + y_p)\tan\gamma, y_1, z_1 + z_{max}) \quad \text{(A.1)}$$

$$B = (x_1 + (\frac{S}{2} + y_p)\tan\gamma, y_1, z_1 - z_{max}) \quad \text{(A.2)}$$

$$C = (x_2 - (\frac{S}{2} - y_p)\tan\gamma, y_2, z_2 - z_{max}) \quad \text{(A.3)}$$

$$D = (x_2 - (\frac{S}{2} - y_p)\tan\gamma, y_2, z_2 + z_{max} \quad \text{(A.4)}$$

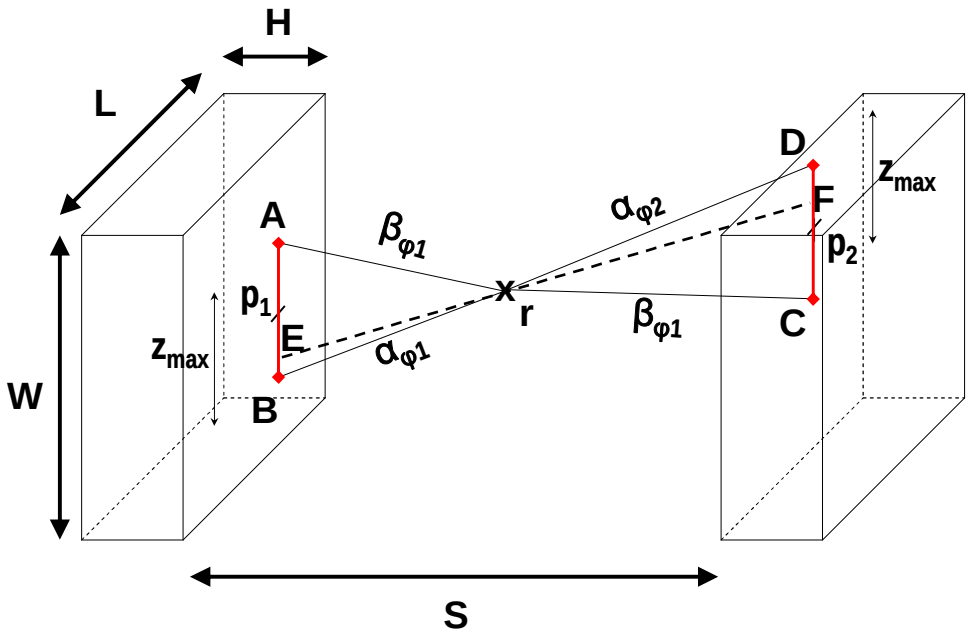

Figure A.2: The angles of view from point **r** into the neighbourhood of LOR d, α_φ , β_φ, are defined by the points A,B,C,D,E and F.

In order to integrate only lines that fully lie within detector limits, the z coordinate of these points must be restricted to $\pm W/2$ (see the definition of the block dimensions in Figure A.1):

$$if|z_1 + z_{max}| > \frac{W}{2} \quad then \quad A = (x_1 + (\frac{S}{2} + y_p)\tan\gamma, y_1, \quad \frac{W}{2}) \tag{A.5}$$

$$if|z_1 - z_{max}| > \frac{W}{2} \quad then \quad B = (x_1 + (\frac{S}{2} + y_p)\tan\gamma, y_1, \quad -\frac{W}{2}) \tag{A.6}$$

$$if|z_2 + z_{max}| > \frac{W}{2} \quad then \quad D = (x_2 - (\frac{S}{2} - y_p)\tan\gamma, y_2, \quad \frac{W}{2}) \tag{A.7}$$

$$if|z_2 - z_{max}| > \frac{W}{2} \quad then \quad C = (x_2 - (\frac{S}{2} - y_p)\tan\gamma, y_2, \quad -\frac{W}{2}) \tag{A.8}$$

The angles seen by $\mathbf{r}$ into the detector heads restricted to the rectangle are (see Figure A.2) are:

$$\alpha_{\varphi 1} = \widehat{B\mathbf{r}E} \tag{A.9}$$

$$\beta_{\varphi 1} = \widehat{A\mathbf{r}E} \tag{A.10}$$

$$\alpha_{\varphi 2} = \widehat{D\mathbf{r}F} \tag{A.11}$$

$$\beta_{\varphi 2} = \widehat{C\mathbf{r}F} \tag{A.12}$$

Points E and F are the ends of the segment resulting from the intersection of the plane $z = z_p$ with the rectangle given by $ABCD$. The analytical expressions for E and F are:

$$E = (x_1, y_1, z_p) \tag{A.13}$$

$$F = (x_2, y_2, z_p) \tag{A.14}$$

Finally, integration angles α_φ , β_φ in the axial direction will be given by:

$$\alpha_\varphi = min(\alpha_{\varphi 1}, \alpha_{\varphi 2}) \tag{A.15}$$

$$\beta_\varphi = min(\beta_{\varphi 1}, \beta_{\varphi 2}) \tag{A.16}$$

Similar reasoning follows for the computation of the azimultal limits in the tangential plane, now based on the scheme shown in Figure A.3. The limits of the neighbourhood imposed by x_{max} are given by points A', B', C', D':

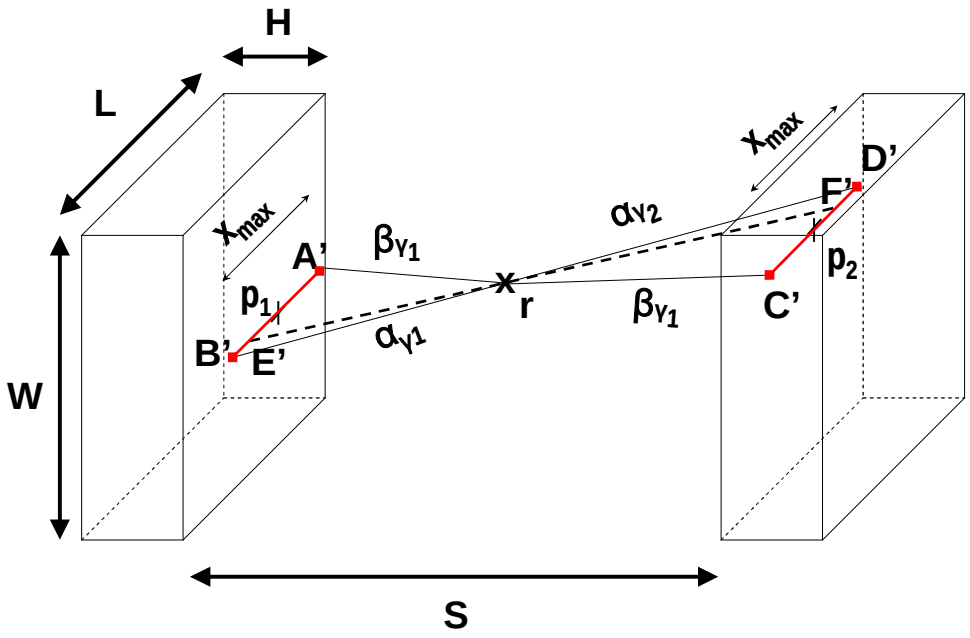

Figure A.3: The angles of view from point **r** into the neighbourhood of LOR d, α_φ , β_φ, are defined by the points A',B',C',D',E' and F'.

$$A' = (x_1 + x_{max}, y_1, z_1) \tag{A.17}$$

$$B' = (x_1 - x_{max}, y_1, z_1) \tag{A.18}$$

$$C' = (x_2 + x_{max}, y_2, z_2) \tag{A.19}$$

$$D' = (x_2 - x_{max}, y_2, z_2) \tag{A.20}$$

but

$$if \quad |x_1 + x_{max}| > \tfrac{L}{2} \quad then \quad A' = (-\tfrac{L}{2}, y_1, z_1) \tag{A.21}$$

$$if \quad |x_1 - x_{max}| > \tfrac{L}{2} \quad then \quad B' = (\tfrac{L}{2}, y_1, z_1) \tag{A.22}$$

$$if \quad |x_2 + x_{max}| > \tfrac{L}{2} \quad then \quad D' = (-\tfrac{L}{2}, y_2, z_2) \tag{A.23}$$

$$if \quad |x_2 - x_{max}| > \tfrac{L}{2} \quad then \quad C' = (\tfrac{L}{2}, y_2, z_2) \tag{A.24}$$

The angles of view from **r** into detector heads within this limits, are (see Figure A.3):

$$\alpha_{\gamma 1} = \widehat{E'\mathbf{r}B'} \tag{A.25}$$

$$\beta\gamma_1 = \widehat{A'\mathbf{r}E'} \tag{A.26}$$

$$\alpha_{\gamma 2} = \widehat{D'\mathbf{r}F'} \tag{A.27}$$

$$\beta_{\gamma 2} = \widehat{C'\mathbf{r}F'} \tag{A.28}$$

where E' and F' are the ends of the intersection of the plane $x = x_p$ with the rectangle given by $A'B'C'D'$:

$$E' = (x_p, y_1, z_1) \tag{A.29}$$

$$F' = (x_p, y_2, z_2) \tag{A.30}$$

The integration limits in tangential direction are:

$$\alpha_\gamma = min(\alpha_{\gamma 1}, \alpha_{\gamma 2}) \tag{A.31}$$

$$\beta_\gamma = min(\beta_{\gamma 1}, \beta_{\gamma 2}) \tag{A.32}$$

Appendix B

Spatial orientation of the photons

In this Appendix, it will be shown how to compute the spatial orientation of the photons of a gamma pair, given by the angles φ, γ, θ_1 and θ_2, defined in Subsections 2.4.3 and 2.4.4. As stated in Subsection 2.4.3, φ and γ define the polar and azimuthal angles of the gamma pair if it were perfectly collinear. In that case, both photons would share its spatial orientation, whose unitary vector in cartesian coordinates is:

$$\begin{bmatrix} \sin\varphi\cos\gamma \\ \sin\varphi\sin\gamma \\ \cos\varphi \end{bmatrix}$$

The effect of the non-collinearity makes each of the photons have a different spatial orientation. The new unitary vectors associated to each of the photons can be obtained by applying three dimensional rotation matrices to the original unitary vector. Following a z-y-z convention, the Euler angles defining the rotation of the vectors are given by $(\theta, \theta_2, 0)$, being $\theta = \frac{\pi - \theta_1)}{2}$ for the photon labeled $p1$ in Figure B.1 and $\theta = \frac{\pi + \theta_1)}{2}$ for the photon labeled $p2$.

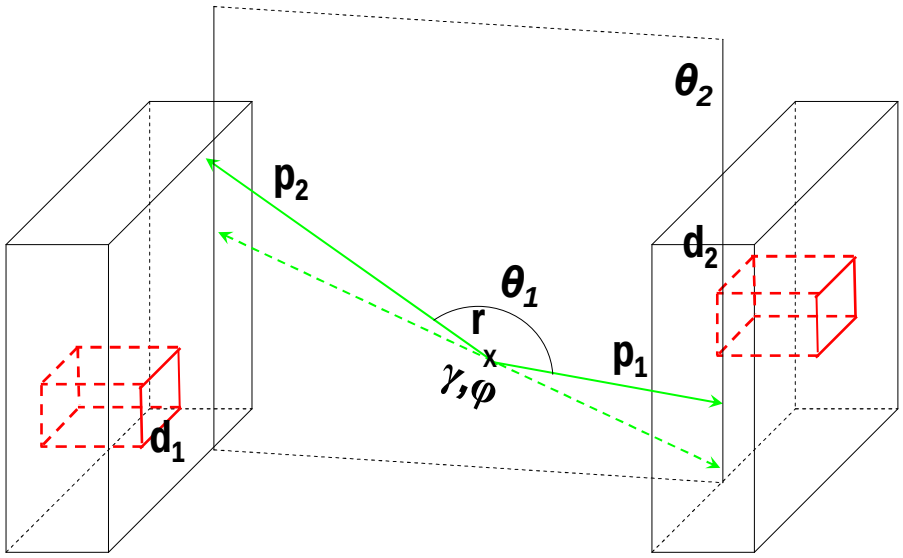

Figure B.1: Non-collinearity. The spatial orientation of the photons of the pair, p_1 and p_2 can be calculated from φ, γ, θ_1 and θ_2.

The resulting rotating matrices (for the corresponding θ angles previously defined) are:

$$\begin{bmatrix} \cos\theta\cos\theta_2 & \cos\theta\sin\theta_2 & -\sin\theta \\ -\sin\theta_2 & cos\theta_2 & 0 \\ \sin\theta\cos\theta_2 & \sin\theta\sin\theta_2 & \cos\theta \end{bmatrix}$$

And its aplication to the original vector in Eq (B.1) leads to the new unitary vectors:

$$\begin{bmatrix} \cos\theta\cos\theta_2\sin\varphi\cos\gamma + \cos\theta\sin\theta_2\sin\varphi\sin\gamma - \sin\theta\cos\varphi \\ -\sin\theta_2\sin\varphi\cos\gamma + \cos\theta_2\sin\varphi\sin\gamma \\ \sin\theta\cos\theta_2\sin\varphi\cos\gamma + \sin\theta\sin\theta_2\sin\varphi\sin\gamma + \cos\theta\cos\varphi \end{bmatrix}$$

Appendix C

Integration limits for the sensitivity matrix

In this Appendix, it will be shown how to compute the integration limits involved in the new methodology for the sensitivity matrix computation developed in Section 3.5.

The angular limits, $\alpha_{\varphi}(\mathbf{r}_0, \gamma)$ and $\beta_{\varphi}(\mathbf{r}_0, \gamma)$, of the integral in Eq (3.4) will be computed first. The angles of view from the point $\mathbf{r}_0$ of coordinates $(x_0, y_{0,} z_0)$ into each detector within the plane Π_{γ}(see Figure C.1) are:

$$\alpha_{\varphi 1}(\mathbf{r}_0, \gamma) = \widehat{D\mathbf{r}_0 F} \quad \text{(C.1)}$$

$$\beta_{\varphi 1}(\mathbf{r}_0, \gamma) = \widehat{F\mathbf{r}_0 C} \quad \text{(C.2)}$$

$$\alpha_{\varphi 2}(\mathbf{r}_0, \gamma) = \widehat{E\mathbf{r}_0 B} \quad \text{(C.3)}$$

$$\beta_{\varphi 2}(\mathbf{r}_0, \gamma) = \widehat{A\mathbf{r}_0 E} \quad \text{(C.4)}$$

According to the dimensions shown in Figure C.1, the analytical expressions for the points

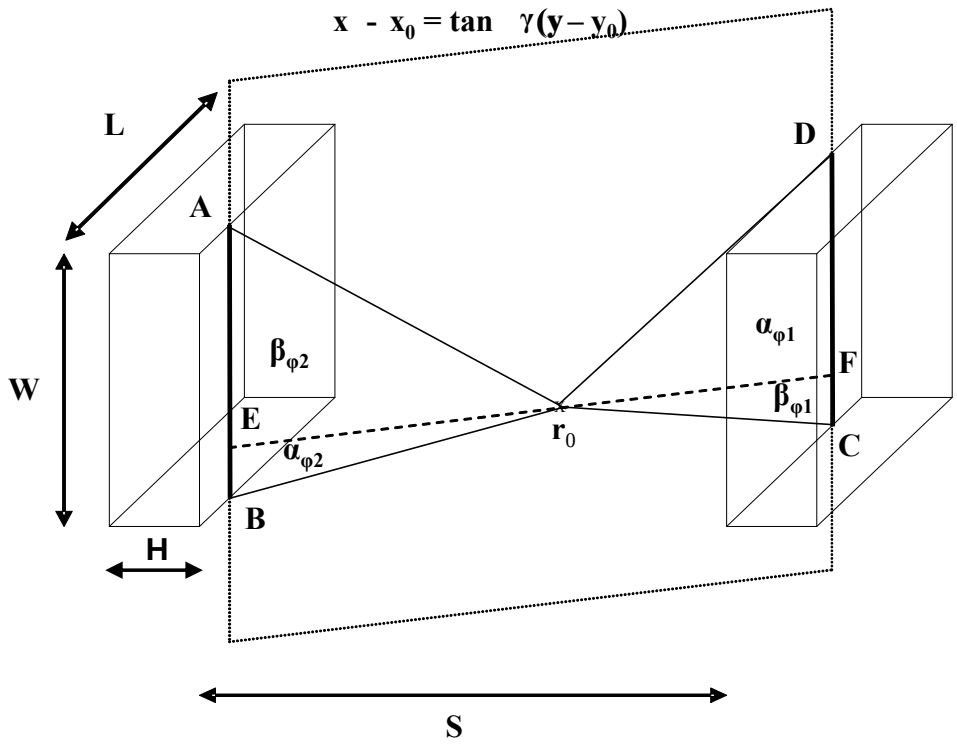

Figure C.1: Geometrical characterization of the range angles of view from point $\mathbf{r}_0$ into the detector heads within the plane Π_γ

A, B, C, D,E and F are:

$$A = (x_0 - (\frac{S}{2} + y_0)\tan\gamma, -\frac{S}{2}, \frac{W}{2}) \quad \text{(C.5)}$$

$$B = (x_0 - (\frac{S}{2} + y_0)\tan\gamma, -\frac{S}{2}, -\frac{W}{2}) \quad \text{(C.6)}$$

$$C = (x_0 + (\frac{S}{2} - y_0)\tan\gamma, \frac{S}{2}, -\frac{W}{2}) \quad \text{(C.7)}$$

$$D = (x_0 + (\frac{S}{2} - y_0)\tan\gamma, \frac{S}{2}, \frac{W}{2}) \quad \text{(C.8)}$$

$$E = (x_0 - (\frac{S}{2} + y_0)\tan\gamma, -\frac{S}{2}, -z_0) \quad \text{(C.9)}$$

$$F = (x_0 - (\frac{S}{2} + y_0)\tan\gamma, \frac{S}{2}, z_0) \quad \text{(C.10)}$$

The total area of detectable lines emitted by $\mathbf{r}_0$ in the plane Π_γ is limited by $\alpha_\varphi(\mathbf{r}_0, \gamma)$ and $\beta_\varphi(\mathbf{r}_0, \gamma)$:

$$\alpha_\varphi(\mathbf{r}_0, \gamma) = min(\alpha_{\varphi 1}(\mathbf{r}_0, \gamma), \alpha_{\varphi 2}(\mathbf{r}_0, \gamma)) \quad \text{(C.11)}$$

$$\beta_\varphi(\mathbf{r}_0, \gamma) = min(\beta_{\varphi 1}(\mathbf{r}_0, \gamma), \beta_{\varphi 2}(\mathbf{r}_0, \gamma)) \quad \text{(C.12)}$$

Next, an analytical derivation of the terms $\alpha_\gamma(\mathbf{r}_0)$ and $\beta(\mathbf{r}_0)$ of Eq(3.5) will be obtained. The expressions for the angle values seen by the point $\mathbf{r}_0$ in the XY plane (as shown in Figure C.2) for the left right side detector are:

$$\alpha_{\gamma 1}(\mathbf{r}_0) = \arctan\left(\frac{\frac{L}{2} + x_0}{\frac{S}{2} - y_0}\right) \quad \text{(C.13)}$$

$$\beta_{\gamma 1}(\mathbf{r}_0) = \arctan\left(\frac{\frac{L}{2} - x_0}{\frac{S}{2} - y_0}\right) \quad \text{(C.14)}$$

and for the left side detector:

$$\alpha_{\gamma 2}(\mathbf{r}_0) = \arctan\left(\frac{\frac{L}{2} - x_0}{\frac{S}{2} - y_0}\right) \quad \text{(C.15)}$$

$$\beta_{\gamma 2}(\mathbf{r}_0) = \arctan\left(\frac{\frac{L}{2} + x_0}{\frac{S}{2} + y_0}\right) \quad \text{(C.16)}$$

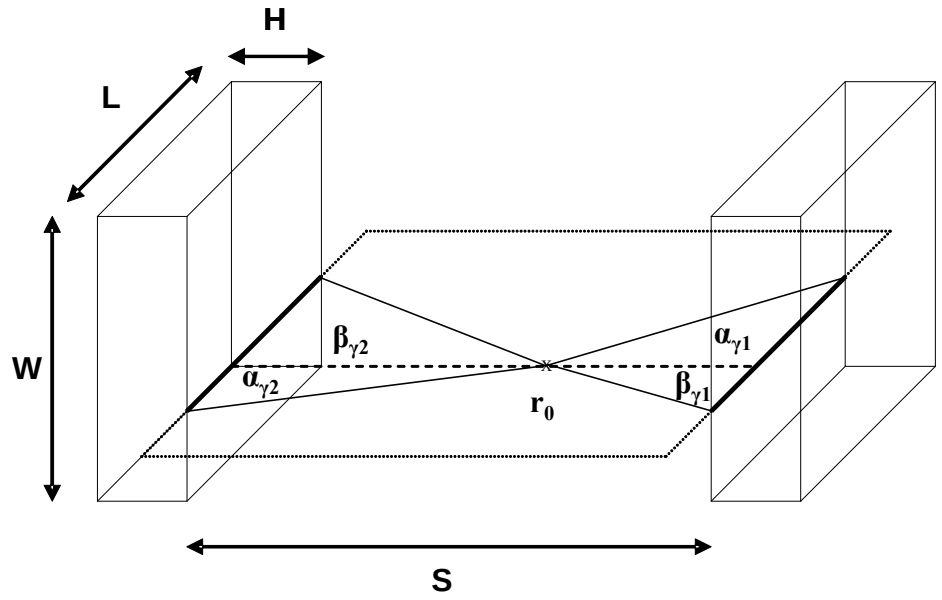

Figure C.2: Geometrical characterization of the range angles of view from point $\mathbf{r}_0$ into the detector heads within the plane XY

The total area of detectable lines emitted by $\mathbf{r}_0$ in the plane XY_γ is limited by$\alpha_\gamma(\mathbf{r}_0)$ and $\beta_\gamma(\mathbf{r}_0)$:

$$\alpha_\gamma(\mathbf{r}_0) = min(\alpha_{\gamma 1}(\mathbf{r}_0), \alpha_{\gamma 2}(\mathbf{r}_0)) \quad \text{(C.17)}$$

$$\beta_\gamma(\mathbf{r}_0) = min(\beta_{\gamma 1}(\mathbf{r}_0), \beta_{\gamma 2}(\mathbf{r}_0)) \quad \text{(C.18)}$$

Nomenclature

BCU: Biocomputing Unit

BGO: Bismuth Germinate

CNB: National Center for Biotechnology

DOI: Depth of Interaction

FBP: Filtered Back Projection

FORE: Fourier rebinning

FOV: Field of View

FWHM: Full Width at Half Maximum

GATE: GEANT4 Application for Tomographic Emission

GPU: Graphics Processing Unit

GSO: Gadolinium Oxyorthosilicate

KKK: Karush-Kuhn-Tucker

KL: Kullback-Leibler

LOR: Line of Response

LYSO: Lutetium-Yttrium Orthosilicate

LRF: Light Response Function

LSO: Lutetium Oxyorthosilicate

MAP: Maximum *a Posteriori*

MC: Monte Carlo

MLEM: Maximum Likelihood Expectation Maximization

MPI: Message Passing Interface

Nai(TI): thallium-doped sodium iodide

NIST: National Institute of Standard Technology

NRMSE: Normalized Root-Mean-Square Error

OSEM: Ordered Subsets Expectation Maximization

PET: Position Emission Tomography

PMT: Photomultiplier

PS-PMT: Position Sensitive Multipliers

RAMLA: Row Action Maximum Likelihood Algorithm

RMS: Root Mean Square

SAGE: Space Alternating Generalized Expectation Maximization

SNR: Signal-to-Noise Ratio

SPECT: Single-Photon Emission Computed Tomography

SSRB: Single Slice Rebinning

WLS: Weighted Least Squares

Bibliography

Agon, P., Kaufman, J.M., Goethals, P., Vanhaver, D., Bogaert, M.G., 1988. Study with positron emission tomography of the osmotic opening of the dog blood-brain-barrier for quinidine and morphine. J. Pharmacy Pharmacology 40, 539–543.

Agostinelli, S., Allison, J., Amako, K., Apostolakis, J., Araujo, H., Arce, P., Asai, M., Axen, D., Banerjee, S., Barrand, G., Behner, F., Bellagamba, L., Boudreau, J., Broglia, L., Brunengo, A., Burkhardt, H., Chauvie, S., Chuma, J., Chytracek, R., Cooperman, G., Cosmo, G., Degtyarenko, P., Dell'Acqua, A., Depaola, G., Dietrich, D., Enami, R., Feliciello, A., Ferguson, C., Fesefeldt, H., Folger, G., Foppiano, F., Forti, A., Garelli, S., Giani, S., Giannitrapani, R., Gibin, D., Cadenas, J.G., Gonzlez, I., Abril, G.G., Greeniaus, G., Greiner, W., Grichine, V., Grossheim, A., Guatelli, S., Gumplinger, P., Hamatsu, R., Hashimoto, K., Hasui, H., Heikkinen, A., Howard, A., Ivanchenko, V., Johnson, A., Jones, F., Kallenbach, J., Kanaya, N., Kawabata, M., Kawabata, Y., Kawaguti, M., Kelner, S., Kent, P., Kimura, A., Kodama, T., Kokoulin, R., Kossov, M., Kurashige, H., Lamanna, E., Lampn, T., Lara, V., Lefebure, V., Lei, F., Liendl, M., Lockman, W., Longo, F., Magni, S., Maire, M., Medernach, E., Minamimoto, K., de Freitas, P.M., Morita, Y., Murakami, K., Nagamatu, M., Nartallo, R., Nieminen, P., Nishimura, T., Ohtsubo, K., Okamura, M., O'Neale, S., Oohata, Y., Paech, K., Perl, J., Pfeiffer, A., Pia, M., Ranjard, F., Rybin, A., Sadilov, S., Salvo, E.D., Santin, G., Sasaki, T., Savvas, N., Sawada, Y., Scherer, S., Sei, S., Sirotenko, V., Smith, D., Starkov, N., Stoecker, H., Sulkimo, J., Takahata, M., Tanaka, S.,

Tcherniaev, E., Tehrani, E.S., Tropeano, M., Truscott, P., Uno, H., Urban, L., Urban, P., Verderi, M., Walkden, A., Wander, W., Weber, H., Wellisch, J., Wenaus, T., Williams, D., Wright, D., Yamada, T., Yoshida, H., Zschiesche, D., 2003. Geant4:a simulation toolkit. Nucl. Instrum. Methods Phys. Res., A 506, 250 – 303.

Aguiar, P., Rafecas, M., Ortuno, J.E., Kontaxakis, G., Santos, A., Pavía, J., Ros, D., 2010. Geometrical and Monte Carlo projectors in 3D PET reconstruction. Med Phys 37, 5691–5702.

Alessio, A., Kinahan, P., Harrison, R., Lewellen, T., 2005. Measured spatially variant system response for PET image reconstruction, in: Nuclear Science Symposium Conference Record, IEEE, p. 5 pp.

Alessio, A., Kinahan, P., Lewellen, T., 2006. Modeling and incorporation of system response functions in 3D whole body PET. Medical Imaging, IEEE Transactions on 25, 828 –837.

Alessio, A., MacDonald, L., 2008. Spatially variant positron range modeling derived from CT for PET image reconstruction, in: Nuclear Science Symposium Conference Record, IEEE, pp. 3637 –3640.

Aykac, M., Li, H., Uribe, J., Wang, Y., Baghaei, H., Liu, Y., Xing, T., Wong, W.H., 2003. A study of coincidence line spread function (CLSF) estimation for small scintillators using quadrant sharing technique. Nuclear Science, IEEE Transactions on 50, 1331 – 1338.

Badawi, R.D., Marsden, P.K., 1999. Developments in component-based normalization for 3D PET. Phys Med Biol 44, 571–594.

Bai, B., Li, Q., Holdsworth, C.H., Asma, E., Tai, Y.C., Chatziioannou, A., Leahy, R.M., 2002. Model-based normalization for iterative 3D PET image reconstruction. Phys Med Biol 47, 2773–2784.

Balcerzyk, M., Kontaxakis, G., Delgado, M., Garcia-Garcia, L., Correcher, C., Gonzalez, A.J., Gonzalez, A., Rubio, J.L., Benlloch, J.M., Pozo, M.A., 2009. Initial performance evaluation of a high resolution albira small animal positron emission tomography scanner with monolithic crystals and depth-of-interaction encoding from a user's perspective. Measurement Science and Technology 20, 104011.

Bao, Q., Sanghee, C., Quanzheng, L., Newport, D., Mu, C., Leahy, R., Chatziioannou, A.F., 2008. Monte Carlo based estimation of detector response in a large solid angle preclinical PET imaging system, in: Nuclear Science Symposium Conference Record, IEEE, pp. 5010 –5013.

Benlloch, J., Carrilero, V., Catret, J., Colom, R., Correcher, C., Gadea, R., Garcia Quiros, F., Gonzalez, A., Herrero, V., Lerche, C., Mora, F., Mora, C., Morera, C., Munar, A., Pavon, N., Ros, A., Sanchez, F., Sebastia, A., Vidal, L., 2006. Design and calibration of a small animal PET scanner based on continuous LYSO crystals and PSPMTs, in: Nuclear Science Symposium Conference Record, IEEE, pp. 2328 –2332.

Bercier, Y., Casey, M., Young, J., Wheelock, T., Gremillion, T., 2004. LSO PET/CT pico performance improvements with ultra Hi-Rez option, in: Nuclear Science Symposium Conference Record, IEEE, pp. 4038 –4042.

Blanco, A., 2006. Positron range effects on the spatial resolution of rpc-PET, in: Nuclear Science Symposium Conference Record, IEEE.

Bloomfield, P.M., Myers, R., Hume, S.P., Spinks, T.J., Lammertsma, A.A., Jones, T., 1997. Three-dimensional performance of a small-diameter positron emission tomograph. Phys Med Biol 42, 389–400.

Bloomfield, P.M., Rajeswaran, S., Spinks, T.J., Hume, S.P., Myers, R., Ashworth, S., Clifford, K.M., Jones, W.F., Byars, L.G., Young, J., Andreaco, M., Williams, C.W., Lammertsma, A.A., Jones, T., 1995. The design and physical characteristics of a small animal positron emission tomograph. Phys Med Biol 40, 1105–1126.

Boning, G., Pichler, B., Rafecas, M., Lorenz, E., Schwaiger, M., Ziegler, S., 2001. Implementation of Monte Carlo coincident aperture functions in image generation of a high-resolution animal positron tomograph. Nuclear Science, IEEE Transactions on 48, 805 –810.

Bowman, A.W., Azzalini, A., 1997. Applied Smoothing Techniques for Data Analysis: The Kernel Approach with S-Plus Illustrations (Oxford Statistical Science Series). Oxford University Press, USA.

Browne, J., DePierro, A.R., 1996. A row-action alternative to the EM algorithm for maximizing likelihoods in emission tomography. Medical Imaging, IEEE Transactions on 15, 687–699.

Bruyndonckx, P., Liu, X., Rajeswaran, S., Smolik, W., Tavernier, S., Zhang, S.P., 1996. Design and physical characteristics of a small animal PET using BaF2 crystals and a photosensitive wire chamber. Nucl. Instrum. Methods Phys. Res., A 382, 589–600.

Byrne, C.L., 1997. Convergent block-iterative algorithms for image reconstruction from inconsistent data. Image Process, IEEE Transactions on 6, 1296–1304.

Cal-González, J., Herraiz, J., España, S., Desco, M., Vaquero, J., Udias, J., 2009. Positron range effects in high resolution 3D PET imaging, in: Nuclear Science Symposium Conference Record, IEEE, pp. 2788 –2791.

Casey, M.E., Gadagkar, H., Newport, D., 1996. A component based method for normalization in volume PET, in: Grangeat, P., Amans, J.L. (Eds.), Three-Dimensional Image Reconstruction in Radiology and Nuclear Medicine, Kluwer Academic. pp. 66–71.

Casey, M.E., Nutt, R., 1986. A multicrystal two-dimensional BGO detector system for positron emission tomography. Nuclear Science, IEEE Transactions on 33, 460–463+.

Champion, C., Loirec, C.L., 2007. Positron follow-up in liquid water: Ii. Spatial and energetic study for the most important radioisotopes used in PET. Phys Med Biol 52, 6605–6625.

Chatziioannou, A., Qi, J., Moore, A., Annala, A., Nguyen, K., Leahy, R., Cherry, S.R., 2000. Comparison of 3D maximum a posteriori and filtered backprojection algorithms for high-resolution animal imaging with microPET. Medical Imaging, IEEE Transactions on 19, 507–512.

Chatziioannou, A.F., 2002. PET scanners dedicated to molecular imaging of small animal models. Mol Imaging Biol 4, 47–63.

Chatziioannou, A.F., Cherry, S.R., Shao, Y.P., Silverman, R.W., Meadors, K., Farquhar, T.H., Pedarsani, M., Phelps, M.E., 1999. Performance evaluation of microPET: A high-resolution lutetium oxyorthosilicate PET scanner for animal imaging. J. Nuclear Medicine 40, 1164–1175.

Chen, C., Lee, S.Y., Cho, Z., 1991. Parallelization of the EM algorithm for 3D PET image reconstruction. Medical Imaging, IEEE Transactions on 10, 513 –522.

Cherry, S., Chatziioannou, A.F., 2004. Small animal PET systems. Academic Press.

Cherry, S.R., Gambhir, S.S., 2001. Use of positron emission tomography in animal research. ILAR J 42, 219–232.

Cho, Z.H., Chan, J.K., Ericksson, L., Singh, M., Graham, S., MacDonald, N.S., Yano, Y., 1975. Positron ranges obtained from biomedically important positron-emitting radionuclides. J. Nuclear Medicine 16, 1174–1176.

Coakley, K., 1991. A cross-validation procedure for stopping the em algorithm and deconvolution of neutron depth profiling spectra. Nuclear Science, IEEE Transactions on 38, 9–15.

Cutler, P.D., Cherry, S.R., Hoffman, E.J., Digby, W.M., Phelps, M.E., 1992. Design-features and performance of a pet system for animal research. J. Nuclear Medicine 33, 595–604.

Daube-Witherspoon, M.E., Muehllehner, G., 1987. Treatment of axial data in three-dimensional PET. J. Nuclear Medicine 82, 1717–1724.

DeBenedetti, S., Cowan, C.E., Konneker, W.R., Primakoff, H., 1950. On the angular distribution of two-photon annihilation radiation. Phys. Rev. 77, 205–212.

Defrise, M., Kinahan, P., Townsend, D., Michel, C., Sibomana, M., Newport, D., 1997. Exact and approximate rebinning algorithms for 3D PET data. Medical Imaging, IEEE Transactions on 16, 145–158.

Del Guerra, A., Bartoli, A., Belcari, N., Herbert, D., Motta, A., Vaiano, A., Di Domenico, G., Sabba, N., Moretti, E., Zavattini, G., Lazzarotti, M., Sensi, L., Larobina, M., Uccelli, L., 2006. Performance evaluation of the fully engineered YAP-(S)PET scanner for small animal imaging. Nuclear Science, IEEE Transactions on 53, 1078 – 1083.

Espallardo, I.T., 2009. Image reconstruction and correction methods for MADPET-II based on Monte Carlo Techniquess. Ph.D. thesis. Universitat de Valencia - CSIC.

Fessler, J., Ficaro, E., Clinthorne, N., Lange, K., 1997. Grouped-coordinate ascent algorithms for penalized-likelihood transmission image reconstruction. Medical Imaging, IEEE Transactions on 16, 166 –175.

Fessler, J.A., 1994. Penalized weighted least-squares image-reconstruction for positron emission tomography. Medical Imaging, IEEE Transactions on 13, 290–300.

Fessler, J.A., Hero, A.O., 1994. Space-alternating generalized expectation-maximization algorithm. Signal Processing, IEEE Transactions on 42, 2664–2677.

Frese, T., Rouze, N., Bouman, C., Sauer, K., Hutchins, G., 2003. Quantitative comparison of FBP, EM, and Bayesian reconstruction algorithms for the IndyPET scanner. Medical Imaging, IEEE Transactions on 22, 258 –276.

Gambhir, S.S., Barrio, J.R., Herschman, H.R., Phelps, M.E., 1999. Assays for noninvasive imaging of reporter gene expression. Nuclear Medicine Biol. 26, 481–490.

Gambhir, S.S., Herschman, H.R., Cherry, S.R., Barrio, J.R., Satyamurthy, N., Toyokuni, T., Phelps, M.E., Larson, S.M., Balatoni, J., Finn, R., Sadelain, M., Tjuvajev, J., Blasberg, R., 2000. Imaging transgene expression with radionuclide imaging technologies. Neoplasia 2, 118–138.

Giménez, E., Benlloch, J., Gimenez, M., Lerche, C., Fernandez, M., Pavon, N., Rafecas, M., Sanchez, F., Sebastia, A., Esteve, R., Martinez, J., Toledo, J., 2004. Detector optimization of a small animal PET camera based on continuous LSO crystals and flat panel PS-PMTs, in: Nuclear Science Symposium Conference Record, IEEE, pp. 3885 – 3889 Vol. 6.

Giménez, E., Mora, C., Gimenez, M., Benlloch, J., Rafecas, M., 2005. Comparison of different Monte-Carlo based approaches to calculating the system matrix for small animal PET, in: Nuclear Science Symposium Conference Record, IEEE, pp. 2085 –2088.

Gordon, R., Bender, R., Herman, G.T., 1970. Algebraic reconstruction techniques ART for 3D electron microscopy and x-ray photography. J. Theoretical Biol. 29, 471.

Green, P., 1990. Bayesian reconstructions from emission tomography data using a modified EM algorithm. Medical Imaging, IEEE Transactions on 9, 84 –93.

Herraiz, J., España, S., Cabido, R., Montemayor, A., Desco, M., Vaquero, J., Udiass, J., 2011.

GPU-based fast iterative reconstruction of fully 3D PET sinograms. Nuclear Science, IEEE Transactions on 58, 2257 –2263.

Herraiz, J.L., España, S., Vaquero, J.J., Desco, M., Udías, J.M., 2006. FIRST: Fast iterative reconstruction software for PET tomography. Phys Med Biol 51, 4547–4565.

Hoffman, E., Guerrero, T., Germano, G., Digby, W., Dahlbom, M., 1989. PET system calibrations and corrections for quantitative and spatially accurate images. Nuclear Science, IEEE Transactions on 36, 1108 –1112.

Hudson, H.M., Larkin, R.S., 1994. Accelerated image-reconstruction using ordered subsets of projection data. Medical Imaging, IEEE Transactions on 13, 601–609.

Hume, S.P., Lammertsma, A.A., Myers, R., Rajeswaran, S., Bloomfield, P.M., Ashworth, S., Fricker, R.A., Torres, E.M., Watson, I., Jones, T., 1996. The potential of high-resolution positron emission tomography to monitor striatal dopaminergic function in rat models of disease. J Neurosci Methods 67, 103–112.

Hun, J.J., Miyaoka, R.S., Lewellen, T.K., 2002. cMiCE: a high resolution animal PET using continuous LSO with a statistics based positioning scheme. Nucl. Instrum. Methods Phys. Res., A 489, 584–598.

Inadama, N., Murayama, H., Tsuda, T., Nishikido, F., Shibuya, K., Yamaya, T., Yoshida, E., Takahashi, K., Ohmura, A., 2006. Optimization of crystal arrangement on 8-layer DOI PET detector, in: Nuclear Science Symposium Conference Record, IEEE, pp. 3082 –3085.

Ingvar, M., Eriksson, L., Rogers, G.A., Stoneelander, S., Widen, L., 1991. Rapid feasibility studies of tracers for positron emission tomography - high-resolution pet in small animals with kinetic-analysis. J. Cerebral Blood Flow Metabolism 11, 926–931.

Iriarte, A., Sorzano, C.O.S., Carazo, J.M., Rubio, J.L., Marabini, R., 2009. A theoretical

model for em-ml reconstruction algorithms applied to rotating PET scanners. Phys Med Biol 54, 1909–1934.

Jan, S., Santin, G., Strul, D., Staelens, S., Assie, K., Autret, D., Avner, S., Barbier, R., Bardies, M., Bloomfield, P.M., Brasse, D., Breton, V., Bruyndonckx, P., Buvat, I., Chatziioannou, A.F., Choi, Y., Chung, Y.H., Comtat, C., Donnarieix, D., Ferrer, L., Glick, S.J., Groiselle, C.J., Guez, D., Honore, P.F., Kerhoas-Cavata, S., Kirov, A.S., Kohli, V., Koole, M., Krieguer, M., van der Laan, D.J., Lamare, F., Largeron, G., Lartizien, C., Lazaro, D., Maas, M.C., Maigne, L., Mayet, F., Melot, F., Merheb, C., Pennacchio, E., Perez, J., Pietrzyk, U., Rannou, F.R., Rey, M., Schaart, D.R., Schmidtlein, C.R., Simon, L., Song, T.Y., Vieira, J.M., Visvikis, D., de Walle, R.V., Wieers, E., Morel, C., 2004. PET: a simulation toolkit for PET and SPECT. Phys Med Biol 49, 4543–4561.

Johnson, C., Yan, Y., Carson, R., Martino, R., Daube-Witherspoon, M., 1994. A system for the 3D reconstruction of retracted-septa PET data using the EM algorithm, in: Nuclear Science Symposium Conference Record, IEEE, pp. 1325 –1329 vol.3.

Johnson, C.A., Seidel, J., Carson, R.E., Gandler, W.R., Sofer, A., Green, M.V., DaubeWitherspoon, M.E., 1997. Evaluation of 3D reconstruction algorithms for a small animal PET camera. Nuclear Science, IEEE Transactions on 44, 1303–1308.

Johnson, V., 1994. A note on stopping rules in EM-ML reconstructions of ECT images. Medical Imaging, IEEE Transactions on 13, 569–571.

Joung, J., Miyaoka, R., Kohlmyer, S., Lewellen, T., 2000. Implementation of ML based positioning algorithms for scintillation cameras. Nuclear Science, IEEE Transactions on 47, 1104 –1111.

Kaczmarz, S., 1937. Angenherte auflsung von systemen linearer gleichungen. Bull. Internat. Acad. Polon.Sci 29, 471–481.

Karp, J.S., Muehllehner, G., 1985. Performance of a position-sensitive scintillation detector. Phys Med Biol 30, 643–655.

Karp, J.S., Muehllehner, G., MankofF, D.A., Ordonez, C.E., Ollinger, J.M., Daube-Witherspoon, M.E., Haigh, A.T., Beerbohm, D.J., 1990. Continuous-slice PENN-PET: a positron tomograph with volume imaging capability. J. Nuclear Medicine 31, 617–627.

Karush, W., 1939. Minima of functions of several variables with inequalities as side constraints. M.Sc. Dissertation. Dept. of Mathematics, Univ. of Chicago, Chicago, Illinois .

Kaufman, L., 1993. Maximum-likelihood, least-squares, and penalized least-squares for PET. Medical Imaging, IEEE Transactions on 12, 200–214.

Kinahan, P.E., Rogers, J.G., 1989. Analytic 3D image-reconstruction using all detected events. Nuclear Science, IEEE Transactions on 36, 964–968.

Klein, O., Nishina, T., 1929. Uber die streuung von strahlung durch freie elektronen nach der neuen relativistischen quantendynamik von dirac. Zeitschrift fur Physik A Hadrons and Nuclei 52, 853–868. 10.1007/BF01366453.

Kornblum, H.I., Araujo, D.M., Annala, A.J., Tatsukawa, K.J., Phelps, M.E., Cherry, S.R., 2000. In vivo imaging of neuronal activation and plasticity in the rat brain by high resolution positron emission tomography (micropet). Nat Biotechnol 18, 655–660.

Kudrolli, H., Worstell, W., Zavarzin, V., 2002. SS3D-fast fully 3D PET iterative reconstruction using stochastic sampling. Nuclear Science, IEEE Transactions on 49, 124 –130.

Kullback, S., Leibler, R.A., 1951. On information and sufficiency. Annals of Mathematical Statistics 22, 49–86.

Kume, H., Muramatsu, S., Iida, M., 1986. Position sensitive photomultiplier tubes for scintillation imaging. Nuclear Science, IEEE Transactions on 33, 359 –363.

Lange, K., Bahn, M., Little, R., 1987. A theoretical study of some maximum likelihood algorithms for emission and transmission tomography. Medical Imaging, IEEE Transactions on 6, 106 –114.

Lapointe, D., Brasseur, N., Cadorette, J., Madeleine, C.L., Rodrigue, S., van Lier, J.E., Lecomte, R., 1999. High-resolution PET imaging for in vivo monitoring of tumor response after photodynamic therapy in mice. J. Nuclear Medicine 40, 876–882.

Leahy, R.M., Qi, J., 2000. Statistical approaches in quantitative positron emissiontomography. Statistics and Computing 10, 147–165.

Lecomte, R., Cadorette, J., Rodrigue, S., Lapointe, D., Rouleau, D., Bentourkia, M., Yao, R., Msaki, P., 1996. Initial results from the Sherbrooke avalanche photodiode positron tomograph. Nuclear Science, IEEE Transactions on 43, 1952–1957.

Lee, K., Kinahan, P.E., Fessler, J.A., Miyaoka, R.S., Janes, M., Lewellen, T.K., 2004. Pragmatic fully 3D image reconstruction for the MiCES mouse imaging PET scanner. Phys Med Biol 49, 4563–4578.

Lerche, C., Benlloch, J., Snchez, F., Pavn, N., Gimnez, N., Fernndez, M., Gimnez, M., Sebasti, A., Martnez, J., Mora, F., 2005. Depth of interaction detection with enhanced position-sensitive proportional resistor network. Nucl. Instrum. Methods Phys. Res., A 537, 326 – 330. Proceedings of the 7th International Conference on Inorganic Scintillators and their Use in Scientific adn Industrial Applications.

Lerche, C., Ros, A., Monzo, J.M., Aliaga, R.J., N., F., Martinez-Perez, J.D., Herrero-Bosch, V., Esteve-Bosch, R., Gadea-Girones, R., Colom-Palero, R., Toledo, J., Mateo, F., Sebastia, A., Sanchez, F., Benlloch, J.M., 2009. Maximum likelihood positioning for gamma-ray imaging detectors with depth of interaction measurement. Nucl. Instrum. Methods Phys. Res., A 604, 359–362. 8th International Conference on Position Sensitive Detectors, Glasgow, SCOTLAND, SEP 01-05, 2008.

Levin, C., 2004. Application-Specific Small Field-of-View Nuclear Emission Imagers in Medicine. Academic Press.

Levin, C.S., Hoffman, E.J., 1999. Calculation of positron range and its effect on the fundamental limit of positron emission tomography system spatial resolution. Phys Med Biol 44, 781–799.

Levkovtiz, R., Falikman, D., Zibulevsky, M., Ben-Tal, A., Nemirovski, A., 2001. The design and implementation of COSEM, an iterative algorithm for fully 3D listmode data. Medical Imaging, IEEE Transactions on 20, 633–642.

Lewellen, T., Janes, M., Miyaoka, R., 2004. DMice-a depth-of-interaction detector design for PET scanners, in: Nuclear Science Symposium Conference Record, IEEE, pp. 2388 – 2392 Vol. 4.

Lewellen, T., Karp, J., 2004. PET systems. Academic Press.

Lewellen, T.K., 2008. Recent developments in PET detector technology. Phys Med Biol 53, R287–R317.

Lewitt, R.M., Matej, S., 2003. Overview of methods for image reconstruction from projections in emission computed tomography. IEEE Proc. 91, 1588–1611.

Lewitt, R.M., Muehllehner, G., 1986. Accelerated iterative reconstruction for positron emission tomography based on the em algorithm for maximum likelihood estimation. Medical Imaging, IEEE Transactions on 5, 16–22.

Liow, J.S., Strother, S., 1991. Practical tradeoffs between noise, quantitation, and number of iterations for maximum likelihood-based reconstructions. Medical Imaging, IEEE Transactions on 10, 563 –571.

Llosa, G., Battiston, R., Bisogni, M., Boscardin, M., Collazuol, G., Corsi, F., Dalla Betta, G., Del Guerra, A., Dinu, N., Levi, G., Marcatili, S., Moehrs, S., Marzocca, C., Piemonte,

C., Pozza, A., Sbarra, C., Quadrani, L., 2006. Novel silicon photomultipliers for PET application, in: Nuclear Science Symposium Conference Record, IEEE, pp. 1875 –1879.

Mair, B., Carroll, R., Anderson, J., 1996. Filter banks and the EM algorithm, in: Nuclear Science Symposium Conference Record, IEEE, pp. 1747 –1751 vol.3.

Marabini, R., Herman, G.T., Carazo, J.M., 1998. 3D reconstruction in electron microscopy using ART with smooth spherically symmetric volume elements (blobs). Ultramicroscopy 72, 53–65.

Marabini, R., Rietzel, E., Schroeder, R., Herman, G.T., Carazo, J.M., 1997. Three-dimensional reconstruction from reduced sets of very noisy images acquired following a single-axis tilt schema: application of a new three-dimensional reconstruction algorithm and objective comparison with weighted backprojection. J Struct Biol 120, 363–371.

Marabini, R., Sorzano, C.O.S., Matej, S., Fernndez, J.J., Carazo, J.M., Herman, G.T., 2004. 3D reconstruction of 2D crystals in real space. Image Process, IEEE Transactions on 13, 549–561.

Marriott, C.J., Cadorette, J.E., Lecomte, R., Scasnar, V., Rousseau, J., Vanlier, J.E., 1994. High-resolution pet imaging and quantitation of pharmaceutical biodistributions in a small animal using avalanche photodiode detectors. J. Nuclear Medicine 35, 1390–1396.

Mendes, P., Bruyndonckx, P., Navarrete, J., Perez, J., Li, Z., 2007. Evaluation of monolithic detector blocks for high- sensitivity PET imaging of the human brain, in: Nuclear Science Symposium Conference Record, IEEE, pp. 2953 –2955.

Milster, T.D., Selberg, L.A., Barrett, H.H., Landesman, A.L., Seacat, R.H., 1985. Digital position estimation for the modular scintillation camera. Nuclear Science, IEEE Transactions on 32, 748 –752.

Miyaoka, R.S., Joo, S.K., Lee, K., 2008. Detector light response modeling for a thick continuous slab detector. J Nucl Sci Technol 45, 634–638.

Moehrs, S., Defrise, M., Belcari, N., Guerra, A.D., Bartoli, A., Fabbri, S., Zanetti, G., 2008. Multi-ray-based system matrix generation for 3D PET reconstruction. Phys Med Biol 53, 6925–6945.

Moore, A.H., Osteen, C.L., Chatziioannou, A.F., Hovda, D.A., Cherry, S.R., 2000. Quantitative assessment of longitudinal metabolic changes in vivo after traumatic brain injury in the adult rat using FDG-microPET. J Cereb Blood Flow Metab 20, 1492–1501.

Muehllehner, G., Karp, J.S., 2006. Positron emission tomography. Phys Med Biol 51, R117–R137.

Mumcuoglu, E., Leahy, R., Cherry, S., Zhou, Z., 1994. Fast gradient-based methods for bayesian reconstruction of transmission and emission PET images. Medical Imaging, IEEE Transactions on 13, 687 –701.

Mumcuoglu, E.U., Leahy, R.M., Cherry, S.R., Hoffman, E., Hoffman, 1996. Accurate geometric and physical response modelling for statistical image reconstruction in high resolution PET.

Ollinger, J., Goggin, A., 1996. Maximum likelihood reconstruction in fully 3D PET via the SAGE algorithm, in: Nuclear Science Symposium Conference Record, IEEE, pp. 1594 –1598 vol.3.

Ollinger, J.M., Fessler, J.A., 1997. Positron-emission tomography. Image Process, IEEE Transactions on 14, 43–55.

Ortuño, J., Kontaxakis, G., Rubio, J.L., Guerra, P., Santos, A., 2010. Efficient methodologies for system matrix modelling in iterative image reconstruction for rotating high-resolution PET. Phys Med Biol 55, 1833–1861.

Palmer, M., Brownell, G., 1992. Annihilation density distribution calculations for medically important positron emitters. Medical Imaging, IEEE Transactions on 11, 373 –378.

Panin, V., Kehren, F., Rothfuss, H., Hu, D., Michel, C., Casey, M., 2006a. PET reconstruction with system matrix derived from point source measurements. Nuclear Science, IEEE Transactions on 53, 152 – 159.

Panin, V.Y., Kehren, F., Michel, C., Casey, M., 2006b. Fully 3-D PET reconstruction with system matrix derived from point source measurements. Medical Imaging, IEEE Transactions on 25, 907–921.

Phelps, M.E., Hoffman, E.J., Huang, S.C., Kuhl, D.E., 1978. ECAT: a new computerized tomographic imaging system for positron-emitting radiopharmaceuticals. J. Nuclear Medicine 19, 635–647.

Phelps, M.E., Hoffman, E.J., Huang, S.C., Ter-Pogossian, M.M., 1975. Effect of positron range on spatial resolution. J. Nuclear Medicine 16, 649–652.

Pichler, B., Boning, G., Lorenz, E., Mirzoyan, R., Pimpl, W., Schwaiger, M., Ziegler, S.I., 1998. Studies with a prototype high resolution PET scanner based on LSO-APD modules. Nuclear Science, IEEE Transactions on 45, 1298–1302.

Pouliot, N., Gagnon, D., Laperriere, L., Gregoire, J., Arsenault, A., 1991. Maximum likelihood positioning in the scintillation camera using depth of interaction, in: Nuclear Science Symposium Conference Record, IEEE, pp. 1878 –1881 vol.3.

Pratx, G., Levin, C., 2011. Online detector response calculations for high-resolution PET image reconstruction. Phys Med Biol 56, 4023–4040.

de la Prieta, R., Hernndez, J., Schiavi, E., Malpica, N., 2006. Analytical geometric model for photon coincidence detection in 3D PET, in: Nuclear Science Symposium Conference Record, IEEE.

Qi, J., Leahy, R.M., Cherry, S.R., Chatziioannou, A., Farquhar, T.H., 1998. High-resolution 3D Bayesian image reconstruction using the microPET small-animal scanner. Phys Med Biol 43, 1001–1013.

Qi, J.Y., Leahy, R.M., 2006. Iterative reconstruction techniques in emission computed tomography. Phys Med Biol 51, R541–R578.

Rafecas, M., Boning, G., Pichler, B., Lorenz, F., Schwaiger, A., Ziegler, S., 2002. Effect of noise in the probability matrix used for statistical reconstruction of PET data, in: Nuclear Science Symposium Conference Record, IEEE, pp. 1787 – 1791 vol.3.

Rafecas, M., Bning, G., Pichler, B.J., Lorenz, E., Schwaiger, M., Ziegler, S.I., 2003. Inter-crystal scatter in a dual layer, high resolution LSO-APD positron emission tomograph. Physics in Medicine and Biology 48, 821.

Rafecas, M., Mosler, B., Dietz, M., Pogl, M., Stamatakis, A., McElroy, D., Ziegler, S., 2004. Use of a Monte Carlo-based probability matrix for 3D iterative reconstruction of MADPET-II data. Nuclear Science, IEEE Transactions on 51, 2597 – 2605.

Raheja, A., Dhawan, A.P., 2000. Wavelet based multiresolution expectation maximization image reconstruction algorithm for positron emission tomography. Comput Med Imaging Graph 24, 359–376.

Rahmim, A., Lenox, M., Michel, C., Reader, A., Sossi, V., 2003. Space-variant and anisotropic resolution modeling in list-mode EM reconstruction, in: Nuclear Science Symposium Conference Record, IEEE, pp. 3074 – 3077 Vol.5.

Rahmim, A., Lenox, M., Reader, A.J., Michel, C., Burbar, Z., Ruth, T.J., Sossi, V., 2004. Statistical list-mode image reconstruction for the high resolution research tomograph. Phys Med Biol 49, 4239–4258.

Rahmim, A., Tang, J., Lodge, M.A., Lashkari, S., Ay, M.R., Lautamki, R., Tsui, B.M.W., Bengel, F.M., 2008. Analytic system matrix resolution modeling in PET: an application to Rb-82 cardiac imaging. Phys Med Biol 53, 5947–5965.

Ranganath, M.V., Dhawan, A.P., Mullani, N., 1988. A multigrid expectation maximization reconstruction algorithm for positron emission tomography. Medical Imaging, IEEE Transactions on 7, 273–278.

Reader, A., Ally, S., Bakatselos, F., Manavaki, R., Walledge, R., Jeavons, A., Julyan, P., Zhao, S., Hastings, D., Zweit, J., 2002a. One-pass list-mode em algorithm for high-resolution 3D PET image reconstruction into large arrays. Nuclear Science, IEEE Transactions on 49, 693 – 699.

Reader, A.J., Erlandsson, K., Flower, M.A., Ott, R.J., 1998. Fast accurate iterative reconstruction for low-statistics positron volume imaging. Phys Med Biol 43, 835–846.

Reader, A.J., Manavaki, R., Zhao, S., Julyan, P.J., Hastings, D.L., Zweit, J., 2002b. Accelerated list-mode EM algorithm. Nuclear Science, IEEE Transactions on 49, 42–49.

Sánchez, F., Benlloch, J.M., Escat, B., Pavon, N., Porras, E., Kadi-Hanifi, D., Ruiz, J.A., Mora, F.J., Sebastia, A., 2004. Design and tests of a portable mini gamma camera. Med Phys 31, 1384–1397.

Sánchez, F., Moliner, L., Correcher, C., Gonzalez, A., Orero, A., Carles, M., Soriano, A., Rodriguez-Alvarez, M.J., Medina, L.A., Mora, F., Benlloch, J.M., 2012. Small animal PET scanner based on monolithic LYSO crystals: Performance evaluation. Med Phys 39, 643.

Scheins, J.J., Boschen, F., Herzog, H., 2006. Analytical calculation of volumes-of-intersection for iterative, fully 3D PET reconstruction. Medical Imaging, IEEE Transactions on 25, 1363–1369.

Schretter, C., 2006. A fast tube of response ray-tracer. Med Phys 33, 4744–4748.

Selivanov, V., Picard, Y., Cadorette, J., Rodrigue, S., Lecomte, R., 2000. Detector response models for statistical iterative image reconstruction in high resolution PET. Nuclear Science, IEEE Transactions on 47, 1168 –1175.

Shakirin, G., Crespo, P., Fiedler, F., Wagner, A., Enghardt, W., 2008. Optimum voxel size for reconstruction of in-beam PET data, in: Nuclear Science Symposium Conference Record, IEEE, pp. 5066 –5069.

Shepp, L., Logan, B., 1974. The Fourier reconstruction of a head section. Nuclear Science, IEEE Transactions on 21, 21–33.

Siddon, R.L., 1985. Fast calculation of the exact radiological path for a 3D CT array. Med Phys 12, 252–255.

Siegel, S., Cherry, S.R., Ricci, A.R., Shao, Y.P., Phelps, M.E., 1995. Development of continuous detectors for a high-resolution animal PET system. Nuclear Science, IEEE Transactions on 42, 1069–1074.

Slijpen, E., Beekman, F., 1999. Comparison of post-filtering and filtering between iterations for SPECT reconstruction. Nuclear Science, IEEE Transactions on 46, 2233–2238.

Snyder, D., Miller, M., Politte, L.T.L.J.D., 1987. Noise and edge artifacts in maximum-likelihood reconsctructions for emission tomography. Medical Imaging, IEEE Transactions on 6, 228–238.

Soares, E.J., Germino, K.W., Glick, S.J., Stodilka, R.Z., 2003. Determination of three-dimensional voxel sensitivity for two- and three-header coincidence imaging. Nuclear Science, IEEE Transactions on 50, 405–412.

Sorzano, C.O., Marabini, R., Boisset, N., Rietzel, E., Schrder, R., Herman, G.T., Carazo, J.M., 2001. The effect of overabundant projection directions on 3D reconstruction algorithms. J Struct Biol 133, 108–118.

Sorzano, C.O.S., Velzquez-Muriel, J.A., Marabini, R., Herman, G.T., Carazo, J.M., 2008. Volumetric restrictions in single particle 3DEM reconstruction. Pattern Recognit 41, 616.

Staelens, S., D'Asseler, Y., Vandenberghe, S., Koole, M., Lemahieu, I., de Walle, R.V., 2004. A three-dimensional theoretical model incorporating spatial detection uncertainty in continuous detector PET. Phys Med Biol 49, 2337–2350.

Stickel, J.R., Cherry, S.R., 2005. High-resolution PET detector design: modelling components of intrinsic spatial resolution. Phys Med Biol 50, 179–195.

Stickel, J.R., Qi, J., Cherry, S.R., 2007. Fabrication and characterization of a 0.5-mm lutetium oxyorthosilicate detector array for high-resolution PET applications. J. Nuclear Medicine 48, 115–121.

Strul, D., Slates, R.B., Dahlbom, M., Cherry, S.R., Marsden, P.K., 2003. An improved analytical detector response function model for multilayer small-diameter PET scanners. Phys Med Biol 48, 979–994.

Sureau, F.C., Reader, A.J., Comtat, C., Leroy, C., Ribeiro, M.J., Buvat, I., Trbossen, R., 2008. Impact of image-space resolution modeling for studies with the high-resolution research tomograph. J. Nuclear Medicine 49, 1000–1008.

Surti, S., Karp, J.S., Perkins, A.E., Cardi, C.A., Daube-Witherspoon, M.E., Kuhn, A., Muehllehner, G., 2005. Imaging performance of A-PET: a small animal PET camera. Medical Imaging, IEEE Transactions on 24, 844–852.

Surti, S., Scheuermann, R., Werner, M., Karp, J., 2009. Improved spatial resolution in PET scanners using sampling techniques. Nuclear Science, IEEE Transactions on 56, 596 –601.

Tai, Y.C., Chatziioannou, A.F., Yang, Y., Silverman, R.W., Meadors, K., Siegel, S., Newport, D.F., Stickel, J.R., Cherry, S.R., 2003. MicroPET ii: design, development and initial performance of an improved microPET scanner for small-animal imaging. Phys Med Biol 48, 1519–1537.

Tanaka, E., 1987. A fast reconstruction algorithm for stationary positron emission tomography based on a modified em algorithm. Medical Imaging, IEEE Transactions on 6, 98–105.

Tavernier, S., Bruyndonckx, P., Leonard, S., Devroede, O., 2005. A high-resolution PET detector based on continuous scintillators. Nucl. Instrum. Methods Phys. Res., A 537, 321 – 325. Proceedings of the 7th International Conference on Inorganic Scintillators and their Use in Scientific adn Industrial Applications.

Terstegge, A., Weber, S., Herzog, H., Muller-Gartner, H., Halling, H., 1996. High resolution and better quantification by tube of response modelling in 3D PET reconstruction, in: Nuclear Science Symposium Conference Record, IEEE, pp. 1603 –1607 vol.3.

Tjuvajev, J.G., Avril, N., Oku, T., Sasajima, T., Miyagawa, T., Joshi, R., Safer, M., Beattie, B., DiResta, G., Daghighian, F., Augensen, F., Koutcher, J., Zweit, J., Humm, J., Larson, S.M., Finn, R., Blasberg, R., 1998. Imaging herpes virus thymidine kinase gene transfer and expression by positron emission tomography. Cancer Research 58, 4333–4341.

Tohme, M.S., Qi, J., 2009. Iterative image reconstruction for positron emission tomography based on a detector response function estimated from point source measurements. Phys Med Biol 54, 3709–3725.

Tomitani, T., Futami, Y., Izeki, Y., Kouda, S., Nishio, T., Murakami, T., Kitagawa, A., Kanazawa, M., Urakabe, E., Shinbo, M., Kanai, T., 1999. Depth encoding of point-of-interaction in thick scintillation cameras, in: Nuclear Science Symposium Conference Record, IEEE, pp. 1182 –1186 vol.3.

Townsend, D.W., 1991. Optimization of signal in positron emission tomography scans: present and future developments. Ciba Found Symp 163, 57–69; discussion 69–75.

Tsui, B.M.W., Zhao, X.D., Frey, E.C., Gullberg, G.T., 1991. Comparison between ML-EM and WLS-CG algorithms for SPECT image-reconstruction. Nuclear Science, IEEE Transactions on 38, 1766–1772.

Vandenberghe, S., Staelens, S., Byrne, C.L., Soares, E.J., Lemahieu, I., Glick, S.J., 2006. Reconstruction of 2d pet data with monte carlo generated system matrix for generalized natural pixels. Phys Med Biol 51, 3105–3125.

Vaquero, J., Lage, E., Ricón, L., Abella, M., Vicente, E., Desco, M., 2005. rPET detectors design and data processing, in: Nuclear Science Symposium Conference Record, IEEE.

Vaquero, J., Pascau, J., A, A.M., Arco, J., Desco, M., 2004. Performance characteristics of the ARGUS-drT small animal PET scanner: preliminary results, in: Nuclear Science Symposium Conference Record, IEEE.

Vaquero, J.J., Desco, M., 2005. Technical limitations of the positron emission tomography PET for small laboratory animals. Rev Esp Med Nucl 24, 334–347.

Vardi, Y., Shepp, L.A., Kaufman, L., 1985. A statistical-model for positron emission tomography. J. Am. Statistical Association 80, 8–20.

Veklerov, E., Llacer, J., 1987. Stopping rule for the MLE algorithm based on statistical hypothesis testing. Medical Imaging, IEEE Transactions on 6, 313–319+.

Veklerov, E., Llacer, J., Hoffman, E., 1988. MLE reconstruction of a brain phantom using a Monte Carlo transition matrix and a statistical stopping rule. Nuclear Science, IEEE Transactions on 35, 603 – 607.

Watanabe, M., Okada, H., Shimizu, K., Omura, T., Yoshikawa, E., Kosugi, T., Mori, S., Yamashita, T., 1997. A high resolution animal PET scanner using compact PS-PMT detectors. Nuclear Science, IEEE Transactions on 44, 1277–1282.

Yao, R., Seidel, J., Liow, J.S., Green, M., 2005. Attenuation correction for the NIH ATLAS small animal PET scanner. Nuclear Science, IEEE Transactions on 52, 664 – 668.